University College London

Doctoral Thesis, Department of Chemistry

Functional silica films: preparation and applications of porous films produced from waterglass

Author:

John Maurice Chapman-Fortune

Supervisors:

Prof. Gopinathan Sankar, Prof. Ivan P. Parkin, Prof. Gregory K. L. Goh

I, John Maurice Chapman-Fortune confirm that the work presented in this thesis is my own. Where information has been derived from other sources, I confirm that this has been indicated in the thesis.

John Maurice Chapman-Fortune

Acknowledgements

Before I signed up for this PhD, which involved leaving the UK for two years, I asked my Mum, Sister and Gran if they would mind me being gone for that long, they were all supportive of me pursuing studies abroad and gave me their blessings. However, a month before I was due to leave, they told me they had forgotten I was leaving, and they were very upset (at least they pretended to be). Hopefully the time we have been stuck together at home during the lockdowns has helped us to make up for our time apart.

Having been lucky enough to study in Singapore, I have two groups of people to thank for their support with my project.

From UCL, Mike Powell, Sanjayan Sathavisam, Kevin To, Premrudee Pomdet and Raul Quesada-Cabrera who helped me with characterization in the final months, Steve Firth endured all of my annoying questions and was always ready to banter. Will Peveler, Tom Macdonald, Filip Ambroz and Mark Portnoi from Engineering assisted me with the quantum dot project and spent lots of time talking through the project with me and helping me to collect data. Big thanks to Alaric Taylor, Alberto Alvarez Fernandez, Barry Reid and Stefan Guldin of the AdReNa group in Chemical Engineering who helped me with characterization for the nanosphere chapter and let me use their equipment.

From IMRE in Singapore I want to thank Yee Fun Lim and my third supervisor Gregory Goh for all of their supervision and the new directions we took with the project, particularly for the first and second chapters as well as the patent we submitted together. Darren Neo, Albertus Denny Handoko and Poh Chong Lim all provided me with a lot of support during my time there. I could not have done any ellipsometry or XPS in Singapore without countless hours of labour from Arash Nemati, Norton West and Muhammed Tanhei.

New friends I made in Singapore helped me to stay sane on a surprisingly cramped island, Kamal, Pepe, Marilyne, Norton and Ben, just to name a few. The years I spent in Singapore were easily some of the best of my life (so far).

Last but not least I would like to thank my supervisors Gopinathan Sankar and Ivan Parkin for giving me this opportunity and also for their continued support throughout, even from many thousands of miles away.

Common Abbreviations

NaWG sodium waterglass
KWG potassium waterglass
BO bridging oxygen
NBO non-bridging oxygen
Na KLL sodium KLL Auger XPS line

TEOS tetraethyl orthosilicate
FCC face-centred cubic
O:W oil water ratio
PQD perovskite quantum dot
PL photoluminescence
QY quantum yield

SEM scanning electron microscopy
EDX energy dispersive X-ray spectroscopy
FE field emission
XPS X-ray photoelectron spectroscopy
XRD X-ray diffraction
FTIR Fourier transform infrared
ATR attenuated total reflection
NMR nuclear magnetic resonance
STA simultaneous thermal analysis
TGA thermogravimetric analysis
DSC differential scanning calorimetry
AFM atomic force microscopy
DLS dynamic light scattering
TCSPC time correlated single photon counting
CPS counts per second

EMA effective medium approximation
IR infrared
UV ultraviolet
E_g band gap
BE binding energy
FWHM full width at half maximum
T_g glass transition temperature

T temperature in degrees Celsius, °C

t time in specified units

Contents

List of figures

List of tables

1. Introduction

Porous materials feature microscopic voids that give them the ability to interact with atoms, ions and molecules throughout the bulk of their structure, in addition to the surface interactions offered by their non-porous counterparts.[1] Their greatly enhanced surface area enables their function as host matrices for supporting other materials, such as nanoparticles or coatings, combining the properties of both materials to make materials with previously unforeseen properties and applications. Scaling down these materials to a surface coating of nanometer or micron scale thickness can provide additional functionality to the underlying support and offer new niche applications. For example, Guldin et al.[2] have used the self-assembly of block copolymer micelles to produce a mesoporous silica film of controlled thickness and incorporated TiO_2 nanocrystals to make a self-cleaning, antireflective film that could be incorporated into solar cells. This film has been deposited onto flexible plastic substrates as evidence of its compatibility with useful substrate materials.[2]

The pore ordering is also vital to many applications. Pores can interact with matter on a molecular level, a property first recognised (synthetically) in zeolites and taken advantage of in applications such as gas absorption, ion exchange, catalysis and molecular sieving.[1] Other metal oxides (including silica) have been proven capable of forming a variety of nanoporous structures. They generally offer the flexibility of being able to form around different templates as well as forming robust structures that can withstand high temperatures and harsh chemical environments, they also have highly active surfaces that can easily be functionalised and are compatible with many other materials.

There is much literature on the generation of micro- and mesoporous metal oxide materials, however only a few methods of reliably generating larger porosity are known, including hard organic polymer and emulsion templates, macrophase separation, and lithographic techniques. Of these methods only certain hard organic templates and lithographic methods can reliably produce ordered pores.

In this work sodium and potassium waterglass solutions were used to produce silica coatings with solution processing methods such as spin and dip coating. Different types of macroporous structures have been generated from these solutions.

1.1 Ordered Porous materials

IUPAC defines porous materials by their pore sizes (pore diameter, d). They are classified as micropores (d ≤ 2 nm), mesopores (2 < d ≤ 50 nm) and macropores (d ≥ 50 nm).[3]

The first ordered porous materials, produced in the 1950's, were synthetic crystalline zeolites (type A, sodium aluminosilicate).[4] These zeolitic materials offered unique ion exchange,[5] gas absorbtion and molecular sieving properties. Their ordered pore sizes offered shape selective separation and catalysis of organic molecules. Their composition involves a 3-dimensional array, (of general formula $M_x/nO[(AlO_2)_x(SiO_2)_y].mH_2O$, M = metal cation of valence n, x ≥ 2), built of tetrahedral units of formula TO_4, where T = Si or Al).[3] Since their initial discovery many more structures displaying similar properties have been developed, for example the non-isostructural aluminophosphate molecular sieves ($AlPO_4$-n) or similar materials generated from the addition of Si,[6] Me (Me = Co, Fe, Mg, Mn, Zn) or El (El = As, B, Be, Ga, Ti, Li). The term 'zeolites' now encompasses a broader range of microporous silica-based solids with crystalline walls including cases where Si in a tetrahedral (T) site has been substituted for either a trivalent (e.g., Al, Fe, B, Ga) or tetravalent (e.g., Ti, Ge) element. Structures are now defined by their Si/T ratio, for zeolites Si/T < 500, for zeosils Si/T > 500. Zeosils are predominately Si-based materials but their porosity is inaccessible, unlike clathrasils. Microporous phosphates are considered as "related porous materials".[3]

Porous materials generally offer greater surface area; small, ordered pores can interact with matter on a molecular level, acting as a molecular sieve for catalysis and separation, but also have potential as optical materials (e.g., low k dielectrics), as well as molecular sensing. Hence there is much motivation to explore their properties.[7] The properties of common porous materials are compared in **Table 1.1**.

Most templated nanostructured materials in the literature are inorganic (silica, metal oxides) or carbon based. The formation of porosity in for example organic polymers is generally thermodynamically unfavourable; polymers chains pack efficiently to minimise void spaces, as the macromolecules can twist and bend to maximise their intermolecular interaction.[8] Creating nanostructures in these materials requires a rigid, highly cross-linked polymer system, found in activated carbons[9] or polymer resins.[10] Porous organic materials would have the low density and readily functionalised surfaces of organic materials as well as properties normally associated with nanostructured inorganic materials including high chemical reactivity and surface area, making them candidates for separation, catalysis, as membranes and optical or dielectric materials.[8]

New types of porous materials have been prepared through the coordination of metal ions to organic 'linkers' known as metal-organic frameworks (MOFs), which feature exceptionally high porosity (pore volume) and low density, making them useful in applications such as gas storage.[11] However they still cannot replace porous metal oxides due to their limited stability at high temperatures and high cost of fabrication. Functionalisation of the organic linker or incorporation of organic groups into the framework enables their use in gas adsorption and catalysis, however organic functionalised porous oxides may now be synthesised that can compete with MOFs in this respect.[1]

There are an abundance of applications of porous materials, spanning almost every aspect of materials science. Zeolites have been used in high-performance liquid chromatography (HPLC) and the separation of biomolecules. They have also been used to separate biopolymers due to the phenomenon of biopolymer absorption on zeolite surfaces.[12] Microchip densities are increasing as their sizes decrease, increasing the demand for insulators with a lower dielectric constant than dense SiO_2 ($k = 3.9\text{-}4.2$). Porous materials have demonstrated lower values ($k < 2.2$).[1] Pores have been introduced into electrode materials of Li ion batteries to increase the electrode surface area for greater interaction between electrode and electrolyte allowing faster diffusion of charges and (Li^+) ions and ensuring penetration of the electrode by the electrolyte.[13] Zeolites and MOFs have been used for gas sensing of pollutants (e.g. NO_x and carbon monoxide) in automotive applications.[14] The efficiency of solar systems used for both energy conversion and storage has been improved by the inclusion of porous materials, e.g. solar heat exchangers and solar heaters experience improved heat transfer rates with a reasonable pressure drop when made with high thermal conductivity materials featuring an abundance of porosity.[15] Colloid based porous materials (CBPM) have been used to produce optical materials with a photonic bandgap, hydrophobic surfaces, porous electrodes and porous materials for catalysis and sensing of various dimensions through manipulation of their composition, pore network and ordering and through patterning of their nanostructured units.[16]

Other more obscure emerging applications of porous materials include using zeolites as hosts for contrasting agents (e.g. Gd^{3+}) that offer improved t_1 (spin-lattice) relaxation times in MRI whilst attenuating their toxicity, as hosts for organic dyes in zeolite-dye microlasers, and as templates or closed-spaces in which porous carbons or single-walled carbon nanotubes can be synthesised.[1]

Table 1.1. Different types of porous materials and their properties are compared. 'Ultraporous' refers to materials with high surface area and pore volume of any type of porosity. Terminology: 'PIMs' are polymers of intrinsic microporosity, a 'cocrystal' is a molecular crystal containing more than one molecular building unit and 'CMPs' are conjugated microporous polymers. (Reproduced from Slater et al., reference 7).

	Zeolites	Metal-organic frameworks	Covelent-organic frameworks	Porous organic polymers	Porous molecular solids
Porosity	Microporous, mesoporous, narrow pore size distribution	Can be ultraporous, mesoporous, narrow pore size distribution	Can be ultraporous, mesoporous, narrow pore size distibution	Can be ultraporous, mostly microporous, broader size distibution	Can be ultraporous, mesoporous, but this is rare so far
Crystallinity	Typically high, can be amorphous	Typically high	Modest to high	Amorphous	High, amorphous examples exist
Stability	High thermal stability, can be acid/base sensitive	Poor to good, growing number of water stable MOFs	Boronates generally poor, imines generally good	Good to excellent, especially hydrothermal	Generally poor, some isolated examples of hydrothermal stability
Modularity/ diversity	High, new structures can be base on known zeolites	Very high even for single-linker MOFs	In principle high, less developed than MOFs	Very high, multiple linkers and linker functions possible	Cocrystals possible, few examples
Processing	Insoluble, but technologies for films, composites and pellets are well developed	Insoluble, but many recent examples of composites and films	Insoluble, but examples of surface growth	Modest processability, with exception of soluble PIMs	Soluble, as for PIMs could be advantage or disadvantage, depending on function
Designability	Excellent, however design of organic templates can be challenging	Excellent, principles of metal-organic bonding well developed	In principle good	Good control over composition, 3D stucture control more challenging	Isolated cage can encode functions, but no general redesign strategy
Unique selling points	Stability, low cost, commercially proven technology	Structural and chemical control for diverse range of materials	Electronic properties	Extended conjugation for CPMs, solution processing for PIMs	Solution processing, physical properties intrinsic to cages
Summary	Developed but still actively growing area, major commercial importance	Established and highly active field	Much less developed than MOFs, early promise for organic electronics	Rapidly growing in number, diverse chemistry, commercial application for PIMs	New area, few examples, but promise for specific molecular separations

1.2 Thin films with ordered porosity and their bulk counterparts

For almost every type of porous material, thin films or unsupported 2-dimensional counterparts are being synthesised and their properties and potential evaluated. For example there is a plethora of work around 2D layered zeolites originating from layered precursors.[17] Further analysis of these nanosized, nanostructured materials should reveal new applications and assist in the understanding of the properties of these materials as well as revealing additional functionality not seen in the bulk.

1.3 Micro-, meso- and macroporous materials and thin films

Templating is the process of 'copying' a structure to form another through structural inversion; they are essentially structure-directing agents. The product is an inverted replica of the templating agent. Thermodynamics generally works to minimise surface area, making the formation of pores unfavourable in the absence of a template as any voids present in the material usually collapse via plastic deformation of their walls.[8]

Hard and soft templates (**Figure 1.1**) are used to define porosity; structures of soft templates tend to vary with the synthesis conditions, whereas hard templates are generally rigid and are introduced to the matrix system in the form they will be used in.

They may still reorganise on a macroscale but will usually not undergo any change in molecular configuration.[18]

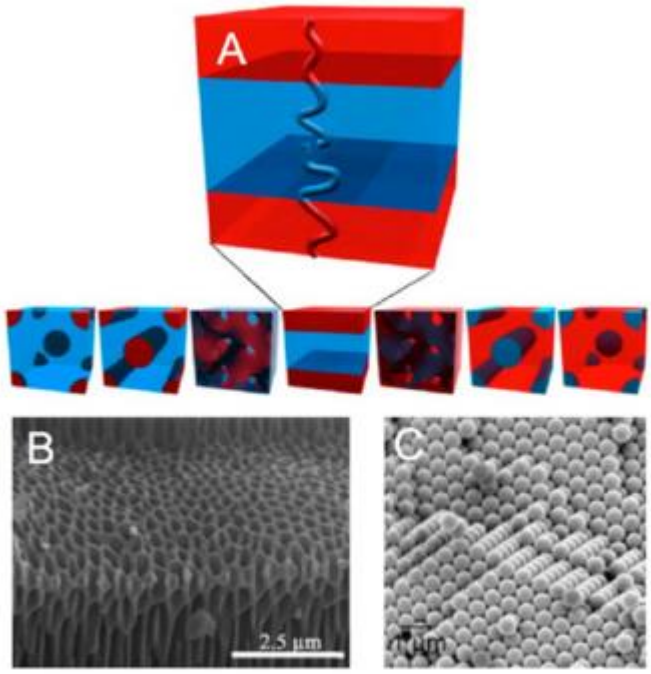

Figure 1.1. Hard and soft templates. a) phases formed by block copolymer self-assembly including spherical, cylindrical, gyroidal and lamellar, b) porous anodic alumina membrane and c) an array of a colloidal crystal template. (Taken from Stein et al., reference 18).

Zeolite crystals have been produced using seed-induced growth in the absence of a templating agent. Nucleation seeds include inorganic cations (e.g., Na) and organic cations (e.g., organic ammonium). This method will not be discussed in detail here.[19]

Molecular organic templates generally increase the cost of zeolite production as well as making their production more energy consuming and producing harmful gases from high temperature calcination used to facilitate their decomposition.[19] Despite the environmentally unfriendly by-products produced from the combustion of organic templates, they have proven capable of reliably and accurately producing microporosity in silicates and aluminosilicates (using molecular organic additives) and meso/macroporosity (with block copolymers (≤ 50 nm) or latex spheres (50 nm – several µm)).[20]

Mesopores can be obtained using surfactant arrays or emulsion droplets as templates.[20] The synthesis of ordered mesoporous materials is generally carried out at low temperatures (< 473 K) and pressures (a few atmospheres) in aqueous solution, usually resulting in a kinetic product as opposed to the most thermodynamically stable form of the material.[1]

Polymerisation induced phase separation involves inducing the hydrolysis-condensation polymerisation of an inorganic precursor around a microphase separated medium in aqueous solution. Templates used for these mediums are generally polymers (e.g., poly(ethyleneoxide)). This technique forms disordered macropores via spinodal decomposition of the two polymer phases, additional mesoporosity can be introduced with the addition of block copolymers.[21]

Hierarchical structures have also been created in both bulk and thin film formats by incorporating both hard and soft templates into their structures. The structures can be any combination of micro-, meso- and macroporosity depending on the combination of templates used. For example combinations of colloidal crystals and surfactants[18] or emulsions and surfactants can be used to make macroporous structures containing microporous voids.[21] Foams have also been used to produce hierarchical porous structures by introducing foam into the metal-oxide sol.[22] Elaborately shaped hierarchical pores have been produced by combining these techniques with mould patterning.[23] This technique extends to the production of crystalline structures such as zeolites.[24]

1.3.1 Templates for micro- and mesoporous materials and thin films

Micro- and mesopores are most commonly generated using soft templates.[18]

Molecular organic templating agents have mainly been used in the synthesis of zeolites. The most commonly used organic templates include quarternary ammonium cations, linear or cyclic ethers and organometallic complexes featuring organic ligands coordinated to a transition metal centre. The template should be sufficiently chemically and thermally stable to maintain its integrity during the autoclave treatment, resulting in its inclusion in the initial synthetic product, but also adding to the stability of the as-synthesised mineral.[3] Organic templates can also be formed in situ through decomposition of a molecular organic precursor, e.g. in the decomposition of alkyl formamides to form alkylamines in aluminophosphate synthesis.[25] Stabilising interactions between the zeolitic framework and the organic template can be achieved via Hydrogen-bonding, van der Waals or Coulombic interaction. The trapped organic template contributes to the total energy of the product by; coulombically balancing the negative framework charge where present (aluminosilicates), literally being grown around, so the resulting porous structure resembles its size and arrangement, chemically modifying the properties of the resulting solution or gel and thermodynamically stabilising its local component (building block) of the zeolite framework.[3]

Zeolite thin films have been synthesised hydrothermally by Bhachu et al.[26] through the steam treatment of amorphous silica or silica/titania in the presence of a molecular organic template, tetrapropylammonium hydroxide (TPAOH). This can be done either

through steam-assisted crystallisation (SAC), where the molecular template is in contact with the film or by vapour phase transport (VPT) where the template is introduced to the amorphous films in vapour form. These syntheses formed crystalline thin films silicalite-1 and titanium silicate-1 as shown by XRD and exhibited a coffin shaped surface morphology (SEM).[26]

Self-assembly is the spontaneous organisation of materials via non-covalent interactions, in the absence of external intervention. Mesoporous materials are generally formed from self-assembly of asymmetric molecules that organise into well-defined supramolecular assemblies. These molecules are typically amphiphilic surfactants of polymers composed of various arrangements of hydrophobic and hydrophilic blocks, known as block copolymers (BCPs). In aqueous solution and above the critical micelle concentration (CMC) and the Krafft temperature surfactants self-assemble into micelles. Different micelle structures can be obtained from this process depending on the surfactant concentration including ordered hexagonal, cubic and lamellar mesophases (**Figure 1.1a)**). In the resulting structure the hydrophilic components of the surfactant stay in contact with water whilst the hydrophobic segments are driven to the interior of the micelles.[27]

Evaporation induced self-assembly (EISA) is a rapid technique for forming ordered mesostructured thin films. For example, spin or dip coating can be used as evaporative techniques to drive self-assembly. It involves the use of a dilute solution of surfactant ($c << CMC$) that forms a liquid crystalline (LC) mesostructure as the solvent is evaporated.[3] These mesophases do not produce robust materials from aqueous solution alone, but when carried out in the presence of a soluble silica precursor, ordered porous metal oxides can be formed around the well-ordered surfactant mesophase.[28] Polymerisation of the inorganic matrix is usually incomplete after evaporation resulting in flexible films; additional chemical or thermal treatments are usually needed to complete this process.[3]

For example, in a system of ethanol, water, non-volatile surfactant and silica species, as the solution was spin coated or dip coated the ethanol would evaporate. As this happens, the surfactant concentration rapidly increases resulting in the formation of silica/surfactant micelles. Mesostructure development is nucleated by silica surfactant mesostructures that exist at solid-liquid and liquid-vapour interfaces when $c < CMC$, i.e. as the solvent begins to evaporate.[27] EISA of a vaporised solution of the same components was used in a process resembling AACVD to deposit porous nanoparticles. It was expected that the solvent evaporation would create a radial gradient of surfactant concentration that increases towards the surface of the droplet. This concentration gradient was expected to steepen with time.[29] The CMC is first reached at the droplet surface and is gradually achieved at the centre of the droplet as evaporation continues,

forming micelles and eventually a complete mesophase particle. The radial CMC gradient and nucleation at the liquid vapour interface cause the mesoporous domains to grow inwards.[30]

Mesoporous silica has been spin coated onto glass, Ti and Si substrates using a solution of tetraethylorthosilicate (TEOS), cetrimonium chloride (CTAC), hydrochloric acid (HCl) and pluronic P-123 to produce porosity parallel to the substrate surface by EISA.[31] Block copolymers have frequently been used as a structure directing agent and there are extensive accounts of how to direct their self-assembly in the literature with the use of an external field in forms such as electric fields, shear, temperature gradients and crystallisation to name a few.[32,33,34]

Mesoporous films of this nature can also be produced by casting, which involves submerging the substrate in the reaction solution for a period of time. The inorganic and surfactant components of the solution may spontaneously self-assemble at the surface of the substrate in acidic media. The films nucleate at the surface of the substrate and tend to form cubic or 2-dimensional hexagonal films with pores perpendicular to the substrate.[35]

Large area perpendicular mesoporous silica has been grown on a variety of substrates from Si wafer to polystyrene, through the addition of oil (e.g., decane, petroleum ether, or ethyl acetate) to a solution of cetrimonium bromide (CTAB), ethanol (EtOH) and TEOS. Different silica sources were used, (TEOS, fumed silica, or zeolite seed). The oil expanded the pores up to 5.7 ± 0.5 nm and was responsible for the vertically aligned porosity. The thickness of the films was controllable between 20 and 100 nm and the films were transparent. Films were grown by immersing the substrate into the reaction solution for several hours and then washing the substrate to remove any mesoporous silica nanoparticle by-products. The films were calcined or washed with an HCl-ethanol solution to remove the template.[36] Mesoporous silica films have also been grown with pulsed laser deposition.[37]

It has been claimed that preparing mesoporous nanoparticles as a powder and then coating them as a film can overcome many of the issues associated with the direct preparation of porous films which include highly acidic precursors (e.g., sol-gel) that can damage certain substrates and the issue of thermal removal of templates creating cracks in thicker films. Pores of nanoparticle-based films have been shown to be accessible; their analysis (e.g., ellipsometric porosimetry) also becomes easier in this format. Coatings of these nanoparticles could be applied under mild conditions. Thickness control could be achieved with multiple coatings or concentration variation in individual coatings.[38]

When pore orientation is less important, porous nanoparticles may be employed. The visible light scattering capability of silica spheres of diameters below ~ 1/10 the wavelength of incident light (below 50 nm) is greatly reduced, making them effectively transparent. In isolation these particles could be used to spectroscopically investigate physical processes or chemical reactions taking place inside them, to encapsulate dyes, improve dispersions or for drug delivery after chemical functionalisation.[38] Coatings of these particles could be used for antireflection.[39]

1.3.2 Templates for bulk macroporous materials and thin films

Macroporosity is most frequently produced with hard templates such as colloidal crystals and dispersions, around the backbone of a porous membrane or with lithographic techniques.[18]

Polystyrene nanospheres (PS spheres) are a popular choice for generating macroporosity due to their high abundance, (potentially) low cost and ease of use. PS latex spheres can be synthesised by emulsion-free polymerisation of styrene in water, initiated by potassium persulphate. The low polydispersity of the spheres is ensured through the use of constant temperature (70°C) and stirring speed (245 rpm) for the duration of the reaction (28 hours).[40] Different initiators have been used in the literature such as a combination of azobiscyanopentanoic acid (ABCPA) and azobisisobutyramidine dihydrochloride (ABIBA).[41]

To form ordered macroporous materials, a close packed (HCP) array of monodisperse nanospheres must first be arranged. The spheres are then infiltrated with a filler matrix that is usually a liquid or sol (i.e. coat with spin or dip coating)[42] but this can also be done by sputtering or evaporation techniques[43] and chemical vapour deposition (CVD) to name a few methods. They can subsequently be removed from the structure via high temperature calcination (450 - 500°C) which may also anneal/convert the matrix phase[42] or etching (e.g. in chloroform).[44]

Techniques used to form a close packed monolayer include the use of a Langmuir-Blodgett trough (**Figure 1.2**),[45] the tilt and drain method[46] and spin coating.[44] Moulds of the inverse PS films can also be made to template the same structure for later use without having to reproduce the initial PS monolayer.[46]

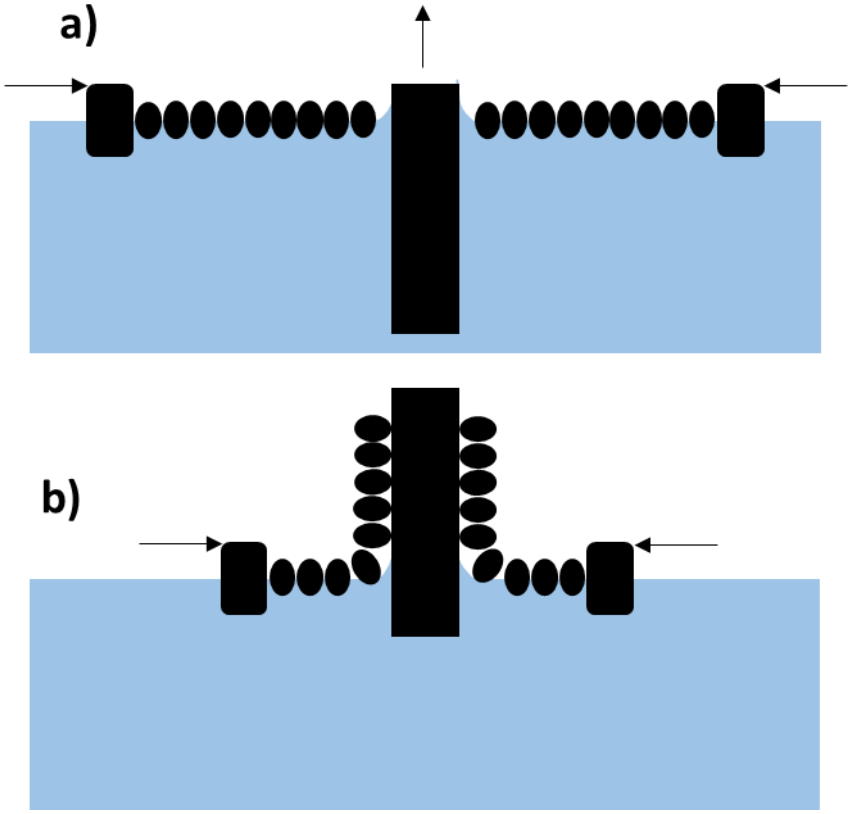

Figure 1.2. The Langmuir-Blodgett method for formation of a close-packed layer of nanoparticles. The original method was designed to coat a layer of surfactant molecules onto a substrate, the same setup can be used for nanoparticles that can float on water. In a) the nanoparticles are compressed into a close packed-monolayer. The substrate is raised out of the water bath b) and with constant pressure (measured via surface tension, mN/m) applied either side of the monolayer, the nanoparticles are guided onto the substrate as it is dip-coated.

The functionality of the surface of the spheres influences how the filler matrix is incorporated into the PS layer or layers. Solutions that can wet the surface of the spheres well will form better films around them. Where the coated layer is sparse, multiple layers can be applied. Adventitious surface carboxyl groups on the PS surface can help catalyse hydrolysis-condensation reactions, thiol-groups on silica nanospheres can act as active sites for the deposition of nanocrystalline metals to catalyse the growth of thicker layers.[42]

Reduction in size of the PS spheres can be achieved after their close packing, creating evenly spaced, smaller nanospheres that can lead to thicker pore walls and smaller pores in the resulting inverse material. This can be done with O_2 plasma etching.[47,48] Limitations to this etching arise when spheres are reduced below a certain diameter, at which point their surface becomes rough and their spherical shape is distorted. This problem can be overcome by using inductively coupled plasma etching (ICP-RIE) at cryogenic temperatures.[49]

Emulsions have also been employed in the formation or ordered macroporosity in silica.[50,51]

Macroporosity has been introduced into silica by spinodal decomposition type macroscopic phase separation. Macropore sizes in these materials could be controlled but pores were not well ordered. The resulting porous structures are a network of interconnected, similarly sized pores as opposed to aligned porous channels.[52]

Starch gel has been used to produce hierarchical bulk porous structures with non-ordered macropores between 0.5 and 50 μm. Materials of silicalite and titania have been made with this technique.[21]

1.4 Macroporous silica thin films

Photopolymerisation induced macrophase separation has been used to produce macroporous silica films in a one-pot synthesis. The synthesis mixture included 3-Glycidyloxypropyl trimethyloxysilane (GPTMS) and poly(diethoxysilane) (PDEOS) without a solvent or water, this mixture was irradiated under UV light in the presence of diaryl iodonium salt, a photoacid generator that catalysed the hydrolysis-condensation of both precursors, to produce macroporous silica films. The size of the macropores could be increased from 100 nm to 50 μm by changing the amount of PDEOS. Unlike poly(ethylene oxide) and poly(acrylic acid) which have been used to make macrophase separated films, the PDEOS becomes part of the structure as opposed to filling the pores after phase separation. Despite the low pore ordering this template-free method removes the need for post synthesis etching or calcination.[53]

Ordered macroporosity has been produced in silica with an emulsion template. The emulsions were stabilised with block copolymer P-123, varying the ratio of emulsion to P-123 formed pores from 50 nm to several μm. The silica network is formed by a sol-gel reaction that takes place around the emulsion. However, this technique cannot be performed in aqueous solution due to the reactions that take place between the metal oxide precursor and the water from the emulsion so a suitable alternative polar solvent must be chosen. The emulsion must also be carefully stabilised to prevent Ostwald ripening that would result in inhomogeneous pore sizes, which is made more difficult by the fact that most sol-gel reactions take place in alcohol.[50] Less ordered macropores have been produced with an emulsion template of hydrophilic and hydrophobic forms of silica.[51]

The silicon alkoxide, TEOS, has been used in the form of a sol to make a silica film with PS spheres. The resulting film has well defined but poorly ordered porosity.[44] Dip coating has also been used to infiltrate a PS monolayer with TEOS. The low-speed dip coating process followed by drying (80°C) to hydrolyse the sol was repeated up to 8 times to

completely fill the voids of the PS monolayer. The 300 – 400 nm PS spheres were removed by calcination at 450°C (5°C/min), for 30 mins to produce an ordered macroporous array.[54] 2-dimensional macroporous silica has even been grown around ice crystals.[55]

1.4.1 Silica sources

The sol-gel chemistry of silicon alkoxides controls the formation of metal oxides. Sol-gel reactions involve the dissolution of metal alkoxides in a lower alcohol; this solution is then hydrolysed by the water (**Figure 1.3**). The polarity of alcohol makes it a suitable choice of solvent for both the apolar alkoxide and the polar water. The resulting sol contains metal oxide nanoparticles which aggregate upon ageing at specific a pH and temperature. Drying the gel product produces a metal oxide and evaporates the solvents.[50] Some alkoxide precursors can also be used directly.[20]

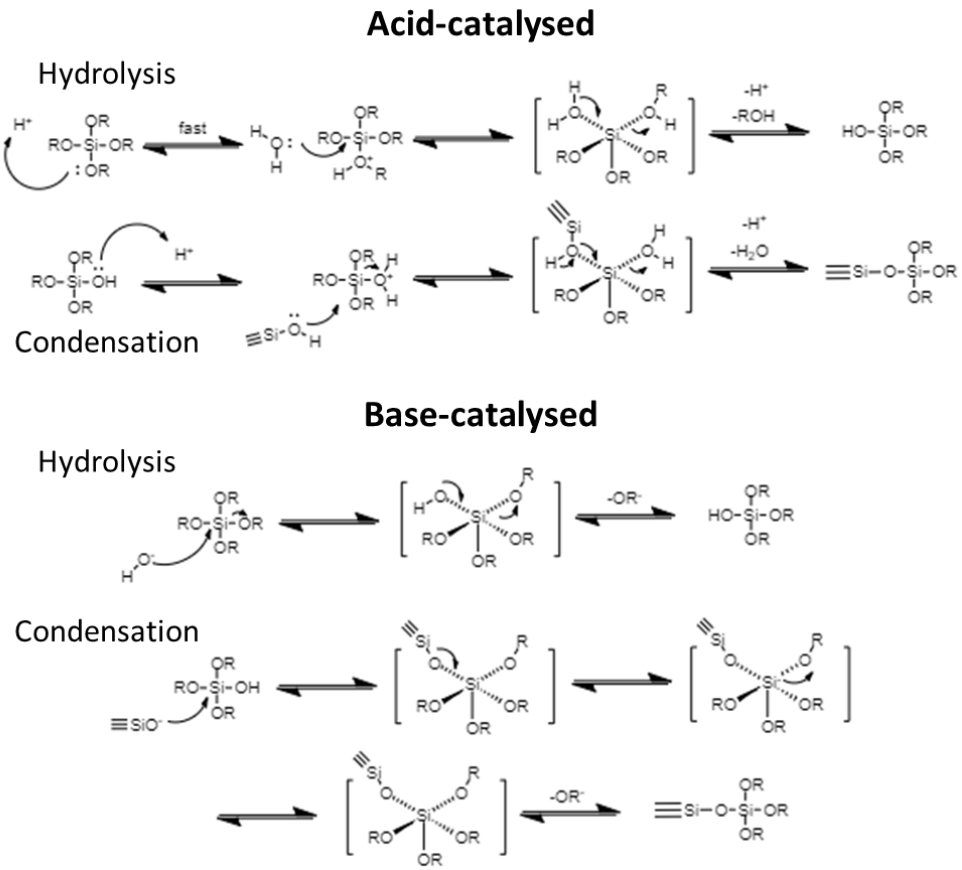

Figure 1.3. The different reaction pathways of silica sol-gel hydrolysis and condensation reactions of silicon alkoxides in acidic and basic conditions. (Reproduced from Nistic et al., reference 234).

The silicon alkoxide sol-gel process is mild, allowing the use of both organic and inorganic components. Adjustment of the pH, temperature and precursor concentration allow the rate of polymerisation and interactions at the inorganic-organic interface to be

controlled to obtain homogeneous products. TEOS is generally favoured over tetramethylorthosilicate (TMOS) due to its lower price and toxicity. However, TEOS is still limited by these factors, preventing commercial scale-up of many sol-gel syntheses.[56] Silica sources will be explored in more detail in the following chapter.

Soluble silicates are much cheaper and less toxic than silicon alkoxides. They are purely inorganic, amorphous glasses mainly seen in the forms of sodium silicate solution (a.k.a. waterglass), fumed silica and colloidal silica. They have already seen much use in chemical grouting and as flocculating agents and detergents. Their low cost is due to their direct production from natural quartz deposits.[56] However the polymerisation of waterglass is harder to control than that of Si alkoxides as it rapidly takes place as soon its pH is lowered, potentially resulting in lower quality nanostructures and decreased hydrothermal stability. High Na^+ content can also lower the degree of possible polymerisation, resulting in materials with lower chemical stability. Silicic acid sols can be prepared by passing waterglass through a H^+-saturated cation-exchange resin. Neutral alkoxysilanes have been prepared by dissolving silica sand, fumed silica or silica gel using ethylene glycol and organic amines. These alkoxysilanes have yet to be employed in the production of mesoporous silica.[56]

Despite the greater difficulty in controlling the polymerisation reaction there are several instances of sodium silicate having been successfully used to produce ordered silica materials. Sodium silicate solutions and a non-ionic surfactant (Triton X100) were used to make mesoporous silica with adjustable pore diameter. Sodium silicate was added to an acidic surfactant solution (pH = 2 - 3) to form polysilicic acids, the solution pH was then adjusted between 3 and 10.5 before being polycondensated between 24 – 45°C. It was shown that order and size of pores was dependent on the polycondensation pH and Na^+ concentration. Pore sizes between 1.5 and 2.5 nm were reproducibly formed between pH 5 - 6 and 8 when Na^+ concentration was consistent. Pores of 4 - 5 nm were formed between pH 8.5 and 10.5.[57]

Surface macroporosity has also been generated by macrophase separation of waterglass and sodium polymethacrylate via a dip coating procedure. The macroporosity develops when the waterglass/sodium polymethacrylate films were dipped into ammonium bicarbonate (NH_4HCO_3). Despite the fact that this macroporosity was not particularly well ordered, iridescent but fragile films were still produced.[58]

Well-ordered mesoporous silica has been produced using waterglass and a block copolymer templating agent (Pluronic-123). Once the reaction solution has been properly homogenised with the use of a blender, this method claims that waterglass can produce SBA-15 with better pore ordering than TEOS.[59,60]

1.4.2 Other materials

Titania (TiO_2, a photocatalyst and wide-bandgap semiconductor), zirconia (ZrO_2, a highly corrosion resistant ceramic) and alumina (Al_2O_3, a chromatography material and catalyst) were used to make bulk macroporous structures from their metal alkoxides with 320 – 360 nm PS spheres.[20] Other materials that have been used as a filler matrix for PS spheres include simple and ternary oxides, chalcogenides, metals and non-metals, alloys, hybrid organic silicates and polymers. The nanospheres themselves can be made of other materials depending on the application and filler matrix, monodisperse silica and polymers (polystyrene and poly(methyl methacrylate)) have been synthesised and employed as templates.[42]

It has been shown that PS spheres can be spin coated onto gold and titania substrates to form fairly consistent monolayers. This opens up the possibility of forming a porous silica layer over a film of another material.[61] Macroporous metal thin films (~ 2 μm thick) of Ni, Cu, Ag, Au, and Pt have been produced by this method, using a thiol funtionalised silica sphere (~ 400 nm) monolayer as a template. After submerging the template into a toluene bath filled with Au nanoparticles (~ 5 nm) and drying, the respective metals were coated via electroless plating. The silica was then etched away to produce (somewhat mangled) ordered porous voids.[62]

Mesoporous TiO_2 has been produced by EISA dip coating, it has been noted that understanding of the rate of the hydrolysis-condensation reactions of the metal oxide precursor is crucial to being able to reproducibly mediate the surfactant assembly process.[63]

Hierarchical meso- and macroporous structures have been made from silica, niobia and titania by combining mould patterning, colloidal crystal templating and block copolymers. Sol-gel chemistry has also been used to make transition metal oxide structures of ZrO_2, tungsten oxide (WO_3), $AlSiO_{3.5}$ and strontium titanate ($SiTiO_4$) by controlling the speed of their hydrolysis-condensation reactions in alcoholic media.[23]

Ordered macroporosity has been produced in titania, silica and zirconia with an emulsion template. This technique can be extended to a variety of oxides and supposedly organic polymer gels. However this process becomes more complex for highly reactive metal oxide precursors such as titanium tetraisopropoxide.[50]

The phase separation technique could theoretically be transferred to the formation of titania, zirconia and alumina.[52]

1.4.3 Applications of macroporous silica

Materials made from colloidal crystal templates could be used in quantum electronics and optical communications components that require ordered porosity and in dielectric materials, as the material and number of dimensions (i.e. 1D, 2D, 3D) can be easily changed.[20] Dielectric, 3-dimensionally ordered macroporous photonic crystals could be used as waveguides, low-threshold lasers and inhibitors of light emission due to their ability to direct photons.[42] To get the complete photonic bandgap (propagation of light in all directions)[53] required for these applications, structures must be optically transparent, have specific 3D order, be of sub-micron dimensions, and have low solid fractions and high refractive index contrast. Some of these requirements are satisfied with the use of PS spheres. The choice of material is important as sufficient refractive index contrast is required to produce a photonic crystal with a complete band gap and impart the desired optical effects.[42] Silica alone may not be able to fulfil this criterion.

Colloidal crystal templated structures could also be used as chemical sensors or supports for catalytically active species. For example, redox active γ-decatungstosilicate clusters (γ-$SiW_{10}O_{36}$) were bound to the walls of macroporous silica via direct synthesis. The material exhibited high catalytic activity for the epoxidation of cyclooctene.[64] Crystal colloid templated silica films could be functionalised selectively with organic groups before and after template removal. Functional groups placed on the surface before thermal or etching template removal would have to be able to withstand the treatment conditions.[65] Finally colloidal crystals have been used to make bioglass, glasses that can rapidly bond with bone and form stable interactions with living tissue. CaO/SiO_2 macroporous glass enabled more rapid apatite growth when immersed in simulated body fluids than the control sample without macropores. The excellent bioactivity was credited to the 3-dimensional system of macropores.[42]

Pore sizes are interchangeable in these materials; they can be manipulated simply by changing the size of the latex spheres. Smaller latex spheres (~ 200 nm) could be used for catalysis and separation or trapping of large organic and biomolecules. They could also be used as thermal or electrical insulators and porous electrodes or electrolytes.[20]

Hierachically porous silica (meso-, macroporous) monoliths could be used in high pressure liquid chromatography (HPLC) as they show improved function over particle packed columns that have been used for over 100 years. Macropores provide high permeability of the stationary phase, fast equilibration occurs between the mobile liquid phase and the stationary solid phase, which in this case is the mesopore walls.[52]

1.5 Abstract, impact of this work and thesis overview

1.5.1 Abstract

Waterglass is a commercially available silicate solution composed of anionic silicates with counter cations. In comparison to commonly used alkoxide sources of SiO_2, these systems are fully inorganic and produced directly from natural silica sources. The objective of this work is to explore the uses and properties of functional films made from waterglass. To this end, spin or dip coating methods were used to cast these solutions onto glass and silicon wafer substrates. The as casted films were not stable, requiring heating and washing with acid to convert the alkali silicate films to SiO_2. XPS, ATR, EDX and solid-state ^{29}Si NMR were used to identify the change in the chemical speciation of these materials. After establishing the preparation procedure, porous films were made via introduction of a sacrificial template, potato starch in this example, into the waterglass solutions before casting, which was then removed via annealing. The optical and wetting properties of the porous films were measured. Addition of a TiO_2 coating to the porous films and annealing, produced multifunctional films with photocatalytic, superhydrophilic and antifogging properties. In a separate synthesis thick sodium waterglass films were annealed to produce a foam which was able to support fully inorganic $CsPbX_3$ perovskite quantum dots. The stability of the supported quantum dots was observed over time and their sensing capabilities for volatile organic solvents (acetone and formaldehyde) were evaluated. In addition to the creation of random pores with and without potato starch, polystyrene nanospheres were used to produce ordered porous systems and their properties were investigated. Finally, potassium waterglass solutions were dip coated onto stainless steel mesh and annealed. The coating enabled over 90% separation of oil-water mixtures for a range of oil-water ratios and oil densities encompassing that of crude oil.

1.5.2 Motivations and Novelty

Waterglass solutions are produced on an industrial scale for a broad range of applications including as an additive for concrete and wastewater treatment. Being cheaper and easier to produce than commonly used sources of silica such as silicon alkoxide solutions, their potential in the production of silica coatings is mostly unexplored. While being hindered by their reaction with atmospheric water and carbon dioxide to form surface carbonates, simple treatments could provide long term stability. Exploring curing conditions of coated waterglass solutions to produce silica coatings of similar durability and transparency as those generated from alkoxide solutions would offer good evidence to the utility of waterglass solutions as a potential alternative.

As described in detail in the introduction of **Chapter 3**, waterglass is not often seen in the literature, it has been used in applications such as antireflection coatings, most articles are dedicated to study of solution properties or their corresponding dried coatings. The intention of this work was to thoroughly characterize a route to stabilising the coatings made from waterglass solutions, gain control over the coating thickness and maximise durability. The transparency, optical properties and wetting were also investigated. The second reason for avoiding waterglass solutions as a source of silica in nanoscience is their polydispersity. Here we have shown that the polydispersity, which has been previously investigated in the literature does not affect the morphology of the coatings. The waterglass solutions can be used to form macroporosity as small as 125 nm from sacrificial organic polymer hard templates. Macroporous coatings were also generated by a natural foaming method. Finally, a macroporous mesh was coated with waterglass, which altered the shape of its porosity. Potential applications of waterglass with these morphologies were investigated in detail.

1.5.3 An overview of this thesis

In **Chapter 3** the stability of spin coated waterglass coatings was investigated, the growth of carbonates from the surface of the coatings known as 'efflorescence' was characterised with several techniques. Methods to cure waterglass coatings to form silica were shown, involving heating the coatings and washing them with acid. A combination of EDX, XPS, ATR and solid-state NMR were used to confirm the conversion to silica. The effect of the curing temperature on the stability, durability, optical and wetting properties was shown. Ellipsometry was used to show that both spin and dip coating could be used to control the film thickness.

Macroporosity was introduced into silica films from potassium silicate in **Chapter 4** using potato starch as a sacrificial template. The potato starch content in the starting solutions was directly related to the porosity and reflectance of the coatings. The macroporous films were coated with TiO_2 to give them superhydrophilic properties in the absence of UV irradiation, which were not observed on flat substrates. The anatase coating decreased the transmittance of the substrate somewhat. Antifogging and Resazurin photodegradation properties of the composite coatings were shown. Curing conditions for enabling crystalline TiO_2 formation on the cured macroporous silica were investigated.

Chapter 5 saw the use of polystyrene nanospheres as templates for ordered macroporosity. Both monolayer and multilayer macroporous coatings were synthesized. The monolayer coatings had greater hydrophilicity than the glass substrates, as well as slightly enhanced transmittance in parts of the visible region.

Stainless steel mesh was coated with potassium silicate in **Chapter 6** to change it from hydrophobic to superhydrophilic (0°). The coated mesh was used as a membrane for oil water separation, it was capable of > 90% separation of oil-water mixtures containing castor, olive and motor oil mixed with water in different ratios.

Finally, **Chapter 7** involves the use of foamed sodium waterglass as a substrate for $CsPbX_3$ perovskite quantum dots. The stability of the quantum dots on the coatings was observed over time, showing some improvements over stability in solutions. Supported mixed halide quantum dots showed some capabilities in the colourimetric or fluorescence sensing of the volatile organic compounds, acetone and formaldehyde.

2. Methodology

The techniques used in this work are described below, with their corresponding abbreviations. After synthesis of the silica films characterization was needed to determine changes to the composition and chemical structure of the stock waterglass solutions upon spin or dip coating onto glass or silicon wafer. Initially non-destructive techniques such as infra-red, UV-vis and XRD were used to determine chemical structure and detect long range order. Non-destructive surface composition and chemical analysis was performed with XPS, fragile samples cracked in the high vacuum; composition at greater depths was determined with EDX, which required coating samples with carbon to prevent charging, making it a destructive technique in this case.

Following this the morphology, physical and optical properties of the coatings were determined. The samples generated in this work were generally insulating and a conductive coating was required to prevent charging during SEM imaging, making it a destructive technique. Coating durability was determined qualitatively with Scotch tape and pencil hardness tests. Film thickness could be destructively determined with SEM, or non-destructively with profilometry and ellipsometry, the latter technique also gave insight into the refractive index of the coatings, however samples needed to be coated onto silicon wafer. The effect of the morphology on the surface energy was investigated by studying the changes in the contact angle of water at the surface. Procedures for investigating additional properties such photoluminescence and photodegradation are discussed below.

2.1 Scanning electron microscopy (SEM) and Energy dispersive X-ray spectroscopy (EDX or EDS)

SEM and EDX were used to image the morphology and determine the composition of samples respectively. The instrument uses an electron gun, which generates electrons and accelerates them to energies of 0.1 – 30 keV. The electron beam is guided using a series of lenses, which demagnify the image of the beam from a diameter of ~ 50 μm (for a heated tungsten gun) to the final spot size of ~ 10 nm on the sample. The beam leaves the final lens and enters the specimen chamber where it penetrates several microns into the sample and generates the signals that are detected for image formation. The depth of penetration depends on the speed of the electrons and the density of the sample with respect to the X-rays. SEM imaging relies on the detection of secondary electrons (5 – 50 nm deep, < 50 eV), generated by the sample through inelastic collisions with electrons from the incident the electron beam, whereas EDX uses characteristic X-rays unique to each atom present to determine the composition, which are emitted from several microns into the sample. Incident electrons from the beam collide with and eject (secondary) electrons from an inner shell of an atom, leaving a positively charged hole.

This hole in turn attracts an electron from an outer shell to fill the vacancy, the energy of this relaxation is emitted in the form of an X-ray characteristic of the transmission and hence the electronic arrangement of the atom. Secondary electrons form images with topographic contrast. As it relies on signal collected from specific elements, EDX is better equipped to detect samples with abundances of at least several weight percent. Due to the great penetration depth of the X-rays, the sampling depth is great and so EDX should be considered a bulk analysis technique. Furthermore, to calculate weight percentages from the EDX spectra certain assumptions are made, mainly that the sample is flat and homogeneous.

Image magnification, M, is the ratio of the length of the rectangular 'raster' on the screen to the length of the raster on the specimen. Manually increasing the magnification results in the scan coils exciting less strongly, deflecting the beam across a smaller area of the sample. Raster size also depends on the working distance, the distance from the specimen to the bottom of the final lens. The sharpness of the images is controlled by the electron probe size and current, the convergence angle of the beam and the accelerating voltage. The spot size of the beam is determined by the diameter of the beam at the sample surface. During imaging the focus and astigmatism are manually adjusted to obtain clear images of the sample surface.

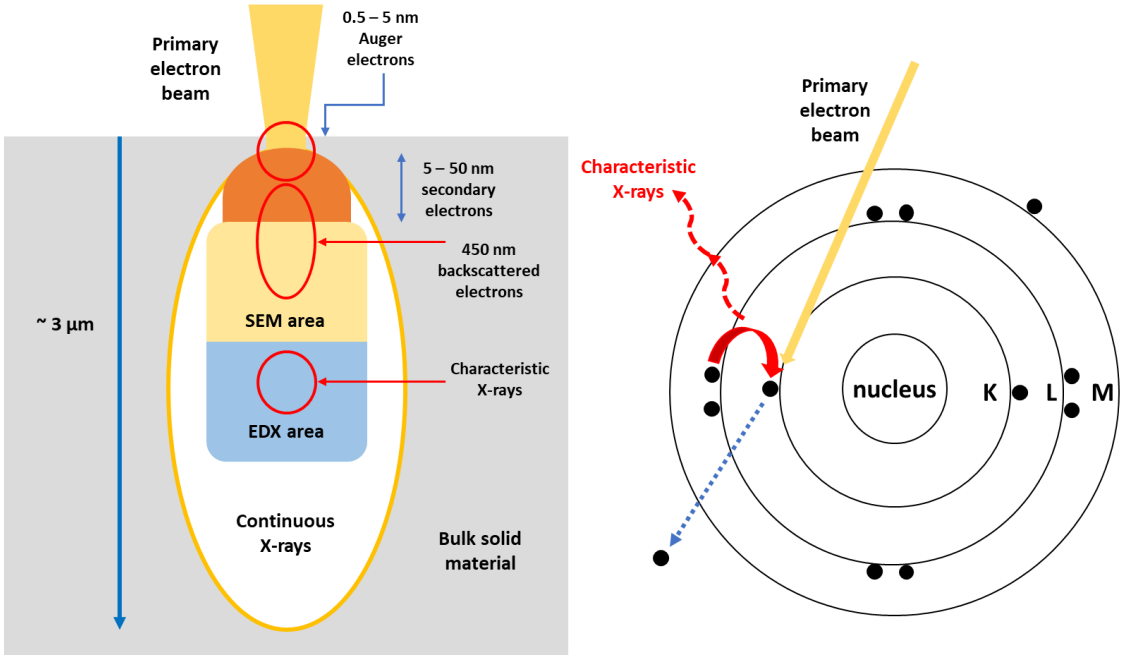

Figure 2.1. The interaction volume formed within the sample when the SEM or EDX electron beam is incident upon the sample surface is shown on the left. The beam penetrates several microns into the sample, the specific depth being dependent on the density of the sample with respect to the incident X-rays. The image on the right is a shell diagram illustrating the interaction of the incident X-rays with an atom in the sample, which results in the liberation of a secondary electron and the emission of X-rays characteristic of the atoms present.

Field emission electron guns (current densities of up to 10^5 A/cm^2) improve the brightness of the electron beam and allow a more focused energy spread than their thermionic counterparts (3 A/cm^2); however, they operate under high vacuum. Field emission cathodes are composed of a wire with a sharp point (radius 100 nm or less). Applying a negative potential to the cathode concentrates the electric field at the tip. When this concentrated field reaches a magnitude of ~ 10 V/nm, the potential barrier is lowered sufficiently in height and width to enable the electrons to 'tunnel' through it and leave the cathode. The wire is usually made of tungsten, the material must withstand the high mechanical stress that results on the tip due to the electric field.[66]

SEM images were collected with a JEOL 6701 FESEM using secondary electron emission (SEI) mode, EDX data was collected with a JEOL 6700 FESEM. Both machines use a field emission source to generate and guide electrons to the focusing slits. Samples were coated with gold or carbon for SEM and EDX respectively, making this a destructive technique. The sample height and working distance used were both either 8 mm or 15 mm for SEM and EDX respectively. EDX data was used to calculate standard deviations of composition in weight percent. Accelerating voltages of 5 kv were generally used, the voltage was lowered for imaging organic samples that degrade rapidly under the electron beam.

2.2 Optical microscopy

SEM offers a greater depth of focus and superior resolving capabilities compared to an optical microscope, in addition to having a significantly lower diffraction limit due to the use of X-rays instead of visible light. However, it can be easier to image micron scale structures with an optical microscope. In this non-destructive technique visible light and a series of lenses are used to magnify objects down to the micron scale. The magnification is limited by the resolving power of visible light. Images were taken with a Nikon system with 10, 100, 500 and 1000 times magnification.

2.3 X-ray photoelectron spectroscopy (XPS)

XPS is a non-destructive, surface sensitive technique, primarily used to determine the oxidation state and abundance of atoms at the surface of a material. The principle is based on the photoelectric effect, in which monochromatic X-rays are absorbed by an atom resulting in the ejection of electrons from a core level to the vacuum level. The kinetic energy (KE) of the removed electron depends on the energy of the incident photon (hv), the energy required to remove the electron from the surface of the atom, known as the binding energy (BE) and the work function of the spectrometer (φ), (**Equation 2.1**).

$$KE = hv - BE - \varphi \qquad (2.1)$$

Measuring the kinetic energy of the emitted electron (and knowing hv) enables calculation of the binding energy and in turn identification of the elements at the surface and their chemical states. The binding energy of the photoelectron depends on the element, energy level and chemical environment from whence it came. The sampling

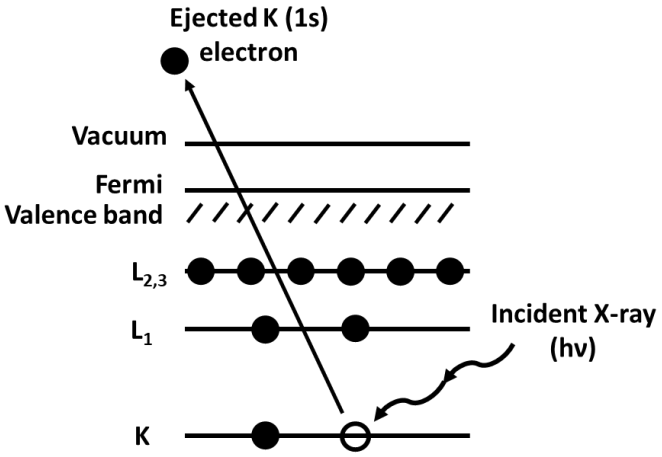

Figure 2.2. Shell diagram of the ionization process that takes place in XPS. The incident X-rays are absorbed by core level electrons in the sample, which are ejected beyond the vacuum level when the incident photon energy is greater than the binding energy of the material, the energy required to completely remove an electron from its surface.

depth for AlKα radiation is 3 – 10 nm.

The initial ionization process is followed by relaxation of a higher energy level electron and the emission of an Auger electron. Modern XPS usually involves collection of a survey spectrum of the sample to show all species present, as well as higher resolution collection of energy ranges corresponding to the atoms in a sample with multiple averaged. High resolution scans can produce smooth peaks that can easily be deconvoluted (if necessary) with gaussian curves. Ionization occurring at the surface due to adventitious, (usually hydrocarbon-based) species is usually corrected for before quantitative analysis of the binding energies.

XPS was conducted on a *Thermo Scientific K-alpha* spectrometer with monochromated Al Kα radiation, a dual beam charge compensation system and constant pass energy of 50 eV (spot size 400 μm). Survey scans were collected in the binding energy range 0 – 1200 eV. High-resolution peaks were used for the principal peaks of C 1s, O 1s, Na 1s and Si 2p. Data was calibrated against C 1s or Au 4f7/2 (binding energy, 285.0 or 84.0 eV). Data was fitted using *CasaXPS* software. Atomic percentages were obtained from the XPS survey spectra. Relative sensitivity factors (RSF) were used to scale the atomic percentages of the elements for their interactions with X-rays so they could be compared

directly. RSF values used for C 1s, Na 1s, O 1s, Si 2p and Ca 2p were 1, 8.52, 2.93, 0.817 and 1.833 respectively.

2.4 X-ray diffraction (XRD)

The final X-ray technique used in this work was XRD. In this work XRD was mainly used for non-destructive phase identification, the diffraction patterns collected were compared with reference spectra from the ICDD website. The monochromatic X-ray beam is incident on a crystalline material, the angle is varied and the diffracted X-rays collected to obtain a diffraction pattern. According to Bragg's law, the condition for constructive interference of incident X-rays diffracted from adjacent planes (when n = 1) is given in **Equation 2.2**.

$$n\lambda = 2dsin\theta \qquad (2.2)$$

In this equation λ is the wavelength of the incident radiation, θ is the angle of incidence of the incident X-rays relative to the plane of the crystalline surface and d is the interplanar spacing of the crystal structure.

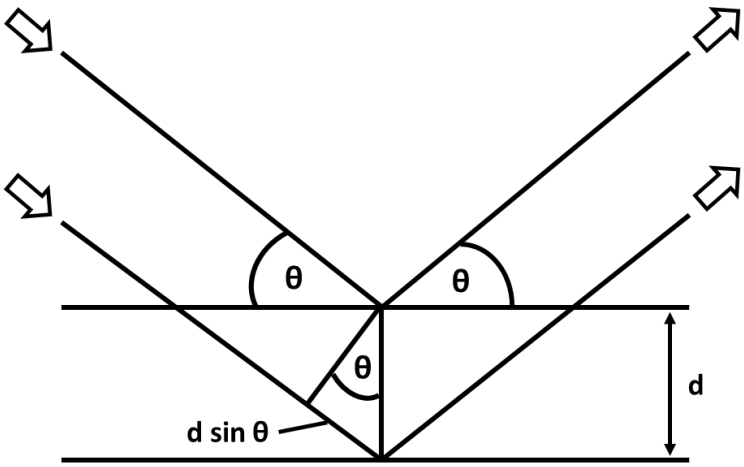

Figure 2.3. A graphical representation of Bragg's law. The incident X-rays are diffracted from adjacent planes in the crystal. For constructive interference of the two diffracted rays, the additional distance travelled by the beam into the material (path length) to reach the nth layer of the structure is accounted for by d sin θ.

The D8 lynx-eye was used to collect thin film XRD patterns. The machine uses Cu Kα radiation (1.54 Å). For most measurements data was collected between 4 and 50° 2θ, θ = 0.8°, with 0.5 s/step collection time per degree 2θ, (0.05 SEP). For the 3T converted zeolite film, 2 s/step was used.

2.5 Fourier transform infrared spectroscopy (FTIR) and Attenuated total reflection (ATR)

In infrared spectroscopy, molecules or basic structural units that can undergo a change in dipole moment absorb incident infrared wavelengths characteristic of the vibrational frequencies of their structures, the energy difference between the initial and final states matches that of the absorbed photon. The frequencies are related to the bond strengths and the masses of the bound atoms. The vibrational modes are also related to the structure. Linear and non-linear molecules have 3N – 5 and 3N – 6 degrees of freedom respectively, where N is the number of atoms. For example, vibrational modes of tetrahedral structural units are symmetric and asymmetric stretching and bending. In FTIR experiments the sample is exposed to a monochromatic IR beam; wavelengths are scanned sequentially across a specified range. The beam passes through the sample in transmission mode, the absorbance is deduced from the unabsorbed light that is

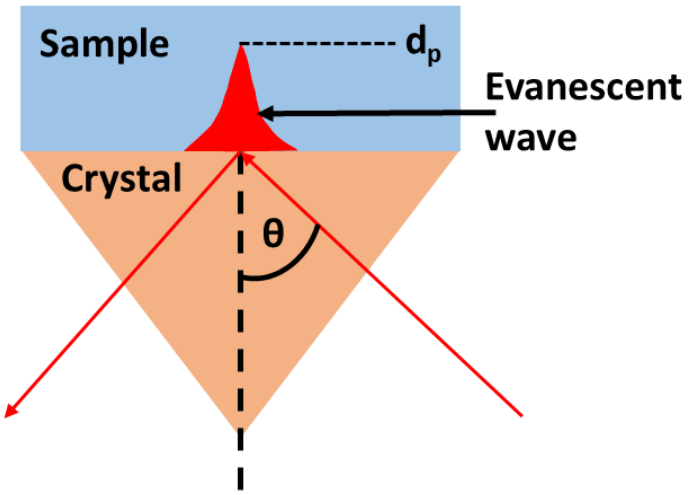

Figure 2.4. Schematic of a single reflection of the incident IR beam from the bottom surface of the crystal when the conditions for total internal reflection are satisfied. The beam is directed to the sample above the critical angle, which is defined as the angle between the normal and the plane of the sample-substrate interface. The evanescent wave penetrates a depth d_p into the sample.

received by the detector. The Shimadzu Tracer-100 scans the entire wavelength range and generates a transmittance spectrum.

ATR involves the use of a crystal of high refractive index such as diamond or ZnSe (both with refractive index of 2.4), it is assumed that the crystal is transparent to the IR beam. The sample surface to be investigated is pressed into the bottom of the crystal and the IR beam is passed through the crystal at a specified angle. The refractive index contrast between the crystal and the external medium, either air or the sample, must be sufficient for total internal reflection of the IR beam from the inner surface of the crystal. The critical

angle, θ_C, is the angle at which the angle of refraction is 90°, at higher angles total internal reflection occurs; see **Equation 2.3**.

$$\theta_C = sin^{-1}\left(\frac{n_2}{n_1}\right) \quad (2.3)$$

The refractive indexes of the crystal and sample are denoted n_1 and n_2 respectively. As the reflection takes place, an evanescent wave passes into the sample. The penetration depth, d_p, of this wave is defined as the distance required for the electric field amplitude to fall to e^{-1} of its surface value, as shown in **Equation 2.4**.

$$d_p = \frac{\lambda}{2\pi(n_1^2 sin^2\theta - n_2^2)^{1/2}} \quad (2.4)$$

The penetration depth is wavelength (λ) dependent. The sample absorbs this evanescent wave and the light that is received at the detector is used to generate a transmittance spectrum that reflects the absorbance of the sample. ATR is usually non-destructive, surface sensitive and for bulk powders only a small amount of sample is needed. For the analysis of coatings, the film thickness must be considered in relation to the penetration depth, additional scans may be required to amplify the signal. ATR spectra collected with the Spectrum 2000 spectrometer were converted to absorbance using the relation A = -log(T), the data was also baseline subtracted. The mid-IR region (4000 – 400 cm^{-1}) is investigated in this work.

2.6 Raman spectroscopy

Raman spectroscopy involves the inelastic scattering of light exposed to a sample; it enables the study of the vibrational properties of a material. Unlike IR spectroscopy the molecule does not undergo any real change in energy level, only the electron cloud is distorted. The experiment involves exposing a sample to a monochromatic beam of light from a laser. Most of this light is transmitted, while some is scattered. When received by a spectrometer this scattered light gives distinct signals, a strong central peak is observed at the same energy as the incident radiation, E_0, this elastic scattering process is referred to as Rayleigh scattering. Either side of this peak, satellites are observed, $E_0 \pm h\nu_i$, the term ν_i corresponds to the vibrational frequencies of the sample and ($E_0 - h\nu_i$) and ($E_0 + h\nu_i$) are known as Stokes and anti-Stokes Raman scattering respectively. The incident photon interacts with a structural unit and takes it to a 'virtual state' that does represent the true electronic state of the sample, from which it immediately releases a photon. Consider a sample in the ground state E_0. If the sample decays back to its original state, Rayleigh scattering has occurred. If the sample decays to an excited state, it emits a photon with energy $E_0 - h\nu$ corresponding to Stokes scattering. If the sample

was initially in an excited vibrational state, E_{ex}, and it emits a photon of energy E_0 + hv and returns to the ground state in an anti-Stokes event.[67]

In Raman spectroscopy, molecules or basic structural units that can undergo a change in polarizability (electron cloud distortion) during vibrations, absorb laser wavelengths characteristic of the symmetry of their structure. The magnitude of the detected signal is proportional to the polarizability. Non-polar structures tend to be Raman active. Tetrahedral subunits such as the tetrahedra of silica $(SiO_4)^{2-}$ are both IR and Raman active as they contain polar $Si^{\delta+}$-$O^{\delta-}$ bonds, the outer surface of the tetrahedra contains only oxygen (O^{2-}) making it non-polar and hence Raman active.

Raman spectra were collected with the Renishaw 1000 spectrometer equipped with a He-Ne laser (l= 633 nm) and coupled to a microscope with a 50× objective lens (1.9 mW when operated at 25 % power, spot size approx. 4.4 mm^2). The Raman system was calibrated using a silicon reference. The acquisition time of all Raman measurements was 10 s.

2.7 Inductively coupled plasma mass spectrometry (ICPMS)

The liquid sample is vapourised and the gas is ionized using inductively coupled plasma to generate both atomic and small polyatomic ions, which are detected and quantified. This technique can detect metals and certain non-metals in liquid samples at parts per million (ppm) concentrations. The PerkinElmer NexION was used to analyse the alkali cation compositions of diluted waterglass solutions in **Chapter 3**.

2.8 Solid state Nuclear Magnetic Resonance (NMR)

Atomic nuclei are made of neutrons and protons, each made of three quarks. Each quark has spin (a form of angular momentum) of ½ and these combine to give neutrons and protons spin of ½. Spin of neutrons and protons combine to give zero or non-zero spin to the atomic nucleus (0, ½, 1, 3/2, 2, etc.), depending on the number of protons and neutrons in a given nucleus. Non-zero spin gives the atomic nucleus a magnetic moment, meaning it will spin when placed in an external magnetic field and pulsed at its resonant frequency.

In the classical depiction of nuclear spin, the normally stationary nucleus of an atom rotates around an imaginary z-axis. When placed in a time-independent magnetic field and exposed to electromagnetic radiation at the resonant frequency of the nuclei present, the nuclei will extract this energy and rotate at the Larmor frequency, ω. The frequency of nuclear precession depends on the gyromagnetic ratio, γ, of the nucleus and strength of the external magnetic field, B_Z, according to **Equation 2.5**.

$$\omega = \gamma . B_Z \qquad (2.5)$$

Consider that the stationary nucleus has an axis of rotation pointing in the z-direction and in a z-oriented magnetic field the axis is pulled into an x-y (transverse) plane upon a radio wave pulse. After exposure to this pulse ends, the nucleus spirals back into its stationary z-axis position in a process known as relaxation. The energy released in this process and the time taken to do so are the origin of the NMR signal, the free induction decay of the nuclei is measured. Relaxation times t_1 and t_2 are related to spin-lattice and spin-spin relaxation, which are responsible for an increase in z-axis magnetization and a decrease in transverse magnetization of these magnetic moments respectively, until the nuclei return to their stationary z-axis orientation and realign with the external field. The strength of the signal depends on the net magnetization vector, M, which is the sum of the number of nuclei that resonated with the electromagnetic wave. At room temperature not all nuclei will align with the external field, due to thermal motion some will oppose the external field direction, resulting in reduced M. NMR experiments are usually carried out at reduced temperatures to maximize external field alignment.

^{29}Si NMR signals represent the degree of connectivity of silicon atoms to other silicon atoms, in the case of silica through siloxane bridges. Signals Q^0 and Q^4 represent silicon atoms bound to 0 and the maximum of 4 other silicon atoms, each signal with its own distinct chemical shift. The chemical shifts differ due to the shielding from the environment surrounding the nucleus. In solid state NMR the molecules or species present do not tumble (due to thermal motion) in all directions as they do in solution where molecular interactions are averaged out, resulting in much broader signals. Magic-angle spinning (MAS, 54.74°, 1 – 130 kHz) can be used to average out nuclear dipolar interactions and chemical shift anisotropy in the solid state, however quadrupolar interactions are only partially averaged by this technique. Homogeneous samples and large sample quantities (at least 100 mg) are also required to ensure signal purity and maximize the obtained signal intensity. ^{29}Si MAS solid state NMR was carried out on a Bruker instrument at 12 kHz.

2.9 Profilometry

Coatings were made with part of the substrate exposed by covering part of the substrate with tape during coating. The KLA stylus profilometer was used for thickness measurement. The tip of the stylus was dragged across the edge of the coating to determine the step height.

2.10 Ellipsometry

In Ellipsometry a sample is exposed to monochromatic radiation of known polarization, usually spherical. The change in the polarization of the light as it is reflected off the

sample to the detector is observed in terms of its phase shift, Δ, and amplitude ratio, Ψ; as shown in **Equation 2.6**.

$$\rho = tan(\Psi)e^{i\Delta} \tag{2.6}$$

To ensure that only reflectance has taken place and to simplify the modelling process, the substrate chosen for this is usually opaque (no reflections from inside substrate), reflective and optically homogeneous, for example [100] silicon wafer. Δ and ψ of the substrate are usually measured before that of the coated substrate and the model developed sequentially for each layer of the coating. The data collected is fitted with a mathematical model, the optical constants in the model are manipulated to give the best fit of the measured data. The most common models used to fit materials that are transparent over a significant wavelength range are Cauchy (**Equation 2.7**) and Sellmeier (**Equation 2.8**), the latter being more appropriate for the modelling of silica.

$$Cauchy: n(\lambda) = A + \frac{B}{\lambda^2} + \frac{C}{\lambda^4} \tag{2.7}$$

$$Sellmeier: \varepsilon_1 = \frac{A\lambda^2\lambda_0^2}{(\lambda^2 - \lambda_0^2)} \tag{2.8}$$

Once a model has been constructed, the refractive index of the material can be determined, the degree of fitting (R^2) indicating the accuracy of the value. Film thickness can then be determined. The refractive index values give an indication of the porosity of the material. Porous materials are usually fitted with an effective medium approximation (EMA), which considers that the materials refractive index is a combination of the void (usually air) and solid fractions.

The refractive index, n, describes the ratio of the speed of light in a vacuum, c, compared to the speed at which it travels through a material, v:

$$n = \frac{c}{v} \tag{2.9}$$

The complex refractive index, ñ, describes how light interacts with a material and is described in terms of the refractive index and the extinction coefficient, k.

$$\tilde{n} = n + ik \tag{2.10}$$

The extinction coefficient described the energy lost to the material as light passes through, it is related to the absorption coefficient, α:

$$\alpha = \frac{4\pi k}{\lambda} \tag{2.11}$$

This term comes from Beer's law, which describes the loss in intensity of light passing through a material due to absorption:

$$I = I_0 e^{-iax} \tag{2.12}$$

The Semilab SE2000 spectroscopic ellipsometer was used to perform spectroscopic ellipsometry (SE) measurements. All SE data analysis was carried out on the Semilabs SEA software (v1.6.2). Structures were modelled using a Cauchy or Sellmeier dispersion law.

2.11 UV-visible and near-IR spectroscopy

When non-ionising electromagnetic radiation is incident on a material it can be transmitted (T), effectively passing through perhaps with negligible attenuation, reflected (R) from the surface, absorbed (A) or scattered. For thin films, where absorbance is often negligible:

$$T = 1 - R \tag{2.13}$$

Absorbance can be calculated from the transmittance:

$$A = -log(T) \tag{2.14}$$

UV-vis instruments enable the identification of these processes in the UV, visible and near-IR regions. The absorbance of a material is related to its band gap, absorbance or diffuse reflectance can be used to determine the band gap (E_g) of the material with a Tauc plot, in which the absorption coefficient (α), a combination of the absorbance (A) and path length (l) of the light through the sample, in the form of $(\alpha hv)^{1/r}$ is plotted against the photon energy, hv, (**Equations 2.15 and 2.16**).

$$\alpha = 2.303 \frac{A}{l} \tag{2.15}$$

$$\alpha hv = B\left(hv - E_g\right)^r \tag{2.16}$$

Where, r = 2 or 3 for direct or indirect band gaps and B is a constant related to the properties of the valence and conduction band. Linear fitting of the curve to the energy axis enables an estimation of the band gap energy. The energy of a wave, E, is related to its frequency, f by the relation:

$$E = hf \cong \frac{1240}{\lambda} \tag{2.17}$$

The measurements are referenced to enable comparison between samples, in solution the solvent is referenced, whereas in the solid-state air or a substrate can be referenced. An integrating sphere enables measurement of light scattered from the sample, placing the sample inside of or adjacent to a highly reflective enclosure enables the capturing of scattered light. When using an integrating sphere, discs of pressed barium sulphate tend to be used as a reference. This white powder is highly reflective and is used to define 100% reflectance.

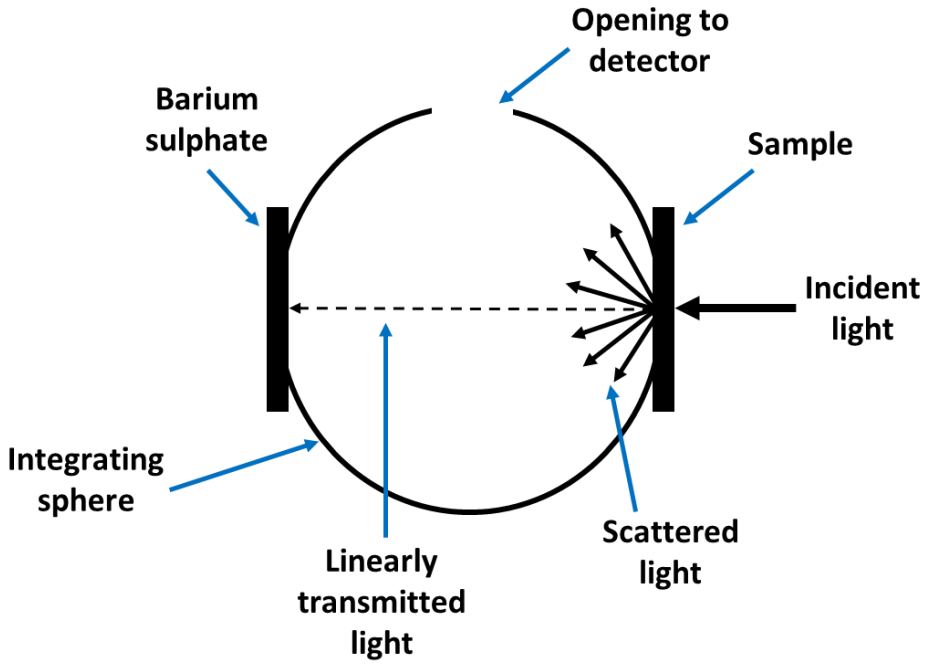

Figure 2.5. Schematic for diffuse transmittance experiments with an integrating sphere. Light transmitted and scattered through the sample is reflected from the reference plate towards the detector. To measure scattering in transmittance mode, the barium sulphate reference plate was removed, eliminating the directly transmitted light from the signal to show the scattering contribution. For diffuse reflectance measurements, the sample was placed in the position of the barium sulphate reference plate.

UV-vis transmission and reflection spectra were recorded on the Shimadzu-2600 or Shimadzu Tracer-100. The background was collected before each set of measurements using flat, white plates as references. The data interval used was 5 nm, integration times of 1500 nm/min were used for both UV-vis and near-IR regions.

2.12 Scratch hardness

Scratch hardness is measured according to the hardness of pencils, ranging from 6B to 6H, where 6H is the hardest pencil. The pencils were sharpened and the tips flattened with sand paper. They were loaded into a weight with wheels and their tips lowered onto the sample surface. The back of the weight was manually pushed across the sample. This was repeated several times to gauge the consistency of the hardness across the

samples. The pencil hardness recorded was the value before which scratches in the samples surface were observed.

2.13 Simultaneous thermal analysis (STA) (Thermogravimetric analysis (TGA) and Differential scanning calorimetry (DSC))

TGA data on solid organic polymer samples were obtained using the Netzch simultaneous thermal analyser (STA 448 F3 Jupiter). The percentage mass loss of weighed samples was recorded with increasing temperature in air. The first derivative of the mass loss curve was calculated to show temperatures at which the greatest mass loss was observed from inflexion points on the mass loss curve. The DSC was used to observe enthalpy changes occurring in tandem with the mass loss to identify major events of sample decomposition.

2.14 Surface Wettability

The wetting of a surface by a water droplet is investigated via the contact angle, θ_{CA}, the angle between the droplet and the underlying surface. The Young equation shows that the features of the contact angle can be summarized by the interfacial energies, γ, at the solid-liquid (γ_{SL}), solid-vapour (γ_{SV}) and liquid-vapour (γ_{LV}) interfaces, the three-phase line. For wetting or spreading of a droplet on a surface:

$$\gamma_{SV} - \gamma_{SL} > \gamma_{LV} \tag{2.18}$$

When the energy gained in forming a unit area of the solid-liquid does not exceed that required to form a unit are of the liquid-vapour surface, the droplet will not spread and an equilibrium contact angle can be determined.[68]

$$cos\ (\theta_Y)\ = \frac{\gamma_{SV}\ -\ \gamma_{SL}}{\gamma_{LV}} \tag{2.19}$$

Equation 2.19 suggests wettability of a surface is related to the chemistry of the substrate material and how it interacts with water (or any liquid), thus high energy surfaces have low contact angles and low surface energies generate high contact angles. This equation can only accurately describe the interactions of a droplet on flat surfaces with no surface roughness or contamination.

In 1936, Wenzel modified this approach to account for surface roughness, showing that its effect is to magnify the chemically inherent wetting properties of the material, for example making a hydrophobic material significantly more hydrophobic.

He defined the roughness factor of a surface, r, as:

$$R = \frac{Flat\ surface\ area}{Roughened\ surface\ area} \tag{2.20}$$

The wetting properties of the material should scale proportionally with r. Wenzel's equation assumes the droplet fills the surface roughness.[69]

$$cos\,(\theta_W) = R \times \frac{\gamma_{SV} - \gamma_{SL}}{\gamma_{LV}} \quad (2.21)$$

Wenzel's contact angle defined in **Equation 2.21** is also referred to as the 'apparent' contact angle. For a flat surface, r = 1. Cassie and Baxter proposed a third iteration of this wetting model in 1944 to account for surface roughness or porosity of dimensions that would enable air to be trapped between the film and the droplet. The Cassie-Baxter contact angle is defined as the ratio between the area of the surface-droplet, σ_1, and droplet-air, $\sigma_2 = 1 - \sigma_1$, interfaces respectively and their associated interfacial tensions and contact angles. In this case the energy, E, gained when the liquid spreads over a given area is described as:

$$E = \sigma_1(\gamma_{S_1V} - \gamma_{S_1L}) + \sigma_2(\gamma_{S_2V} - \gamma_{S_2L}) \quad (2.22)$$

The corresponding contact angle can then be given by:

$$cos\,(\theta_{CB}) = \frac{E}{\gamma_{LV}} = \sigma_1 cos\,(\theta_{Y_1}) - \sigma_2 cos\,(\theta_{Y_2}) \quad (2.23)$$

For a porous surface of solid surface area σ_1 and air pockets represented by σ_2, γ_{S_2V} becomes zero and γ_{S_2L} becomes γ_{LA}:

$$cos\,(\theta_{CB}) = \sigma_1 cos\,(\theta_{Y_1}) - \sigma_2 \quad (2.24)$$

Substituting in Young's equation gives:

$$cos\,(\theta_{CB}) = -1 + f_1[\frac{\gamma_{SV} - \gamma_{SL}}{\gamma_{LV}} - 1] \quad (2.25)$$

Equation 2.25 shows that air trapped in pores under the droplets increases the contact angle compared to that of a flat substrate of the same material. It assumes that the bottom of the droplet is not altered by the surface roughness.[70] More complex mathematical expressions of this final equation have been proposed to describe droplets that partially penetrate the porosity.

It is often mentioned that the Cassie model attributes the spreading of the droplet to the fractions f_1 and f_2 of the contact areas. Consideration of the shape of the droplet at and the wetting of the three-phase line is necessary to fully understand droplet behaviour on a textured surface. The contact angle can also depend on the height from which the droplet falls onto the surface, in the following experiments the droplet was always touched onto the surface. The FTA-100 system was used to collect static contact angle images. Contact angles were measured manually with a protractor. Droplet sizes were

controlled at 3 or 5 µL. Droplets were allowed to relax on the surface before measurements were taken. For superhydrophilic samples with 0° contact angles, the time needed for the droplet to completely wet the surface was recorded.

2.15 Photocatalysis with Resazurin

The photocatalytic dye Resazurin and its function have been discussed in detail by Mills et al.[71] For rigorous measurement of photocatalytic materials stearic acid is commonly deployed as a thin coating on a material and its degradation of the hydrocarbon bands between 2800 – 3200 cm^{-1} observed with FTIR. In **Chapter 4** stearic acid dissolved in chloroform 0.05M was dip coated onto macroporous silica/TiO_2 films, however for most of these samples and a range of dip coating speeds, no homogeneous coating could be obtained. Stearic acid requires 17 electrons to fully break down its 17 carbon-carbon bonds. In comparison, Resazurin (maximum absorbance, λ_{max} 610 nm), a photoreduction dye, requires only a single electron transfer from the photocatalyst for it to be reduced to Resorufin (λ_{max} 580, 454 nm), via removal of the oxygen bound to the nitrogen atom through a dative covalent bond. Neither stearic acid nor Resazurin absorb UV-A.

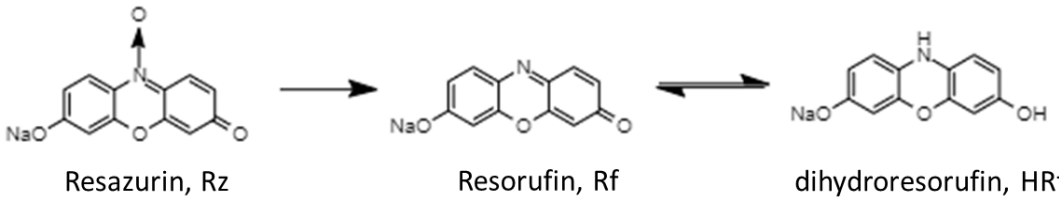

Figure 2.6. Resazurin (Rz) undergoes an irreversible reduction to Resorufin (Rf), with the requirement of only a single electron. This results in a colour change from blue to pink. Rf can undergo a further reversible reaction to form dihydroresorufin (HRf). (Reproduced from Mills et al., reference 71).

Thick films of Resazurin (590 nm) some 39 times thicker than the photocatalyst layer, e.g., a 15 nm layer of TiO_2 anatase on Pilkington Activ glass, have been shown to be a good indicator of photoactivity. This can be achieved with UV-A irradiances typical of those of a bright summer's day, around 4.5 mW cm^{-2}. Within a few minutes of irradiation in the presence of a photoreduction agent the dye changes from blue to pink (**Figure 2.6**). The dye was deployed with a combination of a polymer and a plasticizer, in this case hydroxyethylcellulose (HEC) and glycerol, to enable film formation.

Most technologies in this category utilize thin layers of semiconductor materials and so study of the kinetics of the breakdown of stearic acid can be tedious and laborious under realistic irradiances. Mills et al. have shown good correlation in the initial photodegradation rates of both stearic acid and Resazurin under the same conditions with respect to anatase TiO_2 coatings, the major difference being that the Resazurin reaction occurred within a few minutes, whereas the stearic acid was broken down only

after several hours of UV irradiation. However, unlike stearic acid, which can be easily removed from coatings by dissolving in chloroform or acetone, the reduced form of the ink would not be easily removed from the sample surfaces and so this test can be considered destructive.

Unlike many other photocatalyst ink dyes, which undergo reversible redox reactions (e.g. methylene blue, MB), Resazurin is reduced irreversibly from its blue colour to the pink Resorufin. In their reduced form, dyes such as MB readily react with O_2 to reform the species responsible for the initial colour of the dye. The reaction scheme for the Resazurin-dye ink with TiO_2 is shown in **Figure 2.7**.

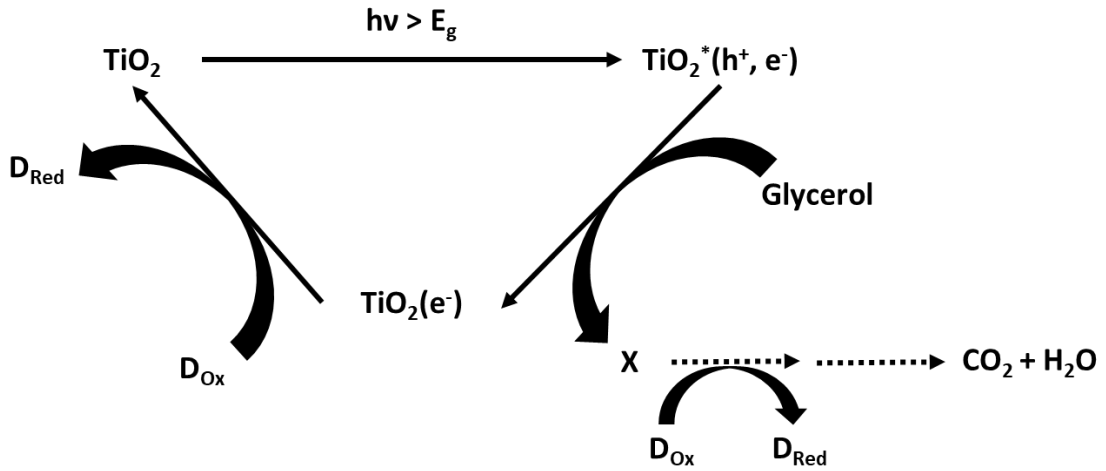

Figure 2.7. The reaction scheme for the reduction of Resazurin in the presence of TiO_2 under UV-irradiation is shown. An electron-hole pair is formed in TiO_2 after UV exposure, the hole is scavenged by the sacrificial electron doner glycerol, the photogenerated electron irreversibly reduces the dye from Rz to Rf. D in this diagram represents the dye species being either oxidised or reduced. (Reproduced from Mills et al., reference 71).

Upon UV-A irradiation of energies greater than the band gap energy, an electron-hole pair forms within the photocatalyst, the hole is scavenged by a sacrificial electron donor (SED), in this case glycerol, leaving the photogenerated electron available for reduction of the dye, resulting in a colour change of the blue Resazurin to the pink Resorufin, an irreversible reaction. Photobleaching, i.e., complete loss of colour in the dye, has been shown to occur with prolonged irradiation, indicating breakdown of the dye, polymer and glycerol as shown by FTIR. This was observed for some of the samples in **Chapter 4**. Upon photobleaching the Resorufin can be further reduced to form dihydroresorufin (**HRf**), as shown in the reaction scheme above. This reaction is reversible as HRf is oxygen-sensitive, when left in the dark the pink colour of Resorufin will return.

Glycerol plays a crucial role as a SED, it has been shown that in the presence of either no or little glycerol the reaction does not take place to any significant extent, indicating

that the HEC polymer alone is not sufficient to facilitate the reduction. The glycerol also acts as a plasticizer to enable greater diffusion of the dye within the polymer matrix.

2.16 Fluorescence Spectroscopy

Unlike Raman spectroscopy, in fluorescence emission spectroscopy a molecule or structure is excited into an excited electronic state through absorption of a photon, usually undergoing some non-radiative transitions to bring it to the energy of the lowest unoccupied molecular orbital (LUMO), before emitting a photon to return to the ground state. The energy difference between the excitation and emission wavelengths is called the Stokes shift. In fluorescence spectroscopy, steady-state emission spectra are obtained by scanning across wavelengths where the emission occurs, in the case of quantum dots giving a symmetrical peak. Time-resolved spectra indicate the time that a species exists in the excited state, to get information about its relaxation mechanisms. They are obtained by pulsing the sample at the excitation wavelength and observing the decay. Fluorescence quantum yield describes the ratio between the absorbed and emitted photons, indicating the efficiency of the fluorescence.

Due to quantum confinement, in the case of quantum dots the entire nanoparticle is considered to become excited after excitation. In bulk only the surface of the material would experience a change in electronic state upon irradiation, nanoparticles exhibiting quantum confinement ‘feel’ the effects or the incident radiation throughout their structure. The significantly smaller amount of total overlapping states in nanoparticles small enough for confinement results in quantization of the energy levels present, unlike in bulk where states overlap to form a continuum and the only forbidden transition is that of the band gap, the difference between the valence and conduction bands and their respective highest occupied molecular orbitals (HOMOs) and LUMOs respectively.

The Horiba FluoroMax-4 spectrometer equipped with a PMT detector was used to collect emission spectra. For quantum yield measurements samples were placed in an integrating sphere, the counts across different samples were controlled using neutral density filters and variations in slit width. Time resolves spectra were collected on an Edinburgh Instruments fluorescence spectrometer.

2.17 Atomic force microscopy (AFM)

AFM was used to investigate the morphology and pore ordering of smaller macroporous samples. The technique uses a tip to scan across a samples surface and determine the surface roughness. The resolution is related to the tip size, in this case the tip radius used was 10 nm. Only small macropores and surface porosity could be scanned by this technique as deviations in height greater than 100 nm can damage the tip. Images were

collected on a Bruker Dimension Icon atomic force microscope with a Bruker ScanAsyst Air Probe (nominal tip radius 2 nm) in ScanAsyst mode.

2.18 Spin coating

In this technique, a substrate is mounted onto a stage and spun. Solutions are added to the substrate either before or during spinning, these different types of spin coating are referred to as static or dynamic. The spin coating speed and solution concentration determine the resulting coating thickness, spin speed is inversely proportional to film thickness, decreasing the concentration reduces the film thickness. In static spin coating, as the speed of rotation increases, excess solution is flicked off the substrate, the remainder of the spinning process encourages evaporation, and hence the humidity and solution/substrate temperatures play a part in determining the thickness of the dry film. Spin coated films are usually flat and homogeneous. Cleaning the substrate thoroughly beforehand is necessary to prevent pinhole formation. A Lawrell brand spin coater was used to coat substrates with waterglass. Substrates were vacuum sealed to the stage with a rubber O-ring before spinning.

2.19 Dip coating

Dip coating involves dipping a clean substrate into a solution and withdrawing at a controlled speed to form a uniform coating. Dip coated films usually have a gradient, their thickness increasing in the opposite direction of withdrawal.

At high speeds, known as the viscous drag regime, the flow of the solution dominates the dip coating process. There is a limit to the thickness of films formed at high speeds and above a certain speed the build-up of solution on the substrate will result in curtaining, where excess solution will run off the coating as it is formed. At lower speeds, usually below 1 mm/min, the evaporation at the drying front drives film formation in the capillary regime. Theoretically the coating thickness can be infinitely increased by reducing the dip coating speed. In this region coatings may become rippled due to overloading of solute at the drying front during evaporation. The region between the viscous drag and capillary regimes is known as the intermediate region, the minimum film thickness is located here and both effects are involved in coating formation. According to Grosso et al.,[72] the viscous drag regime is better suited for impregnating porosity. As with spin coating, reducing the concentration reduces the film thickness, however unlike spin coating, dip coating can form films from very dilute solutions. The relationship between the coating thickness, h_0, and key parameters is shown by the equation:

$$h_0 = k_i \left(\frac{E}{Lu} + Du^{2/3} \right) \qquad (2.26)$$

The terms correspond to solution composition constant, k_i, withdrawal speed, u, evaporation rate, E, the substrate width, L, and the solution physical-chemical characteristics, D. Dip coating in the capillary and intermediate regimes is strongly affected by evaporation at the meniscus, minimizing air flow at the drying front and having homogeneous surface energy are vital in forming homogeneous coatings. Humidity and solution temperature also have a significant effect on evaporation. To a lesser extent the surface energy of the beaker (e.g. hydrophilic glass or hydrophobic PTFE) containing the solution and the relationship between the substrate and beaker size can also affect film formation and should also be controlled.[72] Dip coating was carried out with homemade dip coaters.

3. Preparation of stable, robust, transparent silica films from spin coating of viscous sodium and potassium waterglass solutions

3.1 Abstract

It has long been known that drying a waterglass solution in air would result in the formation of a glassy coating. However, these paint-on methods make it difficult to control the film thickness. Herein we present a simple procedure for the preparation of transparent silica films from sodium or potassium waterglass solutions, involving spin coating of waterglass solutions onto glass or silicon wafer, a short, low temperature heat treatment followed by washing with water or dilute aqueous acid. The washing step was found to be necessary to retain surface homogeneity by inhibiting the formation of surface carbonates. The carbonates formed were identified with XRD, Raman and IR spectroscopy. The chemical structures of the films before and after washing were identified with XPS and IR spectroscopy to determine the changes responsible for their stability. EDX and XPS showed a significant decrease in the alkali cation content after washing. The optical properties of the stable films were inspected with UV-vis spectroscopy and ellipsometry. The mechanical toughness of the glass films was determined with pencil hardness and Scotch tape tests. The water contact angle of the films was also determined.

3.2 Introduction

3.2.1 History of soluble silicates

Soluble silicates are among the largest volume of synthetic chemicals, only commodity acids and bases are produced in greater volumes.[73] Soluble glass has been produced since antiquity. Production of waterglass on industrial scales began in Germany in the early nineteenth century, initially used as a coating for curtains to make them more fire retardant, as a replacement for dung in textile manufacturing and to make bars of soap. The industrial process involved the fusing of sodium carbonate (soda ash) and sand in a furnace to produce a glass, which was then cooled, crushed and finally dissolved in water, hence the name 'wasserglass.'[74]

Modern industrial uses of soluble silicates generally concern three categories, as a cheap builder for soaps and detergents, adhesives and binders, and in the production of siliceous materials such as synthetic pigments, gels, clays, zeolites[74] and colloidal silica.[75] The chemistry of waterglass solutions was previously perceived as intractable, inorganic chemists would refer to the silicate species as 'Cinderella anions.'[74] It was

believed that the chemistry was dependent on the preparation method. However early work by authors such as Svensson et al.[76] and later Brykov et al.[77] helped to decipher the importance of the silica to alkali ratio on the properties of the solutions and encourage further study.

3.2.2 General formula and modulus

Soluble silicates can be described by the general formula:

$$M_2O.mSiO_2.nH_2O \quad (3.1)$$

In this equation, M is usually an alkali metal cation (Li, Na, K),[74] however silicates based on tetramethylammonium (TMA) or tetramethylammonium (TEA) cations also exist.[75] The prefixes *m* and *n* describe the ratios of silica and water respectively. Sodium silicates are the cheapest and most widely used, whereas potassium and lithium silicates are produced for niche applications (**Table 3.1**). The modulus, *m*, of as-synthesised soluble silicate solutions can vary from 0.5 – 4.0 with 3.3 being the most common,[74] ratios of commercial waterglass products tend not to exceed this limit due to the low solubility of glasses beyond these ratios.[75] Other forms of silica such as colloidal silica suspensions synthesised from waterglass can have ratios above 20, solutions with ratios between roughly 4 and 10 are reported to be unstable.[78] The modulus, *m*, describes the silica to alkali ratio (SiO_2/M_2O) and governs the chemical and physical properties of the solutions, as will be discussed in section **3.2.4**. The value of *n* controls the viscosity of the solution.

Table 3.1. Comparison of the weight and molar ratios of sodium, potassium and lithium silicates. (Reproduced from Weldes et al., Reference 75)

	Wt % ratio, SiO_2/M_2O	**Mol ratio, SiO_2/M_2O**
Sodium silicate	2.50	2.56
Potassium silicate	2.50	3.92
Lithium silicate	2.50	1.25

3.2.3 Production of soluble silicate solutions

On an industrial scale the solutions are produced by dissolving silicate glass melts in water at atmospheric pressure.[75] The glasses are formed by the fusion of silica sand and soda ash (sodium carbonate or sodium hydroxide) in a furnace between 1100 and 1200°C to form a molten salt, which is then dissolved in water. This reaction can be described by the following equation:[56]

$$Na_2CO_3 + SiO_2 \rightarrow Na_2SiO_3 + CO_2 \quad (3.2)$$

The fused silicate glass can also be cooled, crushed and then dissolved into water with steam under pressure. On a lab scale, solutions can be produced by first making a basic solution of alkali metal hydroxide and subsequent dissolution of silica. However this method limits the range of moduli of the final solutions, for sodium silicate the modulus is limited to $2.5 \leq m \leq 2.7$ SiO_2/Na_2O.[75] Finally sodium silicate powder of various compositions (e.g. metasilicate) can be dissolved into water, generally at elevated temperatures (< 100°).

In terms of production methods, soluble silicates are advantageous over other silica sources due to their lower environmental impact as the silica can be sourced from natural quartz deposits and the production requires no toxic or harmful organic components. The major disadvantage of soluble silicates is their rapid polycondensation under neutral and acidic pH, somewhat restricting its functionality in synthetic procedures. In solution they form both monomers and multiple oligomers, this is often considered a hinderance in the synthesis of complex nanostructured materials, however there is evidence to suggest this is not a major issue.[56]

3.2.3.1 Silicon alkoxides

Silicon alkoxides such as tetraethylorthosilicate (TEOS), designed to contain purely monomeric silicate units are more costly, toxic and energy intensive to produce in comparison with soluble silicates. Their synthesis involves the alcoholysis of silicon tetrachloride:

$$SiCl_4 + 4ROH \rightarrow Si(OR)_4 + 4HCl \qquad (3.3)$$

The corrosive hydrogen chloride by-product vapours are also cause for practical concern. Another method involves the reaction of anhydrous alcohol with silicon metal in the presence of a catalyst:

$$Si + 4ROH + catalyst \rightarrow Si(OR)_4 + 2H_2 \qquad (3.4)$$

Unlike soluble silicates the alkoxides are only soluble in organic solvents, they typically release alcohols as by-products during hydrolysis condensation reactions, which can be disadvantageous for certain processes. However, these monomers are generally preferred for the synthesis of ordered porous solids such as mesoporous silicas as they are homogeneous in solution. Their condensation reactions can also be carefully controlled at any pH.[56]

3.2.3.2 Natural and recycled silica sources

Gérardin et al.[56] have explained the utility of natural silica sources including clays, diatomaceous earth, natural zeolites and other mineral forms of silica. These are advantageous due to their high abundance and low cost and toxicity. Meso- or

microporous materials can be formed naturally from these materials without the addition of organic surfactants, the porosity being generated by metal cation impurities (e.g. K^+) or natural organic residue such as lignin. However, the purification of these silica sources requires high temperatures and concentrated acids and similarly to soluble silicates, multiple species form in their solutions.

Recycled silica sources include industrial waste products (coal ash, rice husk ash), electronic wastes such as packaging resin, and domestic waste glass to name a few. These recycled silica sources are also abundant, cheap and non-toxic, the residual metal ions from these glasses also offer additional acidity that can be beneficial in certain synthetic processes. Products of recycled glasses tend to be slightly lower in surface area and pore volume than synthetic silica sources.

3.2.4 Chemistry of soluble silicates in solution and solid state

The most direct method used to determine the speciation of soluble silicate solutions is ^{29}Si NMR. Silicate units with a certain connectivity give distinct signals in NMR. Raman and FTIR spectroscopy have been used to a lesser extent. Light scattering techniques have been used to determine particle size. NMR is ideal for examining steady state solutions, whereas IR and Raman are better suited to interpretation of non-steady state systems.

3.2.4.1 Connectivity

Compared to silicon alkoxides, soluble silicates exhibit vastly more complex solution chemistry. The structure of all silica sources and products can be described in terms of their building blocks, the tetrahedral silicic acid monomer $Si(OH)_4$ or orthosilicate unit (SiO_4^{2-}). The sources differ in their degree of connectivity, Q^n, where n defines the number of Si atoms any one Si atom is connected to through siloxane bridges (Si-O-Si) bonds, which are also referred to as bridging oxygens (BO). The value of n ranges from 0 - 4, indicating completely depolymerised and fully polymerised orthosilicate units respectively. This notation was developed by Engelhardt et al.,[79] in their ^{29}Si NMR study they assigned the NMR peaks, as shown in **Table 3.2**.

Table 3.2. Change in chemical shift in ^{29}Si NMR peaks with connectivity in waterglass solutions. (Reproduced from Engelhardt et al., reference 79)

Connectivity / Q^n	**^{29}Si NMR peak / ppm**
Q^0	-72
Q^1	-79
Q^{2c}	-82
Q^2 and Q^{3c}	-87 to -91
Q^{3c}	-96
Q^4	-108

Si atoms with greater connectivity are correlated to a greater chemical shift. As shown in the above table, polymerization can lead to the formation of two- and three-dimensional structures such as rings or cyclic species.

The introduction of network modifiers such as alkali metal cations results in the formation of non-bridging oxygens (NBOs), which refer to the unbonded oxygen atoms associated with the cations present in the solution. It can be considered that every cation present in solution results in the formation of one NBO, which can be visualised with the following equation:

$$Si - O - Si + M_2O \rightarrow 2[Si - O \ldots M^+] \qquad (3.5)$$

The NBOs form ionic bonds with the cations, which are considerable weaker than the corresponding BO covalent bonds.[80]

In his review, Falcone has explained that the connectivity of orthosilicate units in solution can be controlled by the modulus and concentration of the solutions (see **Figure 3.1**).[74] The dilution level and cation have also shown to affect the connectivity of orthosilicate units in solution.

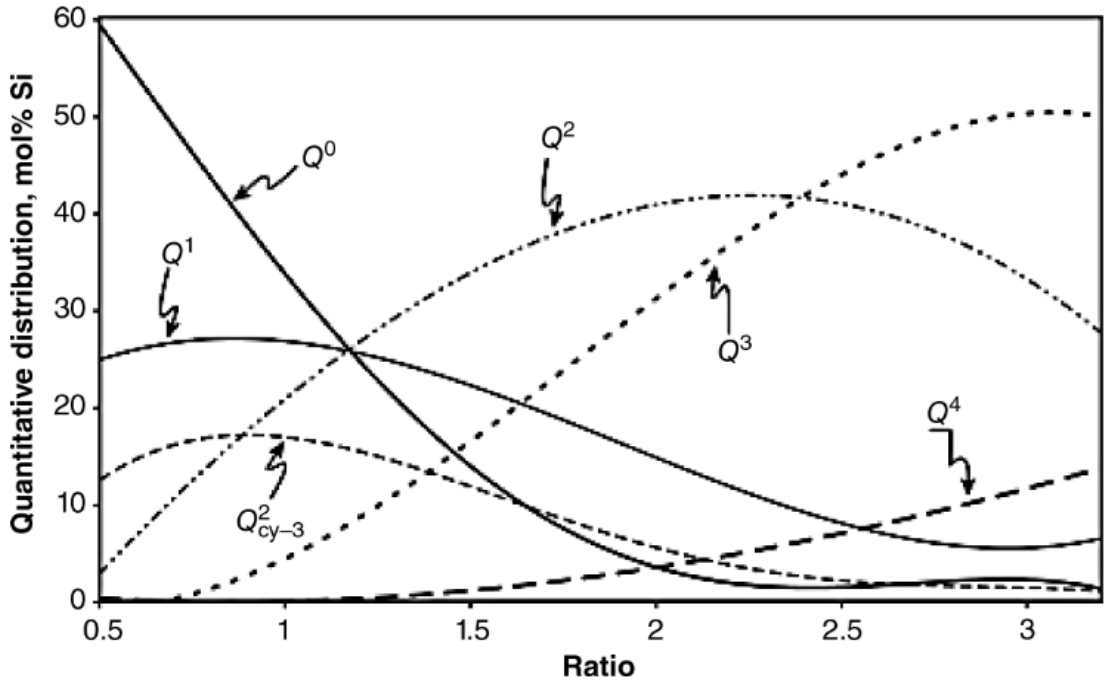

Figure 3.1. Change in connectivity of waterglass solution species with modulus and concentration. The connectivity is represented by Q^n, the value of n varies between 0 and 4, higher connectivity (n = 2, 3, 4) species increase in concentration as the SiO_2:Na_2O ratio increases. The subscript 'cy' refers to cyclic species, cy-3 in this case refers to 3-membered rings of silicon atoms connected through bridging oxygen atoms. (Taken from Falcone et al., reference 74).

The general trend is that the greater the SiO_2/Na_2O ratio, the more polymerized the solution becomes. More specifically as the ratio increases the quantity of Q^0 units decreases and the quantity of higher order units increases. However even at high ratios, orthosilicate units are still present.[74] Vidal et al.[81] have used ^{29}Si NMR to show that for sodium and potassium silicate solutions with a Si/M^+ molar ratio less than 1, the majority of the signal percentage area comes from Q^0 and Q^1 entities (-72, -80 ppm). As the Si/M^+ ratio increased above 1, Q^2, Q^3 and Q^4 species emerged (-88, -97, -106 ppm) and predominated the spectra, indicating greater levels of polymerization. For example, a solution with a molar ratio of 1.7 was shown to contain all types of connectivity, with most of the peak area coming from the Q^2, Q^3 signals (29.0 and roughly 50.0%) for both sodium and potassium silicate solutions. This change occurred independently of the source of the solution.[81]

Relating the bands of FTIR spectroscopy to silicate species alone is challenging. Several groups have verified a correlation between the changes in the NMR chemical shift with changes in the position of FTIR bands.[81–83] Bass et al.[82] have explained that both ^{29}Si

NMR and FTIR spectra become more complex as the ratio increases, corresponding to the condensation of silicate monomers to form linear, planar cyclic, three-dimensional anions and finally polymeric silica.[82] Raman spectroscopy also shows distinct Raman shifts corresponding to the connectivity of solution species,[81] however for the sake of brevity this will not be discussed in detail here.

Vidal et al.[81] have studied the changes observed in FTIR of soluble silicate solution with varying modulus. They identified the FTIR band ranges for silicate species of different connectivity from the literature. 1.7 Si/Na molar ratio sodium silicate solution exhibited a BO peak at 1003 cm^{-1} and a shoulder at 1100 cm^{-1}, which were identified as silicate units with Q^3 and Q^2 connectivity. Decreasing the molar ratio to 0.5 Si/Na resulted in these peaks decreasing in wavenumber to 967 and 914 cm^{-1} respectively, the bands now being associated with Q^1 and Q^0 species and units.[81] The decrease in modulus of waterglass solutions resulting in depolymerization of the silicate species manifested as a decrease in wavenumber of the associated peaks. This was explained by Lucas et al.,[84] decreasing the modulus increases the pH of the solutions, causing BO bonds to break down. Bass et al.[82] observed three IR bands in their most alkaline silicate solutions (SiO_2/Na_2O molar ratio 0.05), 975, 920 and 850 cm^{-1}, which were attributed to monomers. Increasing the modulus resulted in the peaks increasing in frequency and decreasing in intensity. The same trend occurred for a dimer peak at 1000 cm^{-1} that emerged when the modulus reached 0.1, as the modulus increased to 0.52 its frequency increased to 1010 cm^{-1}. This peak has the greatest intensity between moduli of 0.52 and 1.65, in the NMR spectrum of solutions of this modulus, Q^{2c} and linear anions predominate. Linear anions contributed predominately to this peak at lower ratios, larger species including three-dimensional anions contribute more as the ratio increases. At moduli of 0.21 or greater, a shoulder emerged centred around 1055 cm^{-1}, coinciding with Q^{2c} anions in the NMR spectrum. Above a modulus of 2.48 this shoulder merges with another peak around 1090 cm^{-1} in wavenumber, attributed to three-dimensional anions (both Q^{2c} and Q^{3c} species), which are the most abundant at equal or greater ratios. These peaks increased in intensity as the modulus increased to 3.3, where a polymer and Q^{3c} band emerges at 1150 cm^{-1}. Generally 1050 to 1300 cm^{-1} bands increase in intensity and frequency exhibiting similar trends to the NMR data as the modulus increases.[82] Tognonvi et al.[85] have used ATR to show the change in the BO asymmetric stretching band with the connectivity of lithium, sodium and potassium silicate solutions. They show that the band position gradually increases with the connectivity.[85]

Vidal et al.[81] have also shown that diluting potassium waterglass solutions causes a degree of polymerization. For a molar ratio of 1.7 diluted 70% with water, Q^2 signals decrease in percentage peak area (29.0 to 23.0%) while dilution resulted in an increase

in Q^4 species (12.1 to 18.1%).[81] This was also observable in FTIR, BO peaks shifted to higher wavenumbers upon dilution.[81,84] In a DLS study of sodium silicate solutions, Böschel et al.[86] have observed that dilution results in a small increase in particle size, ageing diluted solutions resulted in the formation of agglomerates, which precipitated out of solutions several days later. Bass et al.[82] observed an increase in intensity and wavenumber of the 1090 to 1300 cm^{-1} oligomer and polymer bands as a 3.3 ratio solution was diluted. The main dimer peak around 1000 cm^{-1} also increases in frequency as the solution becomes more dilute.[82]

Vidal et al.[81] compared the effects of dilution for sodium and potassium silicates and found that the FTIR BO peak wavenumber was higher for potassium silicate solutions, implying a greater degree of polymerization for the same concentration and percentage dilution. For a molar ratio of 0.7, potassium silicate solutions contained more polymerized species (15.4 and 17.0% peak area for Q^2 and Q^3 species respectively) than the corresponding sodium solutions (22.1 and 7.7%).[81] Kinrade et al.[87] have used ^{29}Si NMR to show the effects of the alkali cation on the Si connectivity and also concluded that the degree of polymerization is greater in potassium than sodium silicates, the degree of polymerization increasing in the order $Li^+ < Na^+ < K^+ < Rb^+ < Cs^+$. This trend is due to the increasing silicate-M^+ ion pair formation constant.[87] Tognonvi et al.[85] have used ATR on diluted sodium, potassium and lithium waterglass solutions. They observed a decrease in the wavenumber of the BO asymmetric stretching band with decreasing cation size, (e.g. for the Q^2 band, $Li^+ > Na^+ > K^+$, 1026, 1014, 1011 cm^{-1}), they attributed this to the cation affecting the nearest neighbour NBO bond lengths.[85]

This discussion described the fundamental structures present in waterglass solutions as identified by their connectivity and corresponding FTIR trends. The pH, which is controlled by the modulus has the greatest effect on the degree of polymerization in solution. The concentration of the solution and the alkali cation affect the speciation to a lesser extent.

3.2.4.2 Oligomers, clusters and aggregates

Higher order silicates form in waterglass solutions due to condensation that occurs as the modulus is increased. Polymerized species with connectivity greater than Q^0 can form structures such as chains, rings, clusters and particles or agglomerates. As shown in **Table 3.2**, Engelhardt et al.[79] originally identified that cyclic species could also be seen in NMR spectra, namely those based on silicate units of Q^2 and Q^3 connectivity, identifying them as signals appearing between Q^1 and Q^2 peaks and Q^2 and Q^3 peaks respectively. 1D NMR has been used to identify 16 different oligomers (**Figure 3.2**) beyond the dimer in aqueous solutions.[88] Bass et al.[82] have detailed the chemical shifts of these species in solution. Using NMR and FTIR they showed that higher silica

concentration and higher ratio (SiO_2/Na_2O molar ratio 3.3 and 2.9) solutions contained greater relative amounts of Q^3 (4-ring) and Q^4 anions and lower proportions of monomers and smaller oligomers such as linear chains and planar cyclic anions. This distribution remains even after diluting the solutions 50-fold with water. Increasing the pH and thereby decreasing the ratio, particularly below 2.5, was shown to decrease the relative amounts of these large anions in solution, even after 2- or 3-fold dilution. Low concentration, high pH solutions primarily contained monomer, dimer and cyclic trimer species. Ultimately they were able to assign FTIR bands specific to monomer and oligomer species in solution.[82]

Vidal et al.[81] have observed from ^{29}Si NMR that cyclic species based on Q^2 and Q^3 species were more prevalent in solutions with low ratios, in this case below a Si/M^+ molar ratio of 0.7 with percentages areas of roughly 20 and 10% for Q^2- and Q^3-based cyclic species respectively in both sodium and potassium solutions. They hypothesized that the formation of these particular cyclic species was linked to the depolymerization that occurs as the modulus is decreased.[81]

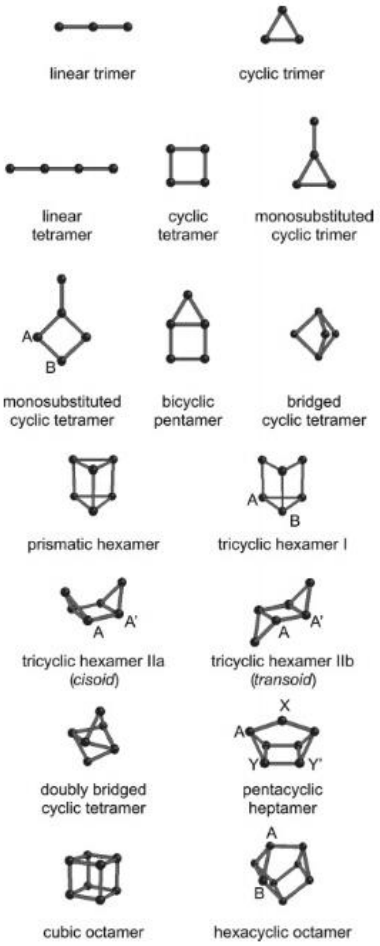

Figure 3.2. Oligomers beyond dimer identified in waterglass solutions, using ^{29}Si NMR. The16 different oligomers have been detected with this method are displayed above. (Taken from Sjöberg et al., reference 88).

2D NMR has been used to identify a further 8 oligomers present in solution in the regions of -91 to -88 ppm and -98 to -96 ppm where the overlap of chemical shifts is significant. These were cis and trans versions of bicyclic hexamers and bicyclic pentamers, and five diastereomers of a tricyclic hexamer. The concentrations of these structures were considered to be comparable to previously discovered oligomers.[89]

Tognonvi et al.[90] have used ^{29}Si NMR and SAXS to identify a neutral cage-structured complex with the formula $Si_7O_{18}H_4Na_4$ in a concentrated sodium silicate solution with Si/Na atomic ratio of 1.71. Diluting the solution resulted in depolymerization which broke these down into $(Si_7O_{18}H_4Na_{4-n})^{n-}$ anions ($1 \leq x \leq 4$). This work suggested that cage structures containing Q^2, Q^3 and Q^4 units exist in concentrated waterglass solutions.[90]

Nordström et al.[78] have used dynamic light scattering (DLS) and small angle X-ray scattering to identify the effect of modulus (SiO_2/Na_2O molar ratio 3.3 – 8.9) on the size of entities in sodium silicate solutions. DLS determined the size of the species present, whereas SAXS was used to interpret both their size and shape. Crucially they used an ion exchange resin to vary the modulus as opposed to the acidification methods used elsewhere. Their results showed that solutions with a modulus of 3.3 contain mostly small silica clusters of radius 0.7 nm, while 11 to 13 wt% of the silica is present as smaller structures including monomers and oligomers (**Figure 3.3**). At this ratio a negligible fraction of the silica also exists as colloidal particles of size 30 nm or greater. Increasing the ratio to 3.8 resulted in most silica forming clusters, with small quantities of monomers and colloidal particles also present. Generally increasing the ratio increased the size of solution entities, with fractals being formed between m = 4.7 and 5.5. The lower degree of polymerization at a ratio of 3.3 was attributed to the higher pH. Decreasing the pH through increasing the ratio shifts the solution equilibrium towards condensation reactions.[78]

An earlier study by Böschel et al.[86] used DLS to determine the size of the species in sodium silicate solutions with SiO_2/Na_2O molar ratios between 2.2 to 3.9. They detected three particle radius groups for all ratios, 0.4 to 0.6 nm, 2.5 to 15 nm and 75 to 90 nm. The 2.5 to 15 nm particles were most affected by changing the ratio, decreasing as the ratio increased.[86] It has been suggested that the persistence of the Q^0 species in spite of variations in the ratio or other variables suggests an equilibrium exists between monomer and polymerized species present in solution.[83]

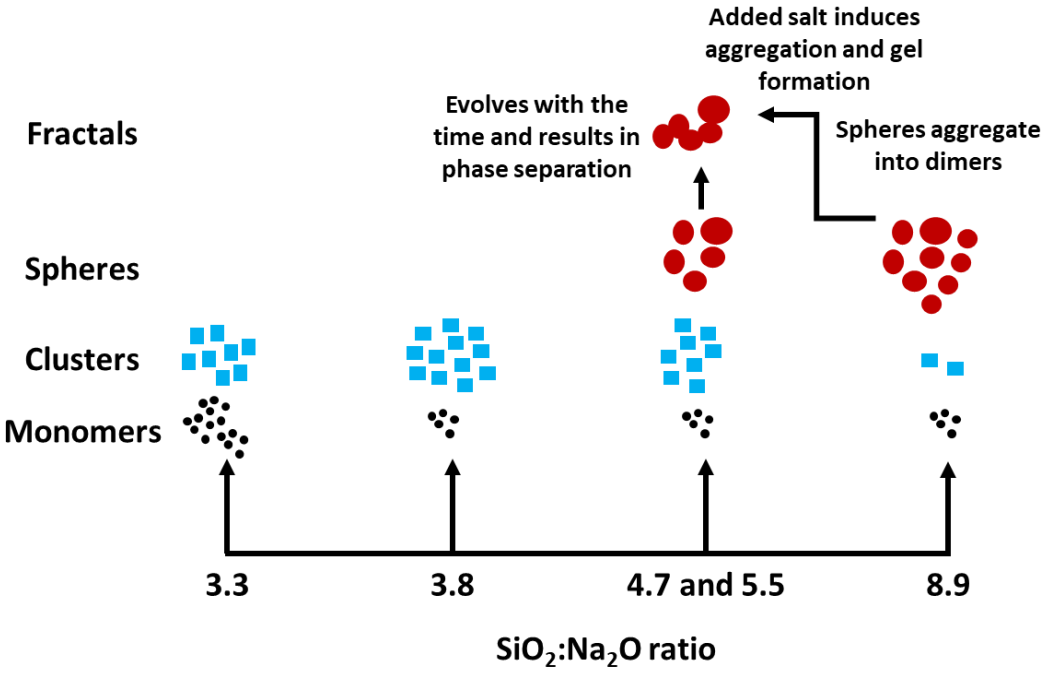

Figure 3.3. Change in the size of entities present in waterglass solutions as the modulus is increased. (Reproduced from Nordström et al., reference 78).

3.2.4.3 Viscosity and solution activity

The modulus also governs the rheology of the solution. Yang et al.[91] studied the static and dynamic viscosities of sodium silicate solutions (SiO_2/Na_2O molar ratio 1.65 – 3.30) as a function of concentration, temperature, modulus and shear rate. Both the static and dynamic viscosities increase with concentration (15 to 55%) and decrease with temperature (15 to 70°C). Viscosity reaches a minimum at a modulus of 1.8, as shown in **Figure 3.4** for three different concentrations.[91]

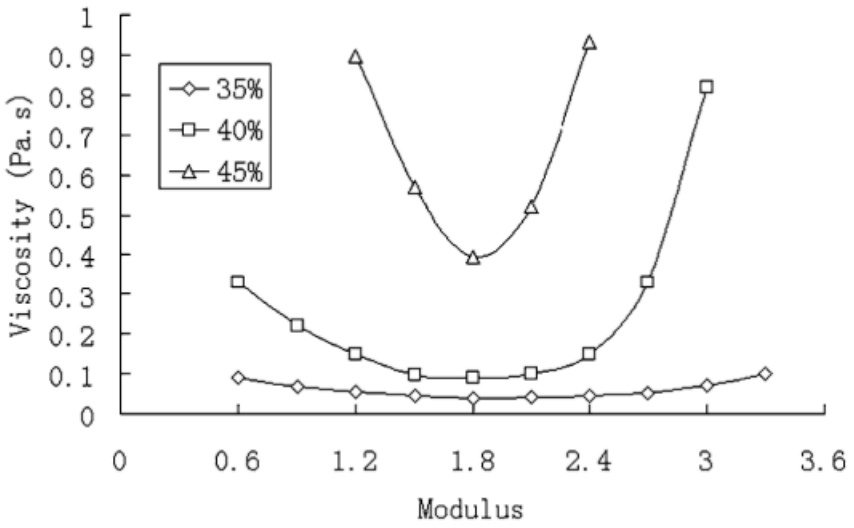

Figure 3.4. Change in viscosity of waterglass solutions with modulus, the same trend being exhibited for three different concentrations. All experience a minimum in viscosity at a modulus of 1.8. (Taken from Yang et al., reference 91).

The effect of shear rate on the dynamic viscosity of sodium silicate solutions was determined. The dynamic viscosity was measured by determining the linear viscoelastic range with constant amplitude to ensure the structure of the solution was not perturbed during measurement. The solutions exhibited two distinct behaviours, dynamic shear thickening in the high shear-rate regime and Newtonian behaviour in the low-shear rate regime. They concluded that waterglass solutions exhibited the properties of a suspension in which lower connectivity Q^1 and Q^2 species acted as a binder for the polymerised species such as clusters and colloidal particles are composed of Q^3 and Q^4 species as well as the cations, which behave as rigid particles in the solutions. Yang et al.[91] also showed that the modulus and consequently the viscosity of waterglass solutions could be modified post-synthesis. The addition of alkali chlorides (NaCl or KCl) or alkali hydroxides (NaOH, KOH) effectively increased and decreased the static viscosity respectively.[91] The viscosity of silicon alkoxide sols is usually adjusted via ageing.

3.2.4.4 Chemistry in the solid-state

Many studies have been undertaken to probe the properties of silicates in the solid-state. Firstly, NMR and particle size analysis techniques such a light scattering have been used to understand the structural transitions that take place as the solution transitions to a gel through either drying or condensation reactions. Secondly the solid glass structures themselves have been examined with NMR to determine the connectivity and relate this to the bonding angles present. Larger sample quantities and significantly longer measurement times compared to those in solution phase limit its utility in thin film analysis. The lack of long-range order means XRD will not provide any useful insights, however scattering techniques such as small- and wide-angle X-ray scattering (SAXS and WAXS) may determine if solution clusters retain their size in the solid state. X-ray absorption spectroscopy have also been used to probe short- and long-range order. This has been supplemented with IR and Raman spectroscopies to gain further insight into the chemistry of the bulk glasses. Finally, techniques such as XPS can now be used to determine the nature of the species created at the interface of the glasses formed with the atmosphere. NMR, Raman, IR, and XPS are generally concerned with the energies and relative ratios of the BO and NBO species within the dried and or condensed waterglass solutions.

3.2.4.5 Properties upon gelation

Gerber et al.[92] have studied gel formation upon acidification of sodium waterglass (Na:Si ratio 0.6, Si concentration 0.5 and 6.5 $molL^{-1}$) with SAXS and WAXS. SAXS showed that the hydrogel formed by acidification contained primary particles 1 to 4 nm in diameter, their size increased with pH. These particles were identified as polyhedra composed of six-membered orthosilicate rings, the internal structure of the polyhedra being dictated by the H_2O network. For this reason, they claim that the polyhedra formed form waterglass are smaller and denser than those in vitreous silica or silica produced in non-aqueous conditions. The water evaporates as the gel dries causing a degree of structural collapse. The primary particles form fractal clusters whose dimensions (d_f) depend on the solution pH. The smallest particles (d_f = 1.71) form at pH = 6, the largest (d_f = 2.30) form at pH = 2, which is the isoelectric point. It was suggested suggest the primary particles form a gel through cluster-cluster aggregation, which involves primary particles aggregating to form clusters that diffuse into solution to form larger clusters. Chemical-limited aggregation, a regime in which aggregates can break apart after a short time, dominates at pH 2, whereas irreversible diffusion limited aggregation occurs at pH 6. This may be due to a change in the surface charge of the primary particles that results in them being bound by covalent bonding instead of hydrogen bonding. The gels are non-crystalline.[92]

In a separate study Nordström et al.[93] studied the changes in the species present in a sodium silicate solution (SiO_2/Na_2O molar ratio 3.2) upon gelation either by reducing the concentration through rotary evaporation or by reducing the pH through addition of acid with viscosity measurements, NMR, FTIR and DLS. Both treatments rendered homogeneous and optically transparent solutions of increased viscosity. ^{29}Si NMR shows that before treatment the solutions contained Q^0 – Q^4 species, predominately Q^2 and Q^4. Rotary evaporation did not significantly change the connectivity of the species present, whereas acidification increased the proportion of Q^3 and Q^4 species while reducing the Q^2 presence, suggesting polymerization. Q^1 signal intensity decreased slightly, whereas the Q^0 species were not significantly affected. Increasing the concentration of the samples resulted in an increase in the absorption over the range of 700 to 1300 cm^{-1} due to the increasing silica concentration, the BO asymmetric stretching band red-shifted from 1001 to 980 cm^{-1} as the concentration was increased from 21.6 to 36.0 wt% suggesting depolymerization. Reducing the pH reduced the absorbance of the spectra and the same BO band blue-shifted slightly. This would indicate some subtle polymerization. Fast and slow DLS relaxation times of the diffusion of particles in solution were related to the presence of small and large particle sizes estimated to be 2 to 3 nm and roughly 40 nm in radius respectively. In agreement with other sources,[78,86] the starting solution contained mostly low molecular weight species, with small quantities of large particles also being present. Increasing the concentration of the solution resulted in the reduction in the sizes of the large particles, however due to the combination of dissolution and condensation processes involved in this change, the connectivity of the solution species was unchanged as observed with NMR. Acidification resulted in condensation, which polymerized the smaller particles and low molecular weight species but left the larger particles unchanged. The results were summarized in **Figure 3.5**.

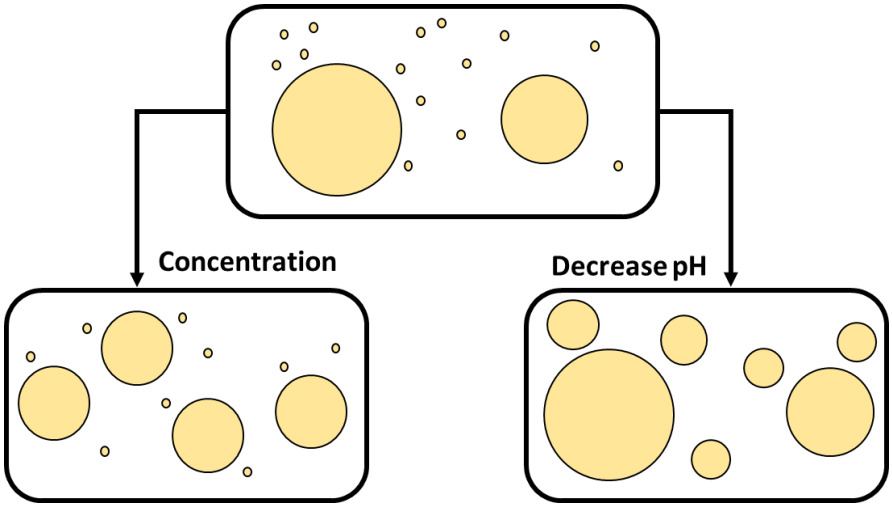

Figure 3.5. Change in the size of solution entities as either the concentration of the solution is increased, or as the pH is decreased. (Reproduced from Nordström et al., reference 93).

Dent Glasser et al.[94] have characterized sodium silicate solutions (SiO_2/Na_2O ratio 3.41) with differential thermal analysis (DTA) upon drying under atmospheric conditions and at higher temperatures ≤ 200°C. All dried samples were amorphous. Two endothermic peaks were present in the DTA curves, only the higher temperature peak was attributed to the loss of water. This was confirmed as the mass loss in dried samples occurred only at the high temperature DTA peaks. As the drying temperature increased (25 to 224°C), the DTA peaks became smaller and broader and shifted to higher temperatures. The weaker low temperature peak (74 to 236°C) was attributed to the rearrangement of interstitial sodium ions and residual water molecules, perhaps the destruction of the coordination sphere of water around the sodium in the dried solutions, as the water molecules shift to energetically more favourable sites. As the drying temperature increases, the degree of polymerization was thought to increase, restricting the motion of sodium and water molecules, resulting in the onset temperature of this peak increasing and its intensity decreasing. The second more intense peak (134 to 304°C) was attributed to the loss of some of the residual water through condensation of adjacent Si-OH groups. As the drying temperature increased, higher energy condensation reactions could take place, and lower energy condensation would have already occurred and the related water lost to the atmosphere, resulting in an increase in the onset temperature of this peak.[94] Roggendorf et al.[95] have examined sodium silicate solutions (SiO_2/Na_2O ratio 3.3) during drying with differential scanning calorimetry (DSC) under hydrothermal conditions. They also confirmed that the dried sodium silicates with less than 45 wt% water were transparent, amorphous and brittle. The data showed that there was some correlation between the decrease in the water content of the silicates and the increase

in the glass transition temperature (T_g). Silicates with water content between ~ 10 and 40 wt% had T_g between ~ 100 and 300°C, compared to a T_g of ~ 500°C for what they referred to as 'conventional glass.' They confirmed that drying sodium silicate solutions of this ratio was an unconventional method to make glass.[95]

3.2.4.6 Properties of silicate glasses and thin films

In section **3.2.4** the effect of cation (e.g., alkali metal) addition on the structure and bonding of the silicate units in solution was considered. These concepts can be extended to understand the chemistry of silicate glasses and dried waterglass solids and films. In comparison with crystalline SiO_2, the increasing addition of alkali cations results in the three-dimensional structure being systematically broken down into sheets and subsequently smaller ring and chain structures, with the cations being associated with NBOs. This charge balancing implies that the cation content imposes physical constraints on the structure but gives no insight into the local structural order in terms of the distribution of the Q^n units.[80]

Both crystalline SiO_2 polymorphs and their glass counterparts exhibit essentially identical short-range order. The lack of long-range order in amorphous SiO_2 can be attributed to the greater variability in Si-O bond lengths (d_{Si-O}) and Si-O-Si bond angles ($\theta_{Si-O-Si}$).[80] The former would be due to a redistribution of charge in a given Si-O bond due to formation of NBO on a neighbouring oxygen atom and the proximity of the associated cation. $\theta_{Si-O-Si}$ has been shown to decrease from 153° to 150.5° as the Na_2O content of the glass was increased from 0 to 33.3 mol%.[96] For a given Q^n species, increases in the ^{29}Si chemical shift, δ_{Si}, have been correlated to increasing d_{Si-O} and decreasing $\theta_{Si-O-Si}$. δ_{Si} has also been shown to increase linearly with the glass modifier content. The rate of change of this relationship increases with connectivity, due to greater chemical shift sensitivity of tetrahedra with more BO bonds (i.e. higher Q^n and greater degrees of freedom) to changes in geometry at ^{29}Si sites.[80]

Through comparison of the NMR spectra of crystalline and amorphous silicate glasses, Dupree et al.[96] have shown that there was no evidence for the existence of crystalline regions in the amorphous glasses. Furthermore, they determined that the chemical shifts present in ^{29}Si and ^{23}Na both vary continuously with composition, indicating a lack of cluster formation of either species in the glasses.[96]

Computational studies have shown that rings of various sizes exist in silicate glass. Rings usually involve 5 to 8 silicate units, rings made of 6 units occur most frequently. NMR has been used to infer bond angles likely to be associated with ring structures but cannot directly observe them.[80]

As in solution phase ^{29}Si NMR, in silicate glass the fully polymerized Q^4 units resonate around -110 ppm, as the connectivity, n, decreases the ^{29}Si nuclei experience roughly 9-12 ppm deshielding due to NBO formation. This was demonstrated for both Na-[97] and K-silicate[98] in the ranges of 20.0 to 55.6 mol% and 14.3 to 50.0 mol% respectively, again showing how the modulus controls the degree of polymerization and also that the chemical shift ranges for each Q^n were the same as in solution.

Stebbins was the first to suggest that the distribution of species in silicate glasses or their corresponding melt may be produced by the disproportionation reaction:[99]

$$2Q^m \leftrightarrow Q^{m+1} + Q^{m-1}, where\ n = 3, 2, 1 \qquad (3.6)$$

Dupree et al.[96] have shown that the degree of connectivity in sodium silicate glass is directly related to the network modifier content. As the Na_2O content increased from 0 to 33.3 mol%, no Q^2 units were present and Q^3 was formed at the expense of Q^4, both were homogeneous in the glass. Only Q^3 signals were observed at 33.3 mol%. Between 33.3 and 50.0 mol%, Q^2 formed from Q^3 units. Likewise at 50 mol% only Q^2 units were present.[96]

Maekawa et al.[97] have shown the distribution of Q^n units in silicate glasses as a function of the alkali cations, Li, Na and K (**Figure 3.6**).[97] The equilibrium in the above equation shifts to the right when the content or charge to radius ratio, Z/r, increases, i.e. $Li^+ > Na^+ > K^+$, the equilibrium constants also follow this order.[98]

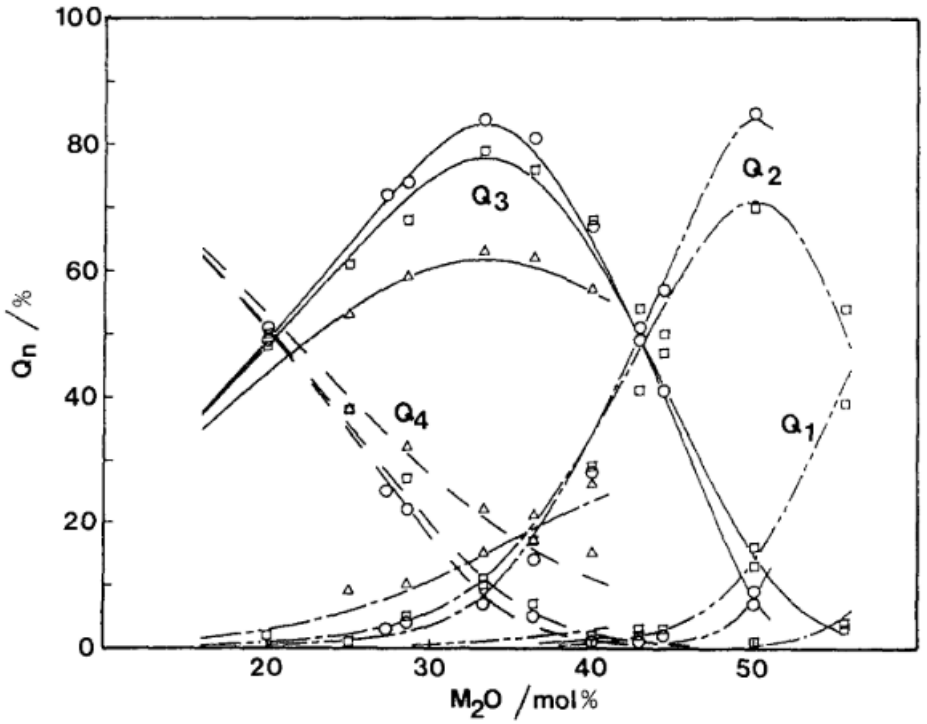

Figure 3.6. Change in the connectivity of silicate units in silicate glasses with modulus and concentration as determined from solid-state ^{29}Si NMR. Lithium, sodium and potassium silicate glasses are represented as triangles, squares and circles, respectively. (Taken from Maekawa et al., reference 97).

Chemical shift is also affected by the second and third nearest neighbour environments, the distribution of chemical shifts being indicated by the FWHM of the NMR peak which is largely determined by variations in local geometry. Several authors have shown that NMR can be used to observe nearest neighbour connectivity in silicate glass, with limited success in identifying specific chemical shifts due to difficulty in overcoming peak overlap.[100] Sen and Youngman have used magic angle spinning (MAS) ^{29}Si NMR to distinguish two types of Q^4 signals, Q^4-Q^4 and Q^4-Q^3 (roughly -106 and -111 ppm), in high silica potassium silicate glasses (2.4 to 13.1 mol% K_2O).[101] 2D NMR is usually limited to phosphate glass due to low signal sensitivity.[80]

The medium-range structure of sodium diffused amorphous silica was investigated by Mazzara et al.[102] using X-ray absorption fine structure spectroscopy (EXAFS), with focus on the order around the sodium atoms. It was previously believed that network modifiers formed NBO oxygens and occupied empty sites in the glass, having no effect on the arrangement of the structure. EXAFS revealed an extended structure around sodium atoms. Firstly, an initial shell of oxygen atoms (NBO) around sodium and a second shell of Si atoms of their associated tetrahedra at distances of 2.30 and 3.80 Å, respectively. The bond lengths were the same for a broad range of compositions. The authors concluded that the silica tetrahedra relaxed locally around the sodium atoms.[102] An earlier EXAFS study by Greaves et al.[103] on the K-edge silicate glass of composition $Na_2Si_2O_5$ determined two coordination shells around Si atoms at distances of 1.61 and 3.17 Å, whereas only a single layer of coordination was found to be around the sodium atoms at 2.30 Å.[103]

IR and Raman spectroscopy are fast, non-destructive and reproducible techniques capable of showing local changes in the structure of silicate glasses.[104] From FTIR reflectance data, Macdonald et al.[105] have shown that the BO asymmetric stretching band of glassy silica is much broader than in the crystalline silicate which has much sharper peaks, due to the narrower distribution of bond parameters. They explain that the interpretation of IR bands in silica is complex, the addition of one or several network modifiers or hydrogen in the form of water or hydroxyls adds additional vibrational modes to the glasses, making structural assignments from IR alone an overwhelming task.[105] The following IR and Raman bands listed were collected by Aguiar et al.[104] in their review of assignments from the literature. FTIR bands identify of both bulk and thin film SiO_2-based structures feature their main bands between 400 and 1300 cm^{-1}. Bridging oxygen bands include an asymmetric stretching mode in the range of 1000 – 1300 cm^{-1}, a bending vibration around 800 cm^{-1} and a rocking vibration near 460 cm^{-1}. The asymmetric stretching band shows additional components, namely transverse and longitudinal

optical (TO and LO) modes. TO modes TO_1 and TO_2 are featured as an intense peak at 1085 cm^{-1} and a shoulder around 1200 cm^{-1} respectively. LO_1 and LO_2 can be found at 1254 and 1170 cm^{-1} respectively. Stretching modes for non-bridging oxygen bands of orthosilicate units with Q^3 connectivity are located between 890 and 975 cm^{-1}, whereas those of Q^2 units can be found at 840 cm^{-1}.[104]

Hydroxyl or silanol (Si-OH) surface groups can also be detected by FTIR, their bands can be divided into hydrogen-bonded and non-hydrogen bonded species. The first group concerns between neighbouring pairs of Si-OH groups bound by either vicinal or geminal hydrogen bonding due to a surface silanol attached to either a Q^3 or Q^2 unit. The second type is related to isolated Si-OH groups. The broad band between 3000 and 3800 cm^{-1} is created by a superposition these two types of surface hydroxyls, with hydrogen bonded and non-hydrogen bonded species having peaks around 3660 and 3750 cm^{-1} respectively. Furthermore, a band at 3540 cm^{-1} is associated with silanol groups hydrogen bonded to molecular water. Absorbed molecular water creates a further broad peak between 3350 and 3500 cm^{-1} and a separate band between 1620 and 1640 cm^{-1}. Finally, an Si-OH stretching band has been located between 900 and 980 cm^{-1}. Carbonate species also produce a distinctive band in FTIR, this will be discussed in more detail in section **3.2.4.7** in the discussion of efflorescence.[104]

Aguiar et al. have observed an increase in the shoulder (TO_2) intensity on the BO asymmetric stretching peak with increasing SiO_2 content in the glass.[104] Agarwal et al.[106] have discussed the effects of changing glass properties such as changes in the fictive temperature, hydrostatic pressure or applied compressive stress on the frequency of the BO asymmetric stretching band in IR spectroscopy. Increasing these properties all result in a decrease in the band frequency due to decreasing $\theta_{Si\text{-}O\text{-}Si}$ bond angle. They verified this through etching glasses affected by these properties with HF and showed that glasses that had undergone the same decreases in BO band frequency had the same etch rates. They explained (with results from other authors) that $\theta_{Si\text{-}O\text{-}Si}$ and therefore the BO band frequency also decrease as density and refractive index of the glass increases, as water diffusion into the glass decreases.[106] MacDonald et al.[105] used a dispersion analysis method to extract quantitative information from FTIR reflection spectroscopy data related to the de-alkalization of sodium and lithium silicate glasses during corrosion. They explain that previous data suggests cation leaching of these glasses has shown complex changes in the intensity and position of the maximum peaks (BO ν_{asym}) in these glasses. With their deconvolution they determine that the position of the BO ν_{asym} band did not change with leaching time. The peak area and intensity did however change gradually as cations were removed from the glasses, specifically the NBO peaks (995

and 965 cm^{-1}) decrease while the BO peaks increase. They also observe the emergence of a 940 cm^{-1} band that grows with corrosion time.[105]

Bridging and non-bridging oxygen species can also be detected by Raman spectroscopy, BO asymmetric stretching, bending and rocking vibrations appear at 1064 to 1183, 783 to 837 and 453 to 490 cm^{-1} respectively. NBO Q^3 and Q^2 Raman peaks appears at 900 to 970 and 860 cm^{-1} respectively. Raman spectroscopy can also be used to identify ring structures in the glass networks, ≥ five-fold rings (w_1), four- and three-membered rings (D_1 and D_2) can also be detected at Raman shifts of 430, 490 and 600 cm^{-1} respectively. The w_1 band originates from the oxygen motion of their symmetric 'ring-breathing' modes, D_1 and D_2 are associated with either defects or breathing modes of planar rings. Finally, in Raman spectroscopy molecular water peaks appear at 3510 to 3540 cm^{-1}. Hydrogen bonded and non-hydrogen bonded silanols have bands at roughly 3680 and 3750 cm^{-1} respectively.[104] Uchino et al.[107] have also confirmed the utility of Raman spectroscopy in the determination of hydrated states in sodium silicate glass. The glasses were hydrated in steam and the progressively heated to observe the removal of water. They observed a non-linear increase and decrease in the bands of the BO asymmetric stretch and NBO stretching bands respectively as the dehydration temperature is increased from 0 to 400°C.[107]

Furukawa et al.[108] have shown the changes occurring in the Raman spectrum of sodium silicate glass with changes in composition for parallel and crossed polarization modes. In the parallel polarization spectrum of pure SiO_2 glass, a broad BO rocking band dominates at 435 cm^{-1}. This diminishes as the sodium content of the glass increases to SiO_2/Na_2O ratio of 5.67 and a narrow band appears at 520 cm^{-1}. As the sodium content increases further this band becomes sharper and increases in frequency to 604 cm^{-1} at a ratio of 1.22. The 5.67 ratio glass also sees the emergence of a sharp BO asymmetric stretching band at 1100 cm^{-1} and a neighbouring NBO (Q^3) band at 955 cm^{-1}. As the SiO_2/Na_2O ratio increases the 955 cm^{-1} peak becomes more intense and at a ratio of 1.75 its intensity becomes comparable to that of the 1100 cm^{-1} peak. At a ratio of 1.22 the 955 cm^{-1} peak becomes greater in intensity than the 1100 cm^{-1} peak and comparable to the intensity of the 604 cm^{-1} band. The 955 and 1100 cm^{-1} bands do undergo changes in frequency with composition but there is no clear trend. The BO bending band appears as Na_2O is introduced into the glass at 790 cm^{-1}, its intensity is low and remains weak at all further increases in Na_2O content. Finally a low intensity NBO (Q^2) band appears at 860 cm^{-1} at an SiO_2/Na_2O ratio of 1.5 and increases slightly in intensity as the ratio increases to 1.22.[108] MacDonald et al.[105] have stated that Raman methods probe too deeply into transparent targets and are therefore not effective in the study of the changes in glass surfaces caused by corrosion.

Attenuated total reflection (ATR) IR has also been used to interpret the structure of silicate glasses and films. ATR is particularly useful for thin film samples as it can be more surface sensitive than transmission-based IR measurements, particularly for thicker samples in which the transmission IR signal is usually dominated by the bulk structure.[109] At higher wavenumbers, features in the ATR spectrum will have lower intensity than in the corresponding transmission FTIR spectrum. With constant angle of incidence and ATR crystal refractive index, the intensity of the spectra decreases as the wavenumber increases due to the inverse relationship between penetration depth and wavenumber (**Equation 2.4**).

Uchino et al.[110] used both a Ge and a mixed TlI and TlBr crystal known as KRS-5 with refractive indices of 4.0 and 2.4 respectively to determine the differences in sodium silicate glass with SiO_2/Na_2O ratio 2.33 before and after hydration via steaming. In the hydrated glass, they identified band positions at 3000 and 1650 cm^{-1}, the same water or hydroxyl bands also observed in transmission FTIR. Bands between 600 and 1300 cm^{-1} obtained with both crystals were attributed to BO asymmetric stretching (1100 cm^{-1}), two NBO stretching bands (970 and 950 cm^{-1}), and BO symmetric stretching and bending bands at 760 and 600 cm^{-1} respectively. Another silicate glass sample was deuterated via steaming, resulting in changes to the silanol or water related peaks, namely the intensity of the 3000, 1650 and 870 cm^{-1} bands was decreased, while neighbouring deuterated bands were created. Their work further identified a band at 870 cm^{-1} associated with non-bridging Si-O bond stretching and Si-OH bending both attributed to the silanol group. Hydrating the glass also decreased the intensity of the 1100 cm^{-1} BO asymmetric stretching band and increased the intensity of the 600 cm^{-1} BO bending band. Finally, they reported a decrease in NBO band position from 950 to roughly 850 cm^{-1} upon aqueous corrosion induced ion exchange, i.e. proton/alkali cation exchange.[110]

Amma et al.[109] used both diamond and Ge ATR in conjunction with specular reflectance (SR) IR to analyse soda lime float glass. They have observed that with either technique, changes occur to the 850 to 1200 cm^{-1} region upon sodium leaching after 320 hours of submersion in 0.1 M HCl acid at 90°. Acid leaching causes the BO band to blue-shift in both SR-IR and ATR, from 1054 to 1060 cm^{-1} and from 990 to 1010 cm^{-1} respectively. They highlight that changes in band position that occur in ATR will be affected by the changes in the refractive index that occur as the composition of the glass is altered by leaching. SR-IR is not affected by this issue and the band shifts can therefore be attributed only to changes in chemical structure.[109]

In the work of Uchino et al.[110] the ATR spectra featured a band at 960 cm^{-1} that broadened on the low frequency side and shifted to lower wavenumbers as the angle of

incidence decreased, indicating variation in the refractive index (dispersion) occurring in the region of the absorption band. The refractive index of this glass composition decreased from roughly 1.5 to 2 in the region of 700 to 1100 cm^{-1}.[110] As mentioned previously, Tognonvi et al.[85] observed a small red-shift in the BO asymmetric stretching ATR band of diluted sodium, potassium and lithium silicates. The peak wavenumber decreased in the order 1026, 1014, 1011 cm^{-1} for Li-, Na- and K-silicate solutions respectively.[85] These small shifts may also have been due to the different refractive indices of the solutions. These examples further highlight that some shifts in band position with composition or chemical structure are observed, but particularly with ATR, interpretation of these shifts alone may be misleading. In general, with Raman and IR spectroscopy, changes in the peak intensity of certain bands can be good indicators of variations in composition.

At the surface of any material the coordination sphere of the atoms is incomplete and therefore surface species differ from those in bulk. For example at the surface of silica, not all oxygens are doubly coordinated, oxygen ions are present.[88] XPS has been used to probe the chemistry of silicate-based films with much greater surface sensitivity than ATR.

Sprenger et al.[111] have observed changes in the O 1s, and Si 2p spectra of sodium silicate glasses with composition. They observe these changes alongside MAS-NMR and Raman spectra of the same glasses. In pure silica glass only one peak is observed at a BE of 533 eV, as sodium is introduced into the glass (SiO_2/Na_2O ratio 8.10) this peak undergoes a chemical shift (roughly -0.5 eV) and an NBO peak emerges just below 531 eV.[111] Nesbitt et al.[112] have explained that the ~ 2 eV decrease in BE for NBO is due to the greater electron density over the NBO atoms, due to the bond formed with the network modifier that results in the almost complete transfer of their valence electrons to the unoccupied molecular orbitals of the NBO.[112] As the sodium content increases the NBO peak increases in intensity relative to the BO peak. As the ratio increases to 1.5, both peaks experience a roughly 1 eV decrease in chemical shift and the NBO peak becomes greater in intensity than the BO peak. They also show that the absolute BE of the Si 2p peak shifts to smaller BEs with increasing sodium content. They note that the specific BEs of Q^4, Q^3 and Q^2 species are 103.40, 102.30 and 101.45 eV respectively.[111] In earlier work they determined the absolute BE and chemical shift of different silicate glass species through comparison of the spectra of the glass surface exposed to vacuum, environmental atmosphere, distilled water and corrosive media. They were able to distinguish between the peaks of H_2O/H_3O^+ (533.55 ± 0.2 eV) and Si-OH (532.86 ± 0.2 eV) species in O 1s spectra.[113] Due to differences in charging between samples and

experimental setups, the absolute BEs of these peaks may differ, despite this the chemical shifts remain useful for interpretation.

Banerjee et al.[114] have shown the changes in the O 1s spectrum of sodium silicate glass before and after leaching without deconvolution. Before leaching the spectra contained three environments attributed to Na KLL, BO and NBO, at BEs of roughly 538, 533.5 and 531.5 eV respectively. After leaching, only the BO environment was present, having undergone a small negative chemical shift. These authors expected the Si-OH at a BE of just over 534 eV.[114]

Nesbitt et al.[112] have detected three different types of BO present in the O 1s spectra of potassium silicate glass, their position determined by the number of K atoms coordinated to the BO, resulting in different BO electron densities. This results in a BO coordinated to a K^+ ion having a lower BE than one that is not. They also speculated the existence of an O^{2-} species present in the glass.[112]

3.2.4.7 Efflorescence

Efflorescence is a cause of concern (mainly aesthetic) in concrete structures. It has been largely ignored in the literature concerning applications of soluble silicate films and coatings, which is surprising considering its detrimental effects on the physical and optical properties of their coatings. Weldes et al.[75] explained that the 'blooming' reaction of sodium silicates results from the reaction of the sodium ion with carbon dioxide (CO_2) or sulphuric acid (H_2SO_4) and moisture to form the hydrated salts, $Na_2CO_3.10H_2O$ or $Na_2SO_4.10H_2O$. These reactions cause the films to expand and weaken accompanied by the formation of a white film at the surface. The state that potassium silicate films do not effloresce as potassium does not form hydrated salt with CO_2 or H_2SO_4.[75]

Veinot et al.[115] have investigated the stability of soluble silicate coatings by drying waterglass of various compositions, drying them for 3 day under normal atmospheric conditions. They then redissolved the coatings in water and titrated the resulting solutions to determine the number of equivalents of carbonate and bicarbonate present in each coating after ageing. They identified that the lack of stability of waterglass films is due to a process known as efflorescence, which changes their appearance and reduces their homogeneity and mechanical rigidity. The reaction between OH^- ions and atmospheric CO_2, which is catalysed by water (or humidity), results in the formation of surface carbonates. The amount of carbonate formation increases with the alkalinity of the surface, i.e., as the molar ratio decreases. The reaction occurs to a greater extent for silicates of sodium than for potassium or lithium. Waterglass coatings produced entirely of lithium silicate contained significantly lower concentrations of carbonate species after ageing.[115]

In solution (pH > 10), this reaction takes the form:

$$CO_2 + OH^- \leftrightarrow HCO_3^-(slow) \quad (3.7)$$

$$HCO_3^- + OH^- \leftrightarrow CO_3^{2-} + H_2O(fast) \quad (3.8)$$

The carbonate species has been identified Aguiar et al.,[104] appearing in Raman spectroscopy as a carbonate stretching vibration 1300 cm^{-1} and in FTIR an asymmetric stretching and bending bands between 1410-1510 cm^{-1} and 860-880 cm^{-1} respectively. Joshi et al.[116] explain that the planar CO_3^{2-} ion has D_{3h} symmetry with IR active vibrational modes v_2 (878 cm^{-1}), v_3 (1450 cm^{-1}) and v_4 (695 cm^{-1}). The v_2 mode is an out of phase bending vibration, the v_3 mode is the doubly degenerate asymmetric stretching vibration and v_4 is a doubly degenerate in plane bending vibration. The bicarbonate anion, HCO_3^-, has lower symmetry (C_{2V}), the same carbonate modes are slightly modified and the C-OH stretching mode generates a 1000 cm^{-1} band. Sodium bicarbonate FTIR shows two peaks at 1000 and 1923 cm^{-1}, whereas the carbonate analogue features only one peak at 1450 cm^{-1}.[116] Sprenger et al.[113] have identified the O 1s BE of sodium carbonate (Na_2CO_3) to be at 531.36 ± 0.4 eV. Lam et al.[117] have used liquid microjet XPS to identify the C 1s BEs of sodium carbonates as 289.1 and 290.1 eV for the carbonate and bicarbonate respectively, both with FWHMs of 1.1 eV.

Dried soluble silicates will rehydrate and gradually dissolve in air, heat-curing alone does not make them completely insoluble. Sodium silicate coatings dry more extensively than potassium silicates of similar composition, water retention is directly related to the alkalinity, high modulus silicates retain the least water. Reaction with either multivalent metal ions to form insoluble silicates, or gelation with an acid can inhibit the reactions of waterglass coatings with water.[75]

3.2.4.8 Applications in the literature

Despite the non-homogenous nature of waterglass solutions, there have been several examples of its use in the formation of highly ordered nanoporous and mesoporous silica. Engelhardt et al.[118] acknowledged the use of sodium silicate solutions in conjunction with sodium aluminate in the formation of zeolites as early as 1985. Later on Sierra et al.[57] used sodium silicate and the non-ionic polyethylene oxide (PEO) surfactant Triton X100 to form mesoporous silica with pores sizes between 1.5 and 5 nm in diameter, with surface areas between 510 to 1220 m^2g^{-1}.[57] Stucky and co-workers[59] used P123 and P85 non-ionic triblock copolymers to template the formation of SBA-type mesoporous silicas from sodium metasilicate nonahydrate ($Na_2SiO_3.9H_2O$) with pore diameters of 3.8 to 7.6 nm and surface areas as high as 1055 m^2g^{-1}. Liu et al.[119] have used sodium waterglass (SiO_2/Na_2O ratio 3.33) and TEOS together with P123 organic template to make highly ordered mesoporous silica with pore diameters of 10 to 18 nm with surface

areas between 403 and 662 m^2g^{-1}. Jo et al.[60] creatively used a blender to form well defined KIT-6 and SBA-15 from sodium waterglass (SiO_2/Na_2O ratio 3.13) and P123, the addition of n-butanol was needed for the KIT-6 synthesis. Their mesoporous powders had pore diameters of 7.2 to 8.9 nm and BET surface areas of 578 to 797 m^2g^{-1}. The structural order and BET surface areas of the products synthesised from waterglass were equal to or surpassed those of powders synthesised with TEOS.[60]

Fireproof coatings have been based on sodium silicate, due to their intumescence they foam upon rapid heating from room temperature to 350 to 500°C and release a steam cloud above the surface which lowers the temperature of the protected surface. Generally, a 4 to 5 mm layer is applied.[120]

Weldes et al.[75] have stated that potassium silicates are often preferred in inorganic water-based paints as they do not effloresce. Loganina et al.[121] have used waterglass as a binder to make water resistant silicate-based paints with the addition of lithium hydroxide and silicic acid sol Nanosil 20.

Waterglass has been used as part of a hybrid epoxy resin coating, alongside polyisocyanate and phosphate organic components, to obtain enhanced flame resistance, static flexural and dynamic mechanical properties than the epoxy resin alone.[122]

Potassium silicate solution (SiO_2/K_2O ratio 2.49) as a silica precursor to encapsulate the organic pigment β copper phthalocyanine in a silica shell ~ 2 to 7 nm thick and inhibit its degradation in the chemical environment created by a TiO_2 photocatalyst.[123]

Nielsen et al.[124] and Huang et al.[125] have used dip coated (double-sided) potassium and sodium waterglass solutions onto glass microscope slides to make antireflection coatings. They modify the thickness of the waterglass films through variations in the dip coating speed and waterglass ratio and concentration, achieving maximum enhancement of visible light transmission of 3.6 and 3.2% respectively on glass microscope slides near 550 nm at normal incidence.

Finally, He et al.[126] have used sodium silicate solution and organic polymers to develop silica thin films (2 to 50 nm) with the degree of incorporated mesoporosity controlled by post-treatment. Alternate layers of polymers (poly(diallyldimethylammonium chloride)), PDDA, poly(acrylic acid), PAA, and waterglass were applied to an electrode via dip coating. Post-treatments with O_2 plasma resulted in the formation of nanoporous films, whereas calcination (450°C) produced a denser film as observed with SEM and AFM.[126]

In this work we have spin coated as purchased sodium and potassium waterglass solutions onto glass or silicon wafer substrates. To our knowledge, spin coating of

waterglass solutions has never been reported in the literature. The films were treated with a short, low temperature hot-plate treatment (120 and 95°C) respectively and washed with dilute, aqueous acid or deionised water, which was needed to prevent efflorescence. The efflorescence as well as the changes in the chemistry of the films before and after heat and acid treatments were characterized with several different methods. Finally, the mechanical and optical properties of the stabilised films were determined.

3.3 Experimental and characterization

Sodium waterglass was purchased from sigma Aldrich (weight (wt) ratio 3.40 - 3.35, molar (mol) ratio 3.51 - 3.46). Potassium waterglass was purchased from Kremer Pigments (weight (wt) ratio 2.60, molar (mol) ratio 4.08). Substrates, DI water, sulfuric acid.

Waterglass films for this study were prepared by statically spin coating waterglass solutions as purchased under atmospheric conditions onto substrates at 4000 rpm, (2 s acceleration, 30 s) with 1 mL of solution being coated onto 1.5*2.5 cm^2 glass substrates.

Coating thickness could be adjusted by varying the spin or dip coating speed or the height of the doctor blade above the substrate. Thickness could also be modified by diluting the stock solution with deionised water. Waterglass was coated onto glass, quartz and silicon wafer. The as coated films were heated on a hotplate for 10-15 minutes and then washed in either water or aqueous acid. The films were gently heated from room temperature to 95°C (ramp rate ~ 5°C/min) and heated at this temperature for 10 to 15 minutes, any higher temperature heating (120, 150, 200, 300, 400, 500°C) was done with ramp rates of 10 to 20°C/min with dwell times of 10 minutes at the target temperature.

For ATR data, the baseline was subtracted to enable comparison of the intensities. It was assumed the ATR crystal did not absorb and the beam was only transmitted. As incident energy increased, penetration depth decreased. The beam was incident at 45°, above the critical angle, which was determined to be 39°, the refractive index of the ZnSe crystal was 2.4, those of the coatings and the glass substrates were assumed to be ~ 1.5.

XPS spectra were charge referenced to the C-C/C-H bonds of adventitious carbon, which was fixed to 284.8 eV. The type of Q species had little effect on linewidth. The state, crystalline or vitreous, would also have had little effect on O 1s linewidth. The error in the XPS measurements was defined as ± 0.2 eV, changes in BE of this magnitude or lower were considered insignificant.

Raman spectroscopy was only used for efflorescence samples, spectra obtained for glass substrates and different coatings were identical suggesting that the signal from the glass was overwhelming. The excitation wavelength of the laser was 633 nm.

EDX spectra of coatings were collected at 5 kV, that of the glass substrate was collected at 15 kV. The average composition was determined from data collected from three different spots on the sample.

ICPMS was carried out on the solutions used to cure the waterglass films. These solutions were not diluted any further before the measurement. For dilute acid washing where only a few drops of the solution were used, after the allotted curing time the film and the washing acid were both submerged into deionised water and this water was used for the measurements. For measurement of the stock solutions one drop of each solution was added to 50 mL deionised water and mixed until homogeneous.

^{29}Si solid state NMR samples were prepared as follows. Waterglass stock solutions were decanted into a polystyrene dish and dried over cobalt chloride ($CoCl_2.2H_2O$) in a desiccator. The dried waterglass was ground to a powder followed by heating and washing with the same conditions as the films. This was necessary to produce the quantities needed for analysis (~ 100 mg).

XRD data was collected on the D8 Discover. The broad amorphous signal from the glass substrates was removed in processing.

Pencil scratch hardness tests were carried out with the Elcometer pencil hardness kit. The pencils (6B to 6H) were loaded into a weight, which was dragged across the sample. The tip of the pencil was dragged across the sample by the weight, with the pencil being increased in hardness until the surface was scratched. The durability was recorded as the maximum hardness the surface could withstand before being scratched.

Ellipsometry was used to determine the refractive index of the coatings and to deduce their film thickness. The Cauchy model was used to fit the experimental data and determine the refractive index and extinction coefficient of the cured potassium silicate films in the range 200 – 1000 nm.

UV-vis spectra were recorded on the Shimadzu UV-2600 with an integrating sphere attachment. Barium sulphate powder pressed into a plate was used as a reference for 100% diffuse reflectance.

3.4 Results and discussion

3.4.1 Chemical properties of spin coated waterglass films

The as-spin coated films were characterized with SEM, optical microscopy, ATR, XPS and XRD. For all samples either unheated or heated up to 500°C, no diffraction pattern was observed with XRD. When supported on glass they did not visibly change the transparency of the substrate. Raman spectra (633 nm excitation) of films supported on glass were all identical suggesting that the signal from the glass overwhelmed the signal from the films due to the penetration depth.

Table 3.3. Compositions of sodium and potassium silicate films supported on glass, as determined by EDX (5 kV) and XPS. EDX data of the glass substrates was also collected as 15 kV.

NaWG untreated

Element (Core Level)	XPS composition / at%	EDX composition / at%
O (1s)	59.1	64.5
Na (1s)	8.7	15.3
Si (2p)	32.2	20.2

KWG untreated

Element (Core Level)	XPS composition / at%	EDX composition / at%
O (1s)	54.7	64.9
Si (2p)	32.0	23.2
K (2p)	13.3	11.9

Glass

Element (Core Level)	XPS composition / at%	EDX composition / at% (15 kV)
O (1s)	54.3	58.8
Na (1s)	N/A	9.2
Mg (1s)	N/A	2.2
Al (2p)	N/A	0.6
Si (2p)	30.2	26.2
Ca (2p)	15.5	2.7

The composition of the films was determined with EDX and XPS, each featured only sodium or potassium as well as silicon and oxygen. KWG films featured more potassium at the surface than in bulk, whereas NaWG films featured less sodium at their surfaces than in bulk, however some of the bulk signal may have come from the glass substrates. EDX of the glass substrates showed the presence of 9.2 at% sodium, as well the additional network modifiers present in the substrate, magnesium, aluminium and calcium. Thus, the NaWG sodium signal may have been boosted somewhat by the substrate. EDX of the supported films was carried out at 5 kV to minimize the sampling depth. XPS of the glass microscope slide substrates detected only Ca, Si and O at the surface, suggesting that the other network modifiers are mainly in the bulk of the glass.

The ATR spectra of the films (**Figure 3.7**) on glass were distinctive from that of the glass substrates, however they feature the same infrared bands due to their similar chemical composition. The penetration depth (d_p) of the evanescent wave must also be taken into consideration.

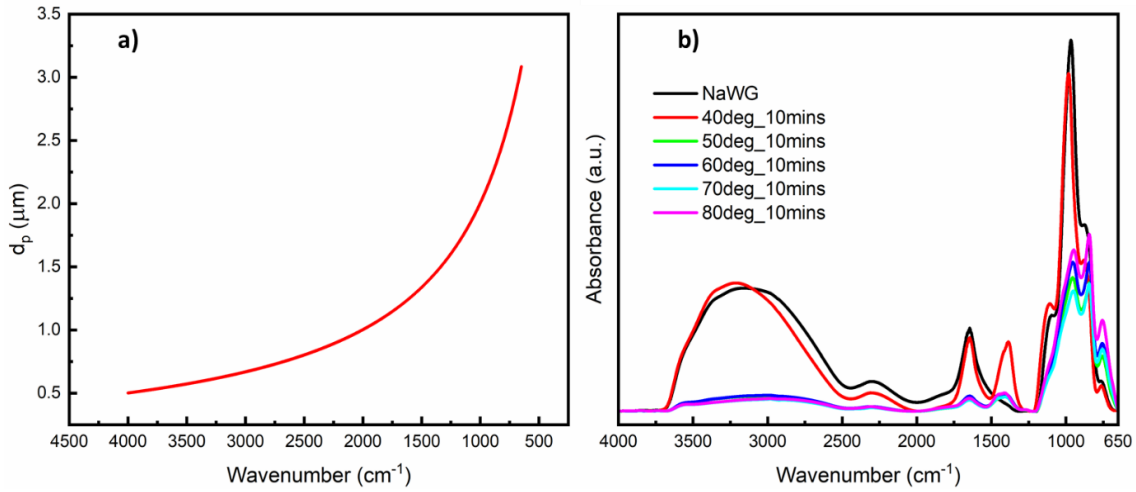

Figure 3.7. Penetration depth of the ATR beam as a function of wavelength a) and the change in the ATR spectrum of sodium silicate films supported on glass with temperature. As the film thickness is reduced, the spectrum features greater contribution from the substrate.

Due to their similar composition, both the glass and the supported films have a refractive index of ~ 1.5 in the visible region. The glass microscope slide substrates have a thickness of 1 mm, whereas the spin coated sodium and potassium waterglass films were 4.05 and 2.00 µm thick respectively, as determined by profilometry. The NaWG film thickness was thought to be greater due to the greater concentration and viscosity of its stock solution. The longest depth of penetration at 650 cm^{-1} was 3.08 µm, meaning that for NaWG, the signal comes only from the film. However, from 650 to 1000 cm^{-1}, the range in which the absorption of the BO and NBO bonds of the silicate attenuate the IR beam, the KWG ATR spectra features at most 1/3rd contribution from the glass substrate, decreasing to 0 as the wavenumber increases to 1000 cm^{-1}. Beyond this region the signal comes only from the film. The variation in d_p with wavenumber means that the signal from the substrate could not easily be subtracted from the combined film substrate spectrum.

The main feature of the ATR spectra was the ratio between the bridging oxygen and non-bridging oxygen peaks, which represents the SiO_2/M_2O ratio, where M = Na or K. For the glass substrate the NBO peak at 895 cm^{-1} is most intense, the neighbouring BO peak merges with the NBO peak at ~ 1060 cm^{-1}. The glass also features another peak at 758 cm^{-1} attributed to a BO bending mode. Both films feature a broad peak at ~ 3000 cm^{-1} and a narrower peak at 1640 cm^{-1}, the former is attributed to the convolution of hydrogen bonded and non-hydrogen bonded hydroxyls and molecular water bands, while the latter is attributed to absorbed molecular water only, as mentioned previously. According to Aguiar et al.[104] the formation of sol-gel glasses from cluster aggregation results in highly porous structures that can accommodate water molecules. The relative intensity of the water peaks was greater for NaWG, however signal contribution from the substrate may

supress the presence of water in the KWG film. Both films also feature a peak at ~ 2300 cm^{-1} from the O=C=O stretching of CO_2. The NaWG and KWG BO peaks were at 967 and 984 cm^{-1} respectively. Conversely the NaWG NBO peak (876 cm^{-1}) had a higher frequency than the 855 cm^{-1} BO peak of KWG. Both NaWG and KWG featured the BO bending mode at 755 and 759 cm^{-1} respectively. The BO/NBO ratios of the films after coating were 1.99 and 0.93 for NaWG and KWG respectively.

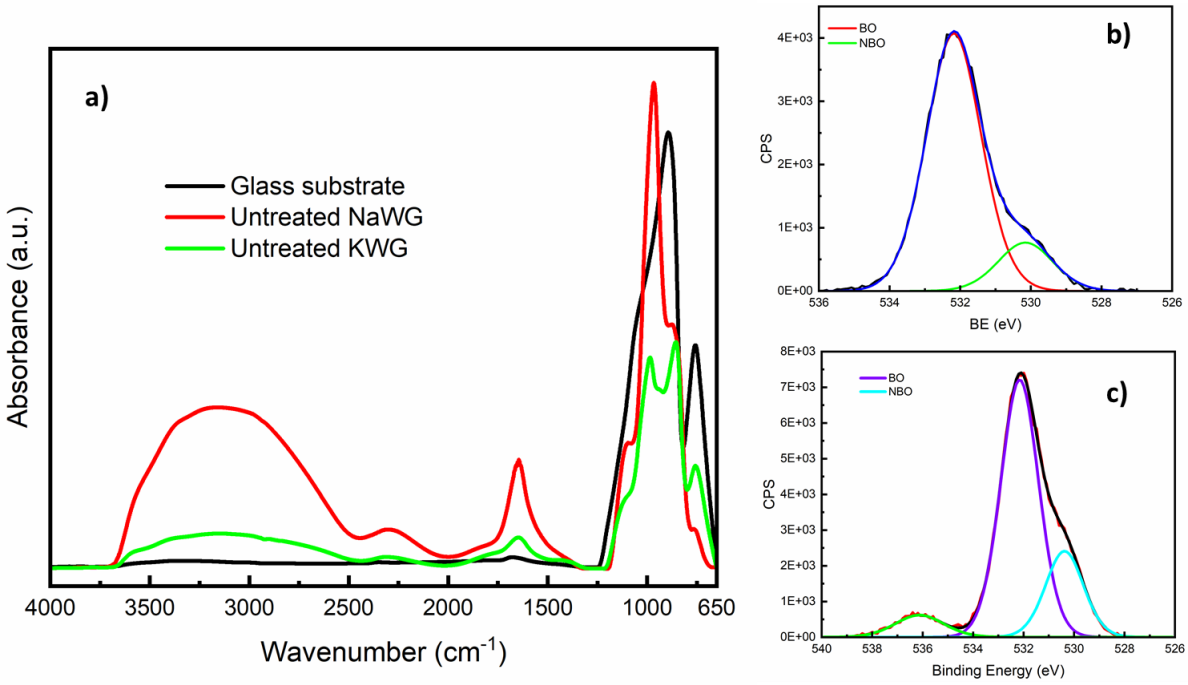

Figure 3.8. ATR spectra a) of the glass substrate and the supported sodium and potassium silicate films. The O 1s XPS spectra of b) KWG and c) NaWG are shown on the right.

The surfaces of spin coated waterglass films were analysed with XPS. The NaWG C 1s spectrum featured only adventitious carbon species. Its O 1s spectrum was deconvoluted with three environments with binding energies (BEs) of 530.4, 532.2 and 536.1 eV, attributed to silicate network NBO and BO and Na KLL[114] respectively. Their percentage intensities were 23.6, 70.4 and 6.0% respectively. The broad Auger peak was thought to be due to non-NBO associated sodium present at the surface. Na 1s and Si 2p environments show only a single peak (1071.4 and 102.4 eV respectively). KWG C 1s also showed only adventitious carbon species. K 2p1/2, K 2p3/2 and K 2s peaks were present with BEs of 293.1, 295.9 (Δ = 2.8 eV) and 377.8 eV respectively. The KWG O 1s spectrum was deconvoluted with two environments also attributed to NBO and BO (530.2 (15.8%) and 532.2 (84.2%) eV respectively). The Si 2p peak present in the as coated film had a binding energy of 102.5 eV. Referring to the work of Sprenger et al.,[111]

the Si 2p BEs of the as-spin coated films suggest that they were related to Q^3 species. The NBO BEs of both films implicate sodium and potassium ions bound to Q^3 silicon through a non-bridging oxygen.[111] O 1s spectra of both films were fitted with only one BO and NBO environment. Nesbitt et al.[112] expected FWHMs greater than ~ 1.25 ± 0.1 eV to indicate composite signal and multiple BO or NBO species, however the lack of asymmetry in these environments suggests that these fits are appropriate. Changes in BO or NBO FWHM after heating and washing will provide greater insight into the potentially broader distribution of species that may be present here at the surface.

3.4.2 Efflorescence of untreated waterglass films

After spin coating, efflorescence appeared on untreated NaWG and KWG films left in air in roughly 5 days and several hours respectively. NaWG films became translucent and were completely covered in crystals, whereas KWG films developed a wet appearance within hours and large crystals formed on the surface over time. Optical microscopy revealed the formation of crystals at the surface of NaWG films (**Figure 3.9**). Crystal formation occurred regardless of the thickness of the original coating, however it occurred much more slowly for very thick films, particularly those of sodium silicate, for example very thick drop casted NaWG featured extensive crystal formation, but only after several months, (**Figure 3.9 b)**). This may suggest a relationship between the evaporation of water from the coatings and efflorescence, namely that the latter only occurs after extensive evaporation. The wet appearance of untreated KWG films suggests the formation of deliquescent potassium carbonate rather than the merely hygroscopic bicarbonate.

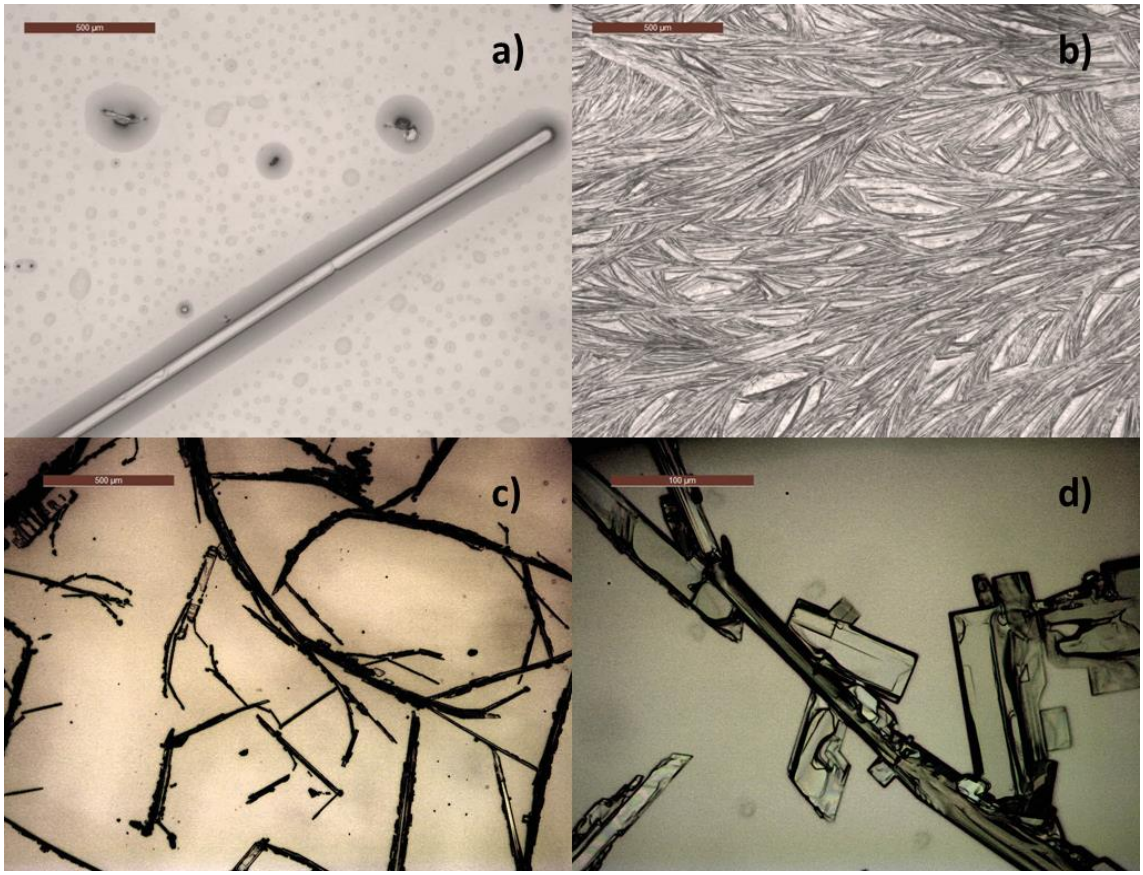

Figure 3.9. Optical microscope images of a) an aged potassium carbonate crystal growing out of the surface of a KWG film, b) shows the surface of an NaWG film after efflorescence has occurred. c) and d) show the more extensive growth of potassium carbonate crystals out of the surface after heating at magnifications of 500 and 100 µm respectively.

ATR spectra of both NaWG and KWG films (**Figure 3.10**) after the change in the appearance feature a peak at ~ 1380 cm^{-1}, attributed to the v_3 doubly degenerate asymmetric stretching vibration of the carbonate group.[116] In the spectrum of effloresced KWG films this band had two peaks at 1379 and 1373 cm^{-1}. The relative intensity of the carbonate peak was greater for NaWG than KWG, signifying its ubiquitous formation across the surface of untreated sodium silicate films. For both NaWG and KWG films, carbonate formation was accompanied by the diminishing of the BO and NBO peaks and the increase in the relative intensity of the convoluted water-silanol band around 3000 cm^{-1}. This may suggest that the formation of hydrated carbonate crystals.

XRD phase identification of the efflorescence crystals of both sodium and potassium silicates revealed them to be sesquicarbonates, a combination of carbonate and bicarbonate salts (**Figure 3.10 d)**). Raman spectra focused on the carbonate crystals showed peaks at 1058 and 1048 cm^{-1} for NaWG and KWG respectively.

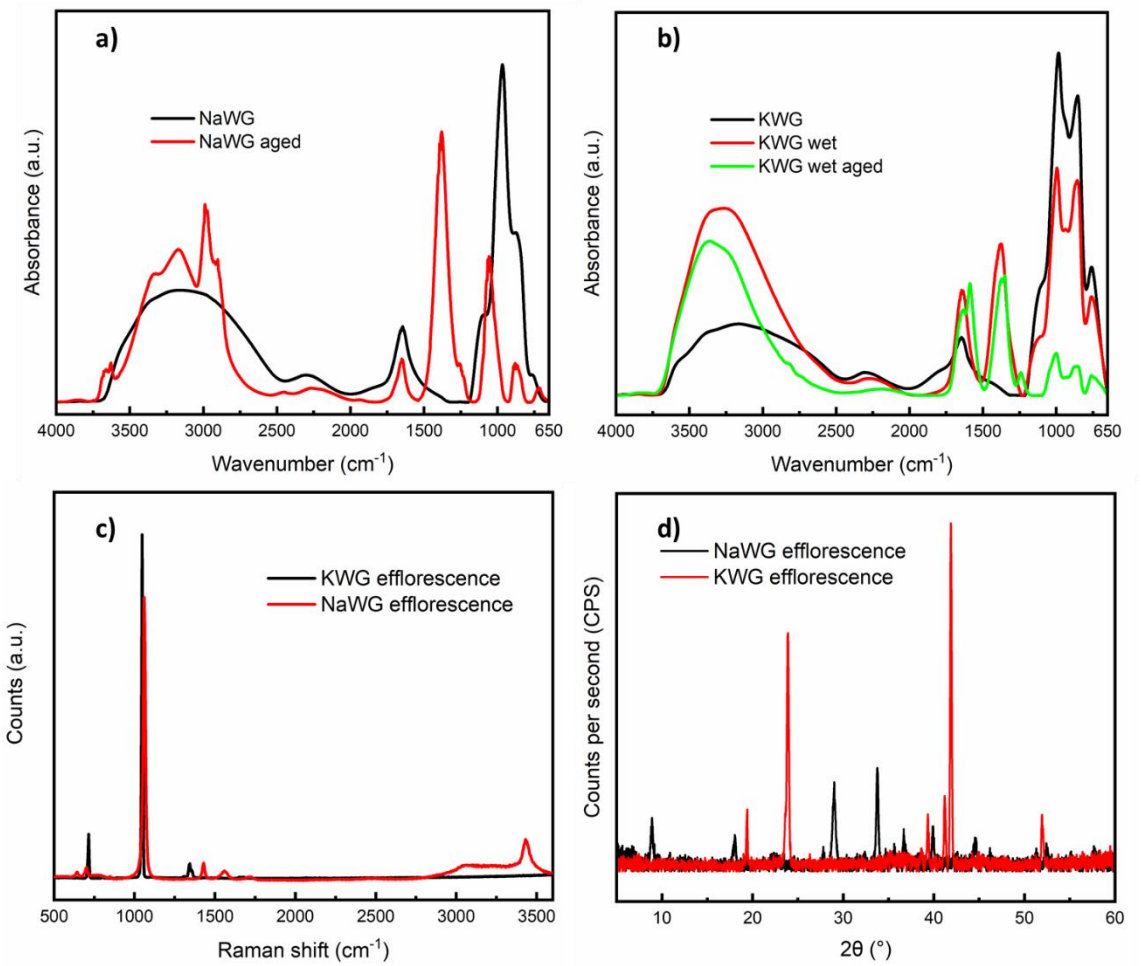

Figure 3.10. ATR spectra of a) NaWG and b) KWG films before and after efflorescence. In c) Raman spectra of the efflorescence crystals are shown, d) shows the XRD patterns of the crystals.

After efflorescence the C 1s and Na 1s environments (**Figure 3.11**) each show the presence of 3 peaks, the O1s spectra was deconvoluted with 5 peaks, whereas the Si2p peak was reduced almost to noise level and increased in BE to 102.6 eV suggesting that the carbonate species covered the silicate species at the surface.

Interestingly the shape and binding energies of the peaks deconvoluted from the KWG spectra (**Figure 3.11**) did not change after initial efflorescence or after the formation of the surface crystals. ATR data also showed that shortly after the efflorescence was visible, the silicate components of the film had greater relative intensity than the carbonate components. The EDX and XPS composition data (**Table 3.4**) show that the NaWG films contained significantly greater amounts of sodium and smaller amounts of silicon at the surface and bulk. The composition of the effloresced KWG samples was surprisingly similar to that of the initial, uneffloresced coating. Notably, samples left in a dessicator did not effloresce until removed from the dessicator, further indicating the effect of humidity on this process.

Table 3.4. The compositions of the effloresced KWG and NaWG coatings are shown. While the NaWG composition shows significantly more surface and bulk sodium and diminished silicon content, the KWG composition is similar to that of the freshly spin coated sample.

KWG efflorescence

Element (Core Level)	XPS composition / at%	EDX composition / at%
O (1s)	57.0	66.5
Si (2p)	32.5	21.6
K (2p)	10.6	11.8

NaWG efflorescence

Element (Core Level)	XPS composition / at%	EDX composition / at%
O (1s)	72.9	71.4
Na (1s)	18.9	25.0
Si (2p)	8.3	3.6

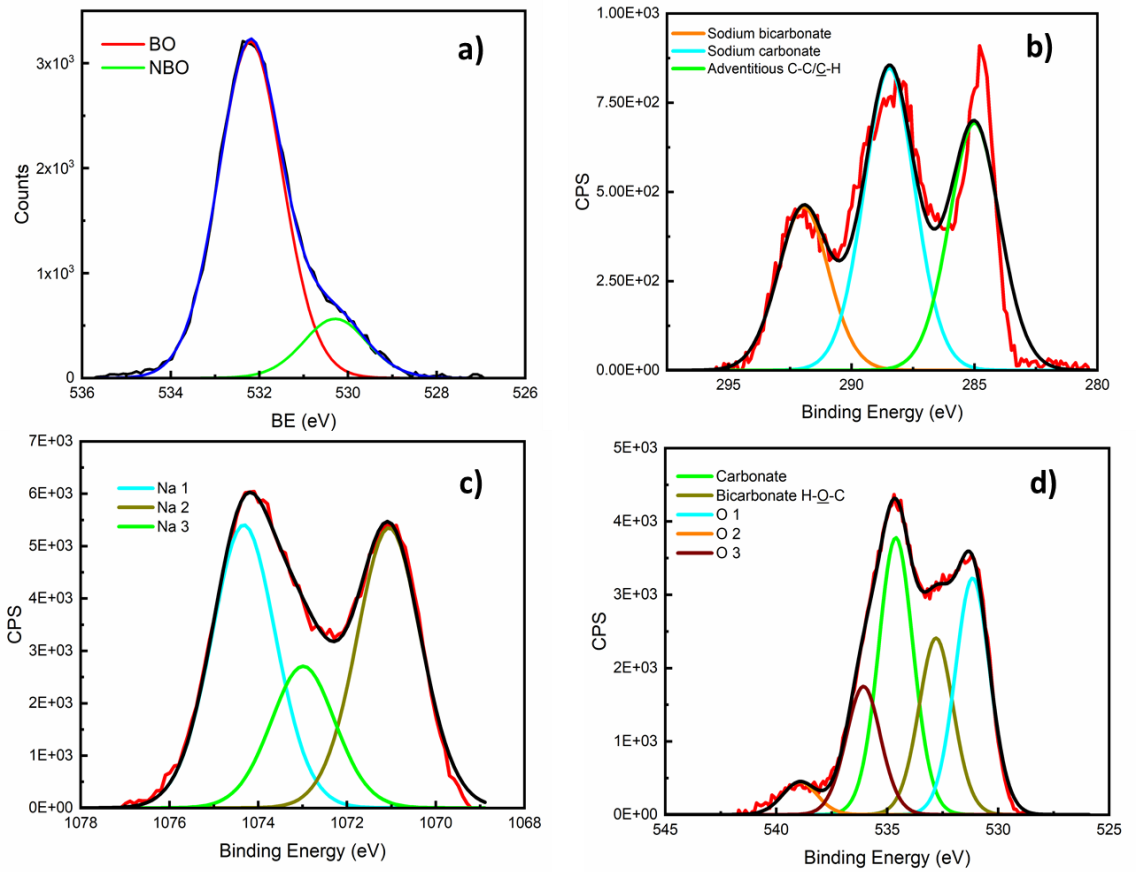

Figure 3.11. XPS spectra of effloresced films, a) KWG (O 1s), b) NaWG C 1s, c) NaWG Na 1s, d) NaWG O 1s. While the O 1s of the KWG samples did not change significantly upon efflorescence, the NaWG C 1s, O 1s and Na 1s regions developed several peaks likely corresponding to the oxidation states of the various carbonates formed.

3.4.3 Treatment of efflorescence

Heating alone did not stop efflorescence, films heated at low temperatures (< 200°C) changed appearance more rapidly, this heating resulted in KWG films developing crystals to a greater extent **(Figure 3.9 c) and d))**. This would suggest that the heating treatment enhances the rate of diffusion of alkali cations to the surface.

3.4.3.1 H_2O washing

After spin coating of waterglass solutions onto glass microscope slides, dried NaWG films were still water soluble and would redissolve upon submersion in deionised (DI) water, whereas KWG films were more stable in water, however after washing they would crack upon heating from room temperature to 50°C and some mass loss was still observed (**Table S3.1**). After drying, unheated KWG films were vulnerable to cracking. It was found that heating NaWG films to ≥ 120°C reduced their solubility in water, heating also improved the robustness of KWG films after washing.

Waterglass was spin coated and heated at 95°C or 120°C (KWG and NaWG respectively) for 15 minutes, films were washed separately in 50 mL DI H_2O for 1 to 30 minutes and dried with a Kimwipe. ATR spectra of the washed films were collected (**Figures 3.12 and 313**) as the water submersion time was increased.

Silica and silicates dissolve in aqueous environments through the hydrolysis of solixane bridges, which releases silicic acid and polysilicates into solution. This process is highly pH dependent.[88] Falcone has explained that the dissolution of dried soluble silicates and silicate glass in water is a two-step process whose rate depends on the modulus, concentration, impurities content, temperature and pressure and glass particle size. The first step is ion exchange:

$$Si - O \ldots Na + H_2O \rightarrow Si - OH + Na^+ + OH^- \quad (3.9)$$

Alkali cations are leached from the glass resulting in an increase in the pH of the solution, as the pH becomes > 9 the rate of the breaking down of BO bonds increases:

$$Si - O - Si + OH^- \rightarrow Si - O^- + Si - OH \quad (3.10)$$

If ion exchange does not generate sufficient hydroxide concentration, the breakdown of the silica network will not be extensive and mostly glass leaching will occur. Falcone also claims that Na^+ slows the rate of dissolution in sodium silicate glass as is hinders hydroxide nucleophilic attack. For potassium silicate glass, the rate of silica breakdown and removal depends on the rate of alkali leaching and not on the quantity of alkali removed. Smaller cations produce less soluble silicate glasses in the order $Li^+ < Na^+ < K^+$.[74] Contrarily, the faster dissolution of the NaWG films in water than KWG films indicates that the rate of alkali cation leaching was faster for sodium than potassium. It was mentioned in the introduction (section **3.2.4**) that in solution, dilution resulted in polymerization. Water submersion may have resulted in polymerization.

After heating, the waterglass film thickness was reduced through the evaporation of some residual water (~ 3000 and 1640 cm^{-1} bands decrease in intensity), KWG and NaWG films heated to 95°C or 120°C had thicknesses of 1.04 and 2.06 µm respectively, as determined with profilometry. KWG and NaWG ATR spectra contained significant contributions from the glass, from wavenumbers of ~1928 and 974 cm^{-1} respectively and lower. The effects of the reduced film thickness and d_p can be observed in the NaWG spectrum, which changes significantly after heating from room temperature to between 40 and 50°C, accompanied by a BO/NBO peak ratio decrease from 1.99 to 1.04. After heating to 95°C the BO/NBO ratio of the heated KWG film was reduced from 0.93 to 0.68. However, all films were heated to the same temperature were of similar thickness

so the glass contribution for each would be very similar, allowing interpretation of changes in the BO/NBO ratio.

ATR results of samples washed with different volumes of water show that after washing, the change in the ratio of BO and NBO peaks was roughly the same for any volume of water greater than or equal to 5 mL. Samples heated for 1-60 mins and overnight all had the similar intensity ratios after washing for 10 mins. This shows that with a volume of 5 mL or greater, only the water washing time influenced the BO/NBO ratio (**Figure S3.2**).

Films water content was not significantly changed with washing time as indicated by the ~3000 cm^{-1} and ~ 1640 cm^{-1} bands. **Figure 3.12** shows that initially the KWG NBO peak at 855 cm^{-1} was more intense than the 984 cm^{-1} BO (BO/NBO = 0.93). After 1 minute of water submersion a NBO shoulder peak emerged but its position could be clearly distinguished. After 6 minutes the BO/NBO intensity ratio was 1, further washing resulted in the intensity ratio becoming greater than 1, indicating that the BO peak relative intensity had become greater than that of the NBO peak. The ratio increased with further washing up to 1.30 after 30 minutes. Despite significant reduction in the Na or K content with washing, the NBO peak was not wholly reduced as the network modifiers of the glass still influenced the spectra due to the penetration depth of the ATR beam.

This change was also observed for NaWG films (**Figure 3.13**); the increase in the BO/NBO ratio of NaWG films was not sequential with increased washing time (1.21 and 2.09 for 1 and 30 minutes in water respectively), however there was a general decrease in the intensity of the NBO peak as washing time was increased. The reduction of NBO peak intensity suggests that alkali cations are being removed from the films, according to the equations of Falcone,[74] this should be accompanied by the formation of silanol groups on and within the film, however no associated ATR peak arises (~ 3000 cm^{-1} region). The intensity of the ATR silicate peaks (650 to 1250 cm^{-1}) after 30 minutes of water submersion was significantly lower for all peaks and compositions. It is likely that the rate of SiO_2 dissolution increased and becomes comparable to the alkali cation leaching rate for longer washing times.

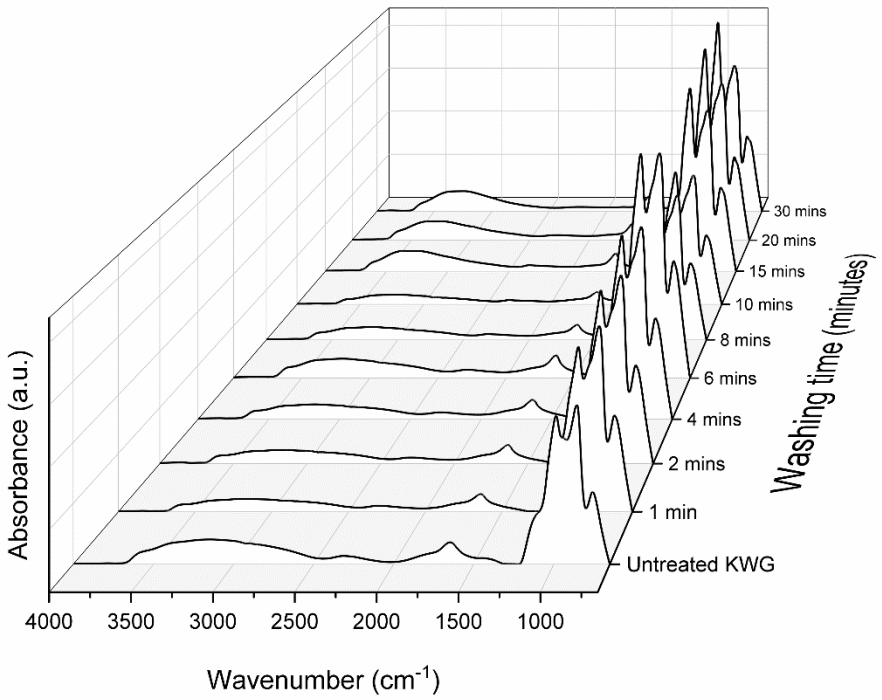

Figure 3.12. Change in the ATR spectrum of KWG films after heating at 95°C with varied water submersion times.

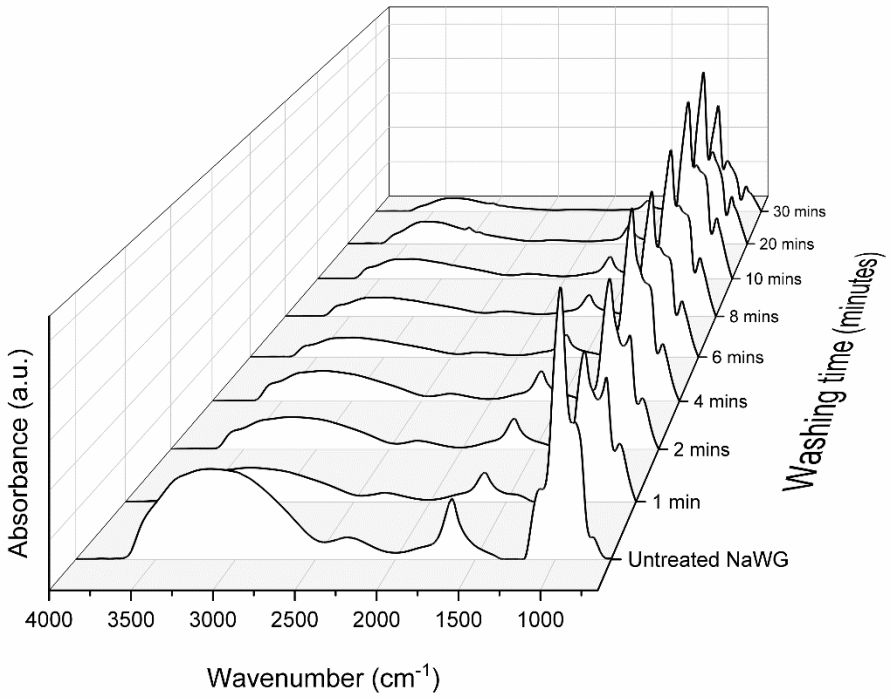

Figure 3.13. Change in the ATR spectrum of NaWG films after heating at 120°C with varied water submersion times.

As water submersion time increased, the percentage of sodium and potassium decreased in the respective films at both the surface and bulk as shown by XPS and EDX (**Figure 3.17**). After 30 minutes in deionised water the sodium content of the bulk and surface are reduced to 3 and 2 at% respectively, whereas potassium content in KWG films were both reduced to 2 at%. For KWG the reduction in potassium content was sequential with washing time, this was also the case for the bulk of NaWG films, however the surface sodium content initially increased before decreasing with further washing.

XPS of NaWG after heating was difficult to record due to its rapid efflorescence. Heated KWG effloresced more slowly, the sample showed a greater atomic percentage of potassium at the surface (25.4 at%) than the untreated film (13.3 at%). The deconvoluted O 1s spectrum of this sample showed NBO and BO environments at 530.6 and 532.2 eV. NBO had a greater relative intensity (19.9%) than in the untreated sample, further suggesting that heating increased the alkali cation content at the surface.

Inspection of the films with optical microscopy shows crystal formation on NaWG after water washing. Despite this, XRD found them to be amorphous (**Figure S3.3**). The XPS composition data also gives no suggestion of such changes at the surface. No crystal formation was observed at the surface of washed KWG, likely due to much higher solubility of carbonate formed.

The NaWG surface crystals grew slightly as water submersion time was increased. Binding energies of the Na 1s and Si 2p core levels increased sequentially with washing time from their positions in the untreated films, after 30 minutes they were 1072.1 eV and 103.2 eV respectively. O 1s spectra (**Figure 3.14**) of all water washed films were deconvoluted BO and NBO, showing that not all sodium was removed from the surface by washing with water. After 1 minute in water the NBO BE and relative peak intensity were greater than in the untreated film (530.9 eV, 38.4%), the BO relative intensity was reduced but its BE was not significantly increased (532.3 eV, 54.3%). The Na KLL relative peak intensity increased after 1 min of water washing to 7.3%, its BE decreased insignificantly to 535.9 eV. After 10 and 30 minutes in water, the NBO relative intensity was decreased to 8.4 and 4.1% respectively, while the BE was reduced to 530.3 eV. The BO peak increased in BE to 532.6 eV (95.9%) after 30 minutes. After 10 minutes in water the Na KLL peak decreased in intensity but increased in BE (536.6 eV, 2.2%), this peak was reduced to noise level after 30 mins in water. According to Sprenger et al.,[111] the increase in the Si 2p and O 1s BEs would be associated with increased connectivity,

rather than the expected network breakdown. C 1s showed only adventitious species before and after washing with water.

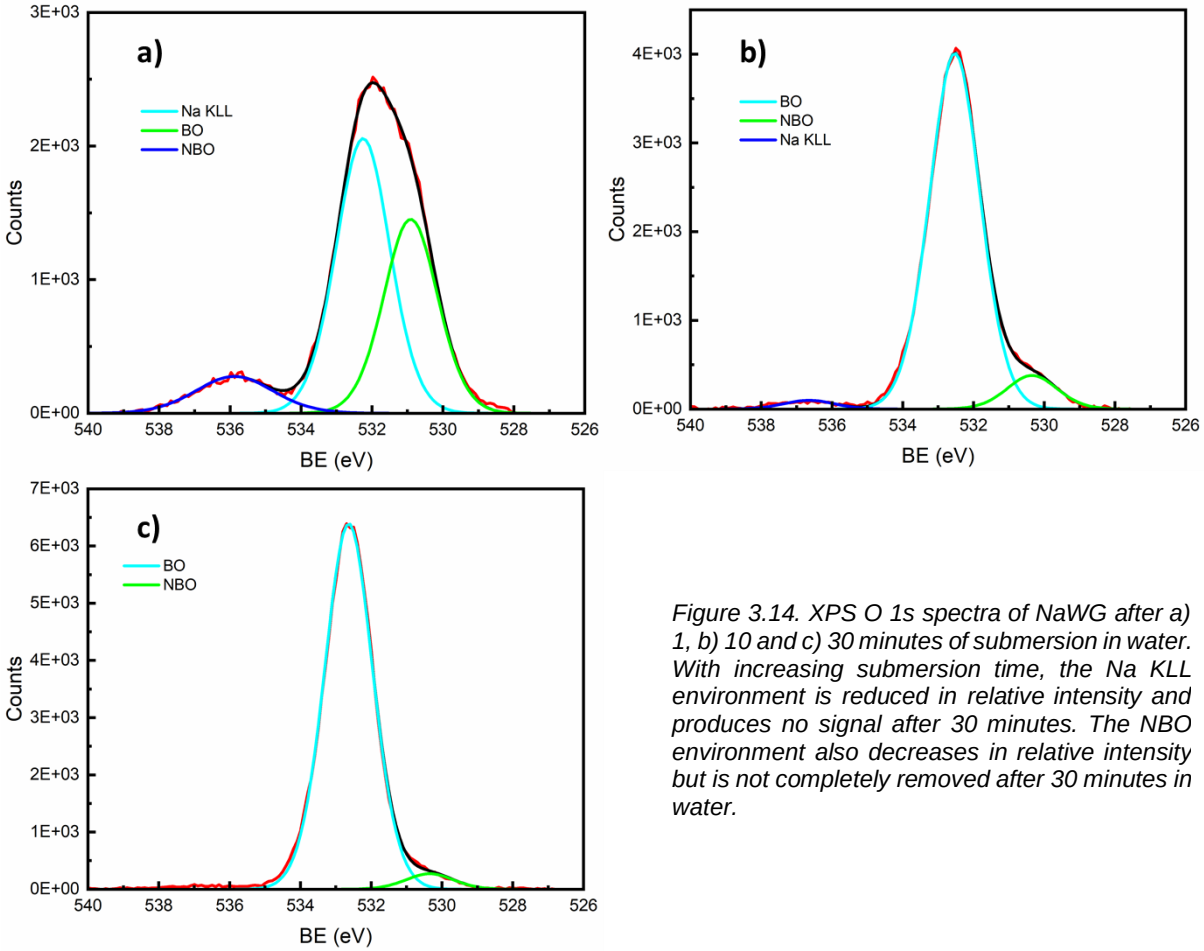

Figure 3.14. XPS O 1s spectra of NaWG after a) 1, b) 10 and c) 30 minutes of submersion in water. With increasing submersion time, the Na KLL environment is reduced in relative intensity and produces no signal after 30 minutes. The NBO environment also decreases in relative intensity but is not completely removed after 30 minutes in water.

Binding energies of KWG XPS core levels were generally greater after washing. K 2p1/2, K 2p3/2 BEs increased to 293.6, 296.4 eV, while the Si 2p BE increased to 103.0 eV. The O 1s spectra of water washed KWG films were also deconvoluted with both BO and NBO peaks with higher BEs of 530.2 and 532.4 eV. The NBO relative peak intensity decreased from 15.8 to 7.4% after heating and 1 minute in water, its intensity further decreased to 3.8% after 30 minutes in water. The K 2s spectra decreased significantly in intensity and increased in energy to 378.2 eV. Water washed KWG showed only adventitious C 1s species. The increases in O 1s BE with washing time were not significant (**Figure S3.4**), however the increased Si 2p BE could suggest greater connectivity.

The ATR spectra of the films washed with water were recorded after several weeks (**Figure S3.5**). NaWG films washed for 6 minutes or less developed a noticeable carbonate peak. Composition at the surface did not change significantly after water washing NaWG samples for 8 minutes or greater. All aged KWG samples contained a

small peak at the carbonate wavenumber (1640 cm^{-1}), regardless of washing time. However, none of the KWG samples changed in appearance despite the emergence of the carbonate peak.

3.4.3.2 Acid washing

In aqueous acidic media polymerization is expected to proceed through silanol condensation.

$$Si - OH \leftrightarrow Si - O^- + H^+ \quad (3.11)$$

$$Si - O^- + Si - OH \leftrightarrow Si - O - Si + OH^- \quad (3.12)$$

Condensation is most favourable at pH values equal to the pK_a of the available silanol groups. As pH increases above 10, the rate of the reverse, depolymerization reaction (k_{-2}) becomes significant. At very low pH values the acidic environment has a catalytic influence on the polymerization.[74]

Washing the heated waterglass films with 12 drops of drop casted 0.5M H_2SO_4 resulted in a rapid change in the BO and NBO peak intensity (**Figure 3.15**). After only 1 minute the KWG BO/NBO intensity ratio was increased from 0.68 after heating at 95°C to 1.34, which was greater than after 30 mins in water. The ratio decreased to 1.26 after 30 mins. The BO and NBO band wavenumbers increased to 1033 and 891 cm^{-1} after 1 minute, they did not significantly change with further washing. NaWG films saw an increase in BO/NBO ratio from 0.67 after 120°C heating to 1.67 after 1 minute in acid, and a further increase to 1.73 after 30 minutes. Both BO and NBO bands were blue-shifted to 1024 and 895 cm^{-1} after 1 minute in acid. After 30 mins the BO band position was unchanged but the NBO band had increased to 899 cm^{-1}. The aqueous acid washed films retained signal from the water peaks at ~ 3000 and ~ 1640 cm^{-1}. The intensity of the 650 to 1250 cm^{-1} silicate bands decreased with washing time, perhaps due to dissolution of some of the silica and hence a decrease in their concentration.

The XPS signal of the alkali cation core levels (K 2p, K 2s, Na 1s) of the films was reduced to noise level after only 1 minute of washing. EDX detected the presence of sodium in NaWG and KWG films even after 30 minutes of washing, however the amounts detected were similar for KWG and NaWG films suggesting that any remaining sodium was from the glass substrates (**Figure 3.17**). EDX spectra of the glass substrates collected at 15 kV show 9.2% sodium and negligible (0.2%) potassium as part of the glass composition.

After 1 minute in acid the BE of the NaWG Si 2p peak increased significantly from 102.4 to 103.1 eV and the NBO peak of the O 1s spectra was no longer present (**Figure 3.16 a)**), accompanied by an increase in energy of the BO peak from 532.2 to 532.6 eV. The C 1s spectrum showed only adventitious species. Further washing did not result in any further change in the number of peaks or their BE.

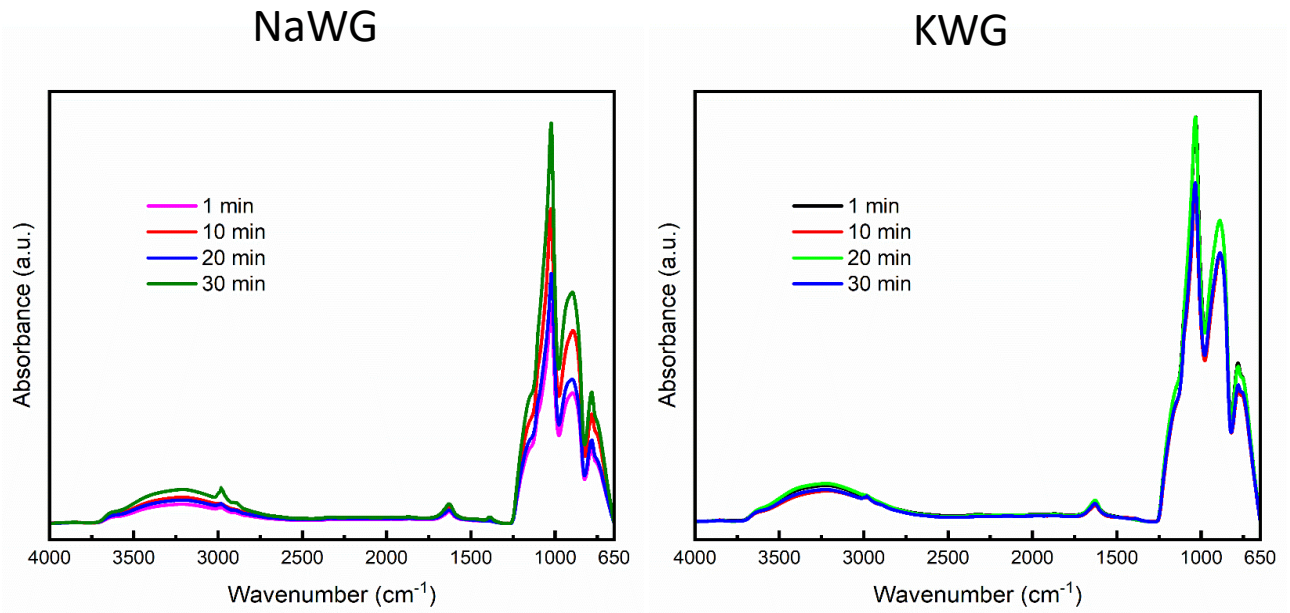

Figure 3.15. ATR spectra of NaWG and KWG films after washing with acid for 1, 10, 20 or 30 minutes. Even after 1 minute in acid, films of both compositions underwent a significant reduction in NBO peak intensity.

Similarly, for KWG films washed with acid for 1 min, the NBO peak of the O 1s spectrum was no longer present (**Figure 3.16 b)**). The Si 2p peak and O 1s BO peaks increased in BE from 102.5 and 532.2 eV to 103.2 and 532.8 eV respectively and did not change upon further washing. The C 1s spectra showed only adventitious species. The increases in Si 2p and O 1s BE indicate an increase in connectivity of the silicate units after aqueous acid submersion.

As previously mentioned, d_p was greater than the film thickness, which explains why the ATR spectra did not show complete removal of all NBO species even after acid treatment despite the absence of surface cations.

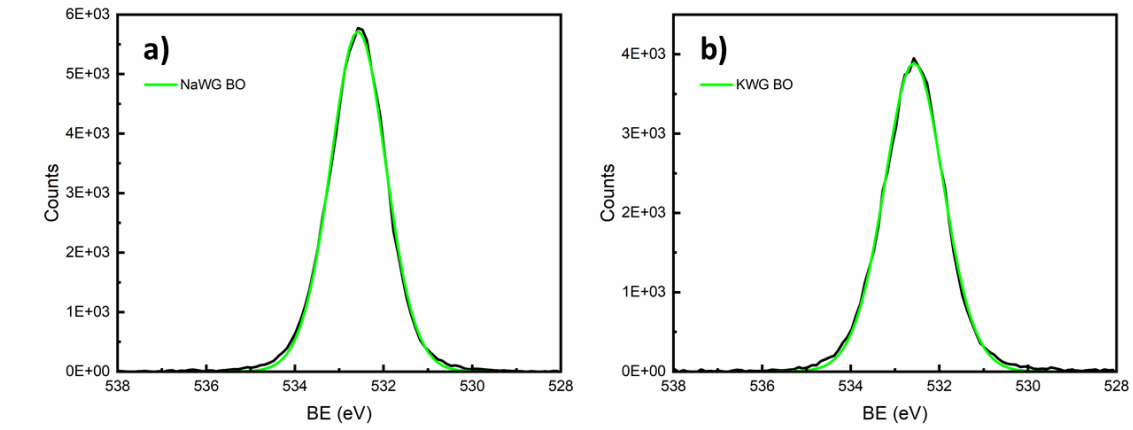

Figure 3.16. XPS O 1s spectra of a) NaWG and b) KWG after washing with acid for 1 minute. Even after 1 minute in acid, films of both compositions lost all NBO trace at their surfaces.

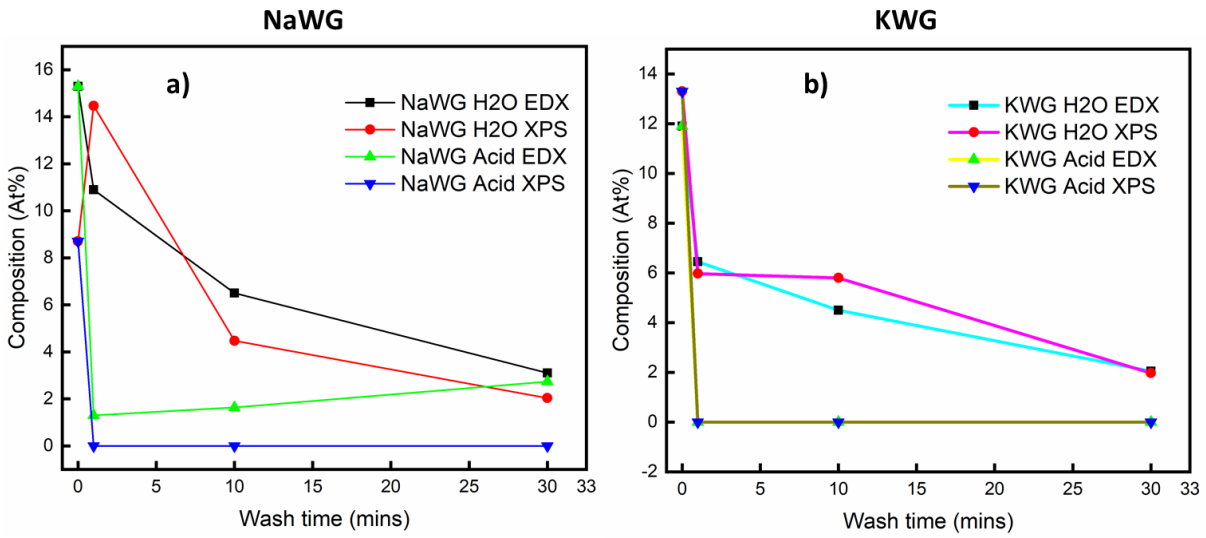

Figure 3.17. Changes in the Na and K composition of a) NaWG and b) KWG films respectively before and after washing with water or acid, as determined by XPS and EDX. After 1 minute in acid the cation content was reduced to noise level, however some Na remained in the bulk of NaWG. After 10 minutes in water the cation content of films of both compositions was reduced to less than half its original value, complete cation removal was not achieved at either surface or in the bulk of the films.

3.4.3.3 Film structure and washing mechanism

The trends in the spectroscopy data implicated various changes taking place in the chemical structure of the films upon washing with acid or water. The binding energy of the O 1s bridging oxygen and Si 2p peaks increased with washing time (**Figure 3.18**). An increase in binding energy is associated with an increase in oxidation state i.e. reduction.

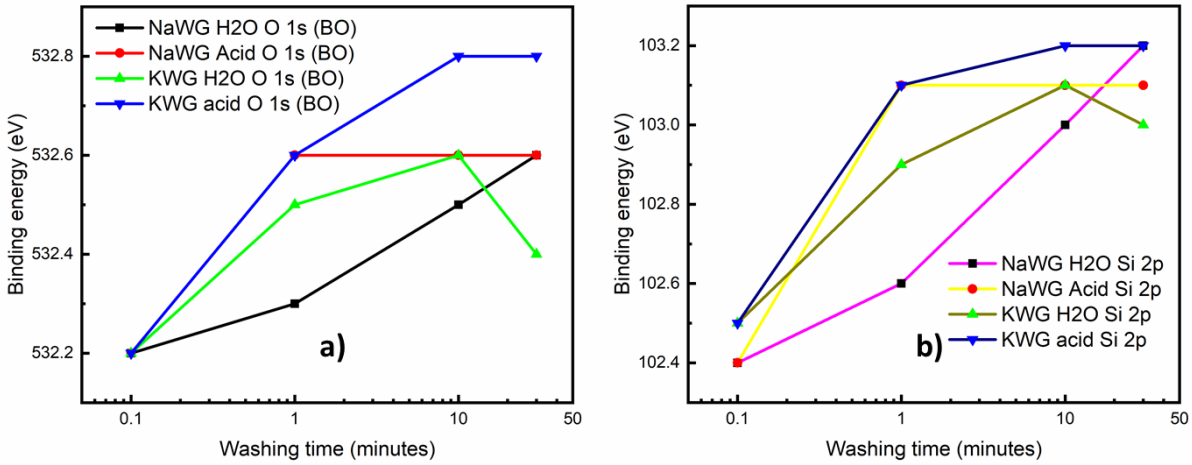

Figure 3.18. Changes in the binding energy of the O 1s (bridging oxygen) and Si 2p core levels with washing time in water or acid. The binding energy and hence oxidation state of the O 1s and Si 2p peaks generally increased with washing time.

XPS alkali cation and NBO peak reduction in water and removal in aqueous acid showed the ion exchange of alkali cations at the surface of the films with the solutions resulting in the formation of hydroxyls, the EDX data also showed a reduced alkali cation content implying that this change happened at greater depths in both NaWG and KWG films.

The O 1s FWHM of deconvoluted BO and NBO components in the untreated samples was 1.8 eV for both NaWG and KWG. This was reduced to 1.6 eV after 30 minutes in water and 1.5 eV after 1 minute in acid, potentially suggesting a reduction in the distribution of types of BO and NBO units present, with a greater change occurring in the acid washed samples. Likewise, the initial Si 2p FWHMs of 1.9 and 2.0 eV for NaWG and KWG respectively were both reduced to 1.6 eV after 30 minutes in water, and to 1.5 and 1.7 eV after 1 minute in acid.

After washing, the relative intensity of the BO and NBO bands in the ATR spectra of the films increased and decreased respectively. ATR data showed an increase in the frequency of the peaks associated with BO and NBO species as the washing time increased. Decreases in the asymmetric stretching frequency have been attributed to a

decrease in the $\theta_{Si\text{-}O\text{-}Si}$ bond angle.[106] The decrease in this bond angle is associated with an increase (positive) in the chemical shift, which in turn is associated with the depolymerization of Q^n units.

As stated in section **3.2.4.6**, certain authors have correlated increases in band position with increasing Q^n in solution[81] and in the solid state.[110,127] In this work, the BO band wavenumber increased from 967 and 984 cm^{-1} to 1024 and 1035 cm^{-1} for NaWG and KWG respectively after washing in aqueous acid. The NBO (2NBO, Q^2) peak wavenumber also increased with the washing time from 876 and 855 cm^{-1} to 899 and 887 cm^{-1} respectively. These authors suggested that increasing the connectivity present in the sample increases the band frequency.

However, the dispersion analysis of Macdonald et al.[105] did not find a clear relationship between network modifier content and changes in band position. Amma et al.[109] have shown that changes in the ATR peak position upon leaching of the surface of glass with acid could be due to the sensitivity of the ATR method to the dispersion of light in the IR region. They imply that changes in band position (~ 990 to 1010 cm^{-1}) could be affected by refractive index modulation of the glass after acid leaching.[109] The magnitude of the change in band frequency observed here was greater, implying more significant changes to the bond angles and lengths in the glass and so the alteration of composition may have been more significant than in their experiments. Intensities of the ATR peaks also changed significantly due to changes in composition. Further characterization is needed to verify the nature of the changes occurring in the films upon washing.

ICPMS was carried out (**Table 3.5**) on the water or aqueous acid solutions after washing to compare their alkali cation content with that of the starting solutions.

Table 3.5. ICPMS data for washing samples compared with that of the diluted stock solutions and deionised water.

Sample	Na / ppb	K / ppb
Water	1193	68
KWG diluted	1782	75606
KWG unheated H2O 10 mins	1298	5452
KWG 95deg 1 min H2O	1264	5208
KWG 1 min acid	2039	6846
NaWG diluted	83735	598
NaWG untreated	10435	187
NaWG 120 deg 1 min H2O	9091	125
NaWG 1 min acid	10530	319

Table 3.5 shows that the alkali cation content of the water is greater after washing, confirming that the alkali cations are exchanged into the solution after washing with water or aqueous acid.

^{29}Si solid state NMR (**Figure 3.19**) was carried out on powder versions of the silicates to observe the change in connectivity of the samples before and after heating and washing, with the same conditions used to stabilise the films. It was expected that removal of alkali cations upon washing would coincide with silicate condensation resulting in an increase in higher connectivity (Q^3 and Q^4) silicon species after washing in acid, whereas some polymer network breakdown or polymerization was expected to have occurred in samples submerged in water. All samples showed slightly overlapping signals for species with Q^2, Q^3, and Q^4 connectivity (-87, -95, -106 ppm). The Q^2/Q^4 intensity ratios in the dried NaWG and KWG samples were 1.83 and 2.77 respectively. The largest peak in all samples is from the Q^3 signal indicating that all samples are significantly polymerized upon drying, we acknowledge that the rate of drying and therefore degree of connectivity may be different with spin coated films.

Heated samples showed a small increase in the intensity of the Q^2 signal, in NaWG the Q^4 signal increased upon heating, whereas it did not change significantly in intensity in KWG (Q^2/Q^4 ratios 2.03 and 2.59 for NaWG and KWG respectively). Washing NaWG with water marginally decreased the Q^2 signal and increased the Q^4 signal back to the intensities observed in the untreated powder. Water washed KWG showed a significant decrease in Q^2 intensity and a slight increase in Q^4 intensity (Q^2/Q^4 ratios 1.80 and 2.46 for NaWG and KWG respectively). For both samples, washing with acid significantly increased Q^4 intensity at the expense of the Q^2 signal. The Q^2/Q^4 intensity ratios for NaWG and KWG after acid washing were 1.02 and 1.19 respectively. The NMR spectra of the acid washed samples were shifted upfield relative to the other samples, observed by a roughly -1 ppm shift in the Q^3 peak, indicative of a greater shielding and hence connectivity in these samples.

Heating samples appears to have marginally decreased their connectivity, whereas washing in water slightly increased their connectivity and washing in aqueous acid greatly increased their connectivity. This also gives insight into the structure of the films after heating and acid washing. Silicate clusters with Q^2 to Q^4 connectivity, (primarily Q^3), grouped together through consolidation during drying.

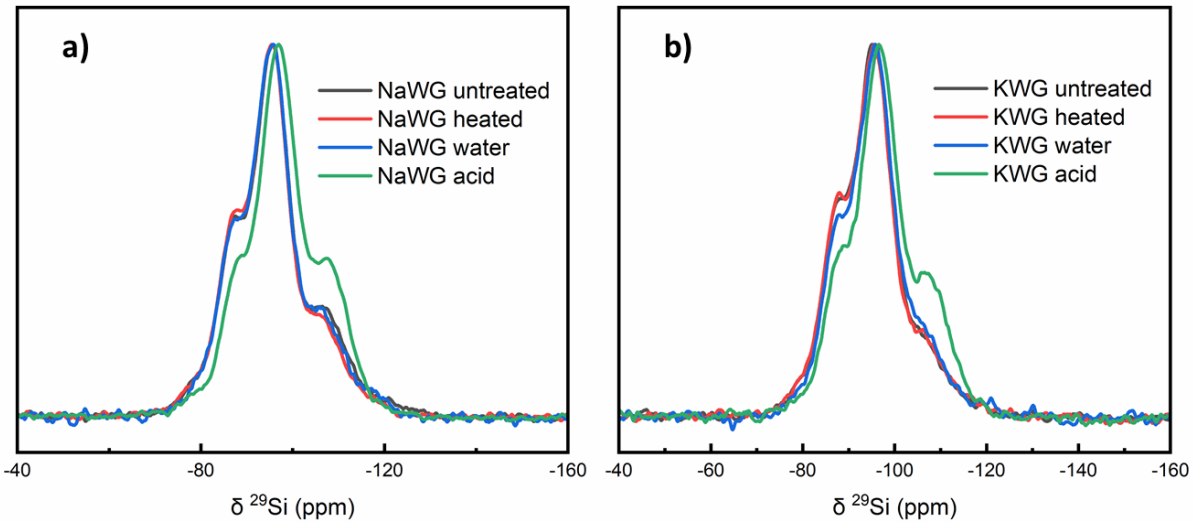

Figure 3.19. Solid-state ^{29}Si NMR of a) NaWG and b) KWG silicate samples. Washing the powder samples with acid resulted in a change in the connectivity of the samples, namely an increase in Q^4 (~ -106 ppm) species and a decrease in Q^2 (~ -88.0 ppm) species. Most of the silicate exhibited Q^3 (~ -95.0 ppm) connectivity.

The removal of alkali cations, the increase in band frequency and decrease in intensity of NBO bands all coincide with the increase in the connectivity of the waterglass films upon washing. In all washed samples the connectivity was increased. The increase in band frequency observed in ATR therefore could be at least correlated with an increase in connectivity, although it may be one of several attributing factors.

3.4.3.4 Higher temperature heating and water removal

To maximise the durability of the films, it may be necessary to heat them more to reach the glass transition temperature. According to the DSC study by Roggendorf et al.,[95] heating between 116 and 288°C was needed to achieve the glass transition. This glassy state can be achieved with drop casting and air drying, but this method does not offer strict control over the film thickness.

Profilometry in **Table 3.6** shows that there was no significant further reduction in film thickness after heating the waterglass films to higher temperatures. After heating to around 100°C the KWG film thickness was stable, the NaWG film thickness continued to decrease up to 500°C.

Table 3.6. Film thicknesses of samples with increasing temperature as measured with profilometry.

Temperature / °C	Thickness / µm	
	NaWG	KWG
Unheated	4.05	2.00
95	-	1.04
120	2.06	0.97
200	1.70	0.96
300	1.75	1.02
400	1.59	0.99
500	1.43	0.96

The surface composition of all films revealed complete sodium or potassium removal except for NaWG heated to 200°C, which still contained 0.5 at% sodium but showed no NBO or Na KLL in its O 1s spectrum. The average O/Si ratio at the surface was ~ 1.4 for both compositions. EDX (5 kV) of heated films also reveal only Si and O present.

With increasing temperature, the intensity of the convoluted 2500 to 3200 cm^{-1} band decreased, indicating a decrease in water present (**Figure 3.20**). The 3000 cm^{-1} bands in KWG films decreased significantly after heating to 200°C and did not decrease in intensity with further heating. 1640 cm^{-1} band continues to flatten up to 500°C. In NaWG films both H_2O related regions were flattened after heating to 200°C, and no significant changes were observed with further heating. Weldes et al.[75] have stated that drying of sodium silicate coatings is more extensive that those of potassium silicate with a similar composition. Water retention is also directly related to the alkalinity, higher modulus waterglass retains less water.

The samples heated to higher temperatures have reduced thickness and therefore the ATR evanescent wave will have a greater contribution from the glass. As shown in **Table 3.6** the minimum film thickness of the NaWG and KWG films was 1.43 and 0.96 µm respectively, meaning that the wavenumber below which the glass will contribute to the spectrum is 1403 and 2089 cm^{-1}.

In the ATR spectra of all KWG samples heated to ≤ 300°C, the NBO intensity was significantly greater than that of BO, with no change in the band position (**Figure 3.20 a)**). When heated to 400°C the peaks are of a similar intensity and at 500°C the peaks merge, likely due to an increasing contribution of signal from the glass in the 650 to 1250 cm^{-1} silicate region as the film thickness was reduced below the minimum penetration depth for this region with is ~ 1.60 µm. This effect is more significant for NaWG films (**Figure 3.20 b)**) as KWG film thickness was already well below this limit after heating to 95°C, films heated beyond this temperature did not decrease significantly in thickness so the substrate contribution for all these samples is similar. For NaWG films the NBO peak is still more intense than the BO peak but the difference is less significant, the peaks also merge at 500°C.

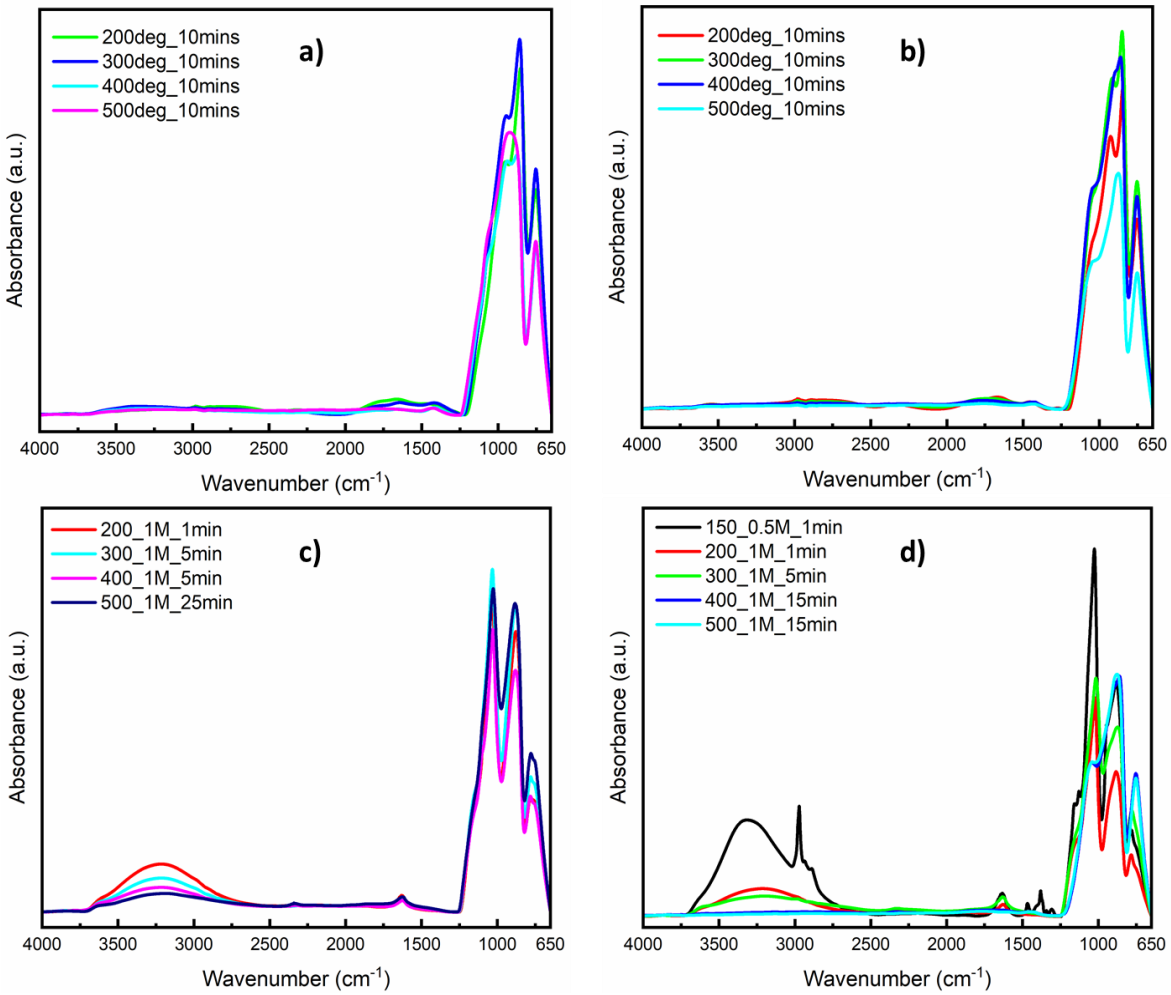

Figure 3.20. ATR spectra of heated a) KWG and b) NaWG and heated, acid washed c) KWG and d) NaWG. Heating alone did affect the peak shape, but did not change the NBO relative peak intensity. After washing all samples except NaWG heated to 500°C underwent a significant reduction in NBO relative peak intensity. The merging of the BO and NBO peaks in the 500°C sample was expected to be due to fusion with the substrate.

More concentrated acid was needed to ensure rapid removal of the alkali cations. This was confirmed qualitatively with ATR. Particularly in KWG samples (**Figure 3.20 c)**) the switch in peak intensity ratio was observed upon curing. The switch in the relative intensities of the BO and NBO peaks washed with 1M H_2SO_4 was observed in 1 minute for 200°C heated KWG, in 5 minutes for 300 and 400°C heated KWG and in 25 minutes for 500°C heated KWG. For NaWG heated at 150°C 0.5M acid could cure the film in 1 minute, 200°C heated NaWG required 1 minute in 1M acid. 300 and 400°C required 5 minutes of 1M acid washing (**Figure 3.20 d)**). The switch in peak intensity ratios was not observed for NaWG heated to 400 and 500°C even after lengthy washing in 1M acid, this was thought to be due to both signal from the glass overwhelming the signal from the samples cured at these higher temperatures.

In the XPS spectra of both NaWG and KWG samples heated at higher temperatures and washed as specified above, the O 1s peak had shifted from 532.2 eV to BEs of 532.6 to 532.8 eV after curing, only BO was present. The FWHM also decreased from 1.8 to 1.4 or 1.5 eV. The Si 2p peak increased from 102.4 eV to between 103.1 to 103.3 eV, with FWHM being reduced from 1.9 to 1.5 eV. No signal was present in the alkali cation core levels. These films exhibit the same curing trends as those treated at low temperatures.

In ATR of the heated samples the position of the NBO shoulder peak can be clearly resolved. This peak was around 940 cm^{-1} and was attributed to an NBO band of higher connectivity.[104]

3.4.4 Physical and optical properties

Films were more fragile after longer washing when heated at these temperatures, making them more prone to cracking upon reheating and when placed in a vacuum. Films washed for > 20 minutes in water or acid tend to crack upon drying. Films washed with 0.5M H_2SO_4 for as little as one-minute crack upon reheating (from 25 to 50°C). This would suggest that porosity is present in the films creating and is either created by washing or present beforehand.

Unheated KWG films and heated KWG and NaWG films would crack upon drying after lengthy washing times. This was thought to be due to evaporation induced capillary pressure in the pores of the film.

3.4.4.1 Durability

Before heat treatment, films produced by spin coating were softer than those produced by air drying. This is possibly due to the lack of rearrangement that takes place in the films upon rapid drying that occurs with spin coating. Analogous to the heat treatment of glass, in which the glass is melted and then held at a temperature just above the glass transition temperature to allow structural relaxation before quenching, slow drying of

waterglass coatings could enable thorough densification. Mass loss of a drop casted, air dried sodium waterglass film was observed with time in comparison to that of a spin coated film. After spin coating, film mass decreased slightly and then remained constant after drying overnight (0.0002 g mass loss, 4.9%), whereas drop casted film mass continued to decrease overnight (0.0382 g mass loss, 52.0%) (**Table S3.6**).

Heating was required to densify the films. The change in durability with heating temperature was determined via pencil hardness test (**Table 3.7**). The maximum of 6H hardness was attainable with both NaWG and KWG films, for both compositions heating for ~ 20 minutes above 200°C was sufficient to obtain this hardness.

All coatings were unaffected by Scotch tape tests, surprisingly even the cracked KWG films cured without heating.

Table 3.7. The variation in scratch hardness of the coatings with hotplate curing temperature was measured with the pencil hardness test. For both NaWG and KWG compositions, heating over 200°C was sufficient for maximum hardness.

Temperature / °C	Scratch hardness	
	NaWG	KWG
0	N/A	N/A
95	N/A	4H
120	5H	3H
200	5H	6H
300	6H	5H
400	6H	6H
500	6H	6H

3.4.4.2 Film thickness control and complex refractive index

Ellipsometry was used to determine the refractive index of the coatings, the Cauchy model was used to fit the experimental data. As with glass and silica, the refractive index was determined to be 1.49 (at 550 nm, **Figure S3.7**). Spin and dip coated samples were made and the relationship between the coating speed, concentration and film thickness was observed. All films were heated at 150°C for 20 minutes and washed with 1M H_2SO_4 for 1 minute.

The film thickness of spin coated films decreased with increasing speed (**Figure 3.21 b)**), the linear inverse relationship held as the concentration of the solutions was decreased. However, below a concentration corresponding to 60% KWG dilution (17.3 wt% solids content), the coated films would no longer cover the entire substrate, limiting the films to ~ 200 nm thickness by this method. Dip coated samples (**Figure 3.21 a)**) produced the expected parabolic relationship, corresponding to speeds dominated by capillary, intermediate and viscous drag forces. Even solutions as dilute as 10% KWG (2.9 wt% solids content) could be dip coated, films as thin as 10 nm could be produced. Films made from dip coating concentrated solutions cracked during curing, particularly after washing with acid. Strangely, dip coating concentrated solutions in the intermediate or capillary region resulted in highly foamed and distorted coatings, bubbles could visibly be seen forming on the substrate in solution under these conditions. Minimum film thickness shifted to lower speeds as the concentration was decreased. For dip coating speeds below 5 mm/min, pinholes were observed in the films. These are likely formed due to evaporative cooling effects. Their presence became less pronounced at lower concentrations. In contrast, all spin coated films were flat and homogeneous.

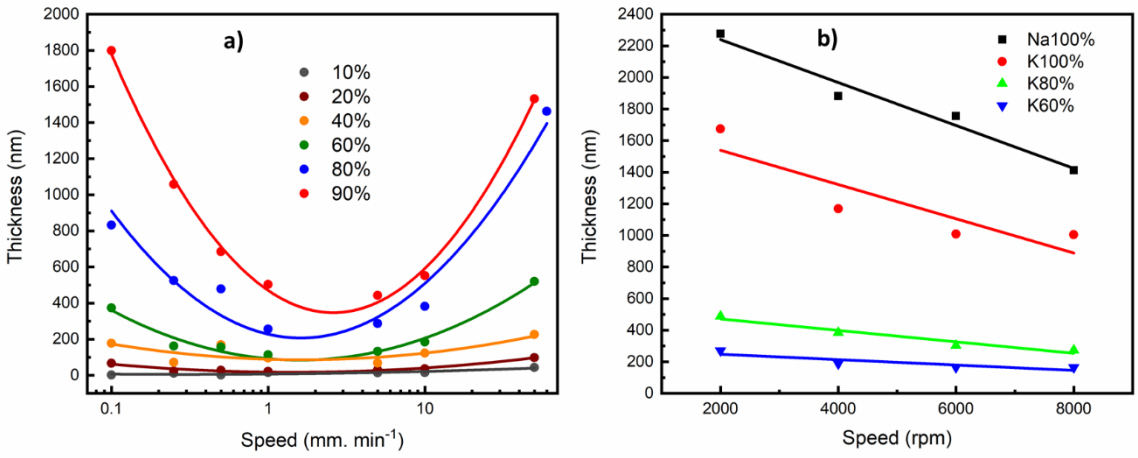

Figure 3.21. The dip and spin coating profiles of the silica coatings are shown in a) and b) respectively. The dip coating thickness follow a curved relationship, whereas the spin coating speed is linear with and inversely proportional to the film thickness. Only KWG was used for dip coating, whereas both NaWG and KWG were used to determine spin coating thickness ranges due to their different concentrations.

3.4.4.3 UV-vis transmittance, absorbance, reflectance, transmission scattering

Removal of network modifiers from the glass would, in theory, reduce the wavelength of the absorption edge of the film towards that of silica, however this was not observed in the transmission spectra due to the significant contribution from the glass substrate and its unchanged network modifier concentration after conversion of the waterglass films to silica (**Figure 3.22**). The coatings did not significantly change the diffuse transmittance or reflectance of the films, nor their absorption edge. The transmittance and reflectance of the coated glass microscope slides remain around 90% and between 0.5 and 1.0% respectively.

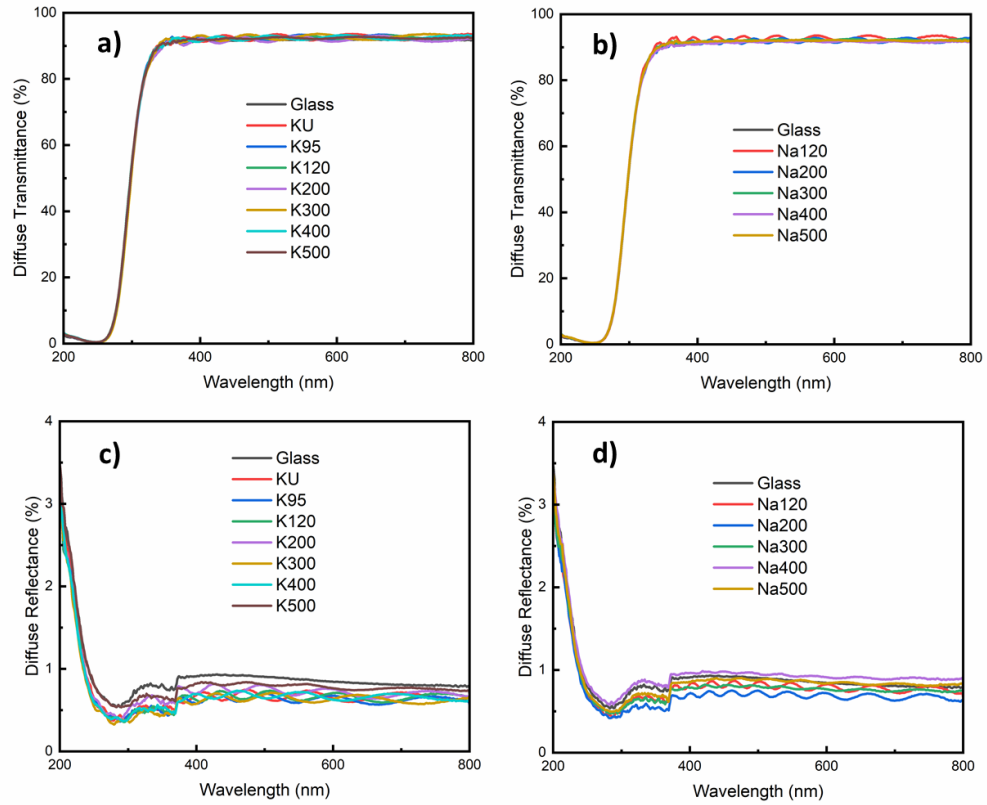

Figure 3.22. The diffuse transmittance and reflectance spectra of the spin coated silica films are shown in a) and b) and c) and d) respectively. The coated samples interaction with the UV-visible and near-IR spectrum closely resembles that of the glass substrates.

3.4.4.4 Contact angle

The water contact angle data for unheated and heated (95-500°C), cured waterglass films on glass is shown in **Figure 3.23**. The coatings all display degrees of hydrophilicity. The as coated films display contact angles around 12°, heating KWG films causes the contact angle to rise to around 42°. Heating NaWG films causes a spike in contact angle

around 100°C, increasing the temperature reduces this below that of the as casted film, with a contact angle of 5° for the 500°C heated sample. The KWG samples exhibited a similar trend, but their contact angle plateaued around 30° at curing temperatures of 200°C or higher.

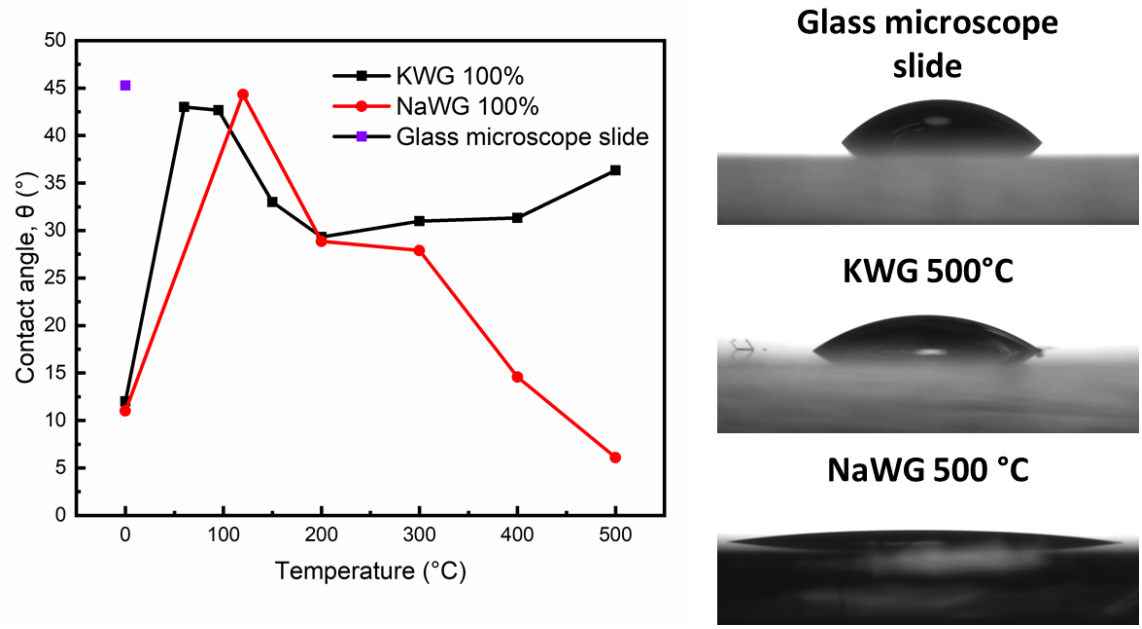

Figure 3.23. Contact angle data for the waterglass films after heating at different temperatures and washing with acid. Examples of the contact angles measured for glass and NaWG- and KWG-coated glass heated to 500°C and washed with acid are shown. Acid washed coatings were always initially superhydrophilic, the cured samples were rinsed with water and dried overnight before recording the contact angle.

3.5 Conclusions

Transparent and thick silica coatings were synthesised from waterglass stock solutions via spin and dip coating. The as-casted films were not stable and carbonate crystals would form on the surfaces of the films over time. The potassium silicate films would develop a sweaty appearance due to the deliquescent nature of the potassium carbonate being formed. The silicate could be cured by washing with aqueous acid. The NaWG films would redissolve upon washing but the KWG films would not redissolve within 1 min of submersion in aqueous H_2SO_4. However, these films would crack upon drying. Heating was necessary to form robust films. KWG films could be cured at temperatures as low as 95°C, whereas a minimum of 120°C was needed to cure NaWG films.

ATR was used to observe the change in the BO/NBO ratio with washing, it was seen that washing with water gradually reduced the NBO content while increasing the BO content, this change happened much more rapidly in aqueous acid solution. It was not possible to determine the change in the BO/NBO ratio for NaWG samples heated to 400 and 500°C, as their ATR spectra became indistinguishable from that of the glass substrate

and no changes were observed upon acid washing even after 30 minutes. XPS and EDX both showed that the potassium was removed from the surface and bulk of the films after washing with aqueous acid even after 1 minute. It was not possible confirm Na removal from these films from composition data alone due to penetration of the EDX x-rays into the glass substrate (even at 5 kV), which also contained a significant amount of Na. XPS spectra were used to further quantify the changes taking place. The high-resolution spectra showed that even after 30 minutes in water, some NBO signal was still observed in the O 1s spectra of the samples, whereas samples washed in acid showed no NBO signal after 1 minute, the resulting peak had a narrower FWHM and a BE resembling that of silica sol-gel samples seen in the literature. Furthermore, the BEs of all spectra generally increased suggesting the films had been reduced by washing in acid and water, at least at their surfaces. The washed films were converted to silica through the removal of sodium or potassium by reaction with the acid to form sodium or potassium sulphate and water.

To further confirm the removal of alkali cations, ICPMS was carried out on the washings, both water and acid solutions showed significantly greater alkali cation contents after washing, both were much greater after acid washing, suggesting that curing took place to a greater extent in acid. ^{29}Si NMR was used to observe the change in connectivity of the silicate with washing in bulk powder samples made with the same washing and heating conditions as the films. The predominate species was Q^3, whose peak shifted by -1 ppm after washing in acid. The Q^4 peak intensity increased at the expense of the Q^2 peak. These observations suggest a general increase in the connectivity of the silicate after washing in aqueous acid.

Profilometry showed that the film thickness of the samples was decreased by roughly half after heating to 200°C, after which negligible changes in thickness were observed. Films cured at 400°C or greater could achieve 6H scratch hardness and all films, surprisingly even the unheated, acid washed KWG film passed the Scotch tape test.

Ellipsometry was used to show the trends in the film thickness of waterglass films made with spin or dip coating. A much greater degree of control was observed with dip coating by changing the dip coating speed or concentration of the stock solutions. The film thickness decreased linearly with greater spin coating speeds, however below 60% KWG incomplete films could no longer be formed with spin coating. Generally, much thicker films could be obtained (micron thick) with the stock solutions or minimally diluted solutions, which is a distinct advantage over the typical sol-gel recipes used to make silica. Thick silica films can usually only be generated with very slow dip coating. Spin coated films were very flat and homogeneous, whereas films dip coated in the viscous drag regime (> 5 mm/min) tended to contain pinholes that were likely formed due to

evaporative cooling effects. This could be overcome by heating the solutions gently upon spin coating and giving the substrate surface some time to equilibrate with the solution before withdrawing, or by increasing the humidity of the atmosphere. The water contact angle on the films was determined, generally the films were all hydrophilic with contact angles around that of the glass microscope slide substrates (~ 40°).

Future work could investigate the relationship between film thickness after casting and the time taken and extensiveness of efflorescence to see if the process is dependent on evaporation of water, perhaps by observing the evaporation of water in situ with IR and seeing how long it takes for efflorescence products to form after evaporation finishes. Further work could also be done to modify the composition of the cured silica films and their aqueous solution chemistry. Dissolving water-soluble metal oxide precursors in the starting solutions and curing with acid would form hetero-condensation structures not easily or commonly formed from aqueous solutions, with simple solution processing methods. Their effect on the physical and optical properties of the silica coatings generated from waterglass should be investigated.

4. Transparent, superhydrophilic, TiO_2-coated macroporous silicate films templated with potato starch with antifogging and photocatalytic properties

4.1 Abstract

Having established the chemistry of the cured, flat silica films made from spin coated waterglass solutions in the previous chapter, the feasibility of changing the morphology of the coatings was investigated with a sacrificial organic template, potato starch. Starch-waterglass suspensions were spin coated onto glass substrates; thermal annealing decomposed the sacrificial template to produce porosity. The porous coatings exhibited higher surface energies than the glass substrates as shown by their lower contact angles, addition of a thin TiO_2 coating produced superhydrophilic, macroporous coatings with antifogging capabilities in the absence of UV lamp irradiation. The photodegradation ability of the coatings was investigated qualitatively with an ink containing the redox dye Resazurin.

4.2 Introduction

In the previous chapter silica films were made from waterglass solutions, the films needed to be heated and washed with acid to insolubilize the waterglass and prevent efflorescence, the process by which carbonate crystals grow from the coatings' surface. Heating before washing was required to insolubilize the waterglass and prevent cracking upon drying after washing. Films heated to higher temperatures could withstand 6H scratch hardness, the coating did not substantially change the transmittance of the glass microscope substrates.

While the uses of flat silica films are limited to applications such as antireflection coatings[124,125] and ion diffusion barrier layers,[128] the introduction of porosity enhances the surface area available for the support to host chemical reactions, (e.g. photocatalysis, gas sensing), and offers the potential to alter the physical, optical and wetting properties of a coating.

Zeolite thin films with anti-scratch and antireflection properties have been made on glass via dip coating, hydrothermal steaming and finally annealing. The microporous coatings had greater than 5H scratch hardness and 98% transmittance at 550 nm.[129,130] Krins et al.[131] have produced a thick and crack-free mesoporous TiO_2 coating on glass with dip coating with a block copolymer template and annealing. The mesoporosity would enhance the surface area and promote high density electron-hole separation while inhibiting recombination, to benefit TiO_2 in applications such as photocatalysis, gas sensing and in dye-sensitized solar cells.[131]

Macroporosity enables access to larger organic and biological molecules and the potential to interact with UV, visible and IR wavelengths via tuning of size features. Proven bottom-up methods for introducing macroporosity into silica include hard organic polymer[20,44,132] or emulsion[50,51] templating and macrophase separation.[53,58] To form a macroporous coating, the matrix material can either be mixed with the template and coated *in situ*[133] or applied over a template structure using a solution[54] or vapour deposition technique.[134] Templates tend to be removed via etching[44] or decomposition.[20]

In this work, a transparent, superhydrophilic, macroporous TiO_2/SiO_2 coating was synthesized on SiO_2 barrier-coated window glass via spin coating and annealing. The macroporosity was generated by dispersing a sacrificial template, potato starch, in the potassium silicate (waterglass) precursor solution, which was used to generate an SiO_2 layer via washing with acid. TiO_2 was then spin coated onto the macroporous stucture. The coatings exhibited superhydrophilicity in the absence of UV-irradiation.

Superhydrophilic surfaces ($\theta_{CA} < 5°$) are identified by the complete wetting of a water droplet upon contact, the definition does not include a wetting time. As discussed in the methodology chapter, wetting models attempt to account for the effect of roughness or porosity on the contact angle. As Wenzel showed, the roughness enhances the intrinsic wettability of the material that originates from the free energy of the surface chemical structure. If the contact angle of a flat surface, $\theta < 90°$, the contact angle of the same material with surface roughness should be even more hydrophilic. The Cassie-Baxter wetting model, in which the water droplet does not penetrate the porosity, predicts that wetting pores or surface roughness in this way would always increase the natural contact angle of the material. Kim et al.[135] have shown that this model predicts contact angles well when the droplet is 40 times larger than the dimensions of the surface roughness. The wetting of a material can be enhanced by doping or coating to further manipulate or alter the surface energy.

Superhydrophilic coatings on mesh or glass have found practical use in oil-water separation, water treatment, ant-fouling, anti-corrosion and antifogging applications.[136] The appearance of fog results from the formation of 1 - 100 μm droplets on the surface that scatter visible and near-IR (NIR) radiation. Fog itself has been shown to be opaque to visible and NIR, limiting transmittance to the same extent between 350 and 1000 nm regardless of its density of droplet size. Very dense fog (visibility < 30 m), with droplets > 2 μm scattered more in the NIR (1000 – 2400 nm) than in the visible (400 – 800 nm) region, whereas fog with droplets > 1 μm (visibility > 100 m) transmittance was equal or greater for NIR.[137] When water comes into contact with a surface with antifogging it should form a sheet instead of beading as it does on glass, maintaining visibility. Qualitative assessment of this property is common in the literature.[138,139,140,141,142]

Superhydrophilic coatings have been made with a variety of methods including chemical and physical vapour deposition, plasma processing, hydrothermal treatment and techniques ideal for coating sol-gel solutions such as spin and dip coating.[136] Huang et al.[143] alternately spin coated TiO_2 and SiO_2 sol gel solutions onto glass, phase separation of the coatings upon 500°C annealing produced a disordered macroporous coating with pores 1.5 – 2.5 μm in diameter on average. The composite coating exhibited contact angles of ~ 5° within 2 seconds with a minimum of 2.5° within 1 s for the 20% SiO_2 coating. The transmittance of the coated glass samples at 550 nm was between 75 and 88%.[143] Song et al.[144] synthesized a superhydrophilic TiO_2 coating on ITO glass. Sodium dodecylbenzenesulfonate modified spherical TiO_2 nanoparticles (5 – 6 nm) were synthesized via hydrothermal processing and spin coated onto the substrate and annealed at 400°C (2 hrs) to sinter the nanoparticles, simultaneously crystallising the TiO_2 to the anatase phase. The hierarchical nano- and macroporous (diameter, 0.6 μm) coating had a near 0° contact angle.[144] Wang et al.[145] spin coated a bilayer superhydrophilic film, firstly a 72.5 nm (SEM) SiO_2 layer from a TEOS sol and secondly a 15.1 nm TiO_2 sol (from titanium tetrabutyloxide, TTBO) containing various weight percentages of the polymer polyethylene glycol, PEG 2000. The coatings were annealed at 550°C (6 hrs) to create porosity by decomposition of the polymer, the type, volume and size of porosity was manipulated with the polymer content. The contact angle without PEG was 68°, 0.5 wt% PEG films with ~ 200 nm diameter pores had a wetting angle of 15°, and a maximum transmittance of 91% at 550 nm, a 0.5% increase over the glass substrate. Storing the coatings in the dark for 60 days further decreased this to 5° and increased the surface roughness.[145] Graphene oxide films were spin coated on glass from a homogeneous suspension and dried at 60°C (3 hrs). The resulting film had a contact angle of 3.7°.[142] Yan et al.[146] dip coated a double layered superhydrophilic coating of a siloxane nucleation layer, TEOS, and silane coupling agent 2-[acetoxy(polyethyleneoxy)propyl] triethoxysilane onto glass. The coating of vertically aligned hydrophilic chains decreased the contact angle of the glass from 52.15° to 4.7°.[146] For these studies the superhydrophilic samples were not tested for antifog properties. Antifogging macroporous anatase TiO_2 glass coatings were spin coated on glass and annealed at 500°C (60 mins). The coating solution was a titania sol from tetrabutyl titanate. The macroporosity was generated via phase separation brought on by a neutralisation reaction, the porosity was tuned by changing the acid/base (HNO_3/NaOH) ratio in the sol. The disordered macroporous (1 – 10 μm) TiO_2 coatings featured a contact angle of 4.5°, lower than that observed on the flat analogue. Coatings made with a NaOH:HNO_3 ratio of 1:1 exhibited good antifogging behaviour in the absence of UV-irradiation, which was assessed qualitatively.[140] Antifogging films are not always superhydrophilic, Zhang et al.[138] reported a self-healing, antifogging film of cross-

linked poly(vinyl alcohol) (PVA) and poly(acrylic acid) (PAA) made with dip coating, which were heated at 150°C (5 mins). The polymer coating reduced the transmittance of the glass by several percent to ~ 89% at 550 nm and had a static contact angle of 62°, yet still exhibited obvious antifogging compared to the glass substrate.[138]

It has been shown that the photocatalytic performance of anatase TiO_2 improves when the more reactive {001} facet is exposed at the surface, however the more thermodynamically stable {101} facet is usually present at the surface of TiO_2. Tian et al.[147] have studied TiO_2 nanosheets with XRD and Raman spectroscopy upon changing the sheet dimensions by hydrothermal reaction with hydrofluoric acid (HF). Increasing the volume of HF decreased the platelet thickness in the [001] direction from 10 to 3 nm, observed in XRD as a decrease in the intensity of the (004) diffraction peak and an increase in its fwhm. Simultaneously, the (200) peak became narrower and more intense, indicating that the width of the nanosheets in the [100] direction had increased from 19 to 28 nm. By changing the sheet dimensions, they were able to increase the available {001} facets at the surface from 38 to 80%. Photocatalytic testing showed greatest efficiency in methylene blue degradation with 50% {001} as calculated with the Raman method. Increasing the volume of HF increased the intensity of the E_g bands at 144 cm^{-1} and 636 cm^{-1}, while the intensity of the B_{1g} and A_{1g} peaks at 394 and 514 cm^{-1} respectively increased. By correlating the changes in XRD and Raman peak intensities and fwhm with the dimensions of their nanosheets, they were able to devise a method for estimating the percentage of the {001} facet from the Raman spectroscopy data of anatase TiO_2.[147] Stearic acid is usually the molecule of choice for quantitatively testing the photodegradation rate. Mills et al.[71] have shown that the redox dye Resazurin can be a suitable alternative for qualitative testing, undergoing an irreversible colour change from blue to pink upon reduction and being stable to reduction under ambient conditions. Many photocatalyst inks such as methylene blue (MB) are frequently used for photodegradation tests despite their reversible colour changes and degradation in the absence of a photocatalyst, making it difficult to isolate the effects of the photocatalyst on the ink. Resazurin can easily be made into a dye by mixing with a polymer, sacrificial electron doner and plasticizing reagent to enable film formation (e.g. hydroxyethylcellulose and glycerol).

There are few examples of hard or soft templating with starch in the literature. Starch-gel has been used as a template for macroporous TiO_2[148] and SiO_2[149] monoliths with pores between 0.5 and 50 µm. In both cases the starch-gel template was removed via thermal decomposition at 600°C for several hours. In their review, Schwieger et al.[24] mention the use of starch as a template for meso- and macroporosity in the zeolite MFI. Gérardin et al.[56] discussed the use surfactants from renewable sources as templates for

generating porosity from silica. Starch has been used to form the hydrophilic component of a surfactant template.

Few examples exist of porous films made from waterglass templated by any kind of porosity. Bulk micro- and mesoporous silica has been made from sodium silicate solution with cationic surfactants such as cetyltrimethylammonium bromide (CTAB).[150] In terms of coatings in the literature, waterglass has been used to make anti-reflection coatings and macroporous silica thin films. Here, a macroporous silica thin film was generated from a potato starch/waterglass suspension, coated with TiO_2 and used as an antifogging coating for window glass with antifogging and photocatalytic properties. The effect of the porosity on the optical properties and wetting of the coating was investigated. The chemical structure of the silica and titania coatings was investigated with ATR, Raman spectroscopy and XPS. SEM and optical microscopy were used to determine the pore sizes. Finally, the photoactivity of the titania-coated samples was determined via a qualitative dye-degradation test.

4.3 Experimental

Materials were used as purchased except for the acid, which was diluted in deionised water (14.9 - 15.0 MΩ.cm) dispensed from an ELGA Purelab, option-R 7/15. Potato starch (CAS no. 9005-25-8), sulphuric acid (CAS no. 7664-93-9), titanium(IV) tetraisopropoxide (CAS no. 546-68-9) and 2-methoxyethanol (CAS no. 109-86-4) were purchased from Sigma-Merck. Barrier glass was purchased from Pilkington. Potassium silicate solution was purchased from Kremer Pigments (product number: 77750).

Glass substrates were cleaned by sonication in acetone, alcohol and deionised water. To prepare the porous silica coatings, potato starch was added to potassium silicate solution (w/w) and dispersed in the solution with a combination of sonication and manual mixing. The suspensions were cooled to room temperature before spin coating onto glass substrates at 4000 rpm, (2000 acc, 30 s). After spin coating the coatings were annealed in a Carbolite furnace at 500°C, (2°C/min), for 5 hours (denoted **A**). Samples with 5 and 10 wt% starch in their initial solutions required an additional 5 hours of annealing at the same temperature to fully decompose the starch. The porous samples were coated with 1M aqueous H_2SO_4 for 30 minutes and then rinsed with water and dried. Another batch of samples (denoted **B**) were heated at 400°C for 30 minutes on a hotplate after spin coating, and then washed with acid of the same molarity for 30 minutes. These samples were then placed in a furnace and the starch was annealed under the same conditions.

The TiO_2 sol was prepared as described by Lim et al., briefly a 0.5M solution of titanium tetraisopropoxide (TTIP) in 2-methoxyethanol was prepared, this was stirred vigorously for 2 hours and then aged for 1 day in a sealed container at room temperature. The aged sol was spin coated directly onto the porous silica coatings at 1500 rpm (1000 acc, 30 s). The coated samples were annealed at 500°C for 3 hours (3°C/min).

Antifogging properties were assessed visually after placing the coatings over a beaker filled with boiled water for ~ 10 seconds. The samples were then removed and placed over an image to assess the change in visible transmittance.

For photocatalysis, an ink was prepared containing the photoreduction dye Resazurin, a polymer, hydroxyethylcellulose (HEC) and glycerol. As shown by Mills et al.,[71] 3 g of a 1.5 wt% aqueous hydroxyethyl cellulose (HEC) solution was mixed with 0.3 g of glycerol and 4 mg of Resazurin to create an ink containing 88 wt% glycerol in HEC upon drying. The ink was blade coated onto the samples alongside bare glass slides coated with Sellotape; the thickness of the ink coatings was assumed to be comparable to that of the tape, i.e. around 25 microns, over 35 (Mills et al., 39) times thicker than the macroporous silica/TiO_2 coatings beneath. After coating the ink was left to dry under a fan for 20

minutes before placing under a 365 nm UV lamp. For the testing, the intensity below four 365 nm UV lamps was measured, the height of the sample stage adjusted to an irradiance of 2 mW cm^{-2}. The lamps were left on for 30 minutes before testing to ensure consistency in the intensity readings. The samples were irradiated for 2 minutes at a time, between which photos of the samples were taken to observe the degree of colour change, a photo was also taken before any UV irradiation for comparison.

The (JEOL 6700) FESEM (5 kV) and optical microscopy were used to image the morphology and estimate pore sizes. Samples were sputtered with gold for 30 seconds before SEM imaging. The Shimadzu 2600 UV-vis, with an integrating sphere attachment and barium sulphate powder ($BaSO_4$) as a reference, was used to investigate the UV, visible and near-IR transmittance properties of the glass samples. For transmittance scattering measurements, the reference plate directly opposite the sample was removed to minimize signal from light directly transmitted through the glass. The Shimadzu Tracer-100 was used to measure the attenuated total reflectance (ATR) spectra of the silica coatings. The measurements were carried out in transmittance mode, with 32 scans per sample and a resolution of 4 cm^{-1}. The data was converted to absorbance and the baseline was subtracted. Contact angle images were recorded on the FTA system using a droplet size of 3 µL. Several measurements were taken across the surface of the samples and averaged. Simultaneous thermal analysis (STA) measurements, particularly thermogravimetric analysis (TGA) and differential scanning calorimetry (DSC) were recorded on the Netzsch STA 449F1 in an alumina (Al_2O_3) crucible. Raman spectra were collected with the Renishaw Ramascope, with 633 nm laser excitation wavelength. For each sample three spots were measured to determine homogeneity. Raman spectra were recorded with the Renishaw 1000 spectrometer equipped with a He-Ne laser (l= 633 nm) and coupled to a microscope with a 50× objective (1.9 mW when operated at 25 % power, spot size approx. 4.4 mm^2). The Raman system was calibrated using a silicon reference. The acquisition time of all Raman measurements was 10 s.

4.4 Results and discussion

Potato starch was added to potassium silicate solution (waterglass), the weight percentage of the starch was varied according to the solution mass. Sonication and manual mixing were used to obtain a suspension, which was spin coated onto glass substrates at 4000 rpm. The samples were then annealed at 500°C to decompose the starch and generate macroporosity. The samples were washed with 1M H_2SO_4 to convert the potassium silicate to silica via hydrolysis and condensation of the silicate and removal of the potassium. The macropore diameters were between 10 and 50 µm with optical microscopy and SEM (**Figure 4.1**). The amount of porosity increased with the initial starch weight percent in solution. The shape of the pores closely resembled that of the starch granules before annealing, giving large, round pores with micron scale dimensions (**Figure 4.1e)**). TGA of the starch powder was carried out in an O_2/N_2 atmosphere (80/20), annealing the powder to 800°C (2°C/min) to observe its decomposition through its mass loss (**Figure S4.1**). After the evaporation of water near 100°C, ~ 85% of the powders mass loss occurred between 250 and 500°C, this was accompanied by a broad, exothermic DSC peak (maximum 2.5 mW/mg at 425°C). It is likely that this signified the decomposition of the starch powder, which was no longer present in the crucible after completion of the annealing process. This shows the ability of the annealing process to remove the starch from the coatings by annealing at 500°C. Above 1 wt% clusters of pores were present, indicating agglomeration of the starch despite lengthy sonication. The macroporous silica films were coated with a TiO_2 sol via spin coating at 1500 rpm, the TiO_2 was crystallised via annealing at 500°C for 3 hours.

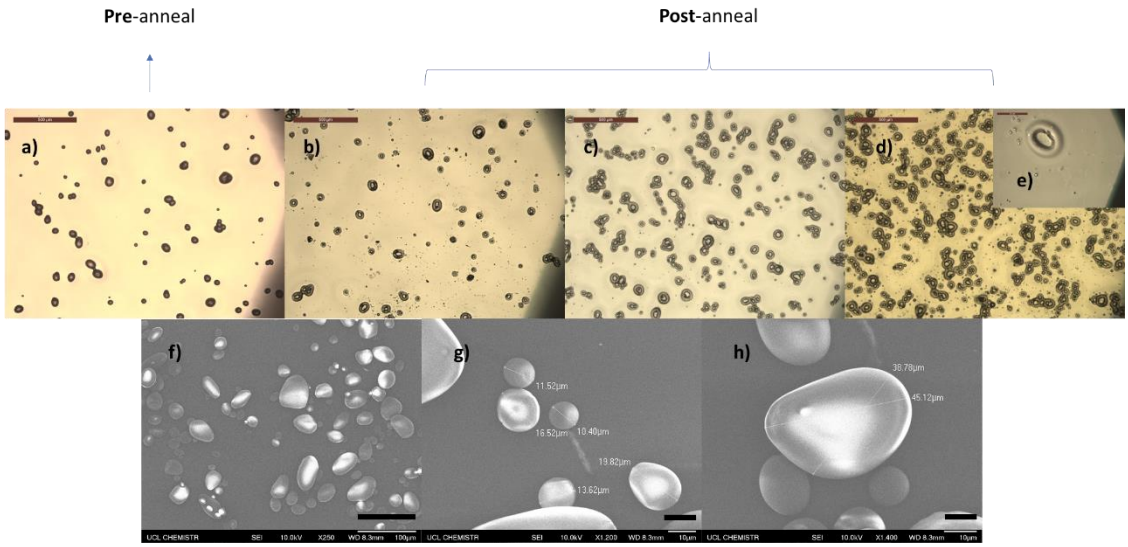

*Figure 4.1. Optical microscope images of macroporous silicate films and the potato starch template. The starch was incorporated into the solution with 1, 5 and 10 wt% of the solution mass, and spin coated. The 1 wt% starch film **before** annealing is shown in a) (scale bar, 500 microns). Annealing the films decomposed the starch and generated macroporosity, the amount of porosity increased with the starch wt% in solution as seen in b), c) and d) for 1, 5 and 10 wt% (500 um). Magnification 100x in e) shows a pore generated by annealing (scale bar, 50 um). The potato starch template, f) 100 um, and the range of starch granule sizes, g) and h) (10 um).*

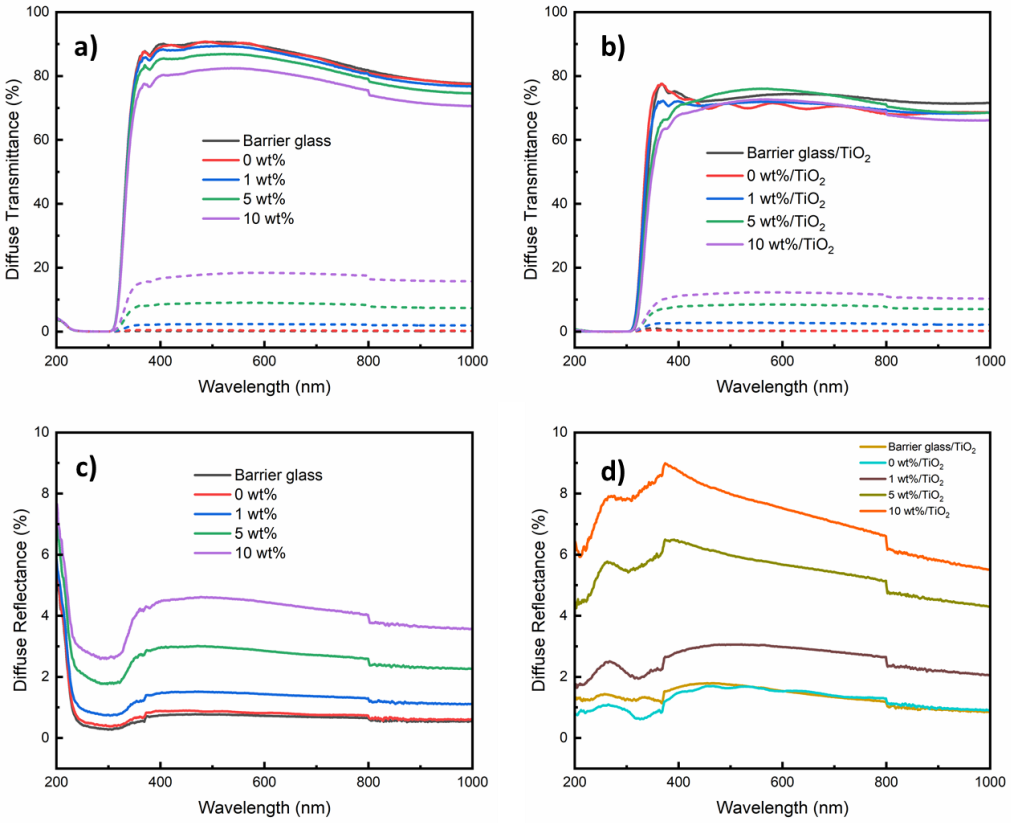

Figure 4.2. Diffuse transmittance and reflectance of the starch templated silicate films before and after coating with TiO_2. Increasing the starch wt% in the films reduces their visible light transmittance and increases their reflectance and scattering in transmittance mode, represented by the dotted lines in a) and b). The addition of the TiO_2 coating generally reduces the transmittance to ~ 70%, the effect of increasing the porosity on the reflectance was enhanced with the TiO_2 coating, while the scattering in transmittance mode was less significant.

The UV-vis profiles of the samples are shown in **Figure 4.2**. Transparency was retained even with the large macropores, the additional TiO_2 coating gave the glass a darker hue. Light incident on a macrostructure of these dimensions (periodicity, d >> λ) would be expected to undergo reflection, scattering and absorbance,[151] reducing the transmittance, as shown by the UV-vis spectra glass absorbs mainly in the UV-A region. The pore clusters would have a different periodicity to isolated pores, but both would experience the reflection and scattering of wavelengths similar to the dimensions of the pores (far-IR, 3 μm – 1 mm). Annealing generated additional porosity 5 – 10 μm in size (**Figure 4.1e)**). For low starch loadings of 1 wt%, the transmittance and reflectance of the samples resembled that of the glass substrate. As the starch content of the starting solution and consequently the porosity of the coatings increased, the diffuse transmittance of the samples decreased, and the reflectance and scattering in transmittance mode increased. The transmittance of the 10 wt% samples was decreased to just under 80% in the visible region, with 19% scattering in transmittance mode and

just over 4% diffuse reflectance in the same wavelength range. After coating with TiO_2 and annealing, the visible light transmittance of all samples was reduced to around 70%. The maximum diffuse transmittance at 550 nm was 76% for 5 wt% starch, the other samples transmitted less than the substrate (74%) at this wavelength. Their visible light scattering in transmittance mode was also lower, with a maximum of 12% at 550 nm for the 10 wt% sample. The diffuse reflectance was generally greater after coating with TiO_2, to around 8% for the 10 wt% sample. The TiO_2 dampened the scattering of the porous coatings and increased their reflectance, however the reflectance and scattering still scaled with the porosity. The TiO_2 sol was also spin coated onto silicon wafer with the same conditions to determine the coating thickness with spectroscopic ellipsometry. An effective medium approximation was needed to accurately model the sample, indicating that the coating contained porosity. The fitting gave a thickness of 69.3 nm for a refractive index of 1.97. Anatase TiO_2 usually has a refractive index of ~ 2.5 in the visible region,[152] the lower value fitted here is indicative of the presence of porosity. The porous TiO_2 coatings increased the reflectance but lowered the scattering of the macroporous films, even at this thickness the high index titania resulted in a noticeably darker film. Fluctuations in the visible light transmittance of the 0 wt% sample indicate thin film interference.

ATR-IR spectroscopy (**Figure 4.3**) was used to detect efflorescence in porous and non-porous silica coatings before and after ageing. With a diamond ATR crystal additional peaks at lower wavenumbers could be seen in the ATR-IR spectra, namely the Si-O-Si rocking peak that usually appears between 450 and 490 cm^{-1}.[104] The BO and NBO stretching bands were overlapping in all samples to the extent that their peaks were indistinguishable. Their signal was weak compared to those of the glass and flat waterglass films, likely due to porosity reducing the surface area of the coatings in contact with the ATR crystal. Notably no water or efflorescence peaks had emerged in the ATR-IR spectra even after ageing the samples for several months, regardless of the heating method. Ratio of stretching (~ 1000 cm^{-1}) to rocking (~ 410 cm^{-1}) for glass and flat silica films from potassium silicate solution was greater than 1. For the porous samples the ratio was always less than 1 and for most porous samples, the stretching intensity was half that of the rocking band, suggesting restricted Si-O-Si stretching in these samples.

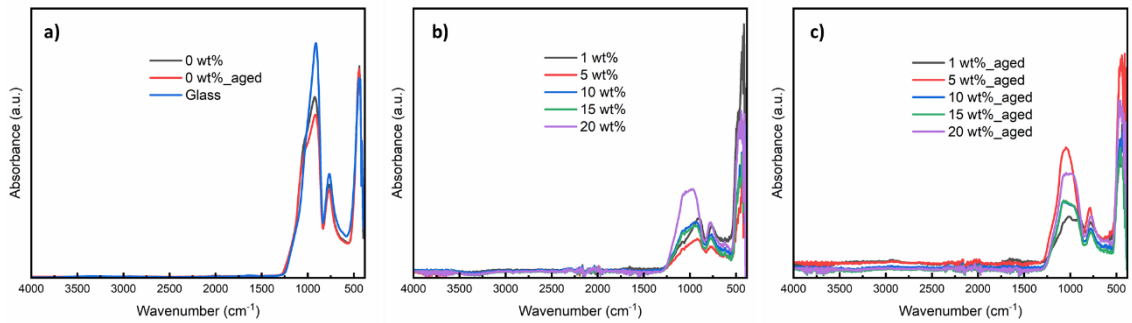

Figure 4.3. Attenuated total reflection infrared (ATR-IR) spectra of the porous silica samples on floating glass. Figure a) shows the spectra of the glass substrate and the non-porous coatings. The signal for the porous samples in b) and c) is lower between 600 – 1250 cm^{-1}, the frequency range of the Si-O-Si stretching bands. The merging of the BO and NBO peaks in this region makes interpretation of the chemical species difficult without deconvolution. Samples were analysed after ageing to observe signals from efflorescence, however no obvious carbonate or water signals could be seen.

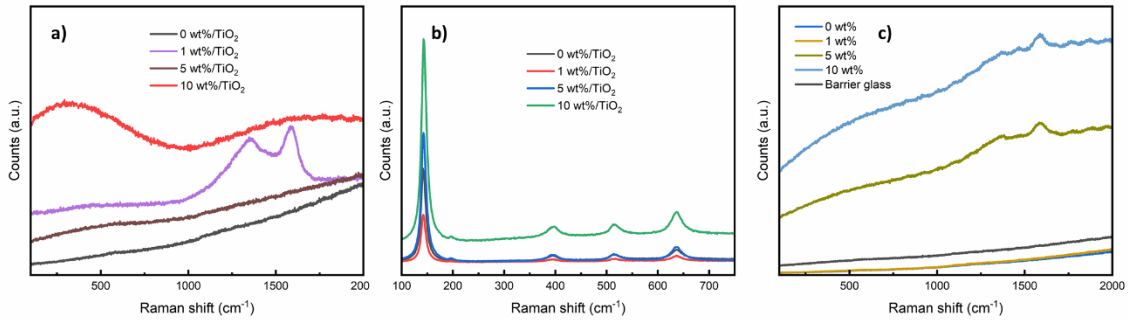

Figure 4.4. Raman spectra of a) the porous silica samples after annealing and washing, b) Barrier glass/porous silica/TiO_2 washed after pre-heating the samples to 400°C on a hotplate before 500°C annealing and c) the TiO_2 coated samples washed after annealing at 500°C. Only the samples washed after heating at a lower temperature became crystalline after the addition of the TiO_2 layer, indicating that residual potassium inhibited the crystallisation of TiO_2 in the samples washed after 500°C annealing.

The TiO_2 coating was identified with Raman spectroscopy (**Figure 4.4**). Before adding the TiO_2, the samples did not exhibit any significant features in their Raman spectra. The most intense peaks due to the glass substrate or the potassium silicate would have been expected between 900 and 1200 cm^{-1}. After coating with TiO_2 and annealing at 500°C for 3 hours (samples **A**), the samples did not show any significant peaks, suggesting they were still amorphous. This was due to insufficient removal of the potassium ions during acid washing. As shown in **Chapter 3**, characterization of the NBO becomes ambiguous above 400°C as the BO and NBO peaks merged when heated to 500°C, making it difficult to determine the reduction in NBO content. This indicates that the alkali cations of samples heated to 500°C were not removed after acid washing. To provoke crystallinity in the TiO_2 after annealing, the starch filled coatings were heated on a hotplate at 400°C for 30 minutes (samples **B**) to evaporate water and compact the silicate structure enough to make it insoluble in water and enable washing, but not so much as to prevent rapid removal of alkali cations via washing with aqueous acid. These samples were still annealed at 500° to decompose the starch. After coating with the TiO_2 sol and annealing, peaks typical of anatase emerged in the Raman spectra, peaks at 142, 196, 397, 515 and 637 cm^{-1} were present in all samples, with relative intensities of 82.8, 0.8, 3.9, 4.0 and 8.4% respectively. These peaks are attributed to the Raman active modes of anatase with symmetries E_g, E_g, B_{1g}, A_{1g} and E_g.[153]

In the Raman spectra of anatase, the E_g, B_{1g} and A_{1g} peaks have been associated with the symmetric stretching, bending and asymmetric bending vibrations of O-Ti-O respectively. For anatase TiO_2 with exposed {101} facets, the main available surface states are saturated, sixfold (octahedrally)-coordinated Ti (Ti-6c) and O-3c and unsaturated Ti-5c and O-2c modes. With exposed {001} facets only the unsaturated Ti-5c and O-2c bonding modes are present.[154] This facet features less symmetric stretching

and more symmetric and antisymmetric bending vibrational modes of the O-Ti-O bond and hence the intensity of the E_g peaks decreases, while the A_{1g} and B_{1g} peaks become more intense. As with XRD the ratio between the E_g and A_{1g} vibrational modes in the Raman spectra of anatase can be used as an estimate for the percentage {001}. As mentioned previously this study found that samples with 50% {001} facets as calculated by the Raman method had the greatest rate of methylene blue degradation after UV-irradiation.[147] There was no trend in the absolute intensity of the most intense peak, (E_g) at 142 cm^{-1}, with the amount of porosity. XRD patterns of the samples were all amorphous (**Figure S4.2**), supporting the idea that the potassium silicate films were amorphous, but also showing that the TiO_2 coating thickness of ~ 70 nm was too thin for the detection of crystalline reflections. Tian et al.[147] have proposed that the percentage of exposed {001} facets in anatase TiO_2 can be estimated from the ratio of E_g (141 cm^{-1}) and A_{1g} (514 cm^{-1}), this was calculated as ~ 5% for all samples in **Figure 4.4**.

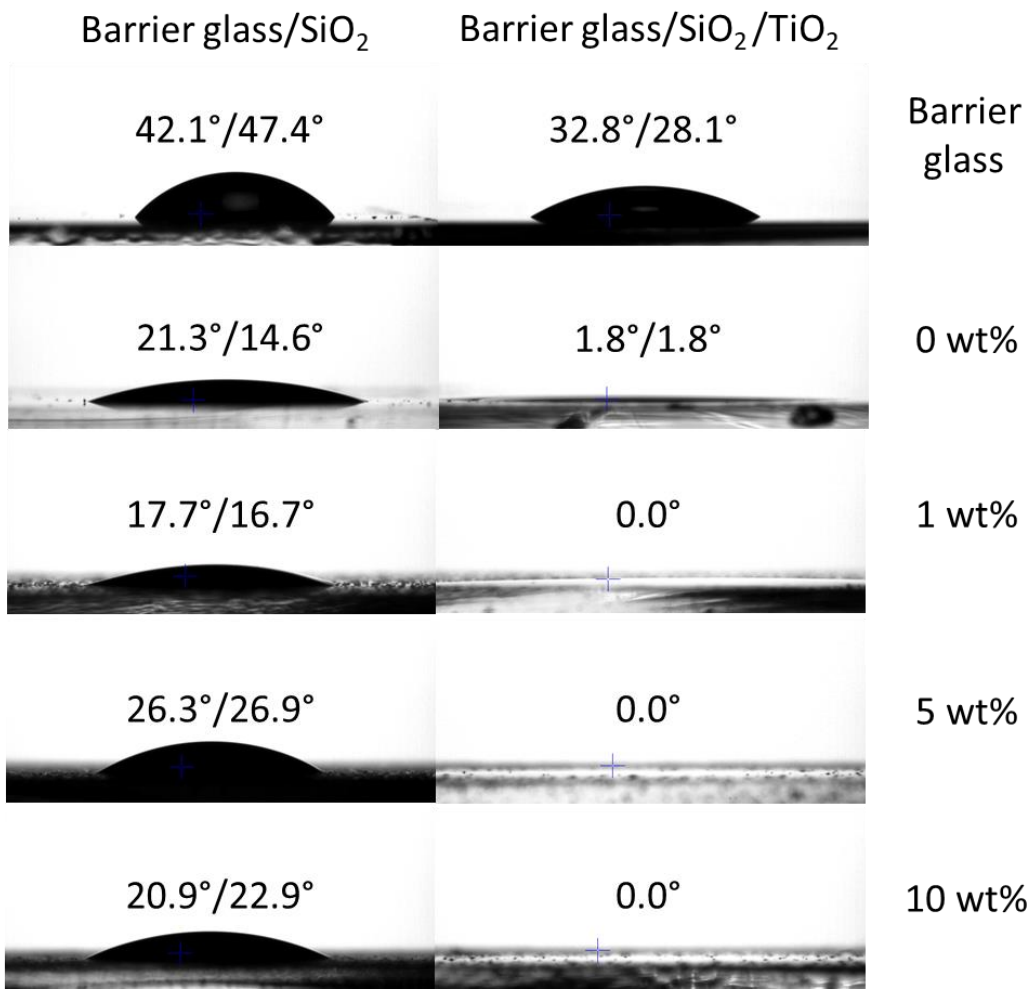

Figure 4.5. Contact angle images of 3 µL deionised water droplets on the macroporous film before and after coating with TiO_2. The silicate films exhibited lower contact angles than the barrier glass. After coating with TiO_2, the starch templated films were superhydrophilic, while the untemplated film supported on barrier glass (0%) shows a very low, but non-zero contact angle of 1.8°.

The water contact angle of the coatings was measured (**Figure 4.5**). Before coating with TiO_2, both the porous and non-porous potassium silicate coatings exhibited a higher surface energy than the glass substrates. After washing with acid, all coating were superhydrophilic, this behaviour faded after washing with water or lengthy exposure to the atmosphere (several days). However, despite their low contact angles, none of them exhibited long-lasting superhydrophilicity. After coating with TiO_2 all porous coatings (1 – 10 wt%) were superhydrophilic on all parts of the sample. The non-porous 0 wt% and barrier glass coated TiO_2 samples had contact angles of 1.8° and 32.8° with water respectively. Samples washed with acid *after* annealing at 500°C also exhibited superhydrophilic behaviour. This efflorescence was not visible to the naked eye. For the superhydrophilic samples the average time taken for a droplet to achieve equilibrium after contacting the surface was 6.7 s, for many measurements the droplet continued to spread even after the recorded time (**Figure S4.3**). For the TiO_2-coated glass sample the droplet did not spread much and equilibrated within 0.2 s, but for the porous sample the droplet continued to spread for a considerably longer time, even after the contact angle was no longer decreasing. For the porous and 0 wt% samples the wetting time was between 5 and 10 s, with no obvious relationship between amount of porosity and average wetting time.

The same coatings formed on glass microscope slides lost their superhydrophilicity after several months. This was likely due to the growth of carbonate crystals from the surface of the waterglass coating, due to insufficient removal of alkali cations during washing. This resulted in less superhydrophilic behaviour from the TiO_2 coated samples (**Figure S4.4**).

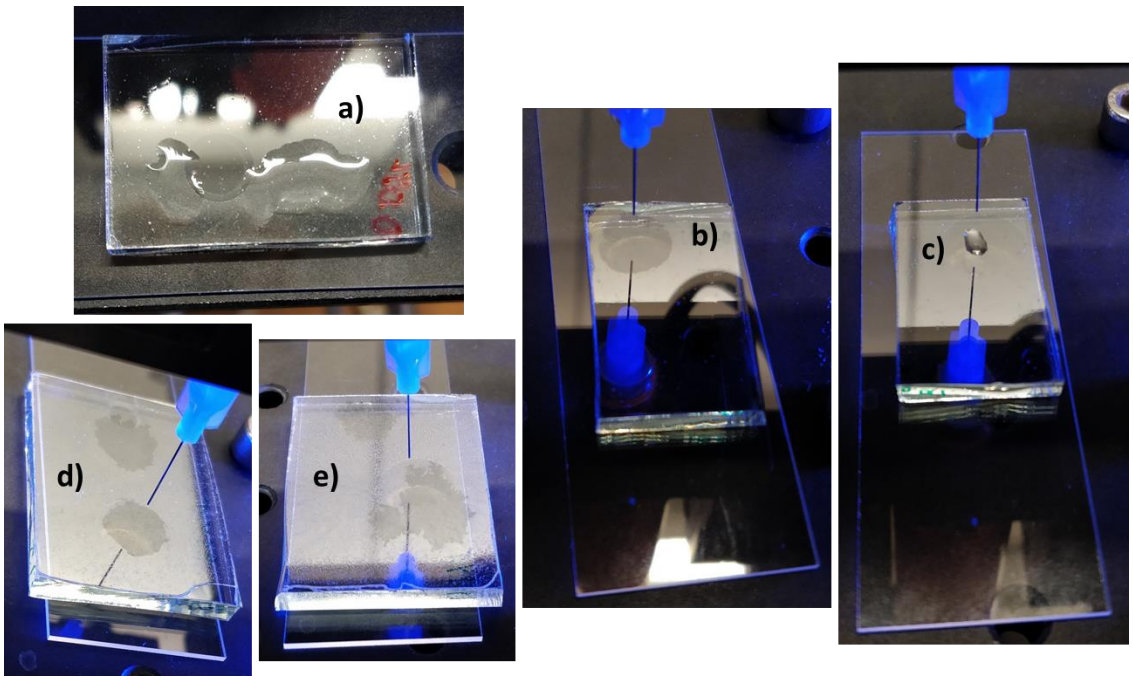

Figure 4.6. Images of sample wetting. Image a) shows the non-centrosymmetric droplet shape on the 0.05 wt% film. Even with low porosities the droplet shape was significantly distorted. In b) and c) the non-uniform wetting on different areas of the 0.01% sample can be seen. Images d) and e) show the superhydrophilic spreading of the water droplets on the TiO_2-coated 0.25 and 1 wt% samples.

Water droplets on either hydrophilic or superhydrophilic macroporous films were non-centrosymmetric with respect to the plane of the substrate, suggesting that that porosity may affect the spreading of the droplet (**Figure 4.6a)**). It appears that the macroporosity causes pinning of the water droplets, causing it to encourage spreading in certain directions and restrict it in others. This can be seen more clearly in the top view images. For a 3 µL droplet, assuming spherical droplet shape, the droplet diameter would be ~ 2000 µm. For the observed range of pores diameters, the droplet was 40 to 200 times greater than the porosity.

Even with porosities as low as those created with 1 wt% solution starch content, the silica film became superhydrophilic after the addition of the anatase coating. The extent of the effect of the porosity on this wetting effect was investigated. Samples with initial starch solution contents of 1.00, 0.75, 0.50, 0.25, 0.10, 0.50 and 0.01 wt% starch were prepared and coated with TiO_2 as stated previously. Superhydrophillicity was observed down to porosities of 0.10%. Below this, the pore density was insufficient to encourage homogeneous surface wetting and the samples had contact angles greater than 0 in many spots. These samples had wetting times between 2.2 and 9.1 s, again there was no relationship between the porosity and the time taken for the droplet to equilibrate. For less homogeneous samples, the wetting time for hydrophilic wetting was much faster (1.5 – 3.0 s) than for the sample areas where the porosity was sufficient for superhydrophilic behaviour (4.5 – 10 s).

The superhydrophilic samples were tested for their antifogging ability (**Figure 4.7**). The appearance of fog is owed to the condensation of water droplets (diameter 1 – 100 μm) on the surface of a coating. After exposure to humidity, the barrier glass developed fog, which blurred the appearance of the image below the glass. The silica/TiO_2 coatings exposed in the same way remained transparent, large water droplets covered the surface of the 1 wt% sample and the porosity appeared to reflect more and appeared whiter. Less beading and more sheeting of water droplets was observed on the other coatings after exposure to the humidity, exhibiting their antifogging capability.

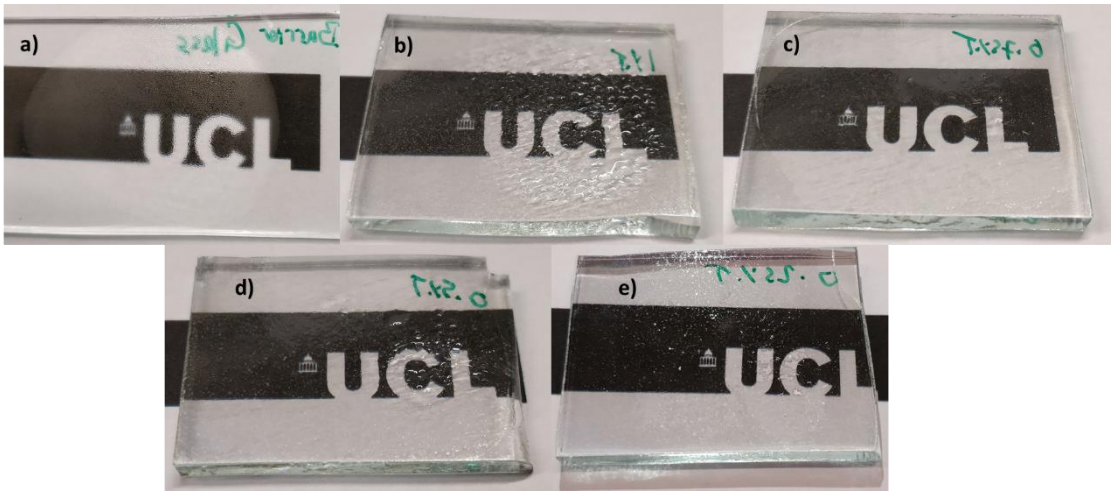

Figure 4.7. The antifogging behaviour of the superhydrophilic coatings was assessed. After exposing to steam, fog formed on the barrier glass surface a)) in the form of small water droplets. Unlike the barrier glass, all SiO_2/TiO_2-coated samples could be clearly seen through after exposing to steam. However, large water droplets formed at the surface of the 1 wt% samples b)). This effect was only observed in small patches on the c) 0.75, d) 0.50 and e) 0.25 wt% samples, upon which the water from the steam generally sheeted instead of beading.

The photocatalytic properties of the TiO_2 layers were assessed qualitatively (**Figure 4.8**) using a layer of ink containing the redox dye Resazurin, which was blade coated onto the samples and exposing them to 365 nm UV-light (2 mW cm^{-2}). After 30 minutes, the dye on samples **A** and glass/TiO_2 had completely changed colour and on the 5 and 10 wt% TiO_2 samples, a significant amount of the dye had been reduced indicating that the films were photoactive. At the edges of some of the samples photobleaching of the pink Resorufin dye could be seen. On the samples **B** (washed at hotplate 400°C, 500°C and then TiO_2 coating), the dye experienced the fastest change in colour for the 0 and 1 wt% samples, partial change in the colour of the dye was also observed on the 5 and 10 wt% samples in this time, however it can be seen that the initial ink coating on these samples was thicker. No change was observed in dye colour on the glass alone.

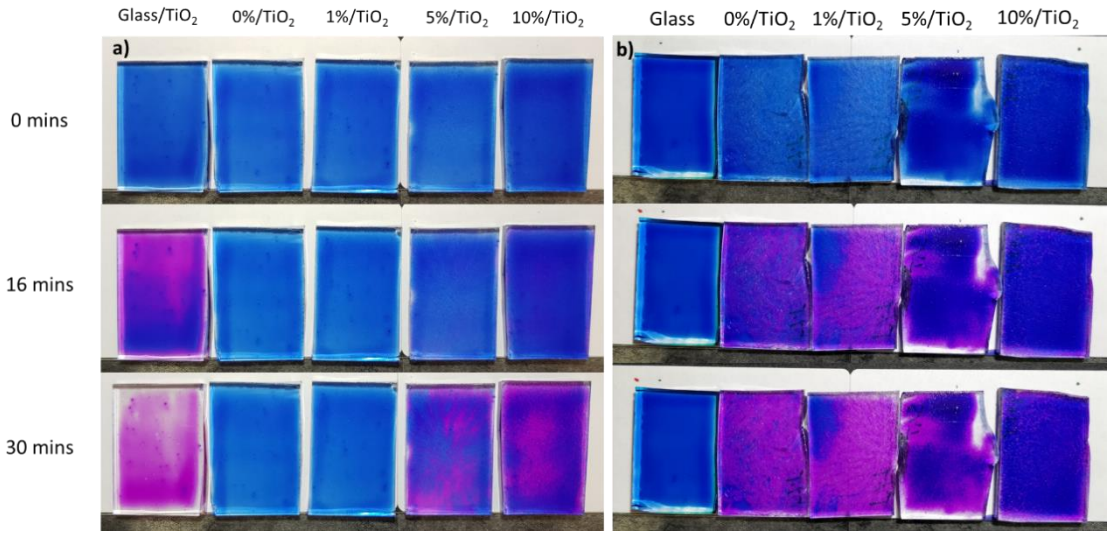

Figure 4.8. The barrier glass/macroporous SiO_2/TiO_2 samples were blade coated with the photoactive dye Resazurin. The images in a) show the results from experiment A (500°C, wash), while b) shows those of experiment B (400°C, wash, 500°C). In A, after exposure to UV-light of intensity 2 mW.cm^{-2} for 30 minutes, only the barrier glass/TiO_2 sample showed complete colour change of the dye. The 5 and 10 wt% starch templated macroporous samples showed partial conversion of the dye, whereas the 0 and 1 wt% samples were unchanged. For experiment B, all samples except the control, dye coated barrier glass changed colour, the 0 and 1 wt% samples almost completely changed colour.

4.5 Conclusion

In this chapter the silica coatings generated from waterglass were made porous via the addition of a sacrificial template, potato starch, to the silicate solution before spin coating. Porosity was generated via annealing (10 – 50 μm). The total amount of porosity was controlled by changing the amount of potato starch in the initial solution. After the addition of a thin layer of TiO_2, the transparency of the porous films was reduced in exchange for antifogging and photocatalytic properties. The barrier glass/macroporous silica/TiO_2 coatings featured 0° contact angle for porosities generated from 0.25 to 10.00 wt% starch contents in the initial starch solution, with an average wetting time of 6.7 seconds. The visible light diffuse transmittance of the samples was reduced from ~ 90 to 70% after the addition of TiO_2 coatings, with a maximum of 76% at 550 nm for the 5 wt% sample. Raman spectroscopy was used to identify the crystallization of the TiO_2 layer. Films with porosities between 0.25 and 0.10 wt% exhibited sheeting of water vapour droplets from a humid atmosphere, retaining their transparency. Photodegradation of ink containing the redox dye Resazurin was observed via colour change for the barrier glass/TiO_2 and 0 – 10 wt%/TiO_2 samples. For experiment **A**, the ink on 0 and 1 wt% samples exhibited no change in colour after UV-light irradiation, while for experiment **B** the dye colour change was observed for all starch samples and the dye reduction was most homogeneous for the 0 and 1 wt% samples.

While the combination of materials used was trite, the use of potato starch as a sacrificial template was a novel approach to introducing large macropores into the silica matrix. The higher viscosity of waterglass compared to a standard silicon alkoxide solution enabled the formation of thicker films from stock solutions. Potassium silicate solution was shown here to be able to template large nanoparticles with a single coating.

The heating conditions before washing affected the removal of alkali cations from the waterglass coating, only being removed in quantities sufficient to facilitate TiO_2 crystallization after heating at 400°C. For both curing conditions used here, the samples were free of measurable efflorescence (Raman or ATR spectroscopy), some carbonate hairs were observed at the surfaces of the samples in contact angle or microscopy images, but they did not impact the properties of the coatings shown here. It is worth noting that the same coatings on glass microscope slides did experience efflorescence, the barrier layer was necessary to prevent diffusion of sodium ions from the glass into the waterglass coatings during annealing.

While a lower temperature synthesis would be desirable, as seen in the introduction high temperature annealing methods are common in the synthesis of macroporous materials and are necessary to crystallize the titania. The multistep synthesis is also commonplace. The porosity could be coated with other materials such as a melamine-

formaldehyde resin[155] to see if the roughness of the macropores is sufficient to encourage superhydrophobic behaviour with sufficient decrease in surface energy. Further work should investigate the effects of the porosity on the droplet shape and the extent to which its arrangement can control droplet shape, the starch could be functionalised to encourage or discourage agglomeration and would also affect the scattering. By controlling the macropore size and arrangement specific wavelengths could be prevented from transmitting through the sample for solar window applications. The quality of the TiO_2 could also be improved to enhance photocatalytic activity, through improving the {001} facet purity. If deposited on quartz, the cured, acid washed samples could be annealed to high enough temperatures to facilitate coating the macroporous films with coatings of both rutile and anatase TiO_2. The effect of the TiO_2 coating thickness on the degradation rate and transmittance should be investigated, with potential to enhance the transmittance. Quantitative, FTIR analysis would be necessary to determine the effect of the pore volume on the degradation rate. The large, accessible macropores could also be coated with a variety of visible light photocatalyst sols.

5. Ordered macroporous silica coatings from waterglass solutions and polystyrene nanosphere templates

5.1 Abstract

It was previously shown that waterglass coatings made via spin or dip coating could be stabilised by converting to silica. Disordered macroporosity (10 – 50 μm) was added to the coatings by incorporating a sacrificial hard organic template, potato starch, into the starting solution. Unlike silicon alkoxide solutions, waterglasses contain larger (> Q^0 connectivity) species, the size distribution of which is governed by the silica to metal oxide ratio and pH. At ratios with viscosities ideal for coating, i.e., commercial ratios, (3.3 and 2.6 for sodium and potassium silicate solutions respectively), micron sized particles are supposed to exist in solution, which would limit the ability of waterglass coatings to form a silica matrix around a nanoscale template. Here we show that polystyrene nanospheres with diameters as low as 125 nm can be used as sacrificial organic templates to form ordered porosity in waterglass coatings, potential applications of ordered macroporous coatings are discussed.

5.2 Introduction

In **chapter 3** it was shown that waterglass coatings can be made stable by converting to silica, in **chapter 4** it was shown that macroporosity could be introduced into the silica with a sacrificial organic template.

Bottom-up methods for producing ordered macroporosity into silica include hard organic polymer[20,44,132] or emulsion[50,51] templating and macrophase separation.[53,58] The template and matrix material can be coated simultaneously, or the template can be arranged in the desired format in advance and the matrix material applied in a separate step. Polymer nanospheres are often chosen as a template for ordered macroporosity as they can be synthesized in a variety of sizes and with different surface functionality.[44] The most common synthesis is the surfactant-free emulsion polymerization of polymers such as styrene in the presence of an initiator such as potassium persulphate. The size and monodispersity of the nanospheres is controlled by ensuring consistent temperature and stirring speed during the reaction.[40,156] These latex spheres can also be made of silica, their removal requires higher temperatures.

The silicon alkoxide, TEOS, has been used in the form of a sol to make a silica film with PS spheres.[44] The resulting film had well defined but poorly ordered porosity. Dip coating has also been used to infiltrate a PS monolayer with TEOS. The low-speed dip coating process followed by drying (80°C) to hydrolyse the sol was repeated up to 8 times to completely fill the voids of the PS monolayer. The 300 – 400 nm PS spheres were

removed by calcination at 450°C (5°C/min), for 30 mins to produce an ordered macroporous array.[54] Due to its higher viscosity and concentration, it is possible that only a single waterglass dip coating would be required to coat such nanospheres due to the micron scale thickness of films produced from stock solutions. Generating the same viscosity from a silicon alkoxide solution would require ageing of a TEOS sol, a significantly lengthier albeit predictable process.

Crack-free multilayer inverse opal structures (ordered macroporous arrays) have been formed with silica and a polystyrene nanosphere template via evaporation methods, annealing at 500°C to remove the organic template. The concentration of the nanospheres and the matrix material controlled the number of layers in the porous structure.[133]

There are few mentions of using waterglass to template porosity in the literature. Mesoporous silica powders SBA-15 and KIT-6 has been synthesised with block copolymer templates and sodium silicate solution.[59,60] Sodium waterglass and the non-ionic surfactant (Triton X100) have also been used to make mesoporous silica powder.[57] Surface macroporosity has been generated via phase-separation methods by dip coating a solution of sodium waterglass and sodium polymethylmethacrylate. Pore channels were generated by dipping the resulting film in a solution of ammonium bicarbonate (NH_4HCO_3). The pore ordering was sufficient to produce iridescence.[58]

Nordström et al.[78] and Böschel et al.[86] have used dynamic light scattering (DLS) techniques to study waterglass solutions. For the waterglass ratios (~ 3.0) used in this work, their studies showed that the major species present were monomers and clusters of diameters ~ 0.7 and 2.5 to 15 nm respectively. Nordström et al. found that at these ratios a negligible fraction of the silicate existed as colloidal particles of diameters 30 nm or greater. The large particles present may make limit the homogeneity of nanostructured coatings made from waterglass.

Here we show that polystyrene nanospheres can be used to template ordered macropores in potassium waterglass, which can be a viable alternative to silicon alkoxide based-sols with several advantages such as aqueous solution processing and greater viscosity enabling more rapid pore filling upon dip coating, hence requiring fewer coating cycles. Templating with ordered porosity offers the potential for form an ordered nanostructure with a tuneable periodicity, the reflectance of the coatings being controlled by the periodicity, d, (and hence the nanosphere size) and the contrast in the refractive index, n, between the matrix material and the matrix of the void spaces, which is usually air.

$$m\lambda = 2d\sqrt{n_{eff}^2 - sin^2\theta_i} \quad (5.1)$$

This equation, a combination of Bragg's and Snell's laws, also shows that the reflected wavelength depends on the angle of incidence, θ_i.[157] The term n_{eff} is known as the effective refractive index, which is that measured or calculated with an effective medium approximation. The incident wavelength and lattice or interlayer spacing are denoted as λ and d respectively. If coupled with an ultraviolet, visible or near infra-red absorbing material, the structure could offer enhancements in heterogeneous catalysis reactions such as photocatalysis.[158,159] If the matrix were to include a material such as quantum dots, the excitation of the dots could be enhanced.[160] In both types of applications, the periodicity of the matrix is tuned to the absorbance of the matrix material. These materials could also be used as colourimetric or spectroscopic sensors, the well-defined reflectance peak of the sample would be sensitive to small changes in refractive index contrast between the matrix and the void spaces, brought about by infiltrating the structure e.g. with different solvents or gaseous media.[16,157]

In this work the synthesis of ordered macroporous coatings with waterglass and polystyrene nanospheres was explored. Monolayer ordered macroporous coatings were made by first forming a monolayer of polystyrene nanospheres by either drop casting and evaporation or the Langmuir-Blodgett method. The nanosphere voids were filled by dip coating the supported monolayers with diluted waterglass solutions and annealing. Multilayer macroporous silica coatings were made by evaporative assembly in a drying oven. The properties of the coatings were briefly investigated, potential applications are discussed.

5.3 Experimental

Polystyrene nanospheres (diameters 125, 500 nm) were purchased from Micromod. Glass microscope slides, and sulphuric acid (CAS: 7664-93-9) were purchased from Sigma Merck. Potassium waterglass was purchased from Kremer pigments (product number: 77750). Sodium waterglass (extra pure) was purchased from Merck Millipore (CAS: 105621).

Drop casting was done in an evaporating dish lined with cleaned glass substrates (acetone, alcohol, water). The dish was filled with water, the nanosphere stock solution was diluted 3:1 v/v with ethanol and dropped onto the surface until it was visibly covered. The water was left to evaporate for several days. The nanosphere coated glass was coated with waterglass via drop casting, the waterglass was left to dry for several days and then the samples were annealed at 450°C for 30 minutes (2°C/min).

To form a monolayer of the 125 nm spheres a Langmuir-Blodgett trough was used. The trough was cleaned with soap and rinsed with water several times. The trough was then filled with deionised water, a paper Wilhelmy plate was used to measure the pressure at the surface. The surface of the water was cleaned with an aspirator, until the change in pressure upon opening and closing the gates was 0.01 mN/m. Glass substrates were cleaned in the same way as mentioned above and dipped into the trough, the nanospheres were diluted 3:1 v/v with alcohol and added to the trough with a hyperdermic needle attached to a syringe pump. The gates of the trough were closed and the nanospheres dip coated onto the glass at a constant pressure of 10.4 mN/m. Waterglass was dip coated onto the samples using a home-made dip coater, the samples were left to dry in air for a short time before annealing at 450°C for 30 minutes (2°C/min) and then washing with 1M H_2SO_4 for 30 minutes. Multilayer samples were formed by diluting ~ 10 µL of the stock nanosphere suspension in 20 mL deionised water. Once homogenised, 48 µL of the stock nanosphere suspension (1 wt% in water) was added to this and mixed by hand. Glass slides were cleaned and placed in the solution, the vessel of which was placed in a drying oven at ~ 61°C until most of the water had evaporated. The coatings formed were annealed at 500°C to decompose the nanosphere templates, the coatings were then washed with 1M H_2SO_4 for 10 minutes.

A Semilab SE2000 spectroscopic ellipsometer was used to perform spectroscopic ellipsometry (SE) measurements. All SE data analysis was carried out on the Semilabs SEA software (v1.6.2). Silica structures were modelled using a Cauchy dispersion law. Ellipsometry was used to determine the thickness of waterglass films coated onto silicon wafer. The Cauchy model was used for modelling with a set refractive index of 1.5. The dip coated samples were dip coated onto silicon wafer [100], heated to 150°C on a hotplate and washed with 1M H_2SO_4 for 1 minute before ellipsometry. The FTA system was used for contact angle measurements, with droplet volumes of 3 µL. The Shimadzu UV-2600 was used for UV-vis measurements, the integrating sphere attachment and barium sulphate reference discs were used to measure diffuse transmittance and reflectance as well as transmittance scattering.

Atomic Force Microscopy (AFM) images were obtained from a Bruker Dimension Icon atomic force microscope with a Bruker ScanAsyst Air probe (nominal tip radius 2 nm) in ScanAsyst mode.

5.4 Results and discussion

In the first experiment polystyrene nanospheres were cast into an evaporating dish lined with glass and filled with water, leaving the water to evaporate formed both monolayers and multilayers. Diluted sodium waterglass was drop casted onto the nanosphere coated glass at various concentrations and left to dry for several days. The dry coatings were

annealed at 450°C for 1 hour. On only a small area of the samples, well-defined and reasonable well-ordered porosity was formed (**Figure 5.1**). The packing of the spheres was generally hexagonal, but long-range order was not produced by this method.

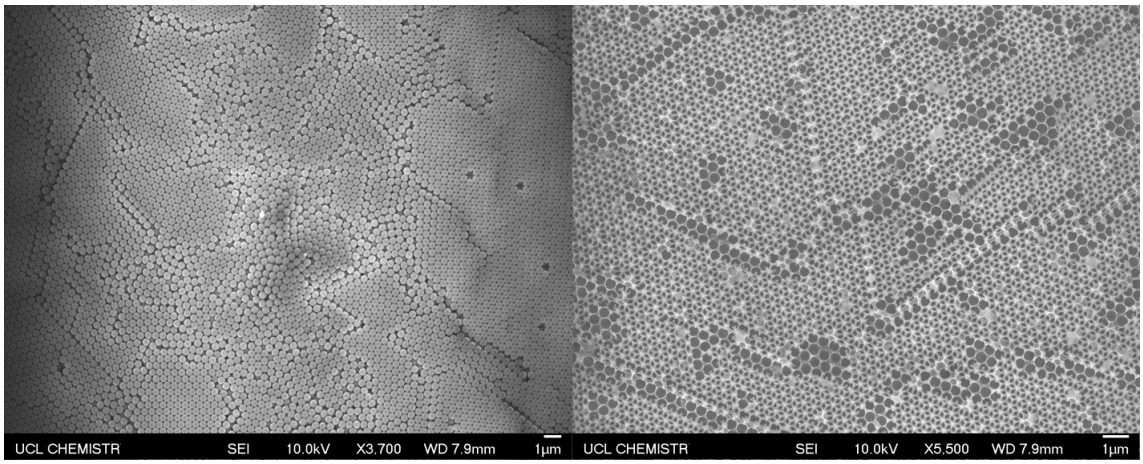

Figure 5.1. The drop casted nanospheres and the corresponding sodium waterglass coating are shown, multilayers were formed in the inverse layer indicating multilayer template formation. Good hexagonal arrangement is seen in the inverse sample. However, this well-ordered porosity was only present on a small area of the sample.

To produce more consistent and homogeneous coatings, the thickness of the waterglass layers was investigated to see the level of control achievable. The dip coating speed and concentration of potassium silicate solutions was varied to obtain dip coating curves (section **3.21**). Ellipsometry was used to determine the film thickness.

Monolayers were formed with the Langmuir-Blodgett method. For this experiment 125 nm diameter spheres were used. The periodicity of nanospheres of this size would be below the diffraction limit for visible light, even if the packing were not as efficient as possible. The filling factor of the nanospheres when close-packed is 0.74 for a hexagonal crystal. The remaining volume was calculated for spheres of this size and halved for the desired hemispherical porosity. From the dip coating curves, coating thicknesses and hence volumes needed to cover the half of the nanosphere monolayers were calculated, this was found to be closest to films produced by 20% KWG solution. For this concentration, several speeds were used to dip coat the waterglass onto the nanospheres (**Figure 5.2**). Speeds of 1 and 0.2 mm/min produced the most homogeneous coatings. Larger samples were produced with waterglass dip coated over the template layer at these speeds.

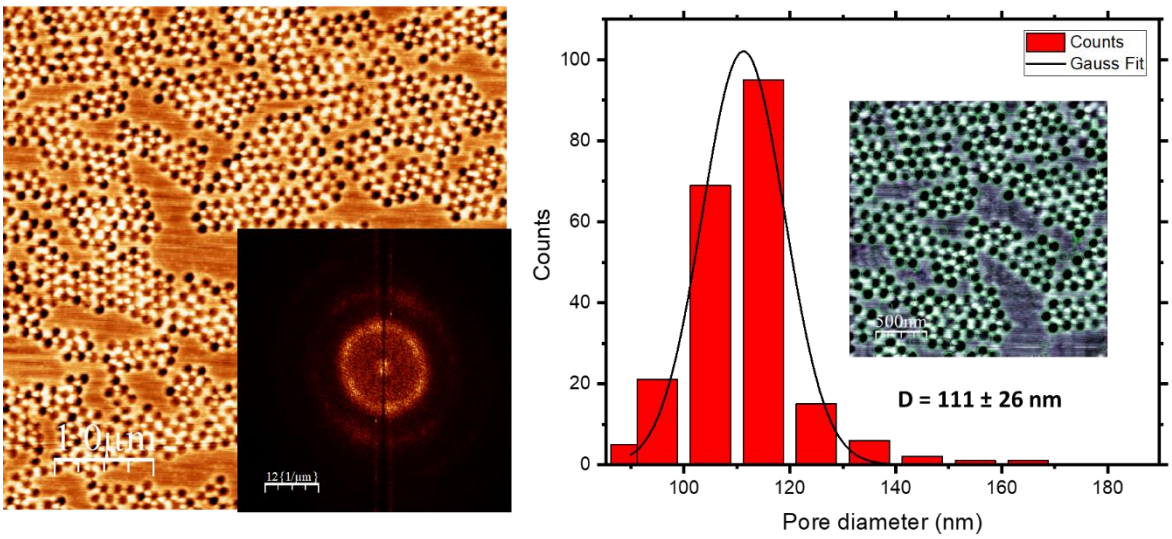

Figure 5.2. The AFM images are shown below, on the left the porosity is visualised, the inset figure shows the fourier transform around the porosity indicating hexagonal pore arrangement. On the right the pore size distribution of a selected area is shown, 111 ± 26 nm.

AFM images in **Figure 5.2** showed the porosity present in the film after annealing and acid washing. Fourier transform of the AFM image showed the hexagonal arrangement of the pores around one another. The pore size distribution was shown to be 111 ± 26 nm.

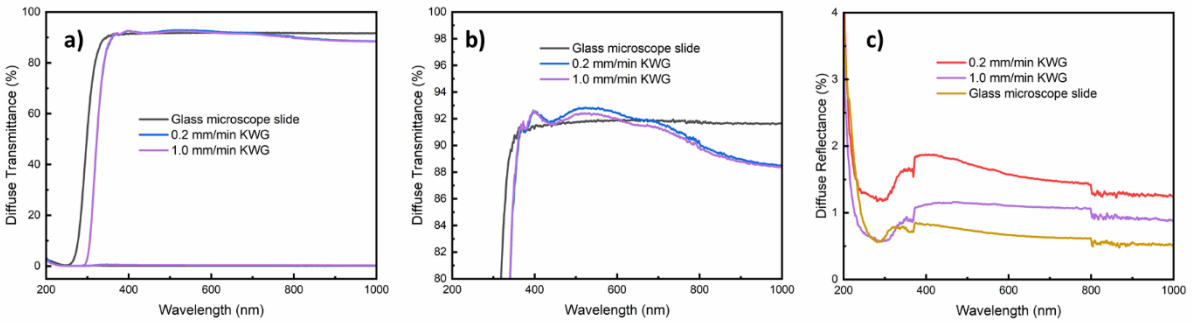

Figure 5.3. UV-vis spectra of macroporous coatings from waterglass. Figures a) and c) show the diffuse transmittance and reflectance, while b) shows a smaller transmittance scale to identify the key differences in the transmittance of the glass and the ordered macroporous substrate. The transmittance of the glass increased slightly in the visible region after coating, however it decreased in the near-IR, the reflectance of the coated samples was generally greater than that of the glass. The transmittance of the porous coating resembled that of barrier glass.

UV-vis spectra of the macroporous coating resembled that of the barrier glass (**Figure 5.3**). In comparison with that of the microscope slide substrate, the absorption edge was red-shifted from an x-intercept of 271 to 299 nm after coating and annealing. While the near-IR transmittance decreased, similar to barrier glass, the visible light transmittance was increased from 91.4 to 92.4% at 400 nm and from 91.8 to 92.7% at 500 nm. The

reflectance of the coated samples was greater than that of the glass microscope slide substrates, 0.2 mm/min reflected just under 2% whereas the 1 mm/min samples reflected around 1%. The scattering in transmittance mode did not increase significantly.

The coated films had a lower contact angle than the glass substrate, the 1 mm/min coating had an average contact angle of 17.4°, whereas the 0.2 mm/min coating had a contact angle of 16.7° (**Figure 5.4**). Extensive surface roughness may have been expected to make the surface superhydrophilic, the clustered porosity may have inhibited complete wetting.

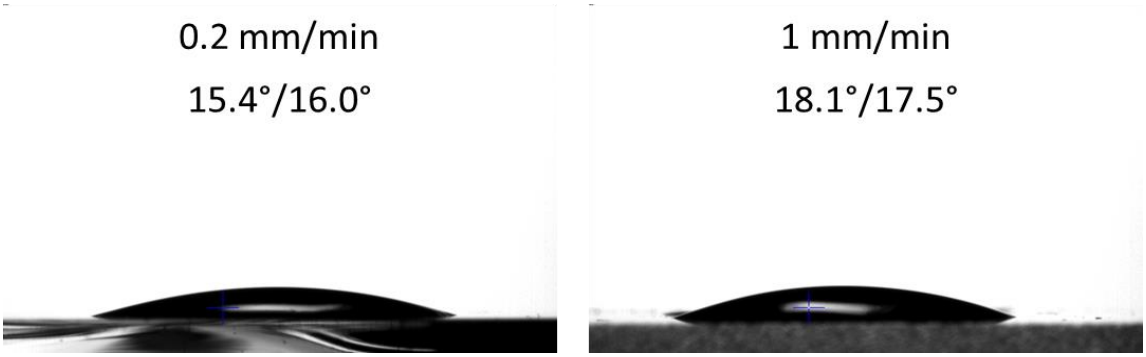

Figure 5.4. The average wetting of the ordered macroporous monolayer inverse coatings is shown. The samples were more hydrophilic than the glass microscope slide substrates.

Table 5.1. The wetting data of the macroporous coatings is tabulated above. LHS and RHS are abbreviations of left- and right-hand side of the droplet image respectively.

Sample	0		1		2		Average	
Droplet side	LHS	RHS	LHS	RHS	LHS	RHS	LHS	RHS
0.2 mm/min	14.5	13.7	15.4	16.0	19.9	16.7	16.6	15.5
1 mm/min	18.1	17.5	22.2	17.9	14.7	16.4	18.3	17.3

The multilayer samples are shown in **Figure 5.5**. Ordered microporosity was generated, however due to high polydispersity of the nanosphere templates, the pore ordering did not strictly obey the expected FCC regime. However, multilayers were clearly formed, the ratio between the silicate and the nanospheres was sufficient for decent connectivity between the nanosphere templates. Large carbonate crystals can be seen at the surface of the sample. The acid washing was insufficient to prevent the formation of or remove any formed carbonate crystals.

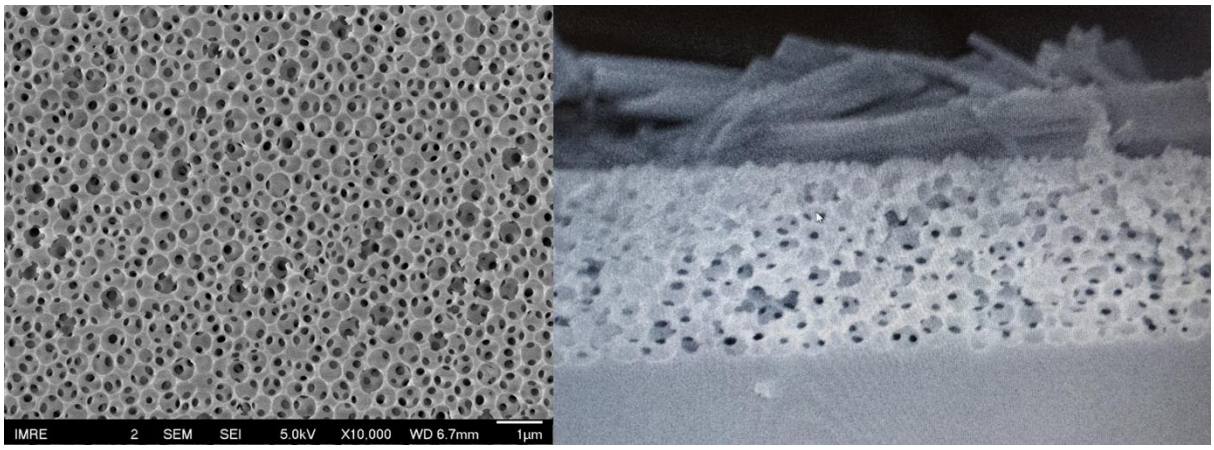

Figure 5.5. On the left a top-view SEM image of the multilayer macroporous sample is shown (scale bar 1 µm). On the right the cross-section of the same coating is shown. Roughly 10 layers of inverse opal material are present. Large potassium carbonate crystals can be seen growing from the surface.

5.5 Conclusion

It was shown that homogeneous, ordered macroporous samples could be formed with waterglass solutions and polystyrene nanospheres. Both monolayer and multilayer structures were formed, the periodicity and pore size distribution were affected only by the quality of the nanosphere templates. The larger silicate solution entities such as clusters and micron sized particles did not interfere with the formation of ordered porosity, despite the porosity being roughly 5 times greater in size then the solution species. It was shown that the dip coating speed and concentration could be tailored to fill the voids between polystyrene nanospheres organised on a glass substrate by the Langmuir-Blodgett technique.

To add additional chemical functionality to the ordered macroporous coating, the silica can either be doped with other metal oxides by adding them to the starting solution, (e.g., zeolites and hetero condensation structures) or by the addition of nanoparticles that will change chemical properties without changing the scattering and transmittance of the coating. The structure can also be coated with a technique that can apply homogeneous coatings to 3-dimensional structures such as dip coating[72] and vapour deposition techniques such as atomic and chemical vapour deposition. An example of the pore coverage achievable with ALD is shown below. Waterglass was coated with aluminium oxide.

In future work this idea should be extended to make mesoporous coatings. It has been shown that waterglass can be used to make bulk mesoporous silica powder using a hydrothermal approach and a block copolymer template. The high reactivity and aqueous medium of waterglass would change the expected chemistry of interactions with typical

mesoporous templates, e.g., CTAB/CTAC, block copolymers, however there are several suitable water-soluble organic templates that would be suitable such a water soluble Pluronics with high percentage hydrophilic content such as F-127. The conditions for multilayer porosity should be optimised to obtain the expected FCC packing, the annealing and washing conditions should also be tuned to prevent carbonate crystal formation. The physical and optical properties of the resulting inverse opals should be investigated. This method would provide a purely aqueous route to inverse opal silica, and potentially more complex heterostructures were the structure to be doped.

6. Oil water separation with waterglass-coated stainless-steel mesh: a density-based approach

6.1 Abstract

A facile method for coating stainless steel to enhance its efficiency in the separation of mixtures of oil and water is presented herein. After dip coating the mesh in potassium silicate solution (waterglass) and a short air drying, the coated mesh was annealed at 500°C. Water separation efficiencies of over 90% were obtained for a range of oil densities and oil and water ratios (3:1, 1:1, 1:3). Motor oil, olive oil and castor oil were chosen for their densities (961, 916, 862 $kg.m^{-3}$), which envelop the density range of crude oil (870 to 920 $kg.m^{-3}$). Saltwater was also used to simulate the separation in a realistic environment and to probe the variation in the densities of the solutions.

6.2 Introduction

Oil spills have a detrimental and long-lasting effect on the quality of marine life. In the most recent major oil spill off the coast of Mauritius, it was estimated that over 1000 tonnes of crude oil were released. Spills such as these result in the 'fouling' of plants and animals, the toxic compounds present in crude oil can cause heart damage, stunted growth and compromise the immune system of animals over time if ingested, while it can cause other animals such as whales and dolphins to suffocate or impair their ability to communicate. In the minutes and hours after a spillage, the oil spreads across the water's surface and evaporates, disperses and emulsifies with the seawater to different extents, depending on the composition of the oil. Some components such as benzene and toluene that do not evaporate may dissolve in small amounts. Over weeks and months, the oil will undergo photo-oxidation, sedimentation and biodegradation. Dispersion of oil fragments into the seawater encourages these latter processes, while emulsification slows them as well as greatly increasing the total volume of oil that can be entrapped in the water.[161] The oil tends to be trapped away from vulnerable areas such as beaches, mangroves and wetlands by booms. The oil can be burnt on the surface of the water; however, the resulting greenhouse gases make this an unfavourable method. Skimmers have been employed to separate oil present at the surface of the water shortly after a spill.

There have been several attempts to develop a coating for stainless steel mesh applied by spray or dip coating as well as solution processing methods that would enable the removal of water from such environments. These tend to be in the form of a superhydrophobic coating applied to the mesh, enabling the oil to pass through while the

water rolls off the top. For example, Lu et al.[162] noted several orientations in which this design could be employed for high-efficiency separation by coating the steel with a low energy silicone elastomer coating, however this method required the steel be pre-etched with $CuCl_2$ solution to enhance the coating adhesion.[162] An alternative iteration of mesh membrane-mediated oil water separation involves using a superhydrophilic coating that accepts water and rejects oil. There are many publications detailing the coating of polymers onto mesh via dip coating or solution methods to impart this effect.[163–166] For example Yang et al.[164] formed a mussel-inspired polydopamine and polyethyleneimine coating on a polypropylene microfiltration membrane in solution, affording superhydrophilicity. The mesh contained micron scale porosity and showed resistance to oil fouling with low density oils such as dichloroethane and n-hexane. This porous membrane could separate emulsions under atmospheric pressure.[164]

Inorganic coatings have also been shown to exhibit superhydrophilicity and highly efficient separation of oil-water mixtures. Wen et al.[167] have grown a superoleophilic and hydrophilic coating of zeolite silicalite-1 (MFI type) crystals on stainless steel mesh with the hydrothermal method, this method also decreased the mesh pore size. They claimed the separation was driven by the difference in density of the two phases, resulting in the water passing through the mesh and the lower density oil remaining above.[167] Zeng et al.[168] coated a zeolite crystal seed layer suspension onto stainless steel mesh, an MFI zeolite coating was grown from this. In air the coating was super amphiphilic, exhibiting a contact angle of less than 5°. Underwater, the coating exhibited superoleophilic contact angles of 160°. The coating exhibited 96 – 98% efficiency in separating low density n-hexane and water mixtures with good recycling capabilities.[168] Other inorganic, superhydrophilic mesh coatings include the use of TiO_2 and ZnO. Li et al.[169] spray coated a suspension of ZnO nanoparticles (mean diameter 70 nm) in acetone and polyurethane onto steel mesh and dried under ambient conditions. This mesh was amphiphilic to oil and water in air with near 0° contact angle, and underwater superoleophilicity (155°). The mesh showed up to 99% separation efficiency and resistance to oil fouling (up to 50 cycles) in the separation of kerosene-water mixtures (over 97%).[169] The same authors also coated steel mesh with TiO_2 nanoparticles applied via spray coating from an acetone/polyurethane suspension. Again, the separation efficiency for kerosene, hexane, petroleum ether, toluene and rapeseed oil in water were up to 99% with oil fouling resistance shown with 97.5% separation efficiency after 40 cycles.[170] Zhou et al.[171] grew titania nanowires on titanium mesh via chemical bath method, the mesh was soaked in a solution of hydrogen peroxide, melamine and nitric acid at 80°C for 12 hours. The textured mesh exhibited underwater superoleophobicity and separation efficiencies of 96 to over 99% for oil with densities ranging from that of aviation gasoline to cyclohexane.[171] Gao et al.[172] produced a hybrid single-walled carbon nanotube coating

decorated with TiO_2 nanoparticles by multi-step solution processing methods. Under UV irradiation the resulting coating had superhydrophilic and underwater oleophilic (>150°) properties. The mesh had high separation efficiencies as high as 99% for toluene and diesel and was shown to be capable of separating emulsions.[172]

As shown previously the waterglass coatings were intrinsically hydrophilic, with contact angles slightly lower than that of glass microscope slides or barrier glass. The addition of a hydrophilic material to stainless steel mesh effectively enhances the surface roughness, and as predicted by Wenzel, enhances the type of wetting typically observed by a flat analogue of the same material. The intrinsically hydrophilic material becomes superhydrophilic when added to the mesh by increasing the surface roughness or in this case surface area of the material.

Here a low-cost, fully-inorganic potassium silicate coating was applied to stainless steel mesh, the oil water separation capabilities of the resulting superhydrophilic mesh under gravity were investigated. The preparation method was simple compared to that of the analogous zeolite-coated mesh. The waterglass was dip coated onto the mesh from aqueous solution within seconds, in comparison the growth of zeolite crystals, which requires hydrothermal methods and annealing can take several days. Furthermore, unlike the zeolite coating no organic template was needed, allowing less intensive annealing and no greenhouse gas production. Moreover, the sample size was limited only by the volume of the dip coating vessel and rather than the volume of the autoclave. The use of high-density oils is not frequently seen in the literature for separations done under gravity. Certain authors have shown their coated-mesh with kerosene or diesel (roughly 820 and 850 $kg.m^{-3}$) and water mixtures.[169,173] In this work the effect of oil density on the extent and efficiency of separation was investigated.

6.3 Experimental

Potassium silicate solution (28/30°) was purchased from Kremer Pigments (product number: 77750). Stainless steel mesh ($FeCr_{18}Ni_{10}Mo_3$, 0.103 mm nominal aperture, 0.066 mm wire diameter, GF36611805) and salt (NaCl, AnalaR NORMAPUR, 27810.295) were purchased from Merck. Deionised water (14.9 - 15.0 MΩ.cm) was dispensed from an ELGA Purelab, option-R 7/15. Castor oil (Pukka), olive oil (refined virgin and olive oils) and motor oil (Shell, Helix, HX7, 10W-40) were purchased from Holland and Barrett, Sainsburys and Shell respectively.

All liquids were used as purchased; saltwater was made by dissolving 35 g of NaCl in 965 g of deionised water. The saltwater solution was stirred vigorously overnight before using. The stainless-steel mesh was cut into ~ 1.7 cm strips and dip coated (10 mm/min)

into the potassium silicate solution without prior treatment. The as coated mesh was dried for 20 minutes in air and then annealed in a furnace (Carbolite) at 500°C (3°C/min), for 1 hour. The annealed mesh was then used for oil water separation without further treatment. The mesh was cut to an appropriate size and placed between two Teflon plates housed in a copper ring for the oil water separation. Oil and water (O:W) mixtures of three different ratios (3:1, 1:1, 1:3) were weighed (10 g total per separation) into a Teflon beaker (oil in, %). The contents of the beaker were poured over the mesh and the separated water was collected in an evaporating dish. The water was pipetted out of any oil that passed with it through the mesh and into a separate container and weighed (water out, %). The evaporating dish and any separated oil were also weighed (oil out, %) at this point. Between measurements the mesh was rinsed with deionised water and any residual liquid was pipetted from the tubes on either side of the apparatus.

The contact angle images of the deionised water, saltwater and oils on the mesh samples were captured with the First Ten Angstroms (FTA) contact angle system. The contact angle was calculated using the FTA drop shape analyser, except for that of motor oil which was very hydrophilic with respect to the coated mesh, for which the contact angle was measured by hand. Scanning electron microscopy (SEM) images were collected with the JEOL 7600 at 5.0 kV and a working distance of 8 mm. Fourier transform Infrared (FTIR) data was collected with the Shimadzu 100-Tracer in transmittance mode, with a resolution of 2 cm^{-1}, (20 scans, Happ-Genzel apodisation).

6.4 Results and discussion

After dip coating (10 mm/min) in waterglass (KWG) the mesh was dried for 20 minutes before annealing at 500°C (3°C/min), for 1 hour. The annealed mesh was used for separation with no further treatment. Increasing the dip coating speed (30, 60, 120 mm/min) did not seem to increase the thickness of the coating or decrease the size of the pores. (**Figure S6.1**). The oil/water mixtures were poured into a tube attached to the top of the metal housing holding the PTFE plates and mesh. The results of the separation experiments are shown in **Figure 6.1**.

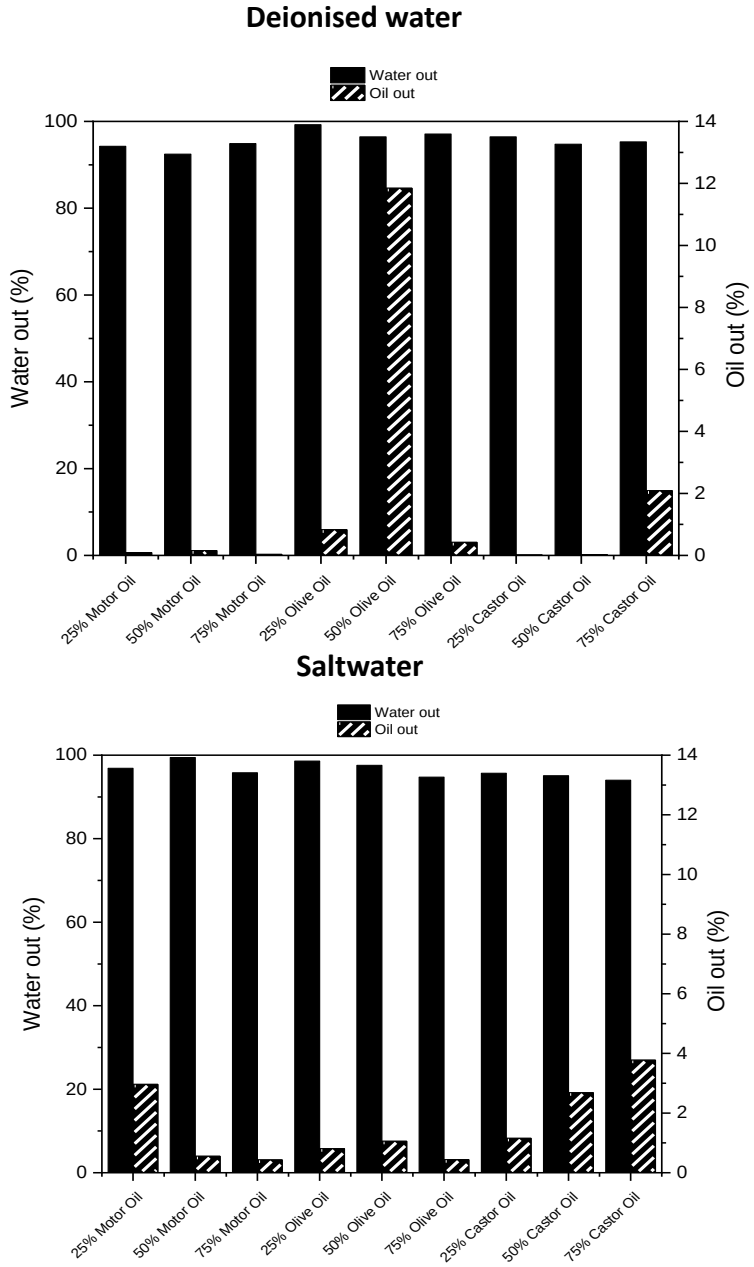

Figure 6.1. Oil water separation data for the different oil densities and ratios with water. Both deionised and saltwater were mixed separately with oil and poured over the KWG coated mesh. Separation rates were generally over 92%, some oil passed through with the water, the amount of oil passing through was generally lower with deionised water-oil mixtures, however the use of saltwater prevented significant amounts of oil passing through the mesh for 50% olive oil mixtures.

The water and saltwater separation rates varied from 92 to 99% and 94 to 99% respectively. The percentage of water collected was generally the highest for O:W ratios of 1:3 and lowest for 3:1, but this trend was not consistent. There was no clear relationship between the density of the oil and the separation rates. The percentage of oil coming out of the mesh was below 2.1% and 3.8% for deionised water and saltwater respectively, with the exception of olive oil. For O:W ratios of 3:1 and 1:1 the olive oil flowed through the mesh after the water had passed through, this was particularly rapid for a ratio of 1:1, for which 11% of the oil had passed through the mesh within the time of the measurements. This did not occur for castor oil or motor oil despite their densities being the closest and furthest to that of the water respectively. With saltwater the olive oil remained above the mesh indefinitely.

Separation speeds were also slowed by the formation of emulsion droplets in the oil water mixture above the mesh. In some cases, particularly when the majority of the water had already passed through the mesh, this prevented the water from passing through the mesh and limited the separation rate. Isolated water droplets that themselves had become emulsified at the bottom of the oil phase would pass through the mesh several minutes after the bulk of the water had passed through. For lower oil contents there was insufficient pressure from the oil layer to push all of these emulsified water droplets through. Emulsified oil/water droplets enabled more of the oil to pass through the mesh.

Table 6.1. The density, viscosity and contact angle on the KWG-coated mesh of each of the oils and the water used in the separation experiments are shown in the above table.

	Density (20°C)	Dynamic Viscosity (20°C)	Contact angle on KWG mesh
	$kg.m^{-3}$	mPa.s	°
Saltwater	1025.00	1.09	0.0
Deionised water	998.20	0.87	0.0
Castor oil	961.00	650.00	23.4
Olive oil	916.00	84.00	38.8
Motor oil (10W-40)	862.90	208.89	8.2

Repeat use of the mesh sometimes resulted in slower separation. This was not an issue for castor or olive oil, however repeated separation of motor oil/water mixtures with mesh resulted in very slow separation of O:W ratios 3:1 and 1:1. This is likely due to it having the lowest density and thus the greatest difference in density between the two phases in the mixture and above the mesh. When separation was slow the phases would separate out above the mesh and then roughly 30 s to 5 minutes later the bottom water phase would rapidly pass through.

The contact angle data of the water and oils on the KWG-coated mesh are shown in **Table 6.1**. Both deionised and saltwater were superhydrophilic (contact angle of 0°) with respect to the coated mesh, with wetting times of 0.70 and 1.70 s respectively (**Figure S6.3**).

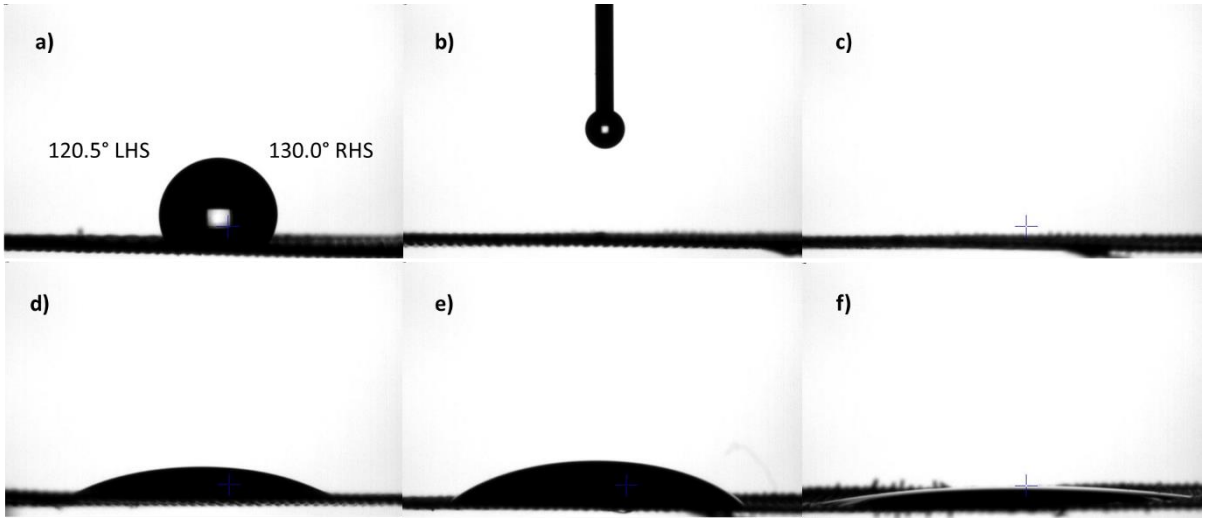

*Figure 6.2. Image a) shows the contact angle of deionised water on stainless steel mesh. The water was superhydrophobic with respect to the porous steel surface. Contact angle photos of the water and oils on KWG mesh are also shown. Both b) deionised and c) saltwater had 0° contact angle on the coated mesh. The coated mesh surfaces were all oleophilic, however the oil did not pass through the mesh after coating, whereas all oils passed through the uncoated mesh (**figure S6.6**). Castor oil d), olive oil e) and motor oil f) all partially wetted the top side of the coated mesh without passing through.*

The KWG coated mesh samples were oleophilic with contact angles of 20.1°, 10.6° and 32.5° for motor, olive and castor oil respectively. The contact angles on the mesh decreased in the order olive > castor > motor oil (**Table 6.1**). It could be seen that the motor oil partially wetted the mesh. Oil droplets would often pass through the uncoated mesh but did not penetrate the pores after KWG coating despite their oleophilic nature.

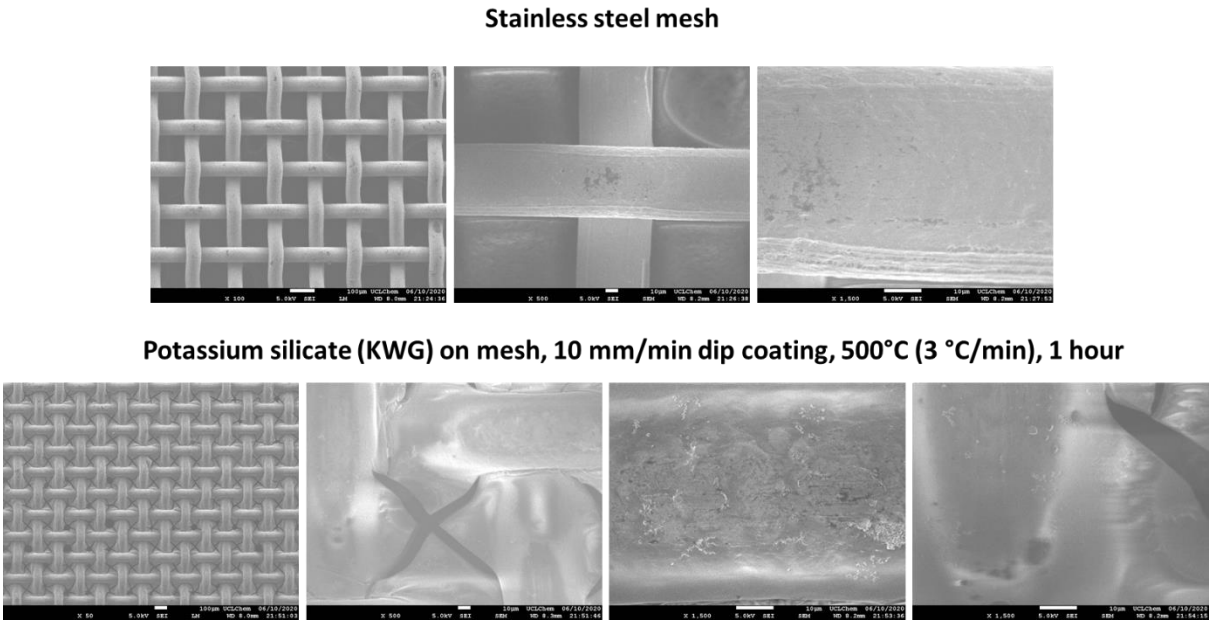

Figure 6.3. SEM images of the mesh are shown above. Below the KWG-coated mesh is shown, the porosity created has a cross shape (scale bars, images on the left side top and bottom, 100 µm, all other images 10 µm). The mesh was coated at 10 mm/min with dip coating and annealed at 500°C, (3°C/min), 1 hour dwell time.

SEM images (**Figure 6.3**) show the porosity of the mesh, the structure was retained after separation for all types of oil. FTIR spectra recorded in transmission mode showed no signal for the mesh alone indicating that there are no components of the steel that undergo a change in dipole moment when probed by infrared light of these energies (**Figure 6.4**). The addition of KWG can be observed by the presence of bands around 1250 to 1000 cm^{-1} and 1000 to 550 cm^{-1} representing bridging and non-bridging oxygens of the potassium silicate. After separation of each of the oils, trace oils remaining on the mesh give rise to distinct bands. Typical hydrocarbon signals are observed in spectra for the mesh samples between the ranges 2800 - 3100 cm^{-1}, 1700 – 1800 cm^{-1} and 900 – 1400 cm^{-1} corresponding to the C-H stretching, C=O stretching and C-H bending respectively.[174] While their features were very similar each oil could still be distinguished. Motor oil residue was identified from the absence of the carbonyl band (~ 1740 cm^{-1}), in the motor oil sample the band representing surface silanol (3620 cm^{-1}) was most intense[175,176] .This frequency is closest to that usually attributed to silanol stretching (~ 3660 cm^{-1}, vicinal or geminal), but in this situation where residual water is likely to be present, this peak could also be assigned to silanol hydrogen bonded to molecular water that usually occurs at 3540 cm^{-1} in silica films.[104] The surface bound water peak was broader in the 3350 – 3500 cm^{-1} range than for the other samples and spread below the C-H stretching bands in all samples. The corresponding 1630 cm^{-1} molecular water peak was also most intense for this sample. The prevalence of these water peaks suggests that separation with motor oil results in the most water residue, perhaps due to the motor oil-water mixture emulsifying to the greatest extent during repeated separations. Both

castor and olive oil featured the carbonyl peak (1745 and 1743 cm^{-1} respectively). Spectra of both oils were very similar, in both a broad peak spread below the C-H stretching bands and the silanol band was of similar intensity. The major difference was the presence of a broad and symmetrical band between 3100 and 3600 cm^{-1} in the castor oil mesh sample, this has been shown to be a feature present in castor oil and absent in olive oil spectra.[174,177] Again, this would suggest more surface bound water on the castor oil sample than the olive oil, suggesting that the order of water retention and potentially emulsification is olive < castor < motor oil.

In the KWG mesh spectra, the broad band from 2000 to 1250 cm^{-1} signifies the presence of surface bound water, however the silanol peak is absent. The carbonyl efflorescence[116] peak that emerges around 1450 cm^{-1} is likely present underneath the broad surface bound water peak. Carbonates were seen as surface inhomogeneities and dark patches in the SEM images.

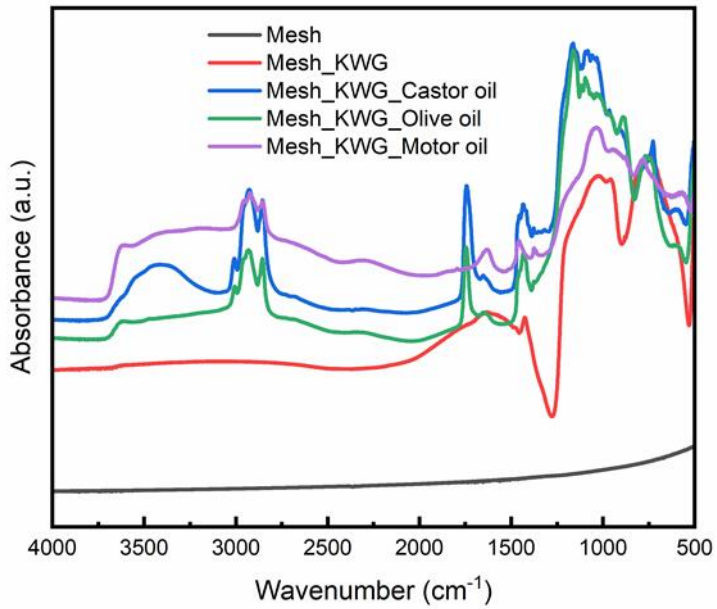

Figure 6.4. The FTIR transmission data of the uncoated stainless-steel mesh is shown as the baseline. The KWG-coated mesh featured distinct silicate signals between 500 - 1250 cm^{-1}. After separation, the coatings contained trace amounts of oil, which could each be seen and identified through their distinctive FTIR features.

6.5 Conclusion

Potassium silicate solution was dip coated onto stainless steel mesh and annealed. The coated mesh successfully separated mixtures of oil and water with separation rates consistently above 90%. Some oil passed through the mesh, particularly alongside the water due to the formation of emulsion droplets. Only for olive oil/water mixtures did oil continue to drip through after the water and this did not occur with higher density saltwater, which increased the difference in density between the two phases. The use of saltwater showed the potential for this formulation to be used in the removal of crude oil from seawater. The densities of the oils chosen envelope that of crude oil (870 to 920 $kg.m^{-3}$). The separation rate remained high at all ratios, there were no clear trends between the density of oil or oil to water ratio and the separation rate.

Increasing the dip speed did not significantly increase coating thickness. Thicker coatings could be obtained by dip coating in the capillary regime (speeds less than ~ 1 mm/min), but the coatings obtained at much faster speeds were sufficient for the purposes of this study and exhibiting the facile nature of the preparation method. In practice the coating could be easily applied to large pieces of mesh. Should the potassium silicate coating become contaminated, it could easily be removed in strong base and a fresh coating reapplied to the mesh. The annealing temperature of 500°C was chosen to ensure curing of the waterglass, but in theory temperatures just over 200°C would be enough to cure the waterglass sufficiently through the removal of water and consolidation of the silicate structure to prevent redissolution.

The vulnerability of the setup to the formation of emulsion droplets was an issue that warrants further study, this could be tackled by introducing further decreasing the pore size or inhibiting the formation of an emulsion in the oil water mixture.

The mesh could be tested at larger volumes to see if the density-based approach to oil water separation can be applied to volumes of oil and water mixtures appropriate to the intended application. In accordance with wetting theory, texturing the coating with additional roughness may encourage better oil-repellency as seen with zeolite-based mesh coatings. However here it was seen that the potassium silicate coating alone was capable of highly efficient separation even in the absence of nanoporosity commonly seen in other works.

7. Fully inorganic perovskite quantum dots supported on foamed sodium silicate films as colorimetric or fluorescence sensors for organic solvents through homogeneous drop casting

7.1 Abstract

The low stability of $CsPbX_3$ (where X = Cl, Br, I) perovskite quantum dots owed to their low energy of formation and moisture sensitivity is one of the major issues currently hindering their commercial viability. Numerous encapsulation approaches have been attempted to improve their tolerance to polar solvents, light, heat and air. Here we present a simple, low-cost support film for fully inorganic $CsPbBr_3$, $CsPb(Br_xI_{1-x})_3$ (where x = 10% or 40%) and $CsPbI_3$ perovskite quantum dots based on sodium waterglass solution. High surface area, macroporous silicate supports were fabricated by spin coating and subsequent annealing. The bumpy topology of the foamed films inhibited coffee ring formation of the drop casted quantum dots directly from toluene solution without excessive washing. After drop casting the colloidal solutions and drying in air, the supported quantum dots exhibited bright, long lasting photoluminescence (over 21 days for $CsPbBr_3$, $CsPb(Br_xI_{1-x})_3$ and over 13 days for $CsPbI_3$), not usually observed on flat glass substrates. Notably, the anion exchange of mixed halide quantum dots observed in colloidal solution was prevented when immobilized on films; the lifetime of the iodide-based quantum dots was extended over that of its unwashed colloidal solution when supported, with superior quantum yield. Solid state, room temperature anion exchange of supported mixed halide quantum dots was shown to be possible through exposure to organic vapour for application as a colourimetric or fluorescence emission peak sensor.

7.2 Introduction

Perovskite quantum dots (PQDs) have emerged as a class of semiconductor nanocrystals (NC) with optical properties superior to those of II-VI (e.g., CdSe) and III-V semiconductors. Fabricated with cheap, simple solution phase techniques[178] and narrow size distribution,[179,180] their high photoluminescence quantum yield (PLQY) and narrow emission linewidths (12 - 50 nm)[178] make them viable candidates for solar cells,[181,182] LEDs, photovoltaics, photodetectors and lasing applications.[183–188] Other than solution phase synthesis, soft templating has also been used to make monodisperse colloidal perovskite solutions of 1-dimensional (1D) nanowires[183,189] 2D nanoplates[190–194] and 3D nanocubes.[195–198] The room temperature photoemission rates of PQDs are ~ 20 times greater than those of typical II-VI and III-V semiconductor QDs due to the lowest energy exciton sublevel in the $CsPbBrX_3$ fine structure being a bright triplet state.[199] This is in contrast to other inorganic semiconductors that typically feature a low lying dark-exciton state in which transitions to the ground state are dipole-forbidden, which greatly hinders the speed and quantity photoemission. In the 3D perovskite structure of formula ABX_3, cation A (e.g. Cs^+, $CH_3NH_3^+$) occupies lattice corners, surrounding an octahedral arrangement of halide anions (Cl^-, Br^- or I^-) with a divalent transition metal centre (e.g. Pb^{2+}, Sn^{2+}).[188] The range of PQD emission wavelengths can be manipulated across the entire visible spectrum by synthesizing with different A or X site substituents or QD size reduction to induce greater quantum confinement.[193,200,201] Post-synthetic band gap fine-tuning can be executed via substitution of the highly labile halide anions without disruption of the NC shape or crystal structure and has been demonstrated in both colloidal solution[202,203] and solid state.[183]

Despite their exceptional properties, commercialisation of PQD products is hampered by the spontaneous anion exchange that occurs upon mixing of different PQD halide compositions.[179,200,204] Furthermore, PQDs become unstable upon exposure to light, air and high temperatures[185–187,205,206] due to their low energy of formation;[187] the strong ionic character of their bonding makes them highly unstable in polar solvents.[178,179,201] Fully inorganic $CsPbX_3$ NCs benefit from a greater melting point (400 - 500°C) than their hybrid counterparts (e.g. $FAPbI_3$ ~ 290 - 300°C).[178] While $CsPbCl_3$ or $CsPbBr_3$ PQDs are stable at room temperature, the ideal cubic phase of $CsPbI_3$ is only stable at temperatures >315°C resulting in the formation of a metastable 3D (α) orthorhombic phase at room temperature that spontaneously converts to the wide bandgap 1D (δ) orthorhombic phase, distinguished by the formation of a yellow precipitate.[207]

Viable strategies to stabilize PQDs include post-synthetic surface passivation or encapsulation. Ligand passivation has been used to stabilize the cubic phase of $CsPbI_3$[207] and improve their air, water and photostability.[208–210] Encapsulation has been

demonstrated with polymers (e.g. PVP/silicone,[206] ethylcellulose,[211] polystyrene,[187] hydrophobic polymers[201] etc.), silica, polyhedral oligomeric silsesquioxanes (POSSs),[205] an AlO_x coating applied via atomic layer deposition (ALD)[186] and more recently boro-germanate glass,[212] all of which inhibit anion exchange and improve stability in water. The use of an insulating encapsulant provides additional thermal stability. Encapsulation in porous materials is another route to preventing anion exchange and increasing stability to heat, light and air, PQDs being incorporated either post-synthetically or in-situ using the porous support as a hard template. Numerous solution and gas phase methods of hard template infiltration have been developed for II-VI and III-V semiconductor QDs, however products were poorly photoluminescent due to the generation of numerous deep-band gap defect states introduced by interfacial interactions between QDs and the support.[213] Hybrid lead halide perovskite NCs with significant quantum confinement were first synthesised ligand-free by Kojima et al.[214] using porous alumina powder as a hard template, producing supported, polydisperse PQD NCs of $CH_3NH_3PbBr_3$. The same method was later used to support hybrid mixed halide QDs,[215] and was employed in the production of perovskite solar cells,[216] however the level of quantum confinement of these QDs will not have been significant considering the polydisperse porosity. Ligand-free hard templating has also produced monodisperse hybrid and inorganic QDs in ordered microporous metal organic framework (MOF)[217] and mesoporous metal oxide thin films[218,219] and powders,[188,213] using the ordered mesoporosity (2 - 50 nm) to control QD confinement. Soft templated, colloidal all inorganic PQDs have also been supported in mesoporous silica;[204] hybrids have been incorporated into their block copolymer templated synthesis, however the latter featured both layered 2D- (A_2MX_4) and 3D-type perovskites.[220]

PQDs have been shown to maintain bright PL on a variety of supports (e.g. silica and alumina) without further surface passivation (required with II-VI and III-V QDs); surface dangling bonds[202] and interaction with support materials do not introduce low-lying trap states in their bad gap. This so called ‘defect tolerance’ stems from several factors; the alignment of the Pb(6s)-I(5p) antibonding and Pb(6p)-I(5p) bonding orbitals[178] and spin orbit coupling of the Pb(6p) atomic orbitals, which widens the conduction band (CB) and lowers the conduction band minimum (CBM).[221] The fortuitous electronic structure results in vacancy defects either falling into resonance with the NC bands or forming shallow trap states that negligibly inhibit the movement of charge carriers across the band gap.[178,213,221] Dangling bonds introduced by anion vacancies result in few surface defects being introduced into the bands or the creation of shallow trap states, indicating that supports, encapsulants, electronic passivators such as ligands, and coatings will not introduce significant trap states into the stop gap.[202,213] Additionally, the highly localised ionic bonding in the PQD structure allows lattice charge neutrality to be easily maintained

upon the formation of X^- and A^+ site vacancies (V_X and V_A). Other point defects such as interstitials and antisites often have energetically unfavourable formation energies which are well above those of the perovskite compound.[178]

Waterglass (soluble silicate) solutions are synthetic, fully inorganic chemicals,[73] whose composition is defined by the ratio, SiO_2/M_2O (where M = Li, Na, K).[222] Higher ratio solutions result in larger silicate clusters but also feature a greater size distribution of species present, including monomers.[78] Commonly used ratios of industrially produced waterglass are 2.5, 3.2 and 3.9.[125] They are more chemically stable (far less prone to combustion) and less toxic than hybrid silicon alkoxide monomers, (tetraethylorthosilicate (TEOS), tetramethylorthosilicate (TMOS)).[56,125] They are also cheaper than monomeric solutions, as they are made directly from natural quartz deposits,[56] sodium waterglass being the cheapest and most commonly produced of these.[125,222] The molten salt resultant from the fusing of silica sand and soda ash at 1100 - 1200°C is dissolved in water:[56]

$$Na_2CO_3 + SiO_2 \rightarrow Na_2SiO_3 + CO_2 \quad (7.1)$$

These viscous, transparent solutions tends to be overlooked in routine silica synthesis due their polydispersity, identified by the wide range of Si connectivity signals (mainly Q^1-Q^4) observed by FTIR[83,124,223] and ^{29}Si NMR. Greater control of the hydrolysis-condensation polymerisation kinetics of monomeric (Q^0) solutions makes them preferable for silica synthesis.[56,224–226] Lowering the pH of waterglass causes rapid polymerization and significant condensation may be disrupted by the presence of alkali metal cations;[56] nevertheless mesoporous powders (SBA-15, KIT-6) with long range structural order have been synthesised from sodium waterglass.[57,59,60,119,224] Waterglass has been used as an inorganic adhesive[125] and anti-corrosion coating for metals, as an antireflection coatings,[226] and as an industrial silica source in the production of paints and detergents.[222]

Here we demonstrate the bright PL of fully inorganic PQDs immobilized on macroporous sodium silicate films. Film composition was investigated with XRD, EDX and XPS; XPS and FTIR were used to identify surface species present at the film/QDs interface. Supported QDs exhibited bright PL; to determine their stability, PL and PLQY of the supported QDs were measured over a period of 21 days for $CsPbBr_3$ and $CsPb(Br_xI_{1-x})_3$ (where x = 10%) and 13 days for $CsPbI_3$ QDs. Anion exchange of supported mixed halide QDs was largely inhibited, $CsPbI_3$ QD lifetime was extended by at least 8 days when supported, accompanied by a greater PLQY than $CsPbI_3$ solution. The intentional anion exchange of the sodium silicate supported mixed halide QDs in the presence of organic

vapour is explored for use as a qualitative, colourimetric or fluorescence emission peak sensor.

7.3 Experimental

Materials

Sodium waterglass (ultrapure, MerchMillipore) was purchased from Sigma Aldrich. The SiO_2/Na_2O ratio was estimated from the acidimetric ratio given by the supplier. Analytical reagent grade acetone (CAS number 67-64-1, 99.98%) and formaldehyde (CAS number 50-00-0, 37% aqueous solution) were used for sensing experiments.

Experimental

Waterglass solution was used as purchased. Glass substrates were cleaned by washing in acetone, teepol, IPA and water, and dried with compressed air. Waterglass was statically spin coated onto the glass substrates. Three successive coatings were applied at 4000, 3000 and 2000 rpm (2000 acceleration, 30 s), samples were dried in air before applying additional coatings. The waterglass films were cured in a furnace at 590°C for 1 hour (10°C/min) to produce foamed, translucent waterglass substrates.

$CsPbBr_3$, $CsPb(Br_xI_{1-x})_3$ (where x = 10% or 40%) and $CsPbI_3$ quantum dots were synthesised by the hot-injection method as described by Protesescu et al.[195] To prepare cesium oleate, 0.2035 g of $CsCO_3$ was loaded into a 25 mL three-neck flask along with 10 mL of octadecene (ODE) and 0.625 mL of oleic acid (OA). The reaction system was dried under vacuum at 120°C for 1 h and then heated under N_2 to 150°C until all $CsCO_3$ reacted with OA. In another three-neck flask, ODE (5 mL), PbX_2 such as $PbBr_2$ (0.069 g), PbI_2 (0.087 g) or their mixtures were loaded together with oleylamine (OAm – 0.5 mL) and OA (0.5 mL) and dried under vacuum for 30 min at 120°C. After complete solubilization of PbX_2 salt, the reaction temperature was raised to 140°C and Cs-oleate solution (0.4 mL) was quickly injected. After 5 sec, the reaction mixture was rapidly cooled down in an ice-water bath. To the crude solution, 5 mL of tert-butanol was added following by centrifugation at 8000 RPM for 10 min. The supernatant was discarded and the precipitate was dispersed in toluene at a concentration of ~ 75 mg/mL. The colloidal solution was drop casted onto the waterglass films until covered and left to dry in air. The average mass of each drop was 0.0073, 0.0081 and 0.0083 g for the iodide, bromide and 40% mixed halide solutions respectively. Drop casting was carried out three times, fewer coatings would fade in patches after 1 – 2 days. The dry films were stored in the dark between measurements. Colloidal QD solutions were stored at 4°C between measurements. QD solutions were also drop casted onto glass microscope slides, however the drop casted solution did not dry in air or in a vacuum sealed dessicator and so PL measurements could not be carried out on these samples.

Organic vapour sensing experiments were carried out by fixing the $CsPb(Br_xI_{1-x})_3$ coated films at the opening of a vial containing 5 mL acetone or formaldehyde. The vial was

sealed and the solvent vapourised for up to 3 minutes. The PL emission wavelength of the films was characterized before and after acetone vapour exposure.

Characterization

X-ray diffraction was carried out using a D8 lynx-eye thin film diffractometer, with a Cu Kα source (1.54 Å). Data was collected between 4 and 50° 2θ, with a θ angle of 0.8° and 0.5 s/step collection time per degree 2θ, (0.05 SEP).

Field emission scanning electron microscopy (FESEM) images and energy dispersive X-ray spectroscopy (EDX) data were collected on JEOL 6701 and JEOL 6700 instruments respectively, the samples were sputtered with gold or carbon before analysis. Sample heights and working distances of 8 and 15 mm were used for SEM and EDX respectively. SEM images were collected at 10 kV. EDX data tabulated in **Table S1** was calculated from the average of area scans from 3 spots, using a voltage of 10 kV at 140 × magnification.

X-ray Photoelectron Spectroscopy was conducted on a Thermo Scientific K-alpha spectrometer with monochromated Al Kα radiation, with a dual beam charge compensated system and constant pass energy of 50 eV (spot size 400 μm). Survey scans were collected in the binding energy range 0 – 1200 eV. High resolution peaks were used for the principal peaks of C 1s, O 1s, Na 1s and Si 2p. Data was calibrated using the Au 4f 7/2 orbital (binding energy, 84.0 eV) from gold sputtered onto a glass substrate. Data was fitted using CasaXPS software. Atomic percentages were obtained from the XPS survey spectra. Relative sensitivity factors (RSFs) were used to scale the atomic percentages of the elements for their interactions with X-rays so they could be compared directly. RSF values used for C 1s, O 1s, Na 1s and Si 2p were 1.00, 8.52, 2.93 and 0.817 respectively.

The standard deviation of all XPS data was ± 0.2 eV. The atomic composition data was used to estimate the SiO_2/Na_2O and O/Si ratios of the films. Fourier transform infrared (FTIR) spectra were recorded with a Shimadzu IR Tracer-100 with an attenuated total reflection (ATR) attachment, measured in the mid-IR region (4000 - 400 cm^{-1}). The uncoated films were pressed into the ATR monolithic diamond crystal (Quest ATR accessory) before data collection. Measurements were carried out with a spectral resolution of 8 cm^{-1} and averaged over 20 scans.

Absorbance spectra were collected on the Lambda 950 between 400 and 800 nm. In the UV-visible region, data was collected with integration time, scan speed and slit widths of 0.04 s, 2000 nm/min and 4.00 nm respectively. In the near-IR region these parameters were set to 0.04 s, 3000 nm/min and 1.00 nm respectively. The background was

collected using barium sulphate ($BaSO_4$) plates as a reference. Solution data was normalised, second derivative analysis was used to find points of inflexion. Band gaps were calculated using a Tauc plot and the path length, d, was accounted for in the following relationship for the absorption coefficient; α = (2.303 × A) / d, where A is the measured absorbance. The path length was the substrate thickness (1.0 mm). Diffuse transmittance and reflectance of the substrates were collected on the Shimadzu UV-2600 with an integrating sphere attachment.

Photoluminescence quantum yield (QY) and emission data were collected on a Horiba FluoroMax-4 spectrofluorometer equipped with a PMT detector. For quantum yield measurements samples were placed in an integrating sphere, neutral-density filters and variation of slit widths were used to prevent detector saturation and to determine the excitation wavelength and band pass needed to standardise the detected number of counts (1×10^6 a.u.). Quantum yield, φ_f, (± 5%) was calculated with data from four emission spectra to determine the ratio of emitted to absorbed photons:

$$\varphi_f = \frac{E_C - E_A}{L_A - L_C} \tag{7.2}$$

Where L_A and L_C are spectral data collected to determine scattering of the uncoated and QD coated silicate films respectively and E_A and E_C are the fluorescence emission spectra of the blank substrate and QD sample respectively. The number of absorbed photons was determined from the difference in the intensity of the scattering peaks of the blank and sample, (i.e., to calculate and eliminate the influence of substrate scattering), whereas the number of emitted photons was calculated directly from the sample emission spectrum. This process was also carried out with solutions, with toluene and QDs in toluene as the blank and fluorescing samples respectively.

Time-resolved photoluminescence data was collected via time-correlated single photon counting (TCSPC) using a fluorescence spectrometer (Edinburgh Instruments) at an excitation wavelength of 350 nm. Samples were each measured on two spots, the corresponding lifetime data from exponential decay fitting was averaged. The curves were fitted to an exponential decay equation;

$$A(t) = A_1 exp\left(\frac{-t}{\tau_1}\right) + A_2 exp\left(\frac{-t}{\tau_2}\right). \tag{7.3}$$

Average PL decay lifetime was calculated as follows:

$$\langle t \rangle = \frac{\int_0^\infty tI(t)dt}{\int_0^\infty I(t)dt}. \tag{7.4}$$

Radiative lifetimes were calculated using the following relationship:

$$\tau_{r,X} = Q^{-1}\langle\tau_X\rangle, \tag{7.5}$$

where Q is the experimentally determined quantum yield of the quantum dots and $\langle\tau\rangle$ is the average exciton lifetime.

7.4 Results and discussion

Sodium waterglass solution was spin coated onto glass substrates. Three coatings were applied to each substrate, the films were dried in air for several minutes between successive applications. The resulting films were annealed for 1 hour at 590°C. XRD revealed both films to be amorphous (**Figure S7.2**). SEM images (**Figure 7.1**) show the wide, micron scale pores of the films' underlying macroporosity. Cross-sectional SEM images showed the films were between ~ 15 - 150 µm thick, the thickness variation was generated by the random nature of the foaming process; the drastic changes in surface topography were made evident by the contrast in SEM images. The difficulty in distinguishing films and the glass substrate post-annealing via indicated either fusion during thermal consolidation but could also have been due to their similar composition. The films mass was used to calculate an estimate for the average film thickness (**Figure S7.3**), assuming a solid sodium silicate density of 2.4 g/cm^3, this gave a value of 358 µm. Considering that the pore wall thickness observed with SEM was only ~10 um, this would suggest that the foamed portion of the silicate was only part of the film and a significant portion of the films mass remained unfoamed under the surface.

QDs were drop casted onto glass microscope slides and foamed waterglass films from their toluene solutions. QDs drop casted on glass from toluene solutions exhibited coffee-ring type inhomogeneity (**Figure S7.4**), only bromide QDs successfully dried on the flat glass microscope slide substrates before losing their fluorescence. The topology of the foamed waterglass films enabled visibly homogeneous coverage of the drop-casted QDs of all compositions.

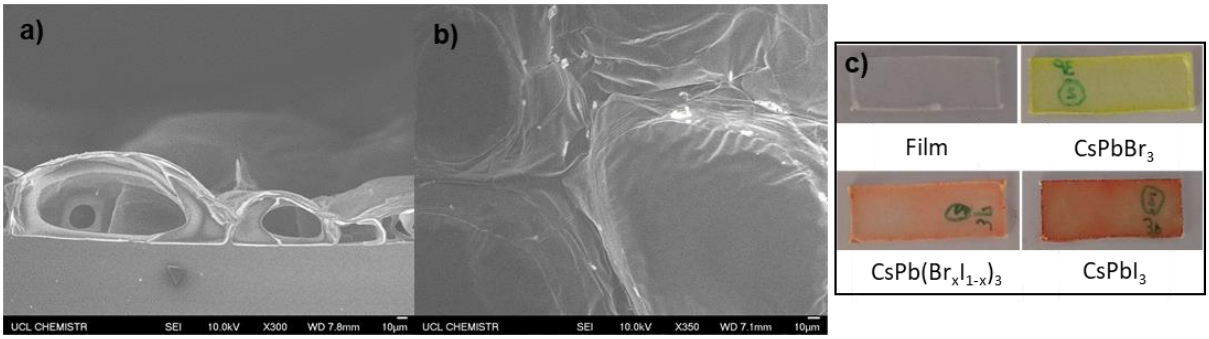

Figure 7.1. SEM micrographs of films before drop casting QDs ex-situ. Side-on SEM images of a) the pure waterglass film, 3P, and show the underlying macroporosity of the swollen films (× 350 magnification for both images). Surface morphology can also be seen in the top-view SEM images of b) 3P and. The appearance of films before and after drop casting is shown in c). The neighbouring images show the appearance of films after the drop-casted colloidal QD solutions have dried.

Mampallil et al.[227] have shown that bumpy topologies can overcome the coffee-ring effect, this also enabled better surface wetting of the toluene suspension resulting in more complete drying of the toluene solutions under atmospheric conditions. It is likely

that the QDs are predominately clustered around the base of the mounds of the foamed silicate films' surfaces, however this requires further characterization to confirm.

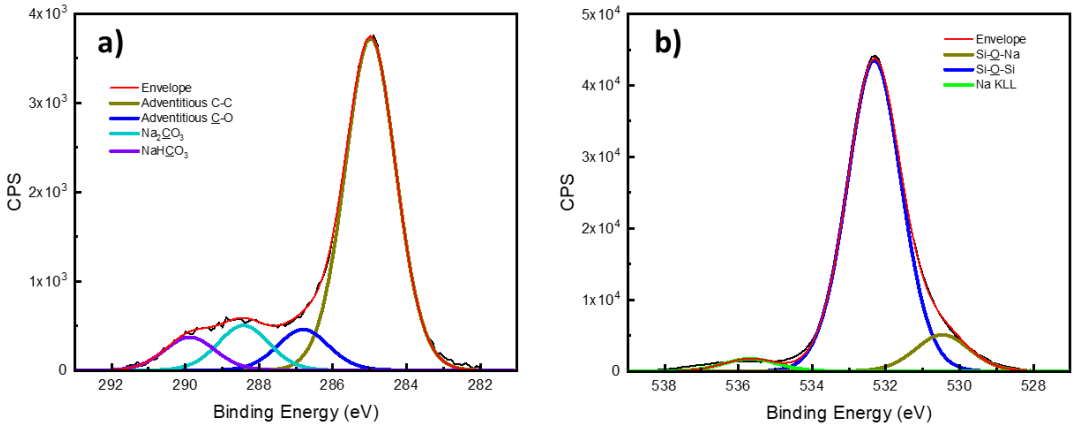

Figure 7.2. XPS a) C 1s and b) O 1s spectra of the foamed waterglass film. The spectra were deconvoluted to determine the binding energies and percentage contributions of each environment.

The composition of the waterglass films as determined by EDX and XPS is shown in **Figure S7.1**. The films had an O/Si ratio of 3.0 and 1.4 and elemental wt. ratios of $NaSi_4O_{12}$ and $NaSi_3O_7$ at the surface and in bulk respectively. The SiO_2/Na_2O ratios at both the bulk and surface were 1.4 and 2.4, both of which are below that of the 3.3 wt. ratio of the waterglass stock solution. The lower silicon content at the surface was thought to be due to the incomplete coordination sphere of surface oxygen. The chemistry of the foamed films' surface can be summarized through its O 1s spectrum (**Figure 7.2a)**). The O 1s spectrum was deconvoluted with three environments at 530.5, 532.2 and 535.7 eV. The first two were identified as components of the silicate network, the non-bridging and bridging oxygen (NBO (10.6%) and BO (85.9%)) units respectively. The third O 1s peak at 535.7 eV was expected to be from Na KLL environments (also seen at ~ 500 eV in the survey spectrum, **Figure S7.5**) usually observed at this position in unleached sodium-based glass.[228] The low relative intensities of the NBO and Na KLL peaks indicate the low sodium ion content at the surface. No distinctive presence of Na_2CO_3 ((531.36 ± 0.4),[113] 532.4 eV), $NaHCO_3$ (531.6, 533.0 eV)[229] or surface silanols (SiO-H, ~ 533.1 eV)[228] was identified through O 1s deconvolution, however they may have been be overshadowed by the large BO and NBO signals due to their low intensity at similar BEs. The Si 2p and Na 1s core levels were deconvoluted with a single peak at 103.5 and 1071.0 eV respectively, the binding energy of the Si 2p peak being typical of an SiO_2 (Q^4) composition.[111] The diffuse transmittance and reflectance are shown in the supplementary data (**Figure S7.6**). The foamed waterglass coating reduced the

transmittance of the glass from 90 to 80%, the reflectance of the substrate in the visible region was increased from 1% to around 16%.

FTIR spectra of films in (**Figure S7.7**) show Si-O-Si BO bending modes at 448 cm^{-1} (Q^4)[105] and 772 cm^{-1}.[105,104] Two overlapping peaks were present around 1000 cm^{-1}. The lower wavenumber peak at 945 cm^{-1} was attributed to a NBO stretch created by the addition of Na^+ cations, expected at 890-975 cm^{-1} in silicate glasses.[104] MacDonald et al.[105] consider the 950 cm^{-1} peak to be from the presence of Si with Q^2 connectivity. The shorter of these overlapping peaks in both spectra (1042 cm^{-1}) from Si-O-Si BO stretching vibrations is usually observed between 1000-1300 cm^{-1}.[104] The small subpeak at ~ 570 cm^{-1} overlapping with the 772 cm^{-1} peak could be due to the presence of ring structures in the sodium silicate films.[105] Smaller peaks were present in the FTIR spectra; firstly a low intensity peak featured at 1458 cm^{-1} from the asymmetric stretch of (CO_3^{2-}) Na carbonate groups.[104,116] Some molecular water[104] was present between 1620-1640 cm^{-1} as are typical CO_2 doublets with peaks at 2345 and 2360 cm^{-1}. The sum of peak intensities of the BO peaks was far greater than that of the NBO peaks created by Na.

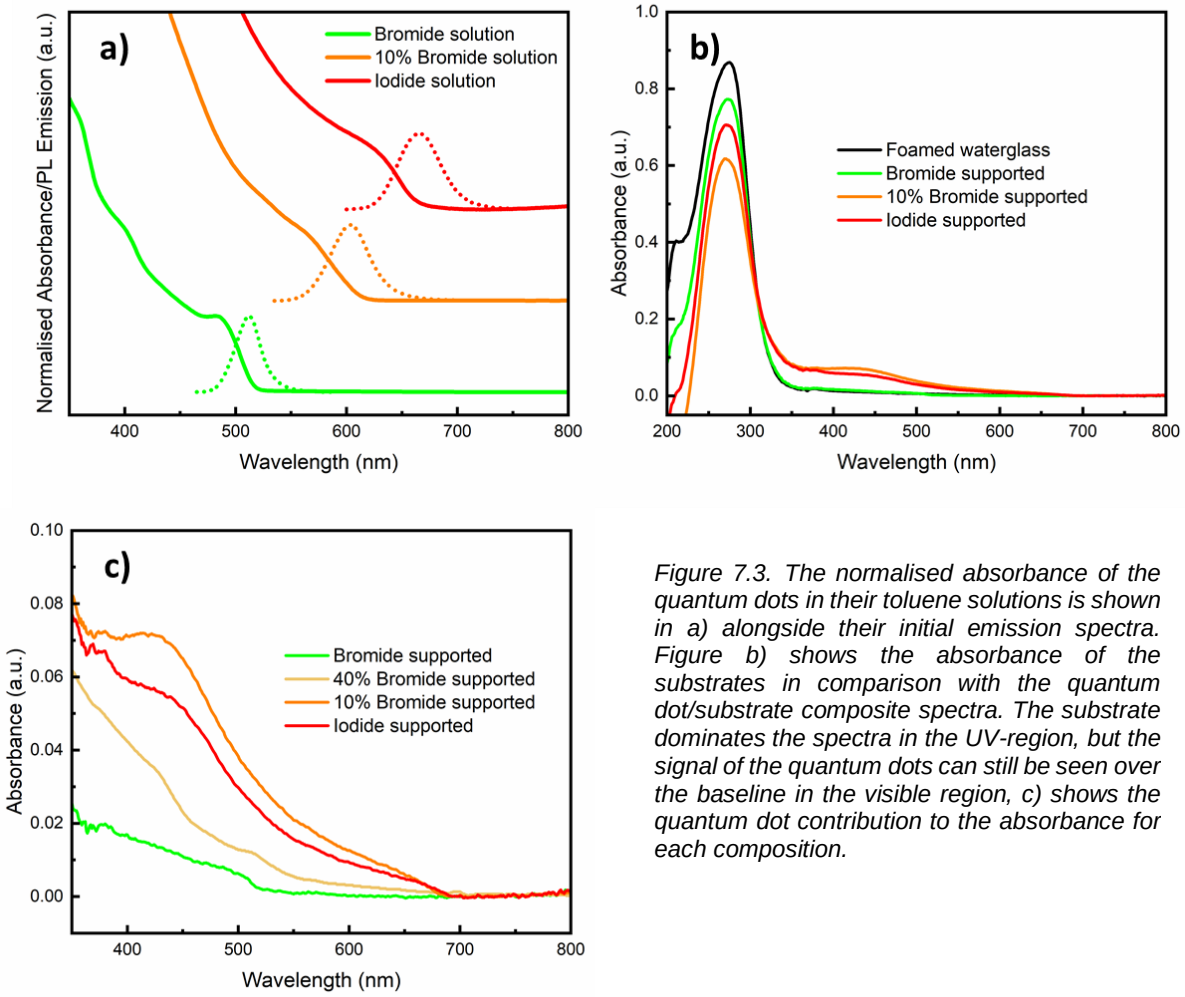

Figure 7.3. The normalised absorbance of the quantum dots in their toluene solutions is shown in a) alongside their initial emission spectra. Figure b) shows the absorbance of the substrates in comparison with the quantum dot/substrate composite spectra. The substrate dominates the spectra in the UV-region, but the signal of the quantum dots can still be seen over the baseline in the visible region, c) shows the quantum dot contribution to the absorbance for each composition.

The absorbance of the QDs before and after drop casting was compared (**Figure 7.3**). QD absorbance profiles were similar after drop casting. Despite the significant absorbance of the substrate between 200 and 300 nm, the absorbance of the supported QDs can clearly be seen over the substrate baseline in the visible region. The absorbance of the foamed waterglass substrate was at least ten times that of the supported quantum dots. The band gap of the QDs in solution was 2.4, 2.1 and 1.9 eV for bromide, mixed halide (10% Br) and iodide QD compositions respectively. After casting the band gaps were 2.3, 2.2 and 1.9 eV. The values are in accordance with the literature[195] and the lack of change in the QD band gap after casting can be attributed to their defect tolerance to trap states that may arise due to interactions with the substrate surface e.g. through dangling bonds.

The initial quantum yield (QY) of the colloidal quantum dots was 43.3%, 53.3% and 77.7% for bromide, mixed halide and iodide solutions respectively. The supported quantum dots had initial QY of 29.6%, 41.9% and 66.7% respectively for the same compositions. In the process of measuring QY, PL emission spectra were also collected,

their analysis provided insight into the changes in QD size distribution and composition with time, to help understand the lower quantum yield of the supported dots.

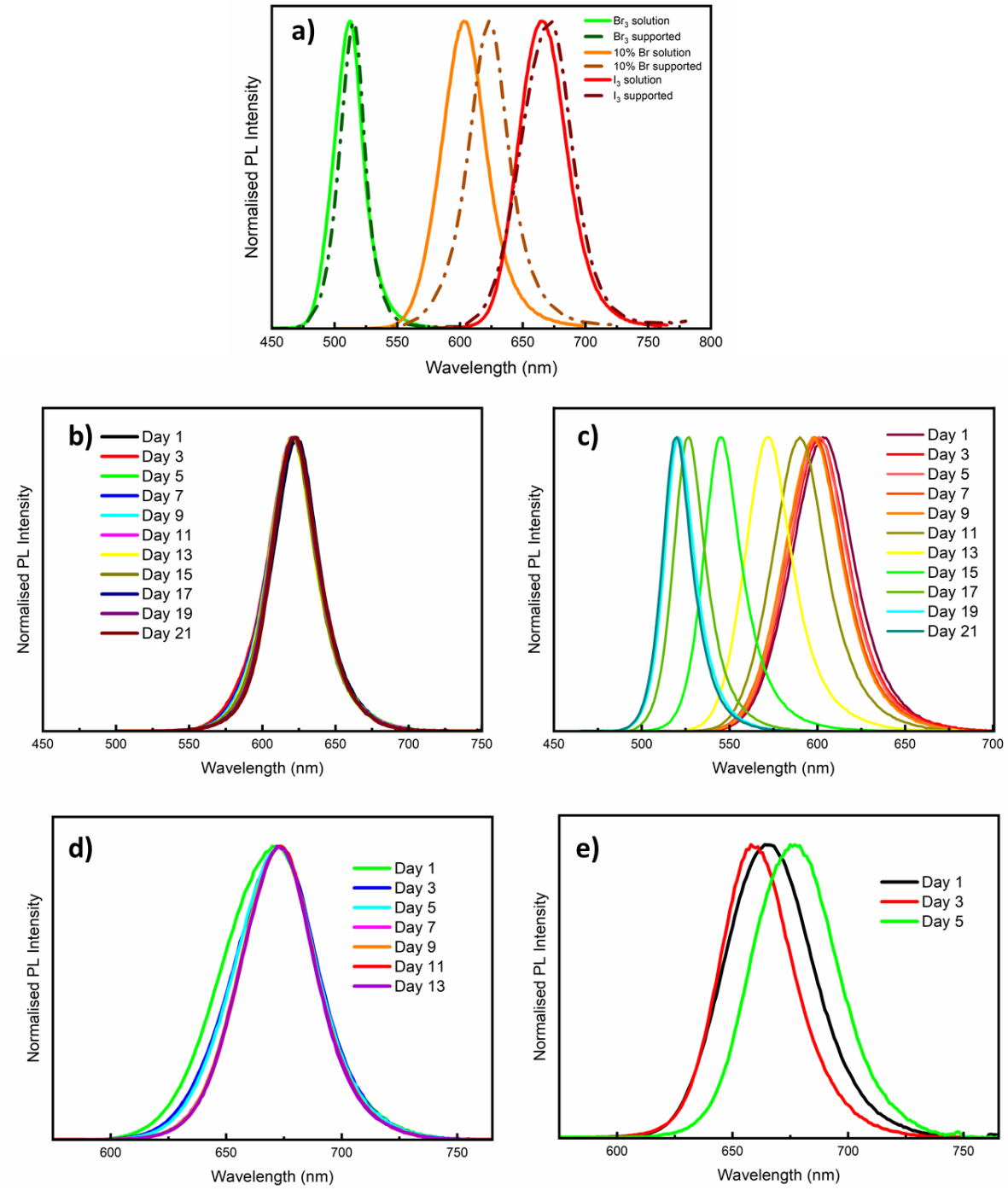

Figure 7.4. Emission spectra of the supported and solution phase quantum dots are shown. In a) the initial emission spectra of the solution and supported quantum dots are compared. The initial emission was always red-shifted when supported. Figures b) and c) show the change in the emission spectra of the supported and solution mixed halide (90%) quantum dots with time. In d) and e) the supported and solution emission spectra are shown for the iodide composition. Supported QDs were resistant to changes in the emission peak wavelength, in solution the emission peak wavelength was subject to fluctuations with time, primarily due to anion exchange.

Figure 7.4 shows the initial emission spectra of QDs when supported or in colloidal solution. Initially, supported QDs were red-shifted from solutions. Red-shifting was smallest for bromide QDs (Δλ = 3 nm) and greatest for mixed halide QDs (Δλ = 20 nm) due to their low stability, resultant from structural hinderances and microdomains formed in their NCs.[188,230] Unmixed iodide and bromide QD red-shifting of 2-11 nm has previously been observed upon QD encapsulation, being attributed to spontaneous NC growth in solution processing[205] or ambient air,[187] Ostwald ripening,[179] or an increase in reabsorption due to QDs being closely packed after encapsulation.[185] Reabsorption is unlikely to have caused significant red-shifting as supported QD peak positions did not show a corresponding blue-shift upon the loss of reabsorption that takes place as QDs began to fade (images in **Figure 7.5**). The increase is more likely to be due to NC growth during solution evaporation. Utzat et al.[231] determined that for PQDs in the intermediate confinement regime, variations in shape, size and stoichiometry between individual NCs contribute significantly to inhomogeneous linewidth broadening; generally, NC linewidth is determined by emission from multiple states of a single NC resulting from interactions of the semiconductor band structure with the exchange energy, exciton fine structure and surface states, and the effects of NC excited states (primarily phonon modes) coupling with the environment.[231] Supported QD initial emission linewidths were similar; FWHM (full width at half maximum) was initially greater in solution except for supported iodide QDs (**Figure S7.8**). There was no relationship between changes in excitation wavelength and FWHM, so the change in FWHM with time was also analysed. Surface interactions could be partially responsible for the shorter linewidths and large red-shifting of supported QDs.

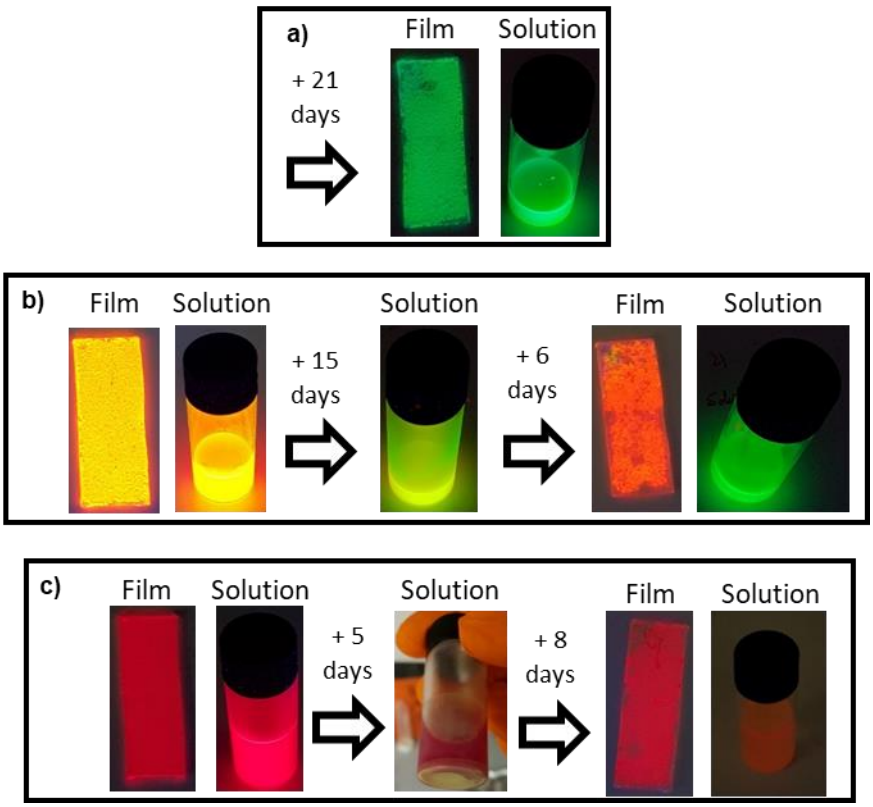

Figure 7.5. Change in appearance of solution and supported quantum dots over time. QDs are illuminated with 365 nm UV lamp. Figures 7a), b) and c) show $CsPbBr_3$, $CsPb(Br_xI_{1-x})_3$ and $CsPbI_3$ quantum dots respectively.

In colloidal solution $CsPbBr_3$ QDs underwent a decrease in peak position from 512 - 510 nm over 21 days; the emission peak FWHM narrowed by 2.3 nm over time. Change in peak position of supported bromide QDs was negligible (1.0 nm). Supported and solution phase QD linewidths narrowed at shorter wavelengths; this suggests PL degradation of smaller QDs, decaying faster due to their greater vulnerability to photo-oxidation owed to their higher surface area to volume ratio.[201] The initial intensity of the bromide QDs was greater in solution (**Figure S7.9**). Final bromide QD emission intensity was also greater in solution, supported QDs had similar PL emission intensity after 21 days. Bromide QD intensity did not vary significantly when supported or in colloidal solution over 21 days (~ 1 million CPS).

The emission peak maximum of colloidal solution mixed halide ($CsPb(Br_xI_{1-x})_3$, where x = 10%) QDs decayed over time from 603 - 520 nm due to halide anion exchange,[232] their final emission peak wavelength was ~ 10 nm greater than that of $CsPbBr_3$ solution; FWHM narrowed from 41.5 down to 19.7 nm as the QD lattices became more bromide in composition. PL peak wavelength decreased drastically between day 11 - 13 measurements and slowed after the measurement on the 15th day. There was negligible change in the emission peak position of supported mixed halide QDs over 21 days, peak FWHM decreased by only ~ 0.2 nm in this time. The left side of the emission peak of

solution and supported mixed halide QDs narrowed over time indicating the decay of smaller QDs. It was expected that immobilisation of QDs on films would limit their ability to undergo anion exchange. Initial intensity of mixed halide QDs was greater when supported (~ 3 million CPS) than in solution (~ 2.5 million CPS), final PL intensity remained at ~ 3 million CPS for supported QDs, having decreased significantly in solution (~ 1.1 million CPS, **Figure S7.10**).

PL peak wavelength of solution phase iodide QDs increased sharply from 664 - 677 nm before decaying before day 7 measurements, the rapid PL decay of iodide QDs prepared by this method has been observed after 3 days in colloidal solution,[207] having the same PL lifetime when supported on glass.[179] Over this time FWHM decreased by ~ 1.4 nm and the emission peak remained broader at longer wavelengths. Peak symmetry increased over time as FWHM decreased by 2.3 nm, becoming narrower at shorter wavelengths as smaller QDs decayed. The emission peak wavelength of $CsPbI_3$ QDs did not fluctuate (673 nm), while initial FWHM decreased from 47.4 to 37.8 nm over the measured time. The linewidth of supported QDs decreased drastically at shorter wavelengths and marginally at longer wavelengths to become much more symmetric indicating the narrowing of QD size distribution, maintaining PL activity for > 13 days. PL intensity was initially greatest for supported QDs than those in solution. Upon their decay, iodide QDs in solution decreased drastically in absolute PL intensity (from 5.1 to 3.4 million CPS), whereas PL intensity of supported iodide QDs fluctuated but remained at ~ 6 million CPS after 13 days (**Figure S7.10**).

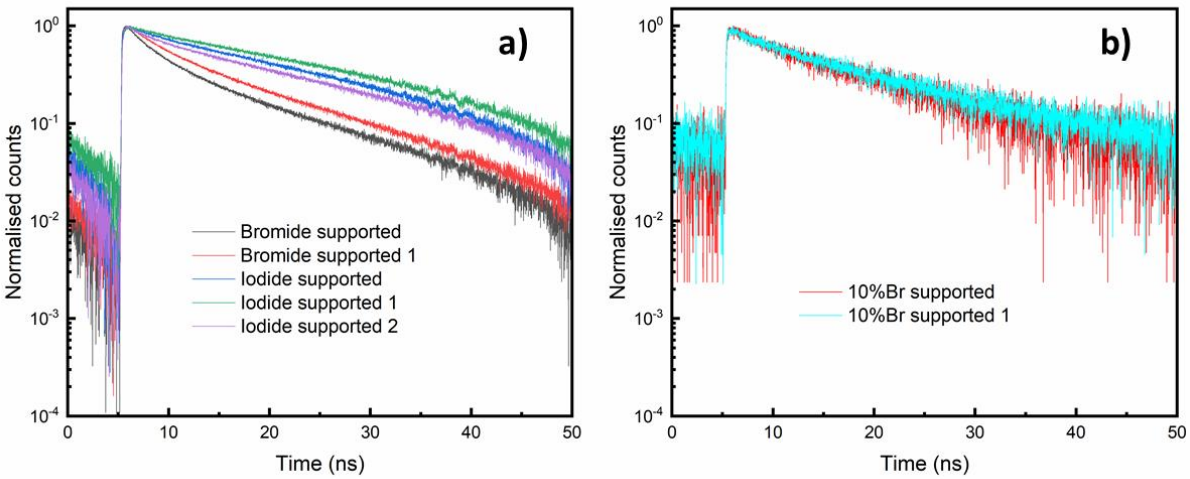

Figure 7.6. The time correlated single photon counting (TCSPC) spectra of the supported quantum dots are shown. The mixed halide composition exhibited much greater fluctuations or noise in their spectra but were more reproducible. The iodide and bromide compositions had distinctive ranges of decay rates, but their spectra were not reproducible indicating a lack of homogeneity in the surface structure of these samples in the spots measured.

The time-correlated single photon counting (TCSP) method was used to collect time-resolved PL decay data of the supported QD samples. Measurements were carried out shortly after drop-casted QD samples were dry. As seen in **Figure 7.6** there was some variation in time-resolved curves between different spots measured on each sample. All samples were fitted to biexponential decay functions, the decay constants are shown in **Figure S7.11**. Short- and long-lived components of multiexponential decay of encapsulated QDs have been attributed to trap-state facilitated (non-radiative) recombination of excitons generated upon initial light absorption and the (radiative) recombination of stable room temperature excitons due to interaction with surface states at the interface respectively.[210,233] Supported QDs had average lifetimes of 15.2, 17.9 and 18.6 ns for bromide, mixed halide and iodide respectively. Radiative lifetimes decreased in the order Br > $(Br_xI_{1-x})3$ > I. Protesecu et al.[195] reported PL decay times, $\tau_{1/e}$, of 1 – 29 ns, with greater decay rate for wider band gap QDs. Decay lifetimes of silicate supported QDs took place over an extended range of 1 - 33 ns. These decay times were similar to those of silica encapsulated bromide and iodide PQDs seen in the literature (average tau 13.6 and 33.8 ns respectively).[179] Longer decay times were observed for iodide than bromide supported QDs as expected, however similar τ_2 lifetimes were observed for supported bromide and mixed halide QDs, mixed halide τ_1 was faster.

Immobilisation of these QD compositions on sodium silicate was shown to either match or improve their stability in solution and prevent anion exchange of mixed halide QDs. It was hypothesised that reintroduction of a vapourised solvent may facilitate the

controlled, solid state anion exchange of mixed halide QDs (observed over time in solution) for use as a sensor. Solid state halide anion exchange of hybrid perovskite QDs nanowire arrays has previously been achieved by Wong et al.[183] using $CH_3NH_3PbI_3$ vapour (140°C) for anion exchange of $CH_3NH_3PbBr_3$ to $CH_3NH_3PbBr_3$. Here the colour change takes place at *room temperature*.

The colour change facilitated by anion exchange did not proceed smoothly from orange to green until the mixed halide QD solution had been aged for some weeks and the anion exchange had already begun to take place. The results of the change in PL emission upon exposure of the supported, aged QDs to acetone vapour for t seconds, (where t = 90, 270 s) is shown in **Figure 7.7**. The peak position of the freshly synthesised, supported mixed halide QDs decreased by only 6 nm.

After ageing the mixed halide QD solution for several weeks the dots were cast on to the films. The effects of ageing manifested as a decrease in the initial emission peak wavelength of the supported QDs from 603 to 591 nm) as well as a reduction in peak intensity. After 90 s acetone exposure halide anion exchange had taken place as the QD emission peaks had been both blue- and red-shifted (to ~ 607 and ~ 559 nm) accompanied by a loss in intensity. Supported QDs breached the low energy side of green wavelength range (495 - 570 nm), while still appearing yellow/orange at this point. It is evident from the breadth of these peaks, uncharacteristic of perovskite QD linewidths but also from the appearance of the films, that there are several compositions of mixed halide QDs present after exposure to acetone vapour. After 270 s mixed halide QDs on films became more blue- and red-shifted and further decreased in peak intensity. A more distinct green peak developed in samples after a blue shift down to 520 nm. The breadth of the peak at ~ 610 nm indicated that the composition was still split in this region. Supported QDs began to fade upon further acetone vapour exposure.

While near homogeneous anion exchange could be achieved and the colour change clearly observed, QD brightness (PL intensity) was significantly reduced and was difficult to detect via measurement of the emission spectrum. Partial anion exchange to yellow was easier to achieve than full conversion to green bromide composition, without significant loss in emission peak intensity.

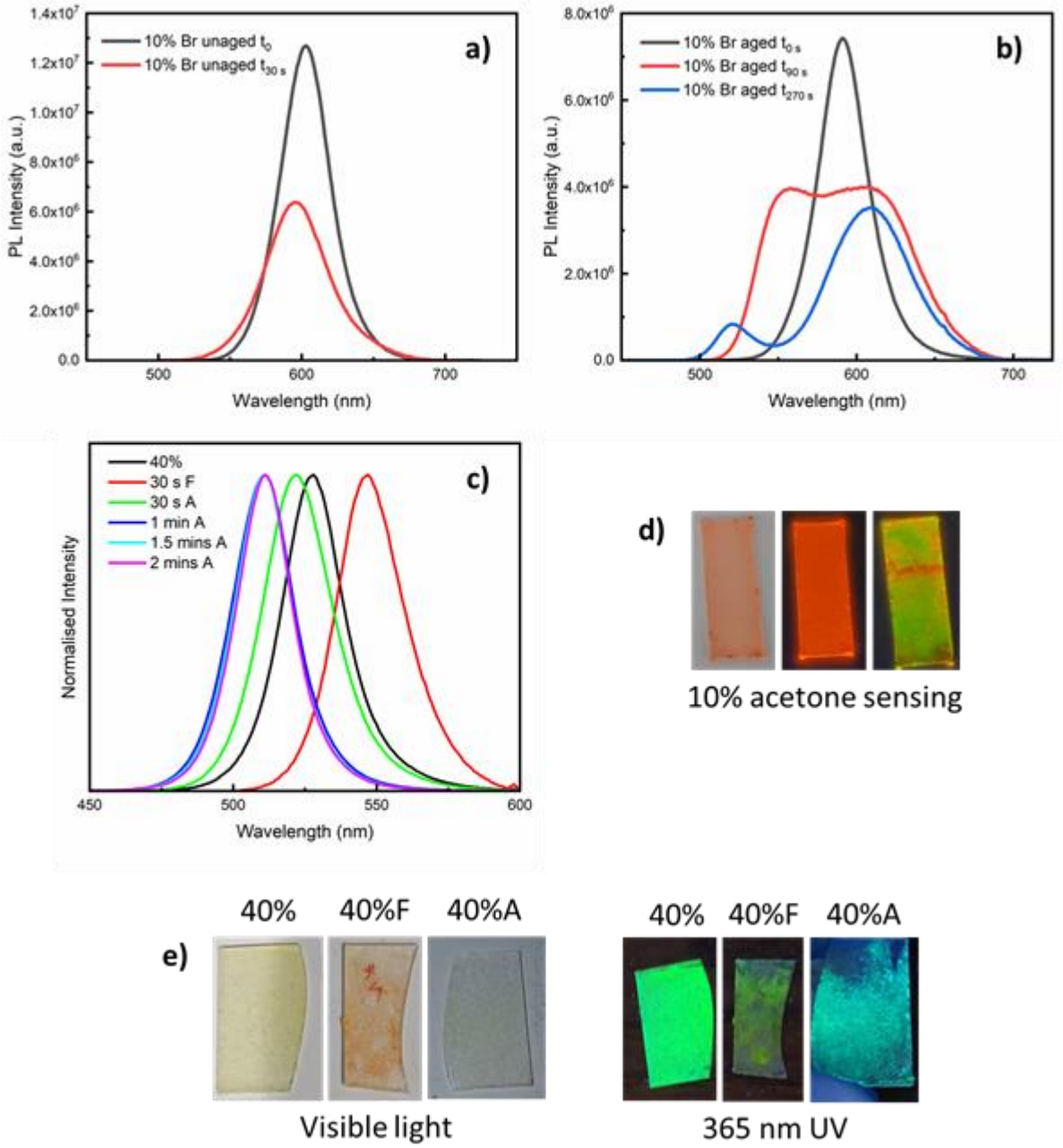

Figure 7.7. Change in the emission spectra of supported mixed halide quantum dots upon exposure to acetone or formaldehyde vapour. Figure a) shows the lack of change in the unaged 10% bromide quantum dots upon acetone exposure. After ageing, the emission peak split, indicating the formation of multiple compositions as seen in b). Image d) shows the change in colour of the 10% bromide quantum dots before and after acetone exposure. In c) the change in the emission peak of 40% bromide quantum dots upon exposure to acetone or formaldehyde vapour is shown. Acetone exposure resulted in a consistent blue-shift of the emission peak, whereas formaldehyde exposure resulted in a red-shifting of the emission peak. Formaldehyde exposed samples became orange under visible light and lost most of their green fluorescence under 365 nm UV-light, while acetone exposed samples retained their green fluorescence after exposure as seen in e). The change in intensity of the data in c) is shown in the supplementary data.

40% bromide QDs were synthesized via the same method and cast onto the foamed waterglass films. The QDs appeared light orange in solution, their appearance changed to green after casting indicating a decrease in emission peak wavelength. This composition responded immediately to vapour sensing and gave clear shifts in the emission peak wavelength (**Figure 7.7 c)**). After 30 seconds of acetone vapour exposure the emission peak of the supported 40% bromide QDs blue-shifted from 528 to 522 nm. After 1 minute in acetone vapour the peak wavelength decreased further to 511 nm, its position did not change upon further exposure, but its FWHM decreased from 25.2 to 22.8 nm between 1 and 2 minutes in acetone vapour indicating a decrease in QD size distribution as discussed previously. After 30 seconds in formaldehyde vapour the emission peak red-shifted to 547 nm, the supported QDs appeared orange under visible light but remained green under 365 nm UV light irradiation, suggesting the formation of a non-fluorescent compound. After 1 minute under formaldehyde vapour the supported 40% QD emission peak wavelength was reduced to near noise level. XPS was carried out on these films (**Figure 7.8**), in the 40% sample the Br 3d, Cs 3d, I 3d and Pb 4f (5/2) peaks were all present in the high resolution XPS data with binding energies of 62.3, 724.8, 619.2, and 137.9 eV respectively. After acetone exposure, the I 3d peak was reduced to noise level, indicating removal of iodine from the QD crystals and explaining the colour change. In the same sample the Br 3d and Pb 4f (5/2) peaks increased in energy to 62.7 and 138.1 eV, while the Cs 3d peak energy decreased to 724.5 eV. The 40% samples exposed to formaldehyde had weak I 3d signal, the Cs 3d signal was reduced to noise level. Br 3d signal was present in both acetone and formaldehyde exposed samples, but the signal intensity was reduced. In this sample the Br 3d and I 3d binding energies decreased to 63.0 and 618.3 eV, while the Pb 4f (5/2) energy increased to 138.2 eV. The complete loss of Cs 3d signal in this sample may suggest breakdown of the QD structure. Finally, the Na 1s peak was present in all samples at 1069.8 eV, only a single peak was present indicating that efflorescence had not yet taken place in these samples. The supported quantum dots could be used as colourimetric sensors either with or without UV light irradiation.

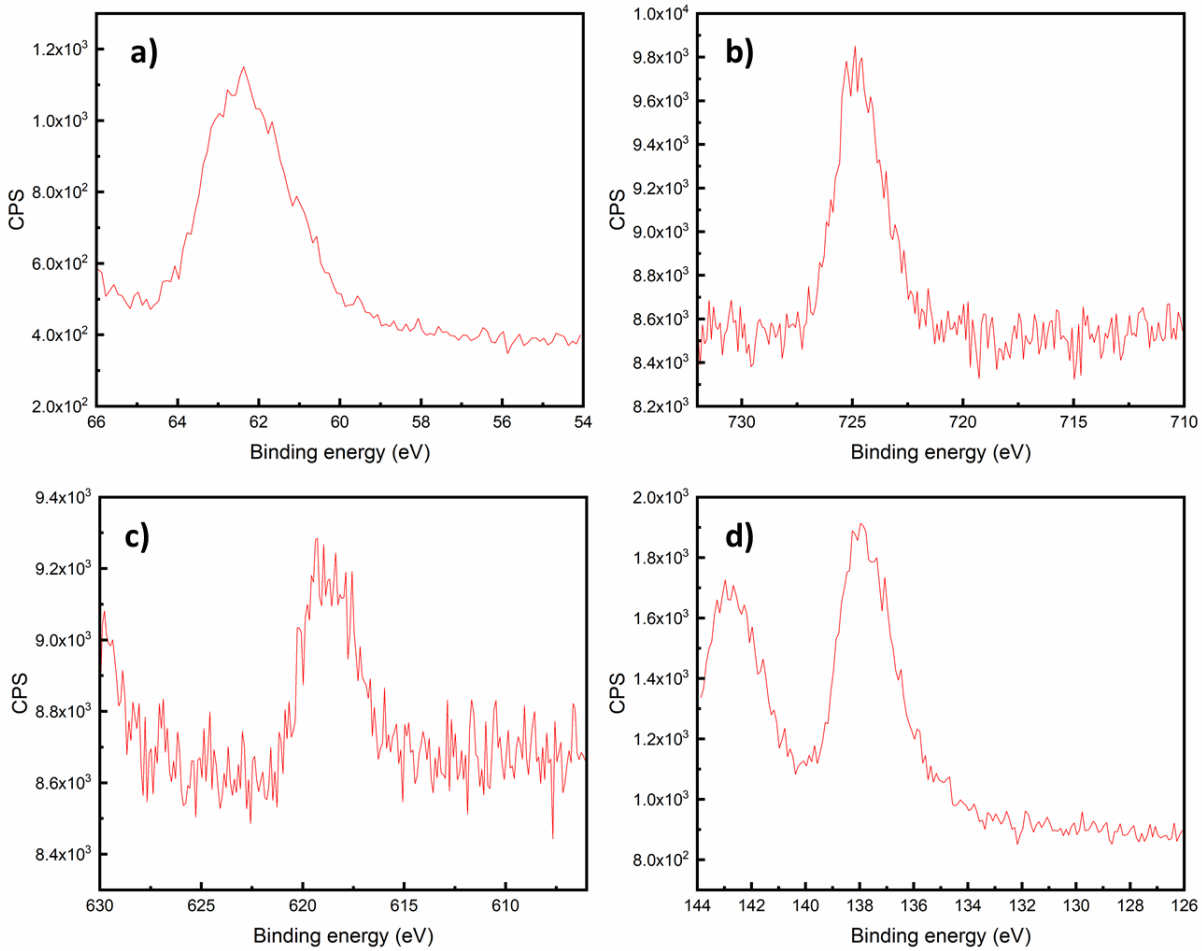

Figure 7.8. The XPS spectra of the 40% bromide samples corresponding to the orbitals, a) Br 3d, b) Cs 3d, c) I 3d and d) Pb 3d are shown. After acetone exposure the I 3d signal was reduced to noise level, whereas formaldehyde exposure samples retained I 3d signal but lost their Cs 3d signal. The noise level spectra and the representative Na 1s spectrum are shown in the supplementary data (S12).

7.5 Conclusion

Fully inorganic PQDs were supported on foamed sodium silicate. Small amounts of sodium bicarbonate were detected on substrates but there were no other indications of excess surface carbonate formation known as ‘efflorescence’. The surfaces of the substrates were mainly composed of Si tetrahedra and bridging and non-bridging oxygen units. High PL emission intensity and narrow FWHM were maintained after supporting QDs onto the silicate substrates. QDs drop-casted onto foamed waterglass appeared visibly homogeneous, the bumpy topology of the foamed film likely inhibited the coffee-ring effect. Further characterization of the physical distribution of the QDs on the foamed films is needed to confirm this. The high QY of the QDs was also maintained, iodide QD lifetime was extended when supported. Furthermore, anion exchange of mixed halide QDs was prevented when supported on foamed glass films. The potential of the silicate supported mixed halide perovskite QDs as colourimetric or fluorescence sensors for acetone and formaldehyde vapour was shown, indicating the utility of the supported QDs in organic vapour detection, even in aqueous solution, despite the sensitivity of the quantum dots to polar environments.

8. Concluding remarks

In this work the use of waterglass solutions in solution processing methods was investigated. Coatings were made from waterglass stock solutions. It was shown that they can be converted to silica to give them long term stability to humid atmospheres by heating at an appropriate temperature and washing with acid. The coatings were durable, transparent with respect to visible light and had controllable film thickness. The silica coatings were more hydrophilic than the glass microscope slide substrates.

Macroporosity was introduced with potato starch and polystyrene nanosphere hard templates. While the starch templated coatings were coated with TiO_2 to afford antifogging and photocatalytic properties, the applications of nanosphere templated coatings require further investigation. Despite several reports of large solution entities preventing the formation of nanostructures with waterglass, porosity closely resembling the shape of 125 nm spherical porosity was successfully created. Further work could establish the formation of smaller pores in thin silica films from waterglass produced in this way using block copolymer templates.

Stainless steel mesh coated with potassium waterglass showed oil-water separation efficiencies of over 90% for castor, olive and motor oil mixtures. To further improve its separation efficiency, methods to improve oleophobicity should be investigated.

Thick waterglass coatings foamed upon heating and were found to be able to support perovskite quantum dots. The sensing of VOCs facilitated by anion exchange of mixed halide quantum dot compositions could be investigated in depth.

In future the coating solutions could be doped with other metal oxides to alter their chemical and optical properties.

9. Appendices

Chapter 3 – Silica films from waterglass solutions

KWG film mass after washing			
Film	1 min H2O	Mass loss	% Mass loss
/g	/g	/g	%
0.0011	0.0006	0.0005	45
0.0011	0.0006	0.0005	45
0.0009	0.0005	0.0004	44
0.0009	0.0004	0.0005	56
0.0012	0.0006	0.0006	50
0.0012	0.0006	0.0006	50

NaWG film mass after washing			
Film	1 min H2O	Mass loss	% Mass loss
/g	/g	/g	%
0.0054	0.0009	0.0045	83
0.0057	0.0040	0.0017	30
0.0052	0.0044	0.0008	15
0.0053	0.0015	0.0038	72
0.006	0.0021	0.0039	65
0.0047	0.0013	0.0034	72

Supplementary table (S3.1). Mass loss of waterglass coatings after heating and washing at 120°C.

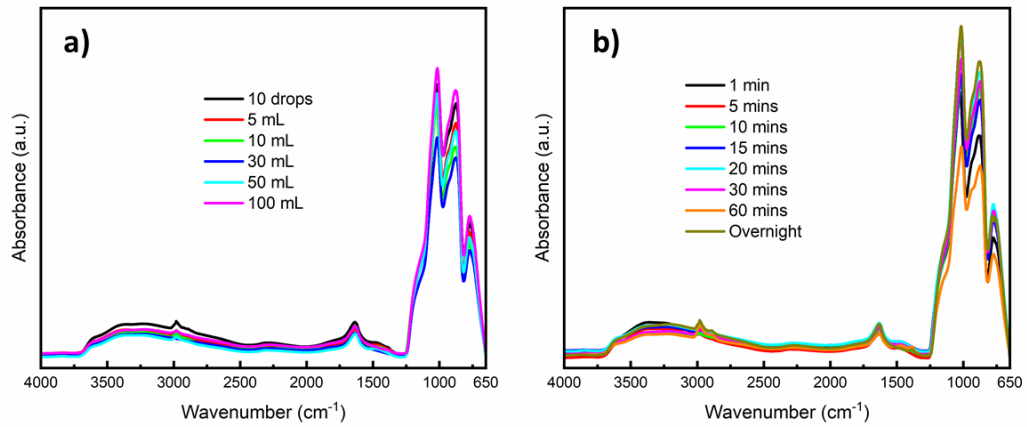

Supplementary figure (S3.2). In a) the effect of the washing volume on the BO/NBO ratio is shown, all samples were washed for 10 minutes. The peak ratio after washing was negligibly affected by the washing volume, only the intensity of the spectra was affected, with no noticeable pattern. KWG samples heated to 95°C for different times before washing with water are shown in b). The change in BO/NBO peak ratio after washing was similar regardless of the heating time.

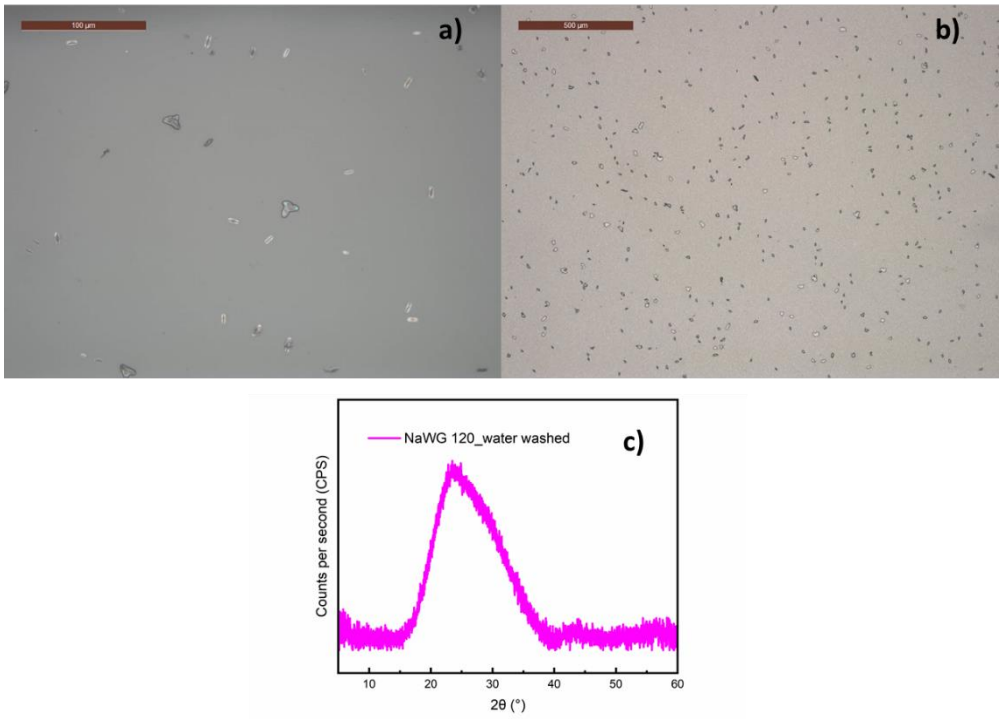

Supplementary figure (S3.3). NaWG film heated at 120°C for 15 minutes and then submerged in deionised water for a) 15 and b) 30 minutes. Crystals began to grow from the surface of some NaWG samples after lengthy submersion in water. The scale bars for a) and b) are 100 and 500 µm. The diffraction data in c) shows the amorphous nature of these films despite the visible surface crystals.

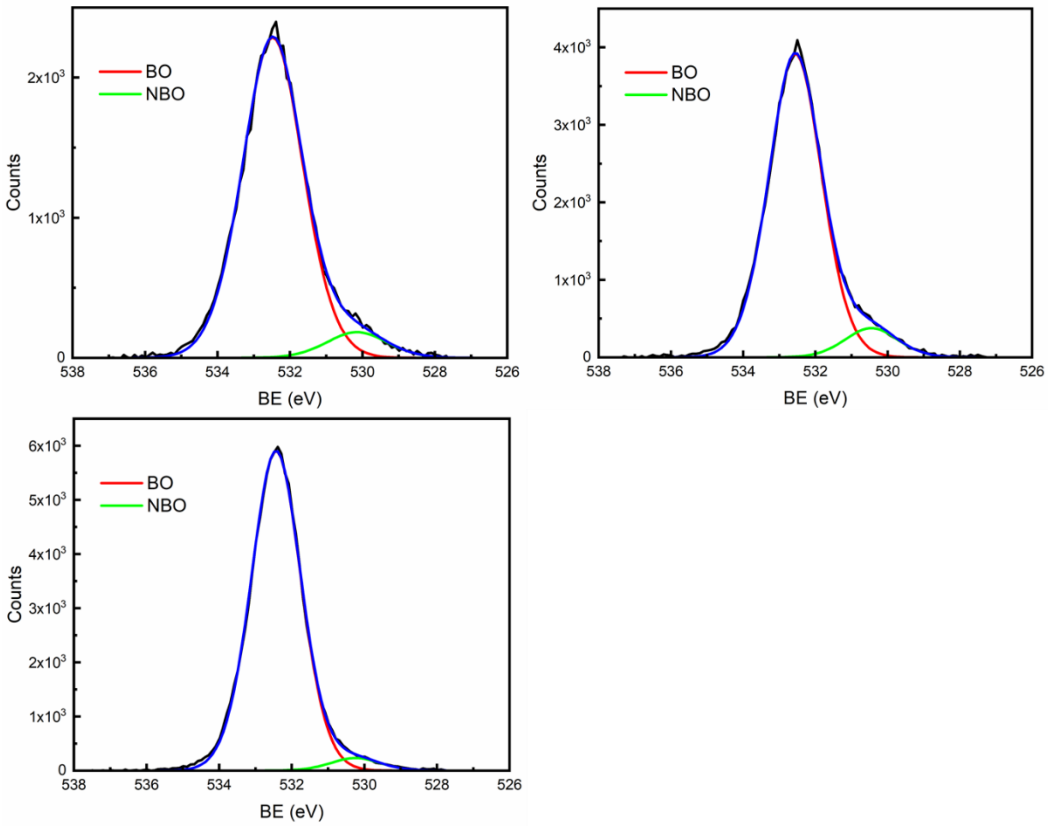

Supplementary figure (S3.4). The XPS O 1s sspectra of KWG samples heated to 95°C and submerged in water for a) 1, b) 10 and c) 30 minutes are shown above. The NBO relative peak intensity decreased as the washing time increased, but its presence was not completely removed.

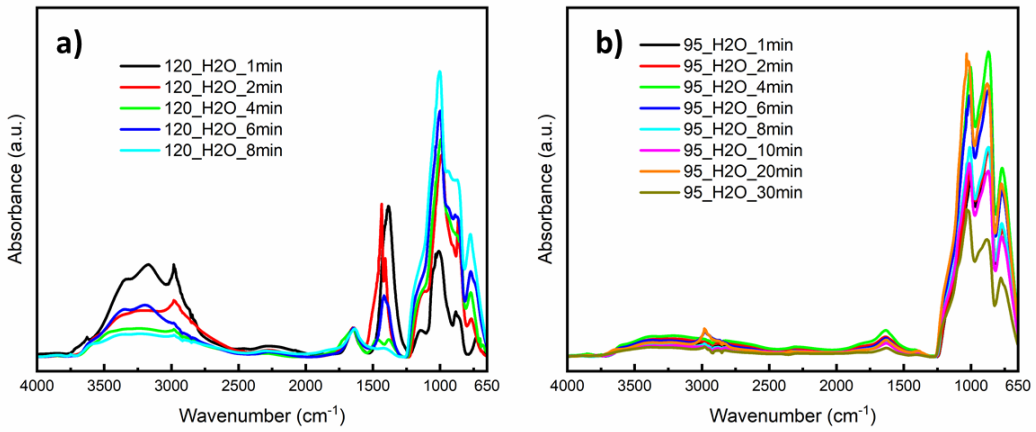

Supplementary figure (S3.5). The ATR spectra in a) and b) show the change in water washed NaWG and KWG samples upon ageing for several months. NaWG film washed for 8 minutes or greater did not develop an efflorescence peak at 1640 cm^{-1}. The KWG samples all featured a carbonate peak, however its intensity did not change with the washing time. It can be seen that the BO/NBO peak intensity switch has not occurred for some of the KWG samples, suggesting that efflorescence is not purely dependent on this occurrence for KWG films.

Time	Spin coat	Drop cast/air dry
	Mass	Mass
/ mins	/ g	/ g
> Glass	0.9644	0.9315
0	0.9685	1.0050
10	0.9683	0.9876
20	0.9683	0.9778
30	0.9683	0.9720
40	0.9683	0.9703
50	0.9683	0.9696
60	0.9683	0.9693
Overnight	0.9683	0.9668
> Film mass	0.0041	0.0735
> Mass loss	0.0002	0.0382

Supplementary table (S3.6). The mass loss of NaWG coatings with drying time is shown. Drop casted films continued to lose mass over a period of 24 hours, whereas spin coated samples did not undergo significant mass loss after coating.

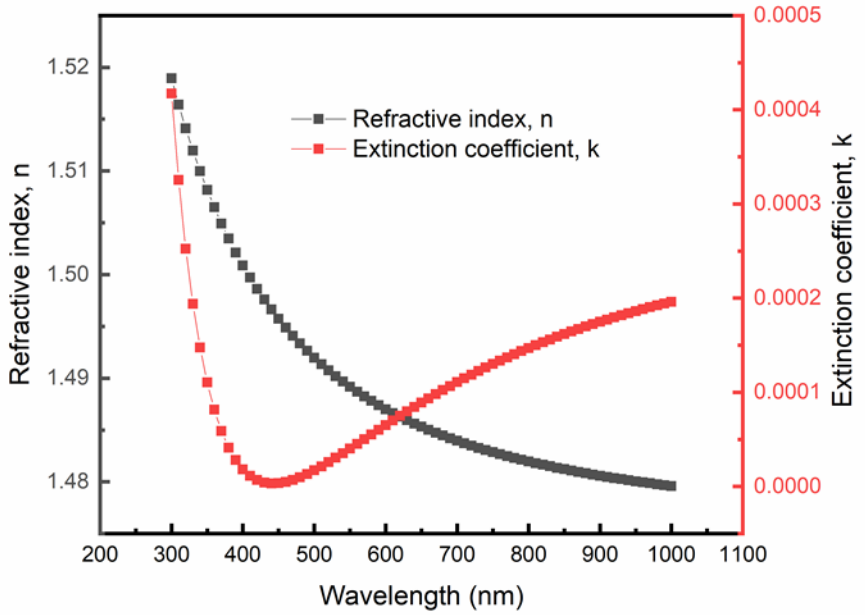

Supplementary figure (S3.7). The complex refractive index of the silica films from potassium silicate is shown above in the form of the refractive index and extinction coefficient curves.

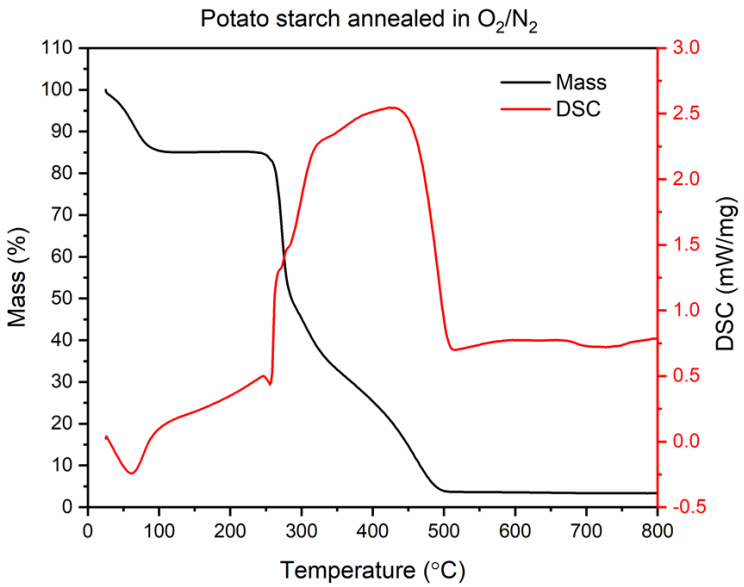

Supplementary figure (S4.1). Thermogravimetric (TG) analysis of the potato starch powder in an air atmosphere. The starch powder was heated to 800°C at a rate of 2°C/min. Much of the mass of the powder was lost by 500°C, after which no further decrease was observed. The differential scanning calorimeter (DSC) recorded a large, broad, exothermic peak between 250 and 500°C, where the majority of the mass loss occurred. The endothermic peak at ~ 60°C was associated with the evaporation of water also seen in the TG as a mass loss at the same temperature.

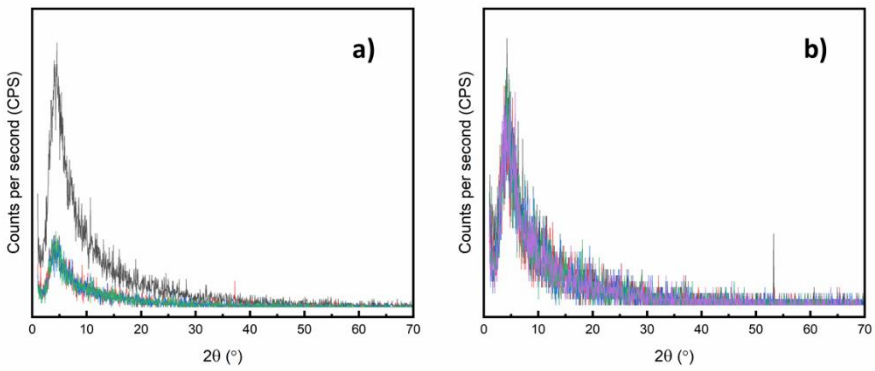

Supplementary figure (S4.2). In a) and b) the amorphous XRD data of the macroporous silica and TiO_2-coated macroporous silica samples are shown. The macroporous silica layer was expected to be amorphous, but the anatase TiO_2 layer, whose crystallinity was confirmed with Raman spectroscopy, was too thin to be detected with this technique.

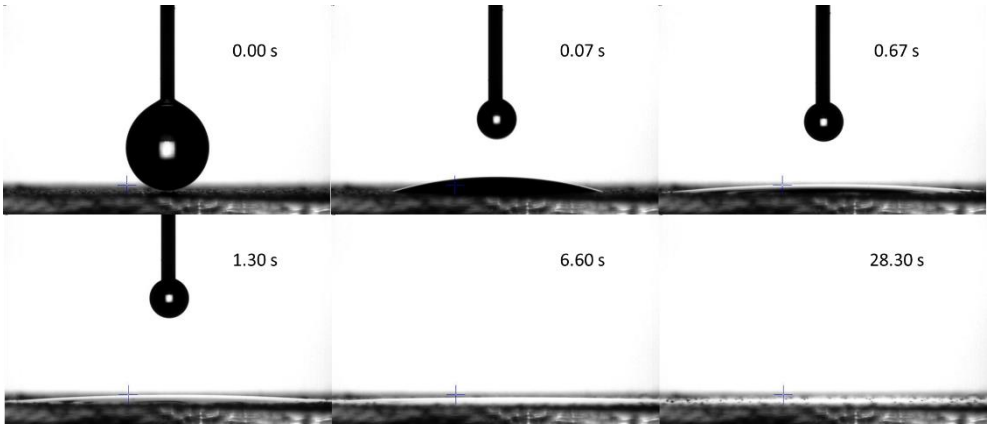

Supplementary figure (S4.3): Wetting of a TiO_2-coated 10 wt% superhydrophilic sample. Within 0.07 s of contacting the surface the droplet reached a contact angle of 15.4°/14.1° (LHS/RHS). Within 28 seconds the droplet had completely wet the surface and the surface texture could again be seen.

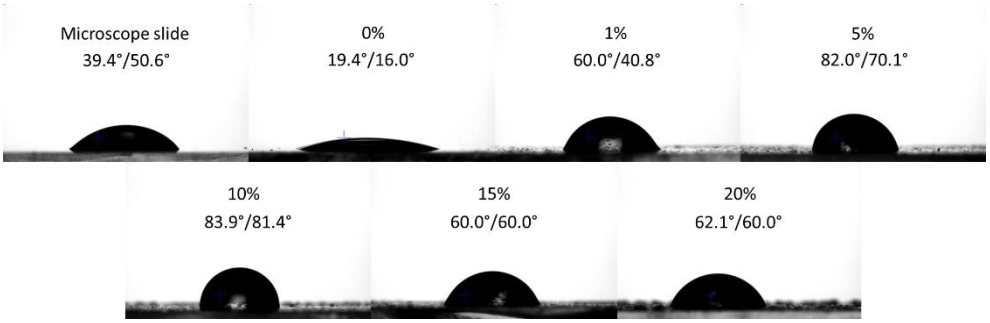

Supplementary figure (S4.4). Aged, TiO_2-coated waterglass samples on glass microscope slides. With no barrier layer, carbonate crystals grew from the surface and drastically increased the contact angle of the samples. The porous samples were more affected by this than the 0% and glass samples, suggesting that the porous samples were the most affected by efflorescence.

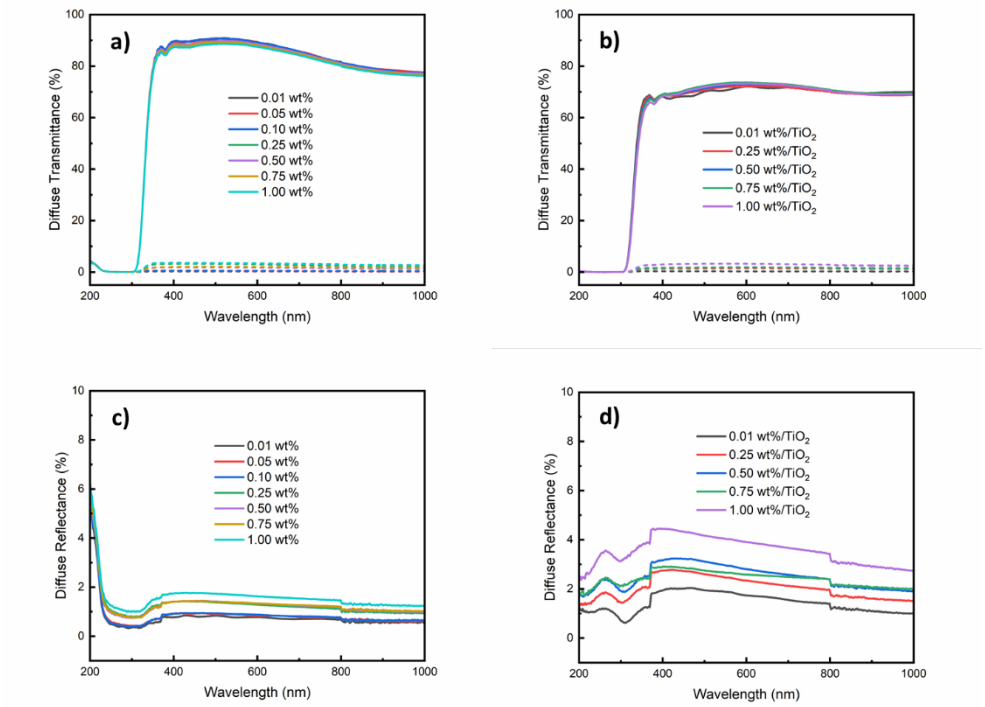

Supplementary figure (S4.5). The diffuse transmittance and reflectance and transmittance scattering of the macroporous silicate films templated with 0.01, 0.05, 0.1, 0.25, 0.5, 0.75 and 1 wt% potato starch. With these low percentages the visible light transmittance of the coated samples is not significantly changed from that of the barrier glass substrates. After coating with TiO_2 and annealing at 500°C the samples all have ~ 70% transmittance, while their reflectance and transmittance scattering remain around 2%.

Chapter 5 – Ordered macroporous silica from polystyrene nanospheres and waterglass

No supplementary data.

Chapter 6 – Oil-water separation with waterglass coated stainless steel mesh

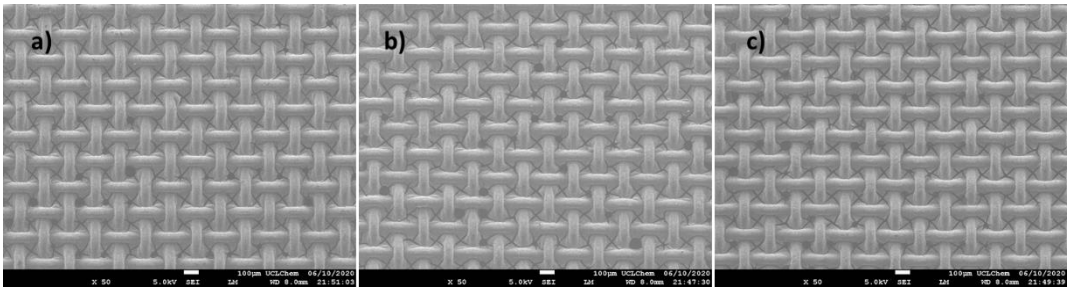

Supplementary figure (S6.1). SEM images of KWG-mesh formed at different dip coating speeds in the viscous drag regime are shown above, a) 10, b) 30, c) 60 mm/min. The dip coating speed had little effect on the porosity in this region. (Scale bars 100 μm).

Deionised water	Density	Oil in	Water out	Oil out
	gcm^{-1}	%	%	%
Motor Oil (10W-40)	0.8629	75	94.87	0.04
Motor Oil (10W-40)	0.8629	50	92.46	0.16
Motor Oil (10W-40)	0.8629	25	94.25	0.09
Olive Oil	0.916	75	97.10	0.42
Olive Oil	0.916	50	96.43	11.85
Olive Oil	0.916	25	99.23	0.83
Castor Oil	0.961	75	95.27	2.09
Castor Oil	0.961	50	94.74	0.03
Castor Oil	0.961	25	96.43	0.02

Saltwater	Density	Oil in	Water out	Oil out
	gcm^{-1}	%	%	%
Motor Oil (10W-40)	0.8629	75	95.80	0.43
Motor Oil (10W-40)	0.8629	50	99.44	0.55
Motor Oil (10W-40)	0.8629	25	96.85	2.96
Olive Oil	0.916	75	94.73	0.44
Olive Oil	0.916	50	97.56	1.06
Olive Oil	0.916	25	98.57	0.81
Castor Oil	0.961	75	93.99	3.78
Castor Oil	0.961	50	95.07	2.69
Castor Oil	0.961	25	95.68	1.16

Supplementary table (S6.2). Raw data for the oil water separation with both deionised and saltwater-oil mixtures poured over KWG-coated stainless-steel mesh.

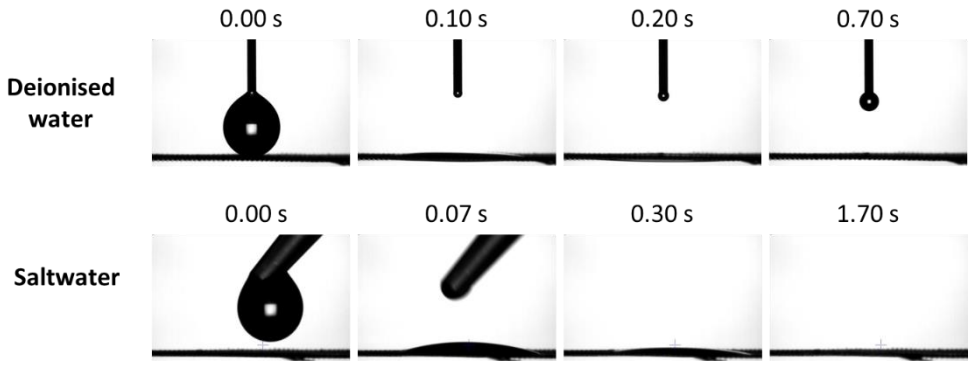

Supplementary figure (S6.3). The wetting time of the deionised and saltwater was visualised. The wetting time was 1 s faster for deionised water 0.70 s.

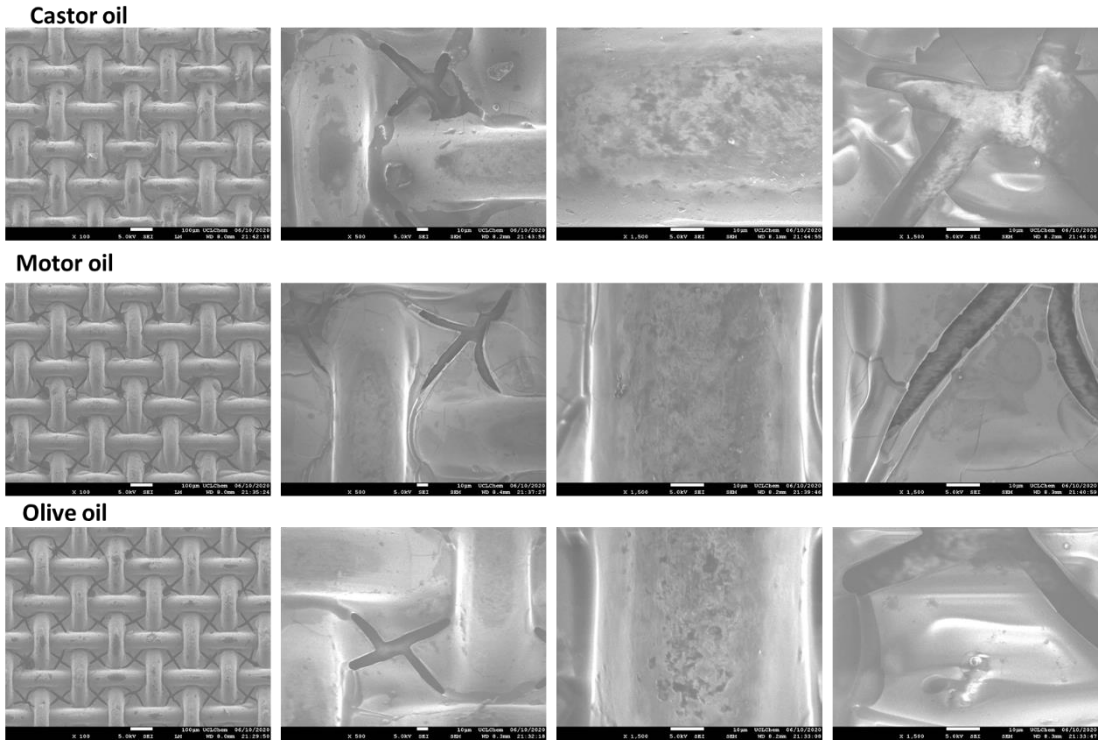

Supplementary figure (S6.4). The KWG mesh after separation of each of the oils is shown. The scale bars for the left-most images are 100 μm, all others are 10 μm.

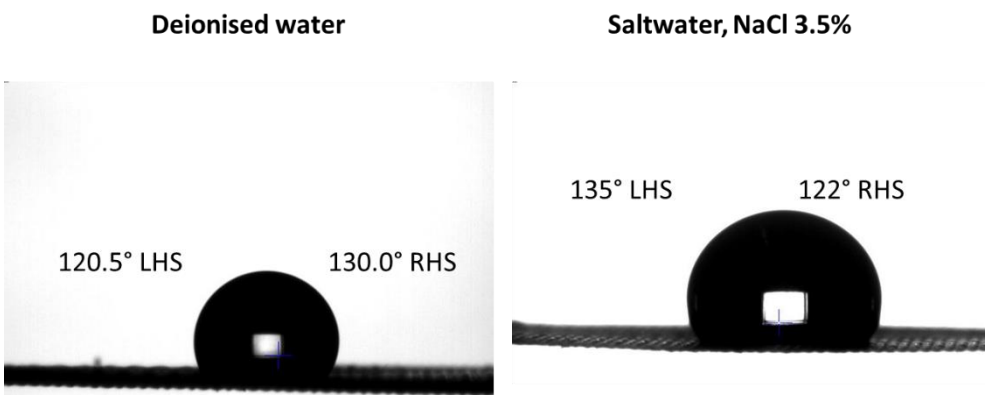

Supplementary figure (S6.5). The contact angles of deionised and saltwater are shown above. Water was hydrophobic with respect to the uncoated mesh.

Supplementary figure (S6.6). The contact angles of the oil on the plain mesh are shown. All the oils wet the stainless-steel well and pass through, each having a similar contact angle.

a)

Element	Atomic percent / at %
C 1s	15
O 1s	50
Na 1s	6
Si 2p	29

b)

Sample	Elemental composition					
	Average / wt%			Standard deviation ± wt%		
	O	Na	Si	O	Na	Si
Film	52	10	38	1.7	1.0	0.8

Supplementary table (S7.1): XPS atomic percentage and EDX weight percent composition are shown in a) and b). The EDX data was calculated from the average of three spots on the sample surface (10 kV, 140 × magnification).

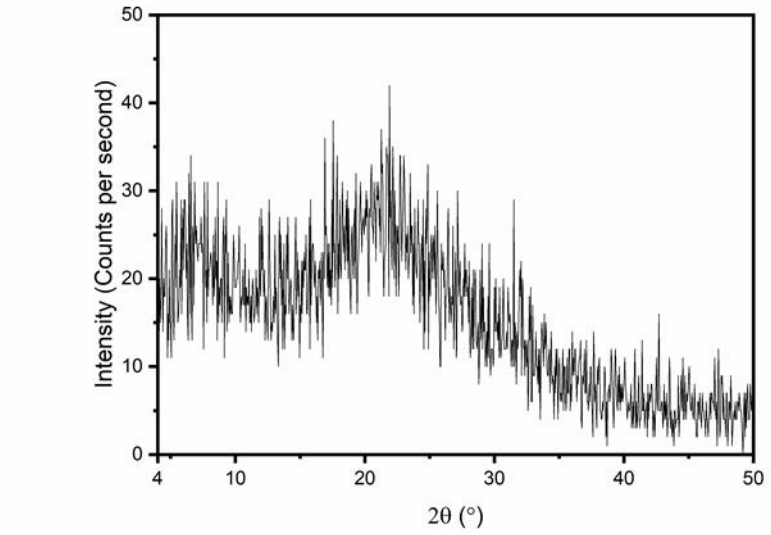

Supplementary figure (S7.2): Amorphous XRD pattern of the foamed waterglass, produced by spin coating a thick film of sodium waterglass and annealing at 590°C for 1 hour (10°C/min).

Sample	Glass / g	and Film / g	Annealed / g
1	1.7119	1.7305	1.7257
2	1.4697	1.4865	1.4820
3	1.7201	1.7383	1.7337
4	1.6461	1.6658	1.6603
5	1.6851	1.7060	1.7003
8	1.5746	1.5926	1.5875
9	1.6443	1.6641	1.6585

Sample	Pre-anneal	Post-anneal	(a.k.a water lost)
	Film mass / g	Film mass / g	Mass loss / g
1	0.0186	0.0138	0.0048
2	0.0168	0.0123	0.0045
3	0.0182	0.0136	0.0046
4	0.0197	0.0142	0.0055
5	0.0209	0.0152	0.0057
8	0.0180	0.0129	0.0051
9	0.0198	0.0142	0.0056
Average	0.0189	0.0137	0.0051

Volume = mass/density

V = length * width * height = area * height

Thickness or height = mass/(density * area)

Area = 2.5 * 2.5 = 6.25 cm^2

Thickness estimate = average film mass/ (sodium silicate powder density * area)

= 0.0137/ (2.4 * 6.25)

= 0.0358 cm

= 358 μm

Supplementary table (S7.3): The mass of the films was determined by weighing substrates before and after spin coating. The film mass after heating was then established. The average film mass was used to calculate an estimate for the average film thickness across the sample.

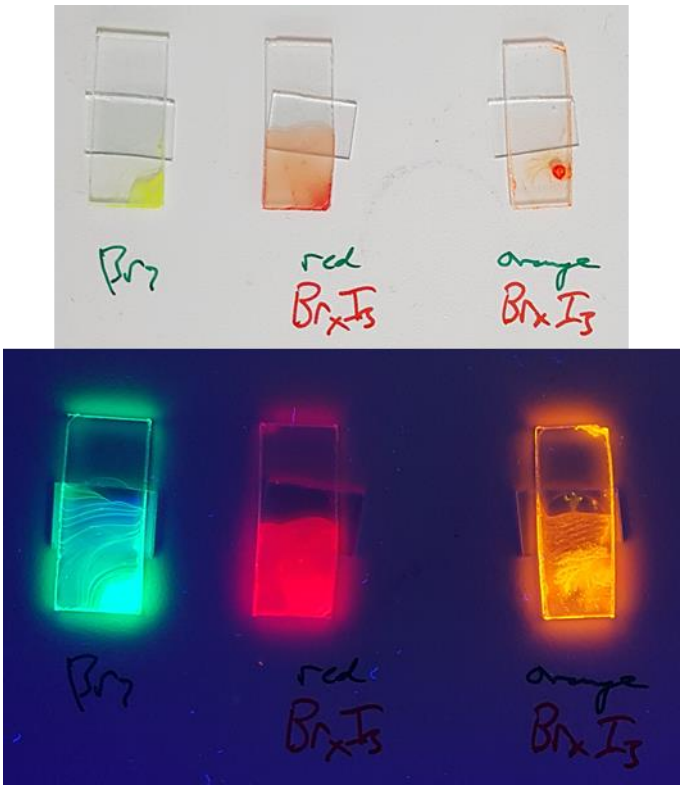
red
orange

Supplementary figure (S7.4): The toluene quantum dot suspensions were cast onto glass and dried in air. The quantum dots did not dry evenly on the flat substrates, forming ring-like patterns. The images show the dried samples under visible and 365 nm UV-light irradiation.

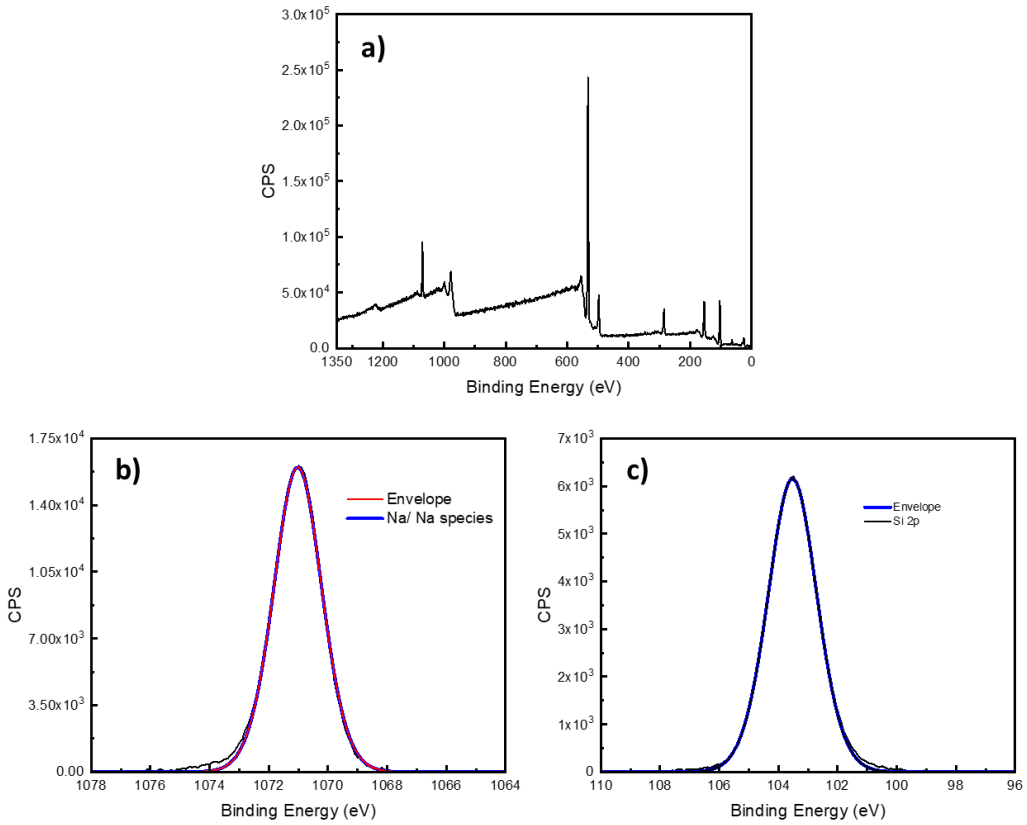

Supplementary figure (S7.5): The survey spectrum of a foamed sodium waterglass film in a), the Na KLL environment can be seen at ~500 eV. Figures b) and c) show the Na 1s and Si 2p peaks respectively. The peaks were fitted but no deconvolution was necessary as only one environment was thought to be present for these orbitals.

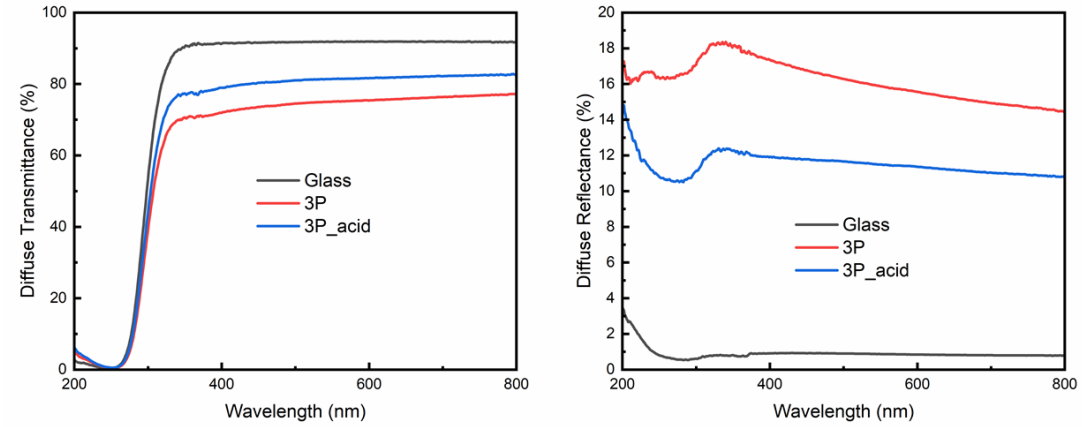

Supplementary figure (S7.6): The diffuse transmittance a) and reflectance b) of the foamed waterglass substrates are shown. The foamed silicate coatings decrease the transmittance and increase the reflectance of the glass, the coatings are translucent.

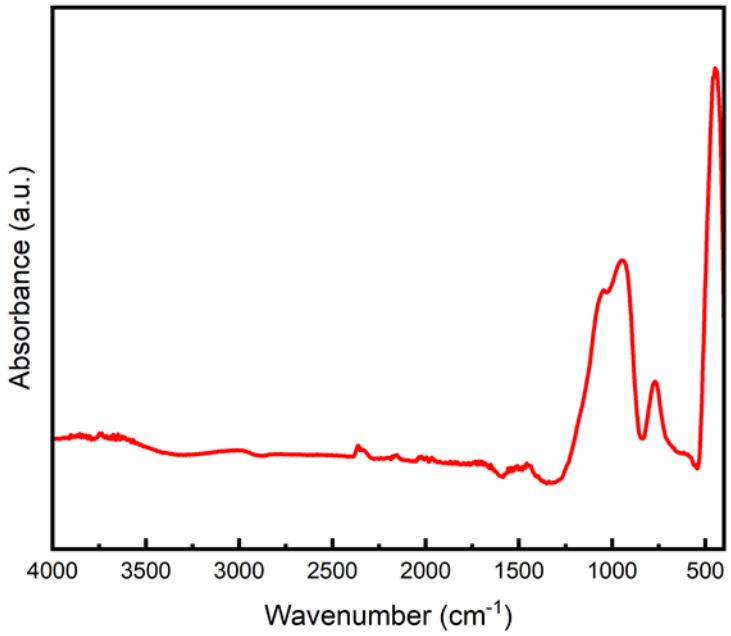

Supplementary figure (S7.7): FTIR absorbance of the foamed waterglass coating was measured. Characteristic silicate BO and NBO peaks can be seen between 450 and 1250 cm^{-1}.

		FWHM shift / nm	
		Film	Solution
Br_3	Day 1	23.5	26.9
	Day 21	22.5	24.6
$(Br/I)_3$ Br = 10%	Day 1	37.6	41.5
	Day 21	37.4	19.7
I_3	Day 1	47.4	44.9
	Day 5	-	43.5
	Day 9	38.6	-

Supplementary table (S7.8): The change in the full width at half maximum (FWHM) of the emission peak of each composition with time for both supported and solution phase nanocrystals. The narrowing of the emission peak was thought to be associated with a decrease in the nanocrystal size distribution.

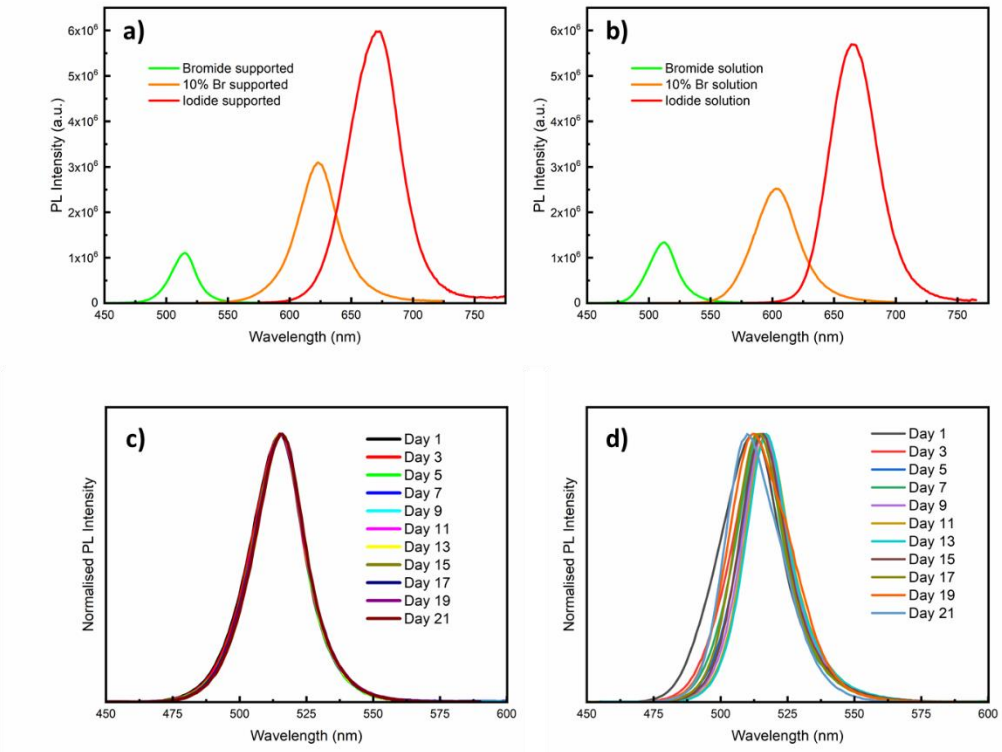

Supplementary figure (S7.9): Initial emission spectra and the differences in the absolute emission intensities are shown in a) and b). Normalised bromide data for supported and solution phase quantum dots are shown in c) and d).

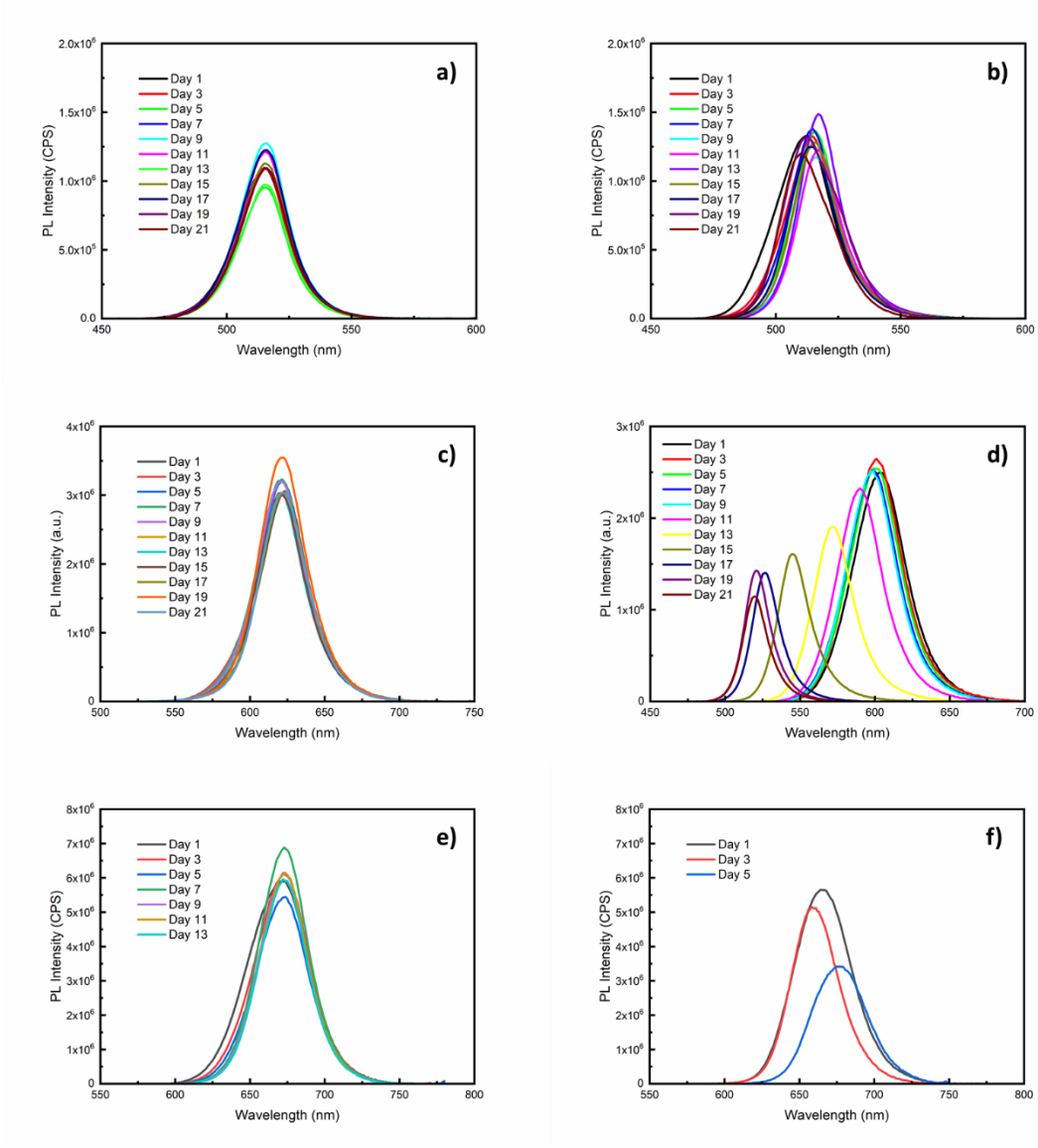

Supplementary figure (S7.10): The change in the intensity of the emission peaks with time is shown. Figures a), c) and d) correspond to the bromide, mixed halide (10%) and iodide emission spectra supported on the foamed sodium silicate. Figures b), d) and f) show the changes in the intensity of the same compositions in solution.

Composition	Lifetime		Initial QY	Average lifetime, τ_a	Radiative lifetime, τ_r	Non-radiative decay, $\tau_{n,r}$
	τ_1	τ_2				
$CsPbBr_3$	3.1	14.6	29.6	15.2	51.4	4.6
$CsPb(Br_xI_{1-x})_3$ (x = 10%)	2.7	14.6	41.9	17.9	42.7	3.2
$CsPbI_3$	4.0	29.8	66.7	18.6	27.9	1.8

Supplementary table (S7.11): The time-resolved photoluminescence data are shown of the supported quantum dots are tabulated.

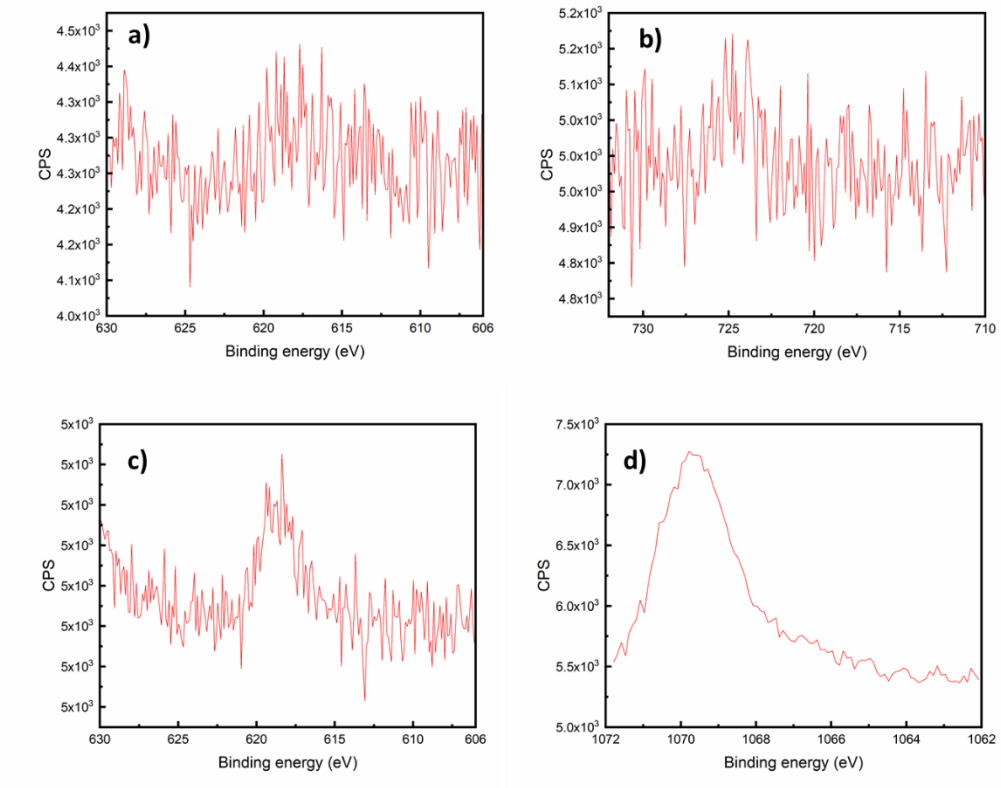

Supplementary figure (S7.12): The XPS spectra of 40% bromide samples after sensing are shown. Spectra in a) and b) show the noise level signals of the acetone and formaldehyde exposed I 3d and Cs 3d regions respectively. In c) the I 3d signal of the formaldehyde exposed sample is shown, while d) exemplifies the Na 1s peak that was present at the surface of all samples.

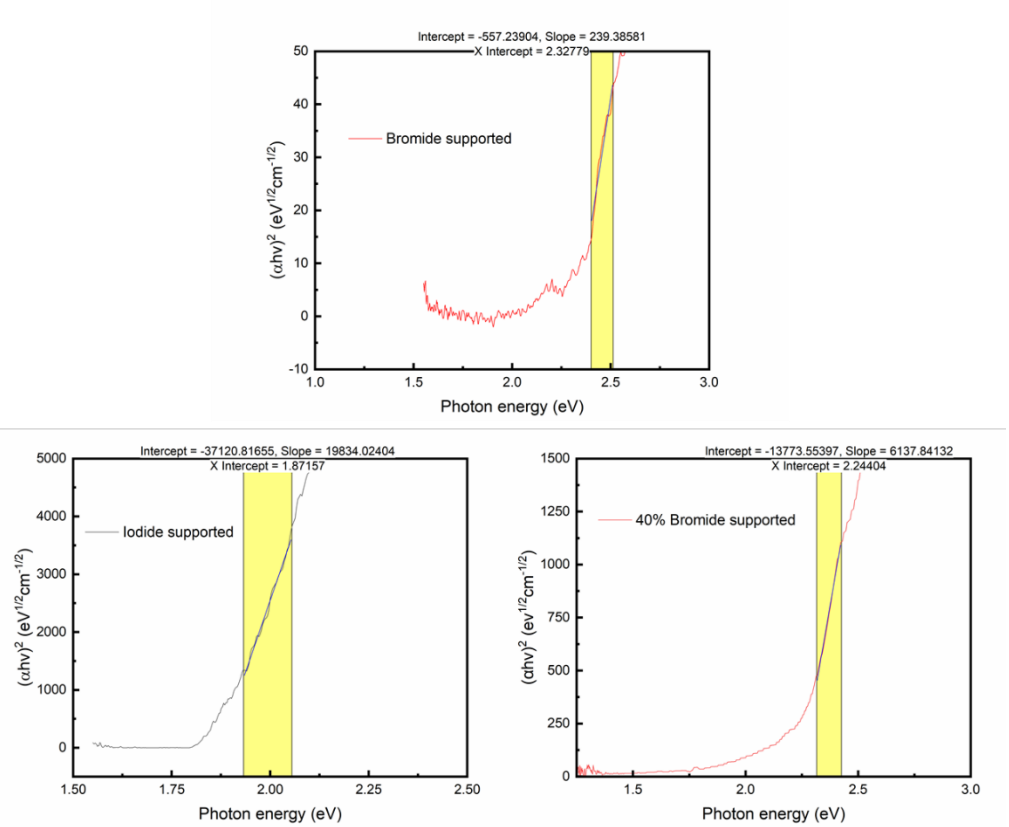

Supplementary figure: The Tauc plots used to determine the band gaps of the supported quantum dots are shown. The linear region was extrapolated to the abscissa to determine the band gap energy.

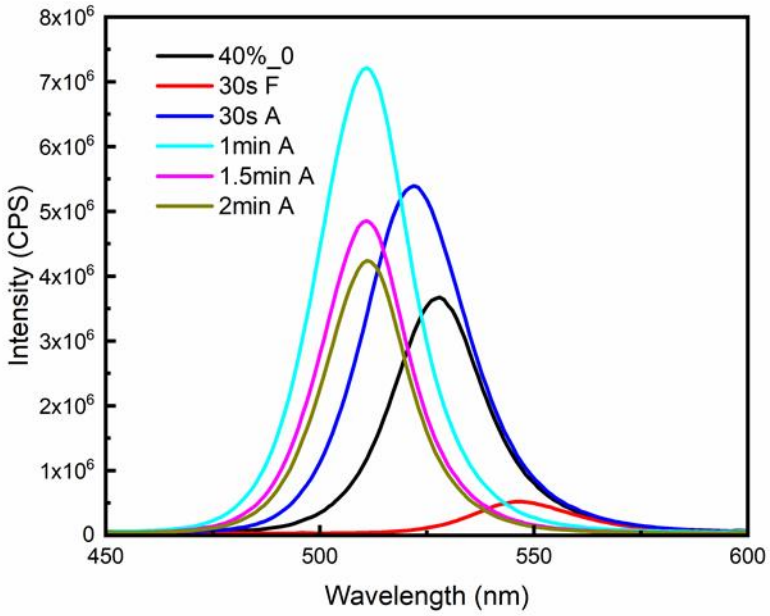

Supplementary data: The change in the intensity of the emission spectra of the supported 40% bromide samples upon exposure to acetone or formaldehyde vapour is shown. The intensity remains consistent upon acetone exposure but is greatly decreased upon exposure to formaldehyde.

10. References

1. Davis, M. E. Ordered Porous Materials for Emerging Applications. *Nature* **417**, 813–821 (2002).

2. Guldin, S. *et al.* Self-Cleaning Antireflective Optical Coatings. *Nano Lett.* **13**, 5329–5335 (2013).

3. Galo J. de A. A. Soler-Illia, †, Clément Sanchez, *, Bénédicte Lebeau, ‡ and & Patarin‡, J. Chemical Strategies To Design Textured Materials: from Microporous and Mesoporous Oxides to Nanonetworks and Hierarchical Structures. *Chem. Rev.* **102**, 4093–4138 (2002).

4. Breck, D. W., Eversole, W. G., Milton, R. M., Reed, T. B. & Thomas, T. L. Crystalline Zeolites. I. The Properties of a New Synthetic Zeolite, Type A. *J. Am. Chem. Soc.* **78**, 5963–5972 (1956).

5. Reed, T. B. & Breck, D. W. Crystalline Zeolites. 11. Crystal Structure. **78**, 5972–5977 (1956).

6. Lok, B. M. *et al.* Silicoaluminophosphate Molecular Sieves: Another New Class of Microporous Crystalline Inorganic Solids. *J. Am. Ceram. Soc.* **106**, 6092–6093 (1984).

7. Slater, A. G. & Cooper, A. I. Function-led design of new porous materials. *Science (80-.).* **348**, 988 (2015).

8. Thomas, A., Goettmann, F. & Antonietti, M. Hard templates for soft materials: Creating nanostructured organic material. *Chem. Mater.* **20**, 738–755 (2008).

9. Lee, J., Kim, J. & Hyeon, T. Recent progress in the synthesis of porous carbon materials. *Adv. Mater.* **18**, 2073–2094 (2006).

10. Lee, J. S. M., Briggs, M. E., Hasell, T. & Cooper, A. I. Hyperporous Carbons from Hypercrosslinked Polymers. *Adv. Mater.* **28**, 9804–9810 (2016).

11. Rowsell, J. L. C. & Yaghi, O. M. Metal-organic frameworks: A new class of porous materials. *Microporous Mesoporous Mater.* **73**, 3–14 (2004).

12. Matsui, M. *et al.* Selective adsorption of biopolymers on zeolites. *Chem. - A Eur. J.* **7**, 1555–1560 (2001).

13. Wang, K.-X., Li, X.-H. & Chen, J.-S. Surface and interface engineering of electrode materials for lithium-ion batteries. *Adv. Mater.* **27**, 527–45 (2015).

14. Burrows, A. D. Gas sensing using porous materials for automotive applications.

Chem. Soc. Rev. **44**, 4290–4321 (2015).

15. Rashidi, S., Esfahani, J. A. & Rashidi, A. A review on the applications of porous materials in solar energy systems. *Renew. Sustain. Energy Rev.* **73**, 1198–1210 (2017).

16. Phillips, K. R. *et al.* A colloidoscope of colloid-based porous materials and their uses. *Chem. Soc. Rev.* **45**, 281–322 (2016).

17. Roth, W. J., Nachtigall, P., Morris, R. E. & Jir, C. Two-Dimensional Zeolites : Current Status and Perspectives. *Chem. Rev.* **114**, 4807–4837 (2014).

18. Stein, A., Rudisill, S. G. & Petkovich, N. D. Perspective on the influence of interactions between hard and soft templates and precursors on morphology of hierarchically structured porous materials. *Chem. Mater.* **26**, 259–276 (2014).

19. Ji, Y., Wang, Y., Xie, B. & Xiao, F.-S. Zeolite Seeds: Third Type of Structure Directing Agents in the Synthesis of Zeolites. *Comments Inorg. Chem.* **3594**, 150409085938001 (2015).

20. Holland, B. T., Blanford, C. F. & Stein, A. Synthesis of Macroporous Minerals with Highly Ordered Three-Dimensional Arrays of Spheroidal Voids. *Science (80-.).* **281**, 538–540 (1998).

21. Yuan, Z.-Y. & Su, B.-L. Insights into hierarchically meso-macroporous structured materials. *J. Mater. Chem.* **16**, 663–677 (2006).

22. Carn, F. *et al.* Rational design of macrocellular silica scaffolds obtained by a tunable sol-gel foaming process. *Adv. Mater.* **16**, 140–144 (2004).

23. Yang, P. Hierarchically Ordered Oxides. *Science (80-.).* **282**, 2244–2246 (1998).

24. Schwieger, W. *et al.* Hierarchy concepts: classification and preparation strategies for zeolite containing materials with hierarchical porosity. *Chem. Soc. Rev.* **45**, 3353–3376 (2015).

25. L. Vidal, C. Marichal, V. Gramlich, J. Patarin, and Z. G. Mu-7, a New Layered Aluminophosphate [CH3NH3]3[Al3P4O16]witha4 × 8 Network: Characterization, Structure, and Possible Crystallization Mechanism. *Chem. Mater.* **11**, 2728–2736 (1999).

26. Bhachu, D. S., Smith, A. J., Parkin, I. P., Dent, A. J. & Sankar, G. Zeolite films: A new synthetic approach. *J. Mater. Chem. A* **1**, 1388–1393 (2013).

27. Brinker, J. C., Lu, Y., Sellinger, A. & Fan, H. Evaporation-Induced Self-

Assembly: Nanostructures Made Easy. *Adv. Mater.* **11**, 579–585 (1999).

28. Kresge, C. T.; Leonowicz, M. E.; Roth, W. J.; Vartuli, J. C.; Beck, J. S. Ordered mesoporous molecular sieves synthesized by a liquid-crystal template mechanism. *Nature* **359**, 710–712 (1992).

29. Jayanthi, G. V., Zhang, S. C. & Messing, G. L. Modeling of Solid Particle Formation During Solution Aerosol Thermolysis: The Evaporation Stage. *Aerosol Sci. Technol.* **19**, 478–490 (1993).

30. Yang, H., Ozin, G. a. & Kresge, C. T. The Role of Defects in the Formation of Mesoporous Silica Fibers, Films, and Curved Shapes. *Adv. Mater.* **10**, 883–887 (1998).

31. Gomez-vega, J. M. *et al.* Spin casted mesoporous silica coatings for medical applications. *Thin Solid Films* **398**–**399**, 615–620 (2001).

32. Kim, S. H., Misner, M. J., Xu, T., Kimura, M. & Russell, T. P. Highly Oriented and Ordered Arrays from Block Copolymers via Solvent Evaporation. *Adv. Mater.* **16**, 226–231 (2004).

33. Park, C., Yoon, J. & Thomas, E. L. Enabling nanotechnology with self assembled block copolymer patterns. *Polymer (Guildf).* **44**, 6725–6760 (2003).

34. Majewski, P. W. & Yager, K. G. Rapid ordering of block copolymer thin films. *J. Phys. Condens. Matter* **28**, 403002 (2016).

35. Guliants, V. V., Carreon, M. A. & Lin, Y. S. Ordered mesoporous and macroporous inorganic films and membranes. *J. Memb. Sci.* **235**, 53–72 (2004).

36. Kao, K. C., Lin, C. H., Chen, T. Y., Liu, Y. H. & Mou, C. Y. A General Method for Growing Large Area Mesoporous Silica Thin Films on Flat Substrates with Perpendicular Nanochannels. *J. Am. Chem. Soc.* **137**, 3779–3782 (2015).

37. Jr, K. J. B., Scott, A. S., Gimon-kinsel, M. E. & Blanco, J. H. Oriented films of mesoporous MCM-41 macroporous tubules via pulsed laser deposition. *Microporous Mesoporous Mater.* **38**, 97–105 (2000).

38. Kobler, J. & Bein, T. Porous Thin Films of Functionalized Mesoporous Silica Nanoparticles. *ACS Nano* **2**, 2324–2330 (2008).

39. Moghal, J. *et al.* High-performance, single-layer antireflective optical coatings comprising mesoporous silica nanoparticles. *ACS Appl. Mater. Interfaces* **4**, 854–859 (2012).

40. Yohanala P. T., F., Mulya Dewa, R., Quarta, K., _ W. & Winardi, S. Preparation of Polystyrene Spheres Using Surfactant-Free Emulsion Polymerization. *Mod. Appl. Sci.* **9**, p121 (2015).

41. Chung-li, Y., Goodwin, J. W. & Ottewill, R. H. Studies on the preparation and characterisation of monodisperse polystyrene latices. *Langmuir* 163–175 (1976). doi:10.1007/bfb0117065

42. Stein, A. & Schroden, R. C. Colloidal crystal templating of three-dimensionally ordered macroporous solids: Materials for photonics and beyond. *Curr. Opin. Solid State Mater. Sci.* **5**, 553–564 (2001).

43. Wang, X., Summers, C. J. & Wang, Z. L. Large-scale hexagonal-patterned growth of aligned ZnO nanorods for nano-optoelectronics and nanosensor arrays. *Nano Lett.* **4**, 423–426 (2004).

44. Khramov, A. N., Munos, J. & Collinson, M. M. Preparation and Characterization of Macroporous Silicate Films. *Langmuir* **17**, 8112–8117 (2001).

45. Ariga, K., Yamauchi, Y., Mori, T. & Hill, J. P. 25th Anniversary article: What can be done with the langmuir-blodgett method? Recent developments and its critical role in materials science. *Adv. Mater.* **25**, 6477–6512 (2013).

46. Jeong, G. H. *et al.* Fabrication of low-cost mold and nanoimprint lithography using polystyrene nanosphere. *Microelectron. Eng.* **87**, 51–55 (2010).

47. Liu, D. F. *et al.* Periodic ZnO Nanorod Arrays Defined by Polystyrene Microsphere Self-Assembled Monolayers. *Nano Lett.* (2006).

48. Huang, Z., Fang, H. & Zhu, J. Fabrication of silicon nanowire arrays with controlled diameter, length, and density. *Adv. Mater.* **19**, 744–748 (2007).

49. Yeom, J., Ratchford, D., Field, C. R., Brintlinger, T. H. & Pehrsson, P. E. Decoupling diameter and pitch in silicon nanowire arrays made by metal-assisted chemical etching. *Adv. Funct. Mater.* **24**, 106–116 (2014).

50. Pine, D. J. & Imhof, A. Ordered macroporous materials by emulsion templating. *Nature* **389**, 948–951 (1997).

51. Binks, B. P. Macroporous Silica From Solid Stabilized Emulsion Templates. *Adv. Mater.* 1824–1827 (2002). doi:10.1002/adma.200290010

52. Nakanishi, K. & Tanaka, N. Sol – Gel with Phase Separation . Hierarchically Porous Materials Optimized for High-Performance Liquid Chromatography Separations. *Acc. Chem. Res.* **40**, 863–873 (2007).

53. Chemtob, A. *et al.* Macroporous organosilica films via a template-free photoinduced sol–gel process. *J. Mater. Chem.* **20**, 9104 (2010).

54. Ye, Y. H., Badilescu, S. & Truong, V. Van. Large-scale ordered macroporous SiO2 thin films by a template-directed method. *Appl. Phys. Lett.* **81**, 616–618 (2002).

55. Nishihara, H., Mukai, S. R., Yamashita, D. & Tamon, H. Ordered macroporous silica by ice templating. *Chem. Mater.* **17**, 683–689 (2005).

56. Gérardin, C., Reboul, J., Bonne, M. & Lebeau, B. Ecodesign of ordered mesoporous silica materials. *Chem. Soc. Rev.* **42**, 4217–55 (2013).

57. Sierra, L. & Guth, J.-L. Synthesis of mesoporous silica with tunable pore size from sodium silicate solutions and a polyethylene oxide surfactant. *Microporous Mesoporous Mater.* **27**, 243–253 (1999).

58. Fujiwara, M. *et al.* Preparation of silica thin films with macropore holes from sodium silicate and polymethacrylate: An approach to formation mechanism of diatomaceous earth like silica hollow particles. *Chem. Eng. J.* **172**, 1103–1110 (2011).

59. Kim, J. M. *et al.* Synthesis of highly ordered mesoporous silica materials using sodium silicate and amphiphilic block copolymers. *Chem. Commun.* **368**, 1159–1160 (2000).

60. Jo, C., Kim, K. & Ryoo, R. Syntheses of high quality KIT-6 and SBA-15 mesoporous silicas using low-cost water glass, through rapid quenching of silicate structure in acidic solution. *Microporous Mesoporous Mater.* **124**, 45–51 (2009).

61. Pillai, S. *et al.* Tunable 3D and 2D polystyrene nanoparticle assemblies using surface wettability, low volume fraction and surfactant effects. *Nanotechnology* **20**, 025604 (2009).

62. Jiang, P., Cizeron, J., Bertone, J. F. & Colvin, V. L. Preparation of macroporous metal films from colloidal crystals. *J. Am. Chem. Soc.* **121**, 7957–7958 (1999).

63. Li, W., Wu, Z., Wang, J., Elzatahry, A. A. & Zhao, D. A Perspective on Mesoporous TiO_2 Materials. *Chem. Mater.* **26**, 287–298 (2014).

64. Schroden, R. C., Blanford, C. F., Melde, B. J., Johnson, B. J. S. & Stein, A. Direct Synthesis of Ordered Macroporous Silica Materials Functionalized with Polyoxometalate Clusters. *Chem. Mater.* **13**, 1074–1081 (2001).

65. Franceschini, E. A., Llave, E. de la, Williams, F. J. & Soler-Illia, G. J. A. A. A simple three step method for selective placement of organic groups in mesoporous silica thin films. *Mater. Chem. Phys.* **169**, 82–88 (2015).

66. Goldstein, J. *et al. Scanning Electron Microscopy and X-ray Microanalysis - Third Edition*. (2007).

67. McMillan, P. F. Raman spectroscopy in mineralogy and geochemistry. *Ann. Rev. Earth Planet. Sci.* **17**, 255–283 (1989).

68. Cassie, B. D. Contact Angles. 11–16 (1948).

69. Wenzel, R. N. Resistance of solid surfaces to wetting by water. *Ind. Eng. Chem.* **28**, 988–994 (1936).

70. Cassie, B. D. & Baxter, S. Wettability of Porous Surfaces. 546–551 (1944).

71. Mills, A., Wang, J. & McGrady, M. Method of rapid assessment of photocatalytic activities of self-cleaning films. *J. Phys. Chem. B* **110**, 18324–18331 (2006).

72. Grosso, D. How to exploit the full potential of the dip-coating process to better control film formation. *J. Mater. Chem.* **21**, 17033–17038 (2011).

73. Van Dokkum, H. P., Hulskotte, J. H. J., Kramer, K. J. M. & Wilmot, J. Emission, Fate and Effects of Soluble Silicates (Waterglass) in the Aquatic Environment. *Environ. Sci. Technol.* **38**, 515–521 (2004).

74. Falcone, J. S. *Silicon Compounds: Anthropogenic Silicas and Silicates*. *Kirk-Othmer Encyclopedia of Chemical Technology* (2015). doi:10.1002/0471238961.1925142006011203.a01.pub3

75. Weldes, H. H. & Lange, K. R. Properties of soluble silicates. *Ind. Eng. Chem.* **61**, 29–44 (1969).

76. Svensson, I. L., Sjöberg, S. & Öhman, L. O. Polysilicate equilibria in concentrated sodium silicate solutions. *J. Chem. Soc. Faraday Trans.* **82**, 3635–3646 (1986).

77. Brykov, A. S., Danilov, V. V. & Aleshunina, E. Y. State of silicon in silicate and silica-containing solutions and their binding properties. *Russ. J. Appl. Chem.* **81**, 1717–1721 (2008).

78. Nordström, J. *et al.* Silica/alkali ratio dependence of the microscopic structure of sodium silicate solutions. *J. Colloid Interface Sci.* **397**, 9–17 (2013).

79. Engelhardt, G., Zeigan, D., Jancke, H., Hoebbel, D. & Weiker, Z. High resolution

29Si NMR of silicates and zeolites. *Z. Anorg. Allg. Chem.* **418**, 17–28 (1975).

80. Edén, M. NMR studies of oxide-based glasses. *Annu. Reports Prog. Chem. - Sect. C* **108**, 177–221 (2012).

81. Vidal, L. *et al.* Controlling the reactivity of silicate solutions: A FTIR, Raman and NMR study. *Colloids Surfaces A Physicochem. Eng. Asp.* **503**, 101–109 (2016).

82. Bass, J. L. & Turner, G. L. Anion Distributions in Sodium Silicate Solutions. Characterization by 29Si NMR and Infrared Spectroscopies, and Vapor Phase Osmometry. *J. Phys. Chem. B* **101**, 10638–10644 (1997).

83. Falcone, J. S., Bass, J. L., Krumrine, P. H., Brensinger, K. & Schenk, E. R. Characterizing the infrared bands of aqueous soluble silicates. *J. Phys. Chem. A* **114**, 2438–2446 (2010).

84. Lucas, S., Tognonvi, M. T., Gelet, J. L., Soro, J. & Rossignol, S. Interactions between silica sand and sodium silicate solution during consolidation process. *J. Non. Cryst. Solids* **357**, 1310–1318 (2011).

85. Tognonvi, M. T., Soro, J. & Rossignol, S. Physical-chemistry of silica/alkaline silicate interactions during consolidation. Part 1: Effect of cation size. *J. Non. Cryst. Solids* **358**, 81–87 (2012).

86. Böschel, D., Janich, M. & Roggendorf, H. Size distribution of colloidal silica in sodium silicate solutions investigated by dynamic light scattering and viscosity measurements. *J. Colloid Interface Sci.* **267**, 360–368 (2003).

87. Kinrade, S. D. & Pole, D. L. Effect of Alkali-Metal Cations on the Chemistry of Aqueous Silicate Solutions. *Inorg. Chem.* **31**, 4558–4563 (1992).

88. Sjöberg, S. Silica in aqueous environments. *J. Non. Cryst. Solids* **196**, 51–57 (1996).

89. Cho, H. *et al.* Solution State Structure Determination of Silicate Oligomers by 29Si NMR Spectroscopy and Molecular Modeling. *J. Am. Chem. Soc.* **128**, 2324–2335 (2006).

90. Tognonvi, M. T., Massiot, D., Lecomte, A. & Rossignol, S. Identification of solvated species present in concentrated and dilute sodium silicate solutions by combined 29Si NMR and SAXS studies. *J. Colloid Interface Sci.* **352**, 309–315 (2010).

91. Yang, X., Zhu, W. & Yang, Q. The viscosity properties of sodium silicate solutions. *J. Solution Chem.* **37**, 73–83 (2008).

92. Gerber, T., Himmel, B. & Hübert, C. WAXS and SAXS investigation of structure formation of gels from sodium water glass. *J. Non. Cryst. Solids* **175**, 160–168 (1994).

93. Nordström, J. *et al.* Concentration- and pH-dependence of highly alkaline sodium silicate solutions. *J. Colloid Interface Sci.* **356**, 37–45 (2011).

94. Dent Glasser, L. S. & Lee, C. K. Drying of sodium silicate solutions. *J. Appl. Chem. Biotechnol.* **21**, 127–133 (2007).

95. Roggendorf, H., Böschel, D. & Rödicker, B. Differential scanning calorimetry at hydrothermal conditions of amorphous materials prepared by drying sodium silicate solutions. *J. Therm. Anal. Calorim.* **63**, 641–652 (2001).

96. Dupree, R., Holland, D., McMillan, P. W. & Pettifer, R. F. The Structure of Soda-Silica Glasses: A MAS NMR Study. *J. Non. Cryst. Solids* **68**, 399–410 (2000).

97. Maekawa, H., Maekawa, T., Kawamura, K. & Yokokawa, T. The structural groups of alkali silicate glasses determined from 29Si MAS-NMR. *J. Non. Cryst. Solids* **127**, 53–64 (1991).

98. Malfait, W. J., Halter, W. E., Morizet, Y., Meier, B. H. & Verel, R. Structural control on bulk melt properties: Single and double quantum 29Si NMR spectroscopy on alkali-silicate glasses. *Geochim. Cosmochim. Acta* **71**, 6002–6018 (2007).

99. Stebbins, J. F. Identification of multiple structural species in silicate glasses by 29Si NMR. *Nature* **330**, 465–467 (1987).

100. Eckert, H. Structural characterization of noncrystalline solids and glasses using solid state NMR. *Prog. Nucl. Magn. Reson. Spectrosc.* **24**, 159–293 (1992).

101. Sen, S. & Youngman, R. E. NMR study of Q-speciation and connectivity in K2O-SiO2 glasses with high silica content. *J. Non. Cryst. Solids* **331**, 100–107 (2003).

102. Mazzara, C., Jupille, J., Flank, A.-M. & Lagarde, P. Stereochemical Order around Sodium in Amorphous Silica. *J. Phys. Chem. B* **104**, 3438–3445 (2000).

103. Greaves, G. N., Fontaine, A., Lagarde, P., Raoux, D. & Gurman, S. J. Local structure of silicate glasses. *Nature* **293**, 611–616 (1981).

104. Aguiar, H., Serra, J., González, P. & León, B. Structural study of sol-gel silicate glasses by IR and Raman spectroscopies. *J. Non. Cryst. Solids* **355**, 475–480 (2009).

105. Macdonald, S. A., Schardt, C. R., Masiello, D. J. & Simmons, J. H. Dispersion analysis of FTIR reflection measurements in silicate glasses. *J. Non. Cryst. Solids* **275**, 72–82 (2000).

106. Agarwal, A. & Tomozawa, M. Correlation of silica glass properties with the infrared spectra. *J. Non. Cryst. Solids* **209**, 166–174 (1997).

107. Uchino, T., Sakka, T. & Iwasaki, M. Interpretation of Hydrated States of Sodium Silicate Glasses by Infrared and Raman Analysis. *J. Am. Ceram. Soc.* **74**, 306–313 (1991).

108. Furukawa, T., Fox, K. E. & White, W. B. Raman spectroscopic investigation of the structure of silicate glasses. III. Raman intensities and structural units in sodium silicate glasses. *J. Chem. Phys.* **75**, 3226–3237 (1981).

109. Amma, S. I., Luo, J., Pantano, C. G. & Kim, S. H. Specular reflectance (SR) and attenuated total reflectance (ATR) infrared (IR) spectroscopy of transparent flat glass surfaces: A case study for soda lime float glass. *J. Non. Cryst. Solids* **428**, 189–196 (2015).

110. Uchino, T., Sakka, T., Hotta, K. & Iwasaki, M. Attenuated Total Reflectance Fourier-Transform Infrared Spectra of a Hydrated Sodium Silicate Glass. *J. Am. Ceram. Soc.* **72**, 2173–2175 (1989).

111. Sprenger, D., Bach, H., Meisel, W. & Gütlich, P. Discrete bond model (DBM) of sodium silicate glasses derived from XPS, Raman and NMR measurements. *J. Non. Cryst. Solids* **159**, 187–203 (1993).

112. Nesbitt, W. H., Sawyer, R., Michael Bancroft, G. & Henderson, G. S. Bridging oxygen speciation and free oxygen (O2−) in K-silicate glasses: Implications for spectroscopic studies and glass structure. *Chem. Geol.* **461**, 13–22 (2017).

113. Sprenger, D., Bach, H., Meisel, W. & Gütlich, P. XPS study of leached glass surfaces. *J. Non. Cryst. Solids* **126**, 111–129 (1990).

114. Banerjee, J., Bojan, V., Pantano, C. G. & Kim, S. H. Effect of heat treatment on the surface chemical structure of glass: Oxygen speciation from in situ XPS analysis. *J. Am. Ceram. Soc.* **101**, 644–656 (2018).

115. Veinot, D. E., Langille, K. B., Nguyen, D. T. & Bernt, J. O. Efflorescence of soluble silicate coatings. *J. Non. Cryst. Solids* **127**, 221–226 (1991).

116. Joshi, S., Kalyanasundaram, S. & Balasubramanian, V. Quantitative analysis of sodium carbonate and sodium bicarbonate in solid mixtures using Fourier

Transform Infrared Spectroscopy (FT-IR). *Appl. Spectrosc.* **67**, 841–845 (2013).

117. Lam, R. K. *et al.* Reversed interfacial fractionation of carbonate and bicarbonate evidenced by X-ray photoemission spectroscopy. *J. Chem. Phys.* **146**, (2017).

118. Engelhardt, G., Fahlke, B., Mägi, M. & Lippmaa, E. High-resolution solid-state 29Si and 27Al n.m.r. of aluminosilicate intermediates in the synthesis of zeolite A. Part II. *Zeolites* **5**, 49–52 (1985).

119. Liu, J., Yang, Q., Zhao, X. S. & Zhang, L. Pore size control of mesoporous silicas from mixtures of sodium silicate and TEOS. *Microporous Mesoporous Mater.* **106**, 62–67 (2007).

120. Yakovlev, G. & Kodolov, V. Intumescent Fireproof Coating Based on Water Glass. *Int. J. Polym. Mater.* **47**, 107–115 (2000).

121. Loganina, V. I., Kislitsyna, S. N. & Mazhitov, Y. B. Development of sol-silicate composition for decoration of building walls. *Case Stud. Constr. Mater.* **9**, e00173 (2018).

122. Castella, N., Grishchuk, S., Karger-Kocsis, J. & Unik, M. Hybrid resins from polyisocyanate, epoxy resin and water glass: Chemistry, structure and properties. *J. Mater. Sci.* **45**, 1734–1743 (2010).

123. Fabjan, E. Š. *et al.* Protection of organic pigments against photocatalysis by encapsulation. *J. Sol-Gel Sci. Technol.* **62**, 65–74 (2012).

124. Nielsen, K. H. *et al.* Large area, low cost anti-reflective coating for solar glasses. *Sol. Energy Mater. Sol. Cells* **128**, 283–288 (2014).

125. Huang, Q. Z. *et al.* Study on sodium water glass-based anti-reflective film and its application in dye-sensitized solar cells. *Thin Solid Films* **610**, 19–25 (2016).

126. He, J., Fujikawa, S., Kunitake, T. & Nakao, A. Preparation of porous and nonporous silica nanofilms from aqueous sodium silicate. *Chem. Mater.* **15**, 3308–3313 (2003).

127. Gaggiano, R. *et al.* An infrared spectroscopic study of sodium silicate adsorption on porous anodic alumina. *Surf. Interface Anal.* **45**, 1098–1104 (2013).

128. Porter, D. A. Coated Glass. 1–9 (1992).

129. Barua, N. K., Ragini, T. & Subasri, R. Sol-gel derived single-layer zeolite-based coatings on glass for broadband antireflection properties. *J. Non. Cryst. Solids* **469**, 51–55 (2017).

130. Chen, C. H., Li, S. Y., Chiang, A. S. T., Wu, A. T. & Sun, Y. S. Scratch-resistant zeolite anti-reflective coating on glass for solar applications. *Sol. Energy Mater. Sol. Cells* **95**, 1694–1700 (2011).

131. Krins, N., Faustini, M., Louis, B. & Grosso, D. Thick and crack-free nanocrystalline mesoporous TiO2 films obtained by capillary coating from aqueous solutions. *Chem. Mater.* **22**, 6218–6220 (2010).

132. Witoon, T., Chareonpanich, M. & Limtrakul, J. Size control of nanostructured silica using chitosan template and fractal geometry: Effect of chitosan/silica ratio and aging temperature. *J. Sol-Gel Sci. Technol.* **56**, 270–277 (2010).

133. Hatton, B., Mishchenko, L., Davis, S., Sandhage, K. H. & Aizenberg, J. Assembly of large-area, highly ordered, crack-free inverse opal films. *Proc. Natl. Acad. Sci.* **107**, 10354–10359 (2010).

134. Guldin, S. *et al.* Dye-sensitized solar cell based on a three-dimensional photonic crystal. *Nano Lett.* **10**, 2303–2309 (2010).

135. Kim, D., Pugno, N. M. & Ryu, S. Wetting theory for small droplets on textured solid surfaces. *Sci. Rep.* **6**, 1–8 (2016).

136. Otitoju, T. A., Ahmad, A. L. & Ooi, B. S. Superhydrophilic (superwetting) surfaces: A review on fabrication and application. *J. Ind. Eng. Chem.* **47**, 19–40 (2017).

137. Duthon, P., Colomb, M. & Bernardin, F. Light Transmission in Fog: The Influence of Wavelength on the Extinction Coefficient. *Appl. Sci.* **9**, 2843 (2019).

138. Zhang, X. & He, J. Hydrogen-Bonding-Supported Self-Healing Antifogging Thin Films. *Sci. Rep.* **5**, 9227 (2015).

139. Zhang, X. & He, J. Antifogging antireflective thin films: Does the antifogging layer have to be the outmost layer? *Chem. Commun.* **51**, 12661–12664 (2015).

140. Huang, W., Chen, Y., Yang, C., Situ, Y. & Huang, H. pH-driven phase separation: Simple routes for fabricating porous TiO2 film with superhydrophilic and anti-fog properties. *Ceram. Int.* **41**, 7573–7581 (2015).

141. Lee, H., Alcaraz, M. L., Rubner, M. F. & Cohen, R. E. Zwitter-wettability and antifogging coatings with frost-resisting capabilities. *ACS Nano* **7**, 2172–2185 (2013).

142. Hu, X. *et al.* Highly transparent superhydrophilic graphene oxide coating for antifogging. *Mater. Lett.* **182**, 372–375 (2016).

143. Huang, T., Huang, W., Zhou, C., Situ, Y. & Huang, H. Superhydrophilicity of TiO2/SiO2 thin films: Synergistic effect of SiO2 and phase-separation-induced porous structure. *Surf. Coatings Technol.* **213**, 126–132 (2012).

144. Song, S., Jing, L., Li, S., Fu, H. & Luan, Y. Superhydrophilic anatase TiO2 film with the micro- and nanometer-scale hierarchical surface structure. *Mater. Lett.* **62**, 3503–3505 (2008).

145. Wang, J. J., Wang, D. S., Wang, J., Zhao, W. L. & Wang, C. W. High transmittance and superhydrophilicity of porous TiO2/SiO2 bi-layer films without UV irradiation. *Surf. Coatings Technol.* **205**, 3596–3599 (2011).

146. Yan, H., Yuanhao, W. & Hongxing, Y. TEOS/Silane-Coupling Agent Composed Double Layers Structure: A Novel Super-hydrophilic Surface. *Energy Procedia* **75**, 349–354 (2015).

147. Tian, F., Zhang, Y., Zhang, J. & Pan, C. Raman spectroscopy: A new approach to measure the percentage of anatase TiO2 exposed (001) facets. *J. Phys. Chem. C* **116**, 7515–7519 (2012).

148. Iwasaki, M., Davis, S. A. & Mann, S. Spongelike macroporous TiO2 monoliths prepared from starch gel template. *J. Sol-Gel Sci. Technol.* **32**, 99–105 (2004).

149. Zhang, B., Davis, S. A. & Mann, S. Starch gel templating of spongelike macroporous silicalite monoliths and mesoporous films. *Chem. Mater.* **14**, 1369–1375 (2002).

150. Tjandra, W., Yao, J. & Tam, K. C. Interaction between silicates and ionic surfactants in dilute solution. *Langmuir* **22**, 1493–1499 (2006).

151. Raut, H. K., Ganesh, V. A., Nair, A. S. & Ramakrishna, S. Anti-reflective coatings: A critical, in-depth review. *Energy Environ. Sci.* **4**, 3779–3804 (2011).

152. Tang, H., Berger, H., Schmid, P. E. & Levy, F. Optical properties of anatase TiO2. *Solid State Comm.* **92**, 267–271 (1994).

153. Zhang, J., Li, M., Feng, Z., Chen, J. & Li, C. UV raman spectroscopic study on TiO2- I. phase transformation at the surface and in the bulk. *J. Phys. Chem. B* **110**, 927–935 (2006).

154. Vittadini, A., Selloni, A., Rotzinger, F. P. & Grätzel, M. Structure and energetics of water adsorbed at TiO2 anatase \(101\) and \(001\) surfaces. *Phys. Rev. Lett.* **81**, 2954–2957 (1998).

155. Crick, C. R. & Parkin, I. P. Aerosol assisted deposition of melamine-

formaldehyde resin: Hydrophobic thin films from a hydrophilic material. *Thin Solid Films* **519**, 2181–2186 (2011).

156. Goodwin, J. W., Hearn, J., Ho, C. C. & Ottewill, R. H. Studies on the preparation and characterization of monodisperse polystyrene latices - III. Preparation without added surface active agents. *Colloid Polym. Sci.* **252**, 464–471 (1974).

157. Sun, J., Bhushan, B. & Tong, J. Structural coloration in nature. *RSC Adv.* **3**, 14862–14889 (2013).

158. Collins, G. *et al.* 2D and 3D photonic crystal materials for photocatalysis and electrochemical energy storage and conversion. *Sci. Technol. Adv. Mater.* **17**, 563–582 (2016).

159. Chen, J. I. L., Von Freymann, G., Choi, S. Y., Kitaev, V. & Ozin, G. A. Amplified photochemistry with slow photons. *Adv. Mater.* **18**, 1915–1919 (2006).

160. Vlasov, Y. a, Yao, N. & Norris, D. J. Synthesis of Photonic Crystals for Optical Wavelengths from Semiconductor Quantum Dots. *Adv. Mater.* **11**, 165–169 (1999).

161. ITOPF.org. Available at: https://www.itopf.org/knowledge-resources/data-statistics/statistics/#:~:text=In the 2010s there were,the quantity of oil spilt.

162. Lu, Y. *et al.* Creating Superhydrophobic Mild Steel Surfaces for Water Proofing and Oil-Water Separation. *J. Mater. Chem. A* **2**, 11628–11634 (2014).

163. Zhang, W. *et al.* Micro/nano hierarchical poly(acrylic acid)-grafted-poly(vinylidene fluoride) layer coated foam membrane for temperature-controlled separation of heavy oil/water. *Sep. Purif. Technol.* **156**, 207–214 (2015).

164. Yang, H. C. *et al.* Mussel-inspired modification of a polymer membrane for ultra-high water permeability and oil-in-water emulsion separation. *J. Mater. Chem. A* **2**, 10225–10230 (2014).

165. Zhang, W. *et al.* Salt-induced fabrication of superhydrophilic and underwater superoleophobic PAA-g-PVDF membranes for effective separation of oil-in-water emulsions. *Angew. Chemie - Int. Ed.* **53**, 856–860 (2014).

166. Ejaz Ahmed, F., Lalia, B. S., Hilal, N. & Hashaikeh, R. Underwater superoleophobic cellulose/electrospun PVDF-HFP membranes for efficient oil/water separation. *Desalination* **344**, 48–54 (2014).

167. Wen, Q., Di, J., Jiang, L., Yu, J. & Xu, R. Zeolite-coated mesh film for efficient oil-water separation. *Chem. Sci.* **4**, 591–595 (2013).

168. Zeng, J. & Guo, Z. Superhydrophilic and underwater superoleophobic MFI zeolite-coated film for oil/water separation. *Colloids Surfaces A Physicochem. Eng. Asp.* **444**, 283–288 (2014).

169. Li, J. *et al.* Superhydrophilic-underwater superoleophobic ZnO-based coated mesh for highly efficient oil and water separation. *Mater. Lett.* **153**, 62–65 (2015).

170. Li, J. *et al.* Facile fabrication of underwater superoleophobic TiO2 coated mesh for highly efficient oil/water separation. *Colloids Surfaces A Physicochem. Eng. Asp.* **489**, 441–446 (2016).

171. Zhou, C. *et al.* Superhydrophilic and underwater superoleophobic titania nanowires surface for oil repellency and oil/water separation. *Chem. Eng. J.* **301**, 249–256 (2016).

172. Gao, S. J., Shi, Z., Zhang, W. Bin, Zhang, F. & Jin, J. Photoinduced superwetting single-walled carbon nanotube/TiO2 ultrathin network films for ultrafast separation of oil-in-water emulsions. *ACS Nano* **8**, 6344–6352 (2014).

173. Zhang, Z. H. *et al.* One-step fabrication of robust superhydrophobic and superoleophilic surfaces with self-cleaning and oil/water separation function. *Sci. Rep.* **8**, 1–12 (2018).

174. Tay, A., Singh, R. K., Krishnan, S. S. & Gore, J. P. Authentication of olive oil adulterated with vegetable oils using Fourier transform infrared spectroscopy. *LWT - Food Sci. Technol.* **35**, 99–103 (2002).

175. Hossain, M. N., Uddin, M. N. & Karim, M. M. Prediction of viscosity index of motor oils using FTIR spectral data and chemometrics. *J. Sci. Innov. Res.* **7**, 43–49 (2018).

176. Sejkorová, M. Application of FTIR spectrometry using multivariate analysis for prediction fuel in engine oil. *Acta Univ. Agric. Silvic. Mendelianae Brun.* **65**, 933–938 (2017).

177. Araújo, S. V. *et al.* FTIR assessment of the oxidation process of castor oil FAME submitted to PetroOXY and Rancimat methods. *Fuel Process. Technol.* **92**, 1152–1155 (2011).

178. Huang, H., Bodnarchuk, M. I., Kershaw, S. V., Kovalenko, M. V. & Rogach, A. L. Lead Halide Perovskite Nanocrystals in the Research Spotlight: Stability and Defect Tolerance. *ACS Energy Lett.* **2**, 2071–2083 (2017).

179. Sun, C. *et al.* Efficient and Stable White LEDs with Silica-Coated Inorganic

Perovskite Quantum Dots. *Adv. Mater.* **28**, 10088–10094 (2016).

180. Liu, F. *et al.* Highly Luminescent Phase-Stable CsPbI3 Perovskite Quantum Dots Achieving Near 100% Absolute Photoluminescence Quantum Yield. *ACS Nano* acsnano.7b05442 (2017). doi:10.1021/acsnano.7b05442

181. Christians, J. A. *et al.* Enhanced mobility CsPbI3 quantum dot arrays for record-efficiency, high-voltage photovoltaic cells. *Sci. Adv.* **3**, eaao4204 (2017).

182. Akkerman, Q. A. *et al.* Strongly emissive perovskite nanocrystal inks for high-voltage solar cells. *Nat. Energy* **2**, 1–7 (2017).

183. Wong, A. B. *et al.* Growth and Anion Exchange Conversion of CH3NH3PbX3 Nanorod Arrays for Light-Emitting Diodes. *Nano Lett.* **15**, 5519–5524 (2015).

184. Ha, S.-T., Su, R., Xing, J., Zhang, Q. & Xiong, Q. Metal halide perovskite nanomaterials: synthesis and applications. *Chem. Sci.* **8**, 2522–2536 (2017).

185. Huang, S. *et al.* Enhancing the Stability of CH3NH3PbBr3 Quantum Dots by Embedding in Silica Spheres Derived from Tetramethyl Orthosilicate in “Waterless” Toluene. *J. Am. Chem. Soc.* **138**, 5749–5752 (2016).

186. Loiudice, A., Saris, S., Oveisi, E., Alexander, D. T. L. & Buonsanti, R. CsPbBr3 QD/AlOx Inorganic Nanocomposites with Exceptional Stability in Water, Light, and Heat. *Angew. Chemie - Int. Ed.* **56**, 10696–10701 (2017).

187. Wei, Y. *et al.* Enhancing the Stability of Perovskite Quantum Dots by Encapsulation in Crosslinked Polystyrene Beads via a Swelling–Shrinking Strategy toward Superior Water Resistance. *Adv. Funct. Mater.* **27**, 1–8 (2017).

188. Malgras, V. *et al.* Observation of Quantum Confinement in Monodisperse Methylammonium Lead Halide Perovskite Nanocrystals Embedded in Mesoporous Silica. *J. Am. Chem. Soc.* **138**, 13874–13881 (2016).

189. Zhang, D., Eaton, S. W., Yu, Y., Dou, L. & Yang, P. Solution-Phase Synthesis of Cesium Lead Halide Perovskite Nanowires. *J. Am. Chem. Soc.* **137**, 9230–9233 (2015).

190. Dou, L. *et al.* Atomically thin two-dimensional Organic-inorganic hybrid perovskites. *Science (80-.).* **349**, 1518–1521 (2015).

191. Tyagi, P., Arveson, S. M. & Tisdale, W. A. Colloidal Organohalide Perovskite Nanoplatelets Exhibiting Quantum Confinement. *J. Phys. Chem. Lett.* **6**, 1911–1916 (2015).

192. Bekenstein, Y., Koscher, B. A., Eaton, S. W., Yang, P. & Alivisatos, A. P. Highly Luminescent Colloidal Nanoplates of Perovskite Cesium Lead Halide and Their Oriented Assemblies. *J. Am. Chem. Soc.* **137**, 16008–16011 (2015).

193. Sichert, J. A. *et al.* Quantum Size Effect in Organometal Halide Perovskite Nanoplatelets. *Nano Lett.* **15**, 6521–6527 (2015).

194. Tong, Y. *et al.* Dilution-Induced Formation of Hybrid Perovskite Nanoplatelets. *ACS Nano* **10**, 10936–10944 (2016).

195. Protesescu, L. *et al.* Nanocrystals of Cesium Lead Halide Perovskites (CsPbX 3 , X = Cl, Br, and I): Novel Optoelectronic Materials Showing Bright Emission with Wide Color Gamut. *Nano Lett.* **15**, 3692–3696 (2015).

196. Huang, H., Susha, A. S., Kershaw, S. V., Hung, T. F. & Rogach, A. L. Control of Emission Color of High Quantum Yield CH3NH3PbBr3 Perovskite Quantum Dots by Precipitation Temperature. *Adv. Sci.* **2**, 1–5 (2015).

197. Sun, S., Yuan, D., Xu, Y., Wang, A. & Deng, Z. Ligand-Mediated Synthesis of Shape-Controlled Cesium Lead Halide Perovskite Nanocrystals via Reprecipitation Process at Room Temperature. *ACS Nano* **10**, 3648–3657 (2016).

198. Li, X. *et al.* CsPbX3 Quantum Dots for Lighting and Displays: Room-Temperature Synthesis, Photoluminescence Superiorities, Underlying Origins and White Light-Emitting Diodes. *Adv. Funct. Mater.* **26**, 2435–2445 (2016).

199. Becker, M. A. *et al.* Bright triplet excitons in lead halide perovskites. *Nature* **553**, 189–193 (2018).

200. Chen, D., Fang, G. & Chen, X. Silica-Coated Mn-Doped CsPb(Cl/Br)3 Inorganic Perovskite Quantum Dots: Exciton-to-Mn Energy Transfer and Blue-Excitable Solid-State Lighting. *ACS Appl. Mater. Interfaces* **9**, 40477–40487 (2017).

201. Raja, S. N. *et al.* Encapsulation of Perovskite Nanocrystals into Macroscale Polymer Matrices: Enhanced Stability and Polarization. *ACS Appl. Mater. Interfaces* **8**, 35523–35533 (2016).

202. Nedelcu, G. *et al.* Fast Anion-Exchange in Highly Luminescent Nanocrystals of Cesium Lead Halide Perovskites (CsPbX 3 , X = Cl, Br, I). *Nano Lett.* **15**, 5635–5640 (2015).

203. Akkerman, Q. A. *et al.* Tuning the Optical Properties of Cesium Lead Halide Perovskite. *J. Am. Chem. Soc.* **137**, 10276–10281 (2015).

204. Wang, H. C. *et al.* Mesoporous Silica Particles Integrated with All-Inorganic CsPbBr3 Perovskite Quantum-Dot Nanocomposites (MP-PQDs) with High Stability and Wide Color Gamut Used for Backlight Display. *Angew. Chemie - Int. Ed.* **55**, 7924–7929 (2016).

205. Huang, H. *et al.* Water resistant CsPbX3 nanocrystals coated with polyhedral oligomeric silsesquioxane and their use as solid state luminophores in all-perovskite white light-emitting devices. *Chem. Sci.* **7**, 5699–5703 (2016).

206. Hai, J. *et al.* Designing of blue, green, and red CsPbX3 perovskite-codoped flexible films with water resistant property and elimination of anion-exchange for tunable white light emission. *Chem. Commun.* **53**, 5400–5403 (2017).

207. Wang, C., Chesman, A. S. R. & Jasieniak, J. J. Stabilizing the cubic perovskite phase of CsPbI3 nanocrystals by using an alkyl phosphinic acid. *Chem. Commun.* **53**, 232–235 (2017).

208. Pan, J. *et al.* Air-Stable Surface-Passivated Perovskite Quantum Dots for Ultra-Robust, Single- and Two-Photon-Induced Amplified Spontaneous Emission. *J. Phys. Chem. Lett.* **6**, 5027–5033 (2015).

209. Ruan, L. *et al.* Stable and conductive lead halide perovskites facilitated by X-type ligands. *Nanoscale* **9**, 7252–7259 (2017).

210. Dirin, D. N. *et al.* Lead halide perovskites and other metal halide complexes as inorganic capping ligands for colloidal nanocrystals. *J. Am. Chem. Soc.* **136**, 6550–6553 (2014).

211. Song, Y. H. *et al.* Design of long-term stable red-emitting CsPb(Br0.4, I0.6)3perovskite quantum dot film for generation of warm white light. *Chem. Eng. J.* **313**, 461–465 (2017).

212. Ye, Y. *et al.* Highly Luminescent Cesium Lead Halide Perovskite Nanocrystals Stabilized in Glasses for Light-Emitting Applications. *Adv. Opt. Mater.* **1801663**, 1801663 (2019).

213. Dirin, D. N. *et al.* Harnessing Defect-Tolerance at the Nanoscale: Highly Luminescent Lead Halide Perovskite Nanocrystals in Mesoporous Silica Matrixes. *Nano Lett.* **16**, 5866–5874 (2016).

214. Kojima, A., Ikegami, M., Teshima, K. & Miyasaka, T. Highly Luminescent Lead Bromide Perovskite Nanoparticles Synthesized with Porous Alumina Media. *Chem. Lett.* **41**, 397–399 (2012).

215. Zhang, M. *et al.* Composition-dependent photoluminescence intensity and prolonged recombination lifetime of perovskite CH3NH3PbBr3-xClx films. *Chem. Commun.* **50**, 11727–11730 (2014).

216. Guarnera, S. *et al.* Improving the long-term stability of perovskite solar cells with a porous Al2O3 buffer layer. *J. Phys. Chem. Lett.* **6**, 432–437 (2015).

217. Chen, Z., Gu, Z., Fu, W., Wang, F. & Zhang, J. A Confined Fabrication of Perovskite Quantum Dots in Oriented MOF Thin Film. *ACS Appl. Mater. Interfaces* **8**, 28737–28742 (2016).

218. Anaya, M. *et al.* Strong Quantum Confinement and Fast Photoemission Activation in CH3NH3PbI3 Perovskite Nanocrystals Grown within Periodically Mesostructured Films. *Adv. Opt. Mater.* **5**, 1601087 (2017).

219. Demchyshyn, S. *et al.* Confining metal-halide perovskites in nanoporous thin films. *Sci. Adv.* **3**, e1700738 (2017).

220. Vassilakopoulou, A., Papadatos, D. & Koutselas, I. Flexible, cathodoluminescent and free standing mesoporous silica films with entrapped quasi-2D perovskites. *Appl. Surf. Sci.* **400**, 434–439 (2017).

221. Brandt, R. E., Stevanović, V., Ginley, D. S. & Buonassisi, T. Identifying defect-tolerant semiconductors with high minority-carrier lifetimes: Beyond hybrid lead halide perovskites. *MRS Commun.* **5**, 265–275 (2015).

222. Falcone, J. *Silicon Compounds: Anthropogenic Silicas and Silicates*. *Kirk-Othmer Encyclopedia of Chemical Tech* (2007). doi:10.1002/0471238961.1925142006011203.a01.pub22005

223. Osswald, J. & Fehr, K. T. FTIR spectroscopic study on liquid silica solutions and nanoscale particle size determination. *J. Mater. Sci.* **41**, 1335–1339 (2006).

224. Setoguchi, Y. M., Teraoka, Y., Moriguchi, I. & Kagawa, S. Rapid Room Temperature Synthesis of Hexagonal Mesoporous Silica Using Inorganic Silicate Sources and Cationic Surfactants under Highly Acidic Conditions. *J. Porous Mater.* **4**, 129–134 (1997).

225. Knight, C. T. & Harris, R. K. Silicon-29 nuclear magnetic resonance studies of aqueous silicate solutions. *J. Chem. Soc., Faraday Trans. 2* **79**, 1525–1538 (1983).

226. Gaggiano, R., Moriamé, P., Biesemans, M., De Graeve, I. & Terryn, H. Mechanism of formation of silicate thin films on porous anodic alumina. *Surf.*

Coatings Technol. **205**, 5210–5217 (2011).

227. Mampallil, D. & Eral, H. B. A review on suppression and utilization of the coffee-ring effect. *Adv. Colloid Interface Sci.* **252**, 38–54 (2018).

228. Banerjee, J., Kim, S. H. & Pantano, C. G. Elemental areal density calculation and oxygen speciation for flat glass surfaces using x-ray photoelectron spectroscopy. *J. Non. Cryst. Solids* **450**, 185–193 (2016).

229. Shchukarev, A. V. & Korolkov, D. V. Central European Science Journals X P S Study of Group IA Carbonates. *Cent. Eur. J. Chem.* **2**, 347–362 (2004).

230. Hoke, E. T. *et al.* Reversible photo-induced trap formation in mixed-halide hybrid perovskites for photovoltaics. *Chem. Sci.* **6**, 613–617 (2015).

231. Utzat, H. *et al.* Probing Linewidths and Biexciton Quantum Yields of Single Cesium Lead Halide Nanocrystals in Solution. *Nano Lett.* **17**, 6838–6846 (2017).

232. Nedelcu, G. *et al.* Fast Anion-Exchange in Highly Luminescent Nanocrystals of Cesium Lead Halide Perovskites (CsPbX3, X = Cl, Br, I). *Nano Lett.* **15**, 5635–5640 (2015).

233. Zhang, F. *et al.* Brightly luminescent and color-tunable colloidal CH3NH3PbX3 (X = Br, I, Cl) quantum dots: Potential alternatives for display technology. *ACS Nano* **9**, 4533–4542 (2015).